

Technical Report Documentation Page

1. Report No. ABC-UTC-2016-C1-UNR01-Final	2. Government Accession No.	3. Recipient's Catalog No.	
4. Title and Subtitle Numerical Modeling Techniques of High-Speed Rail Bridge Structures		5. Report Date September 2020	
		6. Performing Organization Code	
7. Author(s) Andrew Stephenson, Mohamed A. Moustafa (https://orcid.org/0000-0002-1006-7685)		8. Performing Organization Report No.	
9. Performing Organization Name and Address Department of Civil and Environmental Engineering University of Nevada, Reno 1664 N. Virginia St., MS 0258 Reno, NV 89557		10. Work Unit No. (TRAIS)	
		11. Contract or Grant No. 69A3551747121	
12. Sponsoring Organization Name and Address Accelerated Bridge Construction University Transportation Center Florida International University 10555 W. Flagler Street, EC 3680 Miami, FL 33174		13. Type of Report and Period Covered Final Report 01/2018-08/2020	
		14. Sponsoring Agency Code US Department of Transportation Office of the Assistant Secretary for Research and Technology And Federal Highway Administration 1200 New Jersey Avenue, SE Washington, DC 201590	
15. Supplementary Notes Visit www.abc-utc.fiu.edu for other ABC reports.			
16. Abstract High-speed rail (HSR) is a complex system incorporating various technical aspects such as infrastructure, rolling stock (specially-designed train sets), telecommunications, operating conditions, and equipment. With the requirements for deflections, rotations, and natural frequencies of HSR bridge structures, comprehensive understanding of the HSR dynamic interactions is a topic of growing interest. Accordingly, many studies over the past few decades have been conducted, mostly internationally, with a focus on dynamic interaction between the different components of HSR train/bridge systems through sophisticated structural models. The focus of this research is to identify these modeling features and inherent characteristics of HSR bridges, and to provide guidance and demonstration examples on how to develop such models in OpenSees. The main objective of this study was to create a comprehensive modeling guideline for HSR bridge systems. To do so, a thorough literature review was conducted to synthesize various methods of numerical modeling techniques used to model HSR systems. Literature published from national and international sources were reviewed and compiled to demonstrate how the individual components within a train system, track system, and bridge system have been modeled in previous studies. The synthesis also identified the similarities and differences regarding the different finite element modeling techniques for different components. Based on the studies analyzed in the literature search, a prototype train system and track-bridge system were selected to construct a fully detailed example HSR bridge model. The prototypes were selected based on available information regarding the design of the prototype components to minimize assumptions necessary to model the prototype system. A step-by-step guide of the processes of formulating the model and analysis parameters from start to end were documented, accompanied by snapshots from a sample OpenSees model input file for guidance and future use. To exemplify potential use of the developed model for informing future designs using OpenSees data output, sample static and dynamic analyses were performed with load cases without train loading and with train loading on the prototype HSR bridge. Additionally, a brief analytical study was performed to demonstrate the HSR bridge seismic performance using three different ground motions. The ground motions were retrieved from the PEER Ground Motion Database and were amplified to various degrees to perform nonlinear time history analysis. The nonlinear analysis considered four load cases for unloaded bridge and the bridge with a train on top in three sample load cases to observe the sensitivity of seismic analysis based on the addition and location of train loading. From the preliminary analysis results of the prototype HSR bridge modeled as a demonstration, the location of the train loading did not show significant influence on the local and global response of the bridge. At larger scale of ground motions, the bridge showed instances of higher nonlinearity with load cases with train loading which suggest that the train-bridge interaction better be considered when informing and optimizing future HSR bride designs in high-seismic areas.			
17. Key Words HSR, HSR Model, Numerical Modeling Techniques		18. Distribution Statement No restrictions.	
19. Security Classification (of this report) Unclassified.	20. Security Classification (of this page) Unclassified.	21. No. of Pages 142	22. Price

(this page is intentionally left blank)

Numerical Modeling Techniques of High-Speed Rail Bridge Structures

Final Report

August 2020

Principal Investigator: Mohamed A. Moustafa

Department of Civil and Environmental Engineering
Florida International University

Authors

Andrew Stephenson
Mohamed A. Moustafa

Sponsored by

Accelerated Bridge Construction University Transportation Center



ACCELERATED BRIDGE CONSTRUCTION
UNIVERSITY TRANSPORTATION CENTER

A report from

University of Nevada, Reno

Department of Civil and Environmental Engineering, MS 258

1664 N. Virginia St.

Reno, NV 89557

www.unr.edu/cee

DISCLAIMER

The contents of this report reflect the views of the authors, who are responsible for the facts and the accuracy of the information presented herein. This document is disseminated in the interest of information exchange. The report is funded, partially or entirely, by a grant from the U.S. Department of Transportation's University Transportation Program. However, the U.S. Government assumes no liability for the contents or use thereof.

ABSTRACT

High-speed rail (HSR) is a complex system incorporating various technical aspects such as infrastructure, rolling stock (specially-designed train sets), telecommunications, operating conditions, and equipment. The highly sophisticated technology combining these elements, as well as the elements themselves continue to evolve as the new transportation mode continues to expand and its intrinsic characteristics pose design issues unique to HSR systems. With the requirements for deflections, rotations, and natural frequencies of HSR bridge structures, comprehensive understanding of the HSR dynamic interactions is a topic of growing interest. Accordingly, many studies over the past few decades have been conducted, mostly internationally, with a focus on dynamic interaction between the different components of HSR train/bridge systems through sophisticated structural models. The focus of this research is to identify these modeling features and inherent characteristics of HSR bridges, and to provide guidance and demonstration examples on how to develop such models in OpenSees. Such models will aid researchers and designers in conducting parametric studies to test the static, modal, and dynamic performance of future HSR bridge designs to formulate a national standard for HSR infrastructure in the United States.

The main objective of this study was to create a comprehensive modeling guideline for HSR bridge systems. To do so, a thorough literature review was conducted to synthesize various methods of numerical modeling techniques used to model HSR systems. Literature published from national and international sources were reviewed and compiled to demonstrate how the individual components within a train system, track system, and bridge system have been modeled in previous studies. The synthesis also identified the similarities and differences regarding the different finite element modeling techniques for different components. Based on the studies analyzed in the literature search, a prototype train system and track-bridge system were selected to construct a fully detailed example HSR bridge model. The prototypes were selected based on available information regarding the design of the prototype components to minimize assumptions necessary to model the prototype system. A step-by-step guide of the processes of formulating the model and analysis parameters from start to finish were documented, accompanied by snapshots from a sample OpenSees model input file for guidance and future use.

To exemplify potential use of the developed model for informing future designs using OpenSees data output, sample static and dynamic analyses were performed with load cases without train loading and with train loading on the prototype HSR bridge. Additionally, a brief analytical study was performed to demonstrate the HSR bridge seismic performance using three different ground motions. The ground motions were retrieved from the PEER Ground Motion Database and were amplified to various degrees to perform nonlinear time history analysis. The nonlinear analysis considered four load cases for unloaded bridge and the bridge with a train on top in three sample load cases to observe the sensitivity of seismic analysis based on the addition and location of train loading. From the preliminary analysis results of the prototype HSR bridge modeled as a demonstration, the location of the train loading did not show significant influence on the local and global response of the bridge. At larger scale of ground motions, the bridge showed instances of higher nonlinearity with load cases with train loading which suggest that the train-bridge interaction better be considered when informing and optimizing future HSR bridge designs in high-seismic areas.

ACKNOWLEDGMENTS

This study was funded by the Accelerated Bridge Construction University Transportation Center (ABC-UTC) 2016 Grant led by Florida International University. This funding and research opportunity associated with it is acknowledged.

CONTENTS

DISCLAIMER	IV
ABSTRACT	V
ACKNOWLEDGMENTS	VI
CONTENTS.....	VII
LIST OF FIGURES	IX
LIST OF TABLES.....	XVI
Chapter 1. INTRODUCTION	1
1.1. BACKGROUND AND MOTIVATION	1
1.2. PROBLEM DESCRIPTION	2
1.3. RESEARCH OBJECTIVES AND SCOPE OF WORK.....	2
1.4. ORGANIZATION OF REPORT	3
Chapter 2. SYNTHESIS OF NATIONAL AND INTERNATIONAL STUDIES ON THE TOPIC OF NUMERICAL MODELING OF HIGH-SPEED RAIL SYSTEMS.....	4
2.1. MODELING OF TRAIN SYSTEMS.....	4
2.1.1. <i>Traditional Vehicle System</i>	5
2.1.2. <i>Articulated Vehicle System</i>	8
2.2. MODELING OF RAILWAY TRACK SYSTEMS	9
2.2.1. <i>Rail</i>	9
2.2.2. <i>Ballasted Track System</i>	9
2.2.3. <i>Ballastless Track System</i>	12
2.3. MODELING OF BRIDGE SYSTEMS	14
2.3.1. <i>Deck and Girder</i>	14
2.3.2. <i>Pier Column</i>	17
2.3.3. <i>Pier Column Foundation</i>	17
2.3.4. <i>Isolation Bearing</i>	18
2.4. GENERAL MODELING PROCEDURES	19
2.4.1. <i>Rigid Connection Arm</i>	19
2.4.2. <i>Viscous Damping</i>	20
Chapter 3. HSR BRIDGE SYSTEM NUMERICAL MODEL: SELECTION OF PROTOTYPE SYSTEM AND MODELING PROCEDURE.....	21
3.1. SELECTION OF PROTOTYPE HSR SYSTEM	21
3.1.1. <i>Train System Prototype</i>	21
3.1.2. <i>Track and Bridge System Prototype</i>	22
3.2. NUMERICAL MODEL IN OPENSEES.....	23
3.2.1. <i>Basic Model Definitions</i>	23

3.2.2.	<i>Train System Model</i>	25
3.2.3.	<i>Train System Model</i>	31
3.2.4.	<i>Bridge System Model</i>	36
Chapter 4.	DEMONSTRATION OF GRAVITY, MODAL, AND SEISMIC ANALYSIS OF HSR BRIDGE SYSTEM	41
4.1.	GRAVITY LOAD ANALYSIS.....	41
4.1.1.	<i>Gravity Load Analysis Setup</i>	41
4.1.2.	<i>Gravity Load Analysis Results</i>	42
4.2.	MODAL LOAD ANALYSIS	46
4.3.	SEISMIC LOAD ANALYSIS	47
4.3.1.	<i>Seismic Load Analysis Setup</i>	47
4.3.2.	<i>Seismic Load Analysis Results</i>	48
Chapter 5.	SEISMIC RESPONSE OF PROTOTYPE HSR BRIDGE SYSTEM: MORE IN-DEPTH DEMONSTRATION	69
5.1.	MAXIMUM RESPONSE TABLES.....	71
5.2.	SEISMIC BEHAVIORAL GRAPHS.....	85
Chapter 6.	SEISMIC RESPONSE OF PROTOTYPE HSR BRIDGE SYSTEM: MORE IN-DEPTH DEMONSTRATION	105
6.1.	SUMMARY	105
6.2.	CONCLUSIONS.....	106
6.3.	RESEARCH IMPACT	107
6.4.	VALIDITIES AND LIMITATIONS	108
REFERENCES	109
APPENDIX A: OPENSEES COMMANDS	113
APPENDIX B: SELECTED SCRIPTS FROM OPENSEES INPUT FILE.....		120

LIST OF FIGURES

Figure 2-1. China-star high-speed train [41].....	4
Figure 2-2. Views of the KHST (a) panoramic view, (b) articulated bogie located between the car bodies, (c) articulated bogie and (d) composition of the train (front power car) [19].....	5
Figure 2-3. Front view of the sprung-mass dynamic car model [29].....	7
Figure 2-4. Tradition train system modeled by He et al., [13].....	7
Figure 2-5. Traditional train system modeled by Liu et al., [24].....	7
Figure 2-6. Articulated train system modeled by Kwark et al., [19].	8
Figure 2-7. Bogie–bridge interaction system in an articulated train system modeled by Song et al., [36].....	9
Figure 2-8. Photo of ballasted track system [33].	10
Figure 2-9. Ballasted track system modeled by Song et al., [36].	11
Figure 2-10. Ballasted track system modeled by Montenegro et al., [29].....	11
Figure 2-11. Ballasted track system modeled by Guo et al., [11].....	11
Figure 2-12. Photo of ballastless track system [39].....	12
Figure 2-13. Japanese type RCRS slab track on grade [38].	13
Figure 2-14. Track system scheme with fasteners (a) and longitudinal boundary spring hysteresis loop (b) by Li and Conte, [23].	13
Figure 2-15. Modeling schematic of ballastless track system modeled by Li et al., [22].....	13
Figure 2-16. Modeling schematic of track-bridge system by Montenegro et al., [29].	15
Figure 2-17. Modeling schematic of track-bridge system by Li and Conte, [23].....	15
Figure 2-18. Modeling schematic of bridge system by Li et al., [22].....	16
Figure 2-19. Modeling schematic of bridge system by He et al., [13].	16
Figure 2-20. Concrete box girder modeled using shell elements by Song et al., [36].....	16
Figure 2-21. Modeling schematic of bridge pier columns using fiber-based elements by Kaviani et al., [17].	17
Figure 2-22. Pile foundation model using dynamic p-y approach: (a) schematic view of the FE model, (b) pile cap mode [23].	18
Figure 2-23. Modeling schematic of rigid connections by Kaviani et al., [17].....	19
Figure 3-1. Photo of KTX-Sancheon [6].	21
Figure 3-2. Schematic of the prototype bridge: a) Elevation layout of high-speed railway bridge/cm, b) Schematic sketch of track and girder structure [22].....	22
Figure 3-3. Schematic of the prototype bridge typical cross-section of track and girder structure [22].	23

Figure 3-4. Schematic drawing for the numerical modeling of train system (Top: Cross-section, Bot: Elevation).....	26
Figure 3-5. Schematic of track system.....	31
Figure 3-6. Schematic of track-bridge system.	32
Figure 3-7. Parameters of zero-length connection elements in the track-bridge system as adopted from Li et al., [22].	33
Figure 3-8. Force-deformation behavior of track system connection layers: (a) Fastener, (b) CA mortar, (c) Shear reinforcement, (d) Sliding layer, and (e) Lateral blocking.....	34
Figure 3-9. Schematic of track-bridge system.	35
Figure 3-10. Force-deformation behavior of bridge bearings: (a) Fixed bearing, (b) Sliding bearing.	37
Figure 3-11. Finite element model of bridge.	38
Figure 4-1. Train load cases used for Chapter 4.	45
Figure 4-2. Vertical bridge girder displacements under static analysis for both load cases.	45
Figure 4-3. Vertical bridge girder displacements under Load Case 1.	51
Figure 4-4. Vertical bridge girder displacements under for Load Case 8.....	51
Figure 4-5. Transverse bridge girder displacements under Load Case 1.....	52
Figure 4-6. Transverse bridge girder displacements under Load Case 8.....	52
Figure 4-7. Displacement time-history of column #2 under Load Case 1 in:.....	53
Figure 4-8. Displacement time-history of column #6 under Load Case 1 in:.....	54
Figure 4-9. Displacement time-history of column #8 under Load Case 1 in:.....	55
Figure 4-10. Displacement time-history of column #11 under Load Case 1 in:.....	56
Figure 4-11. Displacement time-history of column #2 under Load Case 8 in:.....	57
Figure 4-12. Displacement time-history of column #6 under Load Case 8 in:.....	58
Figure 4-13. Displacement time-history of column #8 under Load Case 8 in:.....	59
Figure 4-14. Displacement time-history of column #11 under Load Case 8 in:.....	60
Figure 4-15. Force-displacement relationship of column #2, #6, #8, and #11 in the longitudinal direction for: (a) Load Case 1, (b) Load Case 8.	61
Figure 4-16. Force-displacement relationship of column #2, #6, #8, and #11 in the transverse direction for: (a) Load Case 1, (b) Load Case 8.	62
Figure 4-17. Bridge girder shear in the longitudinal direction (V_x) for Load Case 1.	63
Figure 4-18. Bridge girder shear in the transverse direction (V_y) for Load Case 1.	63
Figure 4-19. Bridge girder shear in the vertical direction (V_z) for Load Case 1.....	64
Figure 4-20. Bridge girder moment in the longitudinal direction (M_x) for Load Case 1.....	64

Figure 4-21. Bridge girder moment in the transverse direction (M_y) for Load Case 1.....	65
Figure 4-22. Bridge girder moment in the vertical direction (M_z) for Load Case 1.	65
Figure 4-23. Bridge girder shear in the longitudinal direction (V_x) for Load Case 8.	66
Figure 4-24. Bridge girder shear in the transverse direction (V_y) for Load Case 8.	66
Figure 4-25. Bridge girder shear in the vertical direction (V_z) for Load Case 8.....	67
Figure 4-26. Bridge girder moment in the longitudinal direction (M_x) for Load Case 8.....	67
Figure 4-27. Bridge girder moment in the transverse direction (M_y) for Load Case 8.....	68
Figure 4-28. Bridge girder moment in the vertical direction (M_z) for Load Case 8.	68
Figure 5-1. Train load cases used in the seismic analysis in Chapter 5.....	70
Figure 5-2. PEER database ground motions used for the seismic performance assessment: (a) Northridge, (b) Kobe, and (c) Loma Prieta.	70
Figure 5-3. Longitudinal displacement time-history for columns #3, #6, and #11 at 100% – (Row: (1) Northridge, (2) Kobe, and (3) Loma Prieta, Column: (1) Load Case 1, (2) Load Case 6, and (3) Load Case 9).	88
Figure 5-4. Longitudinal displacement time-history for columns #3, #6, and #11 at 200% – (Row: (1) Northridge, (2) Kobe, and (3) Loma Prieta, Column: (1) Load Case 1, (2) Load Case 6, and (3) Load Case 9).	89
Figure 5-5. Transverse displacement time-history for columns #3, #6, and #11 at 100% – (Row: (1) Northridge, (2) Kobe, and (3) Loma Prieta, Column: (1) Load Case 1, (2) Load Case 6, and (3) Load Case 9).	90
Figure 5-6. Transverse displacement time-history for columns #3, #6, and #11 at 200% – (Row: (1) Northridge, (2) Kobe, and (3) Loma Prieta, Column: (1) Load Case 1, (2) Load Case 6, and (3) Load Case 9).	91
Figure 5-7. Longitudinal force-displacement relationship for columns #6, #8, and #11 at 100% – (Row: (1) Northridge, (2) Kobe, and (3) Loma Prieta, Column: (1) Load Case 1, (2) Load Case 6, and (3) Load Case 9).	92
Figure 5-8. Longitudinal force-displacement relationship for columns #6, #8, and #11 at 200% – (Row: (1) Northridge, (2) Kobe, and (3) Loma Prieta, Column: (1) Load Case 1, (2) Load Case 6, and (3) Load Case 9).	93
Figure 5-9. Transverse force-displacement relationship for columns #6, #8, and #11 at 100% – (Row: (1) Northridge, (2) Kobe, and (3) Loma Prieta, Column: (1) Load Case 1, (2) Load Case 6, and (3) Load Case 9).	94
Figure 5-10. Transverse force-displacement relationship for columns #6, #8, and #11 at 200% – (Row: (1) Northridge, (2) Kobe, and (3) Loma Prieta, Column: (1) Load Case 1, (2) Load Case 6, and (3) Load Case 9).	95
Figure 5-11. Longitudinal moment-curvature relationship for columns #1, #6, and #10 at 100% – (Row: (1) Northridge, (2) Kobe, and (3) Loma Prieta, Column: (1) Load Case 1, (2) Load Case 6, and (3) Load Case 9).	96

Figure 5-12. Longitudinal moment-curvature relationship for columns #1, #6, and #10 at 200% – (Row: (1) Northridge, (2) Kobe, and (3) Loma Prieta, Column: (1) Load Case 1, (2) Load Case 6, and (3) Load Case 9).	97
Figure 5-13. Transverse moment-curvature relationship for columns #1, #6, and #10 at 100% – (Row: (1) Northridge, (2) Kobe, and (3) Loma Prieta, Column: (1) Load Case 1, (2) Load Case 6, and (3) Load Case 9).	98
Figure 5-14. Transverse moment-curvature relationship for columns #1, #6, and #10 at 200% – (Row: (1) Northridge, (2) Kobe, and (3) Loma Prieta, Column: (1) Load Case 1, (2) Load Case 6, and (3) Load Case 9).	99
Figure 5-15. Longitudinal displacement time-history for columns #3, #6, and #11 at Northridge 300% – (Left: Load Case 1, Middle: Load Case 6, Right: Load Case 9).	100
Figure 5-16. Transverse displacement time-history for columns #3, #6, and #11 at Northridge 300% – (Left: Load Case 1, Middle: Load Case 6, Right: Load Case 9).	100
Figure 5-17. Longitudinal force-displacement relationship for columns #6, #8, and #11 at Northridge 300% – (Left: Load Case 1, Middle: Load Case 6, Right: Load Case 9).	101
Figure 5-18. Transverse force-displacement relationship for columns #6, #8, and #11 at Northridge 300% – (Left: Load Case 1, Middle: Load Case 6, Right: Load Case 9).	101
Figure 5-19. Longitudinal moment-curvature relationship for columns #1, #6, and #10 at Northridge 300% – (Left: Load Case 1, Middle: Load Case 6, Right: Load Case 9).	102
Figure 5-20. Transverse moment-curvature relationship for columns #1, #6, and #10 at Northridge 300% – (Left: Load Case 1, Middle: Load Case 6, Right: Load Case 9).	102
Figure 5-21. Force-deformation relationship of fasteners supporting rail 1 under Northridge 300%: (a) Above column #4, (b) Above column #6.	103
Figure 5-22. Force-deformation relationship of fasteners supporting rail 2 under Northridge 300%: (a) Above column #4, (b) Above column #6.	103
Figure 5-23. Force-deformation relationship of CA mortar layers supporting track 1 under Northridge 300%: (a) Above column #4, (b) Above column #6.	104
Figure 5-24. Force-deformation relationship of sliding layers supporting track 1 under Northridge 300%: (a) Above column #4, (b) Above column #6.	104
Figure A-1. <i>model</i> command parameters [32].	113
Figure A-2. <i>node</i> command parameters [32].	113
Figure A-3. <i>fix</i> constraint command parameters [32].	113
Figure A-4. <i>equalDOF</i> constraint command parameters [32].	113

Figure A-5. <i>geomTransf Linear</i> transformation command parameters [32].....	114
Figure A-6. <i>Steel01</i> material command parameters [32].....	114
Figure A-7. <i>Steel02</i> material command parameters [32].....	114
Figure A-8. <i>Concrete02</i> material command parameters [32].....	114
Figure A-9. <i>ViscousDamper</i> material command parameters [32].....	115
Figure A-10. <i>Elastic</i> material command parameters [32].....	115
Figure A-11. <i>elasticBeamColumn</i> element command parameters [32].....	115
Figure A-12. <i>dispBeamColumn</i> element command parameters [32].....	115
Figure A-13. <i>zeroLength</i> element command parameters [32].....	116
Figure A-14. <i>twoNodeLink</i> element command parameters [32].....	116
Figure A-15. <i>section fiber</i> command parameters [32].....	116
Figure A-16. <i>patch rect</i> command parameters [32].....	117
Figure A-17. <i>layer straight</i> command parameters [32].....	117
Figure A-18. <i>section aggregator</i> command parameters [32].....	117
Figure A-19. <i>mass</i> command parameters [32].....	118
Figure A-20. <i>eigen</i> analysis command parameters [32].....	118
Figure A-21. <i>Rayleigh</i> damping command parameters [32].....	118
Figure A-22. <i>timeSeries</i> path command parameters [32].....	118
Figure A-23. <i>UniformExcitation</i> pattern command parameters [32].....	119
Figure B-1. Predefined geometric locations for train nodes.....	120
Figure B-2. Node set up for rear power car.....	121
Figure B-3. Node set up for rear intermediate passenger car.....	121
Figure B-4. Node set up for first intermediate passenger car.....	122
Figure B-5. Rigid elastic beam-column element for bogie arms in the x-direction.....	122
Figure B-6. Rigid elastic beam-column element for bogie arms in the y-direction.....	122
Figure B-7. Rigid elastic beam-column element for primary suspension arms in the.....	122
Figure B-8. Rigid elastic beam-column element for primary suspension arms in the.....	122
Figure B-9. Rigid elastic beam-column element for car-bodies.....	122
Figure B-10. Primary suspension system model for the power cars.....	123
Figure B-11. Power car primary suspension node MP-constraints with <i>equalDOF</i>	123
Figure B-12. Secondary suspension system model for the power cars.....	124
Figure B-13. Power car secondary suspension node MP-constraints with <i>equalDOF</i>	124
Figure B-14. Mass assignment for train car-bodies.....	125

Figure B-15. Mass assignment for train bogies.	125
Figure B-16. Mass assignment for power and exterior passenger car axle wheels.	126
Figure B-17. Mass assignment for intermediate passenger car axle wheels	126
Figure B-18. Node set up for rail 1 of track 1.....	127
Figure B-19. Node set up for base plate of track 1.	127
Figure B-20. Node set up for track plate of track 1.	127
Figure B-21. Elastic beam-column element for rail 3 of track 2.	127
Figure B-22. Elastic beam-column element for track plates of track 1.	127
Figure B-23. Elastic beam-column element for base plates of track 1.	127
Figure B-24. Zero-length element for fastener	128
Figure B-25. Zero-length element for lateral blocking.	128
Figure B-26. Zero-length element for CA layer.	128
Figure B-27. Zero-length element for sliding layer.	128
Figure B-28. Zero-length element for shear reinforcement.	129
Figure B-29. CA layer node MP-constraints with <i>equalDOF</i>	129
Figure B-30. Mass assignment for first two rail 1 nodes.	129
Figure B-31. Node set up for the first bridge girder span.	129
Figure B-32. Example elastic beam-column elements for bridge girder.	130
Figure B-33. Node set up for bearings supporting the first span of the bridge.....	130
Figure B-34. Zero-length elements for fixed bearings supporting the first span of the bridge.	130
Figure B-35. Zero-length elements for sliding bearings supporting the first span of the bridge.	131
Figure B-36. Bearing node MP-constraints with <i>equalDOF</i>	131
Figure B-37. Material properties for pier columns.	131
Figure B-38. Section designer for pier cross-section.	132
Figure B-39. Predefined geometric values for pier columns.	132
Figure B-40. Node set up for first two columns.	133
Figure B-41. Displacement-based fiber-section beam-column elements for first pier column.....	133
Figure B-42. Node set up for column footings and ground.	133
Figure B-43. Column footings and ground node SP-constraints using <i>fix</i>	134
Figure B-44. Zero-length element for bridge-soil interaction.	134

Figure B-45. Rigid elastic beam-column element for footings of columns #1 and #2.....	135
Figure B-46. Rigid elastic beam-column element for column-bearing connections at column #1.....	135
Figure B-47. Rigid elastic beam-column element for girder-bearing connections above	135
Figure B-48. Rigid elastic beam-column element for first two girder-track system connections.	135
Figure B-49. Mass assignment for first two nodes of bridge girder.	135
Figure B-50. Mass assignment for first two nodes of column #1.....	135
Figure B-51. Mass assignment for footings of column #1 and #2.....	135
Figure B-52. Dead loads for train car-bodies and bogies.	136
Figure B-53. Dead loads for power and extreme passenger car axle-wheels.	137
Figure B-54. Dead loads for intermediate passenger car axle-wheels.....	138
Figure B-55. Dead loads for rail 1 (first four nodes).	138
Figure B-56. Dead loads for track plate for track 1 (first four nodes).	138
Figure B-57. Dead loads for base plate for track 1 (first four nodes).	138
Figure B-58. Dead loads for first bridge girder span.	139
Figure B-59. Dead loads for first pier column.	139
Figure B-60. Dead loads for foundations.....	139
Figure B-61. Definition of gravity load analysis parameters.....	140
Figure B-62. Performance of gravity load analysis.	140
Figure B-63. Set up for modal analysis.	140
Figure B-64. Set up for Rayleigh damping.	141
Figure B-65. Definition of seismic load analysis parameters.	141
Figure B-66. Definition of ground motion parameters.	141
Figure B-67. Application of ground motion in both directions.	141
Figure B-68. Performance of seismic load analysis.....	142

LIST OF TABLES

Table 3-1. Prototype HSR Model Element and Material.....	25
Table 3-2. Dynamic Characteristics of Train Model [19].....	28
Table 3-3. Masses for Track-Bridge System.	31
Table 3-4. Section parameters of elastic beam elements in track-bridge system as adopted from Li et al., [22].....	36
Table 4-1. Example HSR bridge system load cases based on the train position above the bridge (the cases represent instances of the train crossing the bridge).	44
Table 4-2. Column Base Reactions (kN) in Direction 3 from Static Analysis.	44
Table 4-3. Periods for first 10 modes.....	46
Table 5-1. Maximum Local Responses – Northridge 100% Scale.	73
Table 5-2. Maximum Local Responses – Northridge 200% Scale.	74
Table 5-3. Maximum Local Responses – Kobe 100% Scale.....	75
Table 5-4. Maximum Local Responses – Kobe 200% Scale.....	76
Table 5-5. Maximum Local Responses – Loma Prieta 100% Scale.....	77
Table 5-6. Maximum Local Responses – Loma Prieta 200% Scale.....	78
Table 5-7. Maximum Global Responses – Northridge 100% Scale.	79
Table 5-8. Maximum Global Responses – Northridge 200% Scale.	80
Table 5-9. Maximum Global Responses – Kobe 100% Scale.....	81
Table 5-10. Maximum Global Responses – Kobe 200% Scale.....	82
Table 5-11. Maximum Global Responses – Loma Prieta 100% Scale.	83
Table 5-12. Maximum Global Responses – Loma Prieta 200% Scale.	84

Chapter 1. INTRODUCTION

1.1. Background and Motivation

A transportation solution that has always been considered for the past few decades is the high-speed rail (HSR). The successful commercial operation of the Japanese Shinkansen, (bullet train) in 1964 marked the beginning of a new era for HSR and the development of HSR spread throughout the world. Plans for HSR in the United States date back to the High-Speed Ground Transportation Act of 1965 (Public Law 89-220, 79 Stat. 893) which was the first attempt by the U.S. Congress to foster the growth of HSR. Although the United States was one of the world's first countries to have a high-speed rail service in place with the Metroliner operating between Washington, D.C., and New York City in 1969, the trend did not spread through the rest of the country. Various state and federal HSR propositions followed but full implementation of an inter-state HSR has never been accomplished. The closest the United States currently has to an HSR system is the Acela, formerly known as Acela Express. The Acela is a high-speed service along the Northeast Corridor in the Northeastern United States operated by Amtrak and replaced the aging Metroliner [4]. The Acela provides a route from Washington, D.C. to Boston with 16 intermediate stops which makes the service inter-state, but the top speeds of 240 km/h limits the service to be categorized as a higher-speed rail (HrSR). Higher-speed rail is the jargon used to describe inter-city passenger rail services that have top speeds higher than conventional rail but are not high enough to be considered high-speed rail services [5]. Typically, an inter-city rail service must have a minimum speed of 250 km/h to be considered as a high-speed rail service.

In 2008, the California HSR network was authorized by voters with Proposition 1A which would mark the largest project for American HSR, connecting the bay area to southern California. At the time of the proposal, the project was sold to voters with a projected cost of \$33.6 billion; however, by 2018 the California High-Speed Rail Authority revised its estimate to \$77.3 billion and up to \$98.1 billion anticipating a 2033 completion year [16]. Unfortunately, the fluctuating project cost estimates and delays has led to cancelation of major federal grants which funded the project. Construction for the maiden California HSR infrastructure finally started in 2017 but all segments besides the Central Valley segment from Bakersfield to Merced are indefinitely postponed due to cost overruns and delays as of 2020.

On the contrary, an interstate project between California and Nevada and a project in Texas is progressing towards success as of 2020. XpressWest, a passenger rail project connecting Las Vegas and greater Los Angeles, has received the rights to build on the median of Interstate 15 which runs through Southern California and Intermountain West. This privately funded project was acquired by Florida-based passenger rail operator Virgin Trains USA and anticipates its first service in 2023 [8]. An HSR line is also being proposed between Dallas and Houston by a private railroad company called Texas Central. Current plans include utilizing technology based on that of the Central Japan Railway Company with rolling stock based on an international version of the N700 Series Shinkansen [7].

Independent of the California HSR progress, privately funded HSR projects are bringing an upward trend to a successful implementation of monumental HSR in the United States. Thus, providing guidance on the modeling, analysis, and design of HSR infrastructure and structural systems could be greatly beneficial to inform future national and local HSR research and projects within the United States.

1.2. Problem Description

Bridges are a key component of the HSR infrastructure because it can avoid the interruption of existing roadways and the occupation of land. China, the world's largest user of HSR, incorporates bridges as a major part of their HSR infrastructure, covering more than 50% of their total HSR mileage [43]. As of February 2020, China has over 35,000 km of HSR track in operation and continues their advancement as the world's unrivaled largest user of HSR in operation with the next largest being Spain with 3,000 km [28]. Several other European countries have built extensive HSR networks that now include several cross-border international HSR links and the European Union continues to invest in the development of HSR infrastructure. Countries within these regions have developed a standard design for their HSR infrastructure and stands as a great design reference for future projects within the United States.

The inherent characteristics of HSR raise new problems beyond those found in typical highway construction, so comprehensive numerical approaches on the bridge structure modeling are needed. Good understanding of the sensitivity of a bridge span vertical deflections and rotational deformations, as well as train-track-bridge dynamic interactions and coupling vibrations are of great importance when designing HSR bridges. Compared with a conventional railway bridge, the design of HSR bridges require a higher service limit to minimize deformations and avoid excessive vibrations or resonance due to the crossing of trains to improve the riding comfort for passengers. The focus of this research is to identify these modeling features and inherent characteristics of HSR bridges and provide guidance and demonstration examples on how to develop such models. These models will aid researchers and designers in conducting parametric studies to test the static, modal, and dynamic performance of HSR designs to inform and optimize future designs, and eventually formulate a national design standard for HSR infrastructure in the United States.

1.3. Research Objectives and Scope of Work

The main objectives of this study were to: (1) synthesize available national and international literature on modeling and numerical simulation of HSR systems, (2) identify critical modeling features needed to develop a detailed finite element model, based on synthesized literature, that captures HSR train-track-structure interaction when simulating service loads and extreme events such as earthquakes, and (3) develop a step-by-step guide on the modeling and analysis of HSR bridge systems in OpenSees, an open source framework developed by the Pacific Earthquake Engineering Center.

To achieve the first objective, modeling techniques from literature published by researchers around the world were analyzed and compiled to understand the dynamic train-track-bridge interactions. Studies modeling different types of high-speed train systems, track systems, and bridge systems were explicitly researched to offer a comprehensive literature search that will allow the reader to gain insight on the modeling techniques of various HSR systems.

From previous studies, a prototype train, track, and bridge system were selected based on available information that can be incorporated into a prototype model. The selections were then used to create a detailed HSR model in OpenSees using the modeling techniques synthesized in the extensive literature search to achieve the second objective. The model was created to demonstrate the functionality of the modeling techniques highlighted in the first objective. The model was further tested under service loads and ground motion excitations to demonstrate the various capabilities and analyses that can be performed.

To achieve the third objective, a walk-through of the steps taken to model the selected prototype HSR system from start to finish was documented along with recommendations and assumptions made during the process. Further demonstration of the nonlinear seismic response of the prototype HSR bridge was presented through a brief analytical study. The latter highlighted the performance under various train loading scenarios and ground motions amplified to various degrees. This objective aims to encourage better understanding of HSR bridge behavior in high seismic areas. Overall, this study contributes to the advancement of research involving HSR systems by creating a readily comprehensible guideline for students, researchers, and bridge designers to embark on creating their own HSR models for future studies.

1.4. Organization of Report

This report is organized into six chapters and two appendices. Following the first introduction chapter, Chapter 2 provides an in-depth literature review on the numerical modeling of train, track, and bridge systems that make up HSR systems. Chapter 3 presents a guide on modeling a sample high-speed rail system by selecting prototype train, track, and bridge systems and demonstrating the numerical modeling techniques researched in the literature. Chapter 4 provides a demonstration for gravity load analysis, modal analysis, and seismic analysis of the structural model created in Chapter 3 along with interpretations for the structural response from the respective analyses. Chapter 5 presents a more in-depth seismic performance analysis of the structural model by conducting nonlinear time history analysis under three different ground motions with various intensities and for different train load cases. Chapter 6 outlines the summary and conclusions from this research, along with providing the research impact and recommendations for future works. The first appendix provides screenshots for the key adopted OpenSees commands and syntax for reader convenience. The second appendix provide the step-by-step script examples from a sample OpenSees input file.

Chapter 2. SYNTHESIS OF NATIONAL AND INTERNATIONAL STUDIES ON THE TOPIC OF NUMERICAL MODELING OF HIGH-SPEED RAIL SYSTEMS

Following the rapid growth of high-speed railway transportation and the advancement of railway technology driven by an increasing demand for more efficient, cost-effective, and safer railway transportation, precise analysis of dynamic interaction for vehicles and bridges has become an issue of great significance. To encourage comprehensive understanding of proper idealization of such systems, modeling techniques for train, track, and bridge systems from national and international studies, and available design guidelines have been studied and synthesized in their respective sections. The scope of the literature search conducted herein focuses mainly on the modeling of superstructure components, and only briefly touches upon the modeling methods of substructure components.

2.1. Modeling of Train Systems

High-speed train systems are mainly constituted by two vehicle systems: traditional vehicle systems and articulated vehicle systems. A traditional vehicle system is characterized by two bogies or trucks in the fore and rear parts of the car-body, and each passenger car behaves independently (Figure 2-1). Each vehicle has one car-body, two bogies, and four wheelsets. On the contrary, an articulated vehicle system as shown in Figure 2-2 connects successive passenger cars by a single bogie frame (Figure 2-2b), but the power car and motorized car at each end of the high-speed train are still supported by their own bogies like a traditional vehicle system (Figure 2-2d). The articulated vehicle system restrains the composition of the train but is proven to effectively improve the riding conditions compared to traditional vehicle systems by reducing the vibration generated in each car body [36].

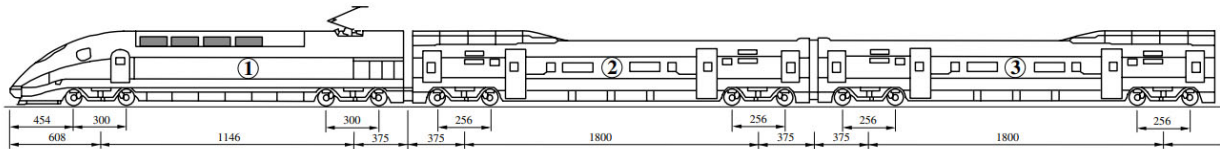


Figure 2-1. China-star high-speed train [41].

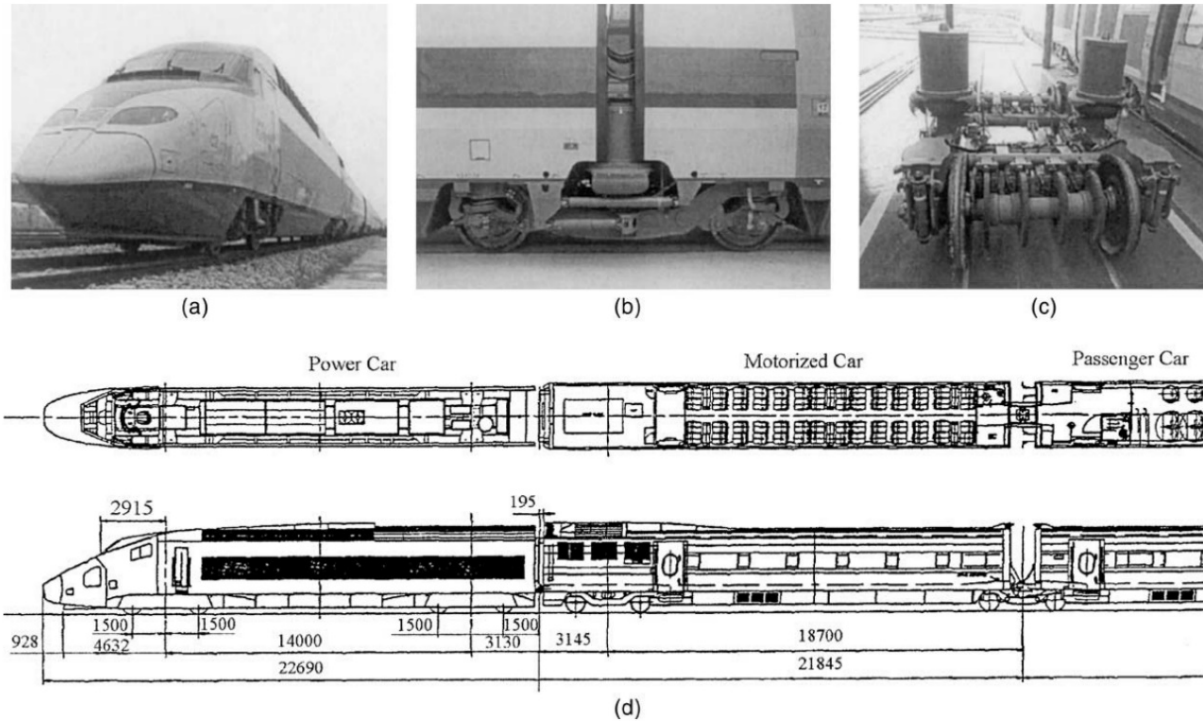


Figure 2-2. Views of the KHST (a) panoramic view, (b) articulated bogie located between the car bodies, (c) articulated bogie and (d) composition of the train (front power car) [19].

2.1.1. Traditional Vehicle System

In early studies, vehicles were often approximated as a moving mass model to consider the inertial effects of moving vehicles and to allow the problem to be solved analytically. However, the effect of the suspension system must be considered for accurate vehicle response. The simplest model in this regard is a lumped mass supported by a spring-dashpot unit, often referred to as the sprung-mass model [2, 9, 14, 15, 26, 27, 37, 40, 41, 44, 45, 50]. The sprung-mass dynamic system can reflect the motions of the vehicle in both the vertical and horizontal directions. The car-body, bogies and wheelsets in each vehicle are assumed as rigid bodies, neglecting elastic deformation, and are connected to each other three-dimensionally by linear springs and dampers. The primary and secondary suspension systems of the bogies are simplified as an elastic system with linear springs and viscous dampers. Placement of the spring-dashpot units within each suspension system differ slightly among studies depending on the type of HSR train system and the specific bogie design, as can be seen by comparing the various train model schematics in Figure 2-3 through Figure 2-7.

Another method is to model the car-bodies, bogies, and wheelsets as beam finite elements and the suspension system as a variation of bilinear and multilinear springs in the three directions. Montenegro et al., [29] have modeled all springs characterized by a bilinear behavior, except the one used to model the secondary transversal suspension which follows a multilinear law to simulate the presence of rubber stoppers whose stiffness increases gradually (Figure 2-5). Nonlinear springs can be used to model the suspension system, but most of the studies have simplified the analysis by assuming a linear behavior.

The car-bodies and bogies are typically assumed to move along a well-maintained straight track at a constant speed, and the wheels and the track to always keep in contact, neglecting sliding, climbing or derailment phenomena [13, 24, 26, 36, 47, 50]. The assumption of perfect contact between wheel and track is commonly represented as the vehicle-track interaction by coupling the displacement degree-of-freedom (DOF) relationships between the rail and wheel-set subsystems. A Hertzian contact spring can be placed in-between each wheel and rail to accurately model the wheel-rail contact stiffness by consider the changing contact area caused by the indentation of the rail due to the geometry of the wheel [3, 30, 35].

The main difference of vehicle modeling among studies is the selection of the DOFs to be concerned in the car-body, bogies, and wheelsets. Each node has a maximum of six DOFs in finite element modeling but not every DOF is taken into consideration depending on the study. Typically, each car-body and each bogie have five DOFs in consideration: lateral displacement, roll displacement, yaw displacement, vertical displacement, and pitch displacement. The sliding displacement is often omitted because the high-speed train is assumed to be in motion and not stationary [2, 24, 37, 42]. Although rolling and sliding motions would be excited due to torsional vibrations and track irregularities, these motions are commonly constrained for efficiency of formulation [36]. On the contrary, Xia and Zhang, [41] and Liu et al., [24] have included the rolling motion in the concerned DOFs. If the train system is being modeled in a scenario where seismic loading is present, the rolling motion should be accounted for because the seismic loading would heavily excite the rolling motion in the car-bodies and bogies, as the wheel-sets are assumed to stay in direct contact with the rails. The concerned DOFs for the wheelsets can be limited to the lateral displacement, vertical displacement, and the roll displacement [24, 26]. The other DOFs can be neglected because the wheelset is constantly in rotation and the wheels always stay in contact with the track system. Various schematics of traditional vehicle systems are shown in Figure 2-3, Figure 2-4, and Figure 2-5 as previously mentioned.

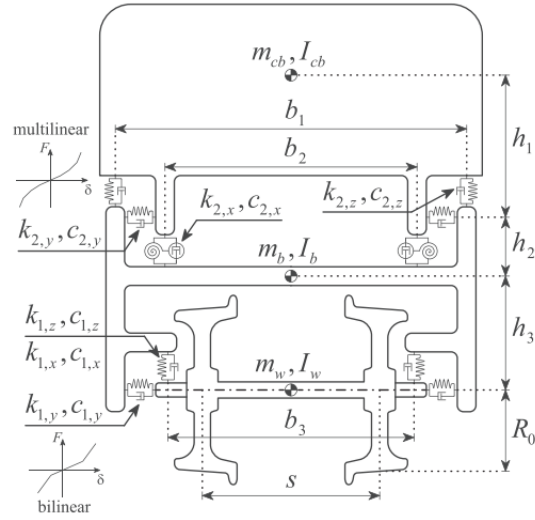


Figure 2-3. Front view of the sprung-mass dynamic car model [29].

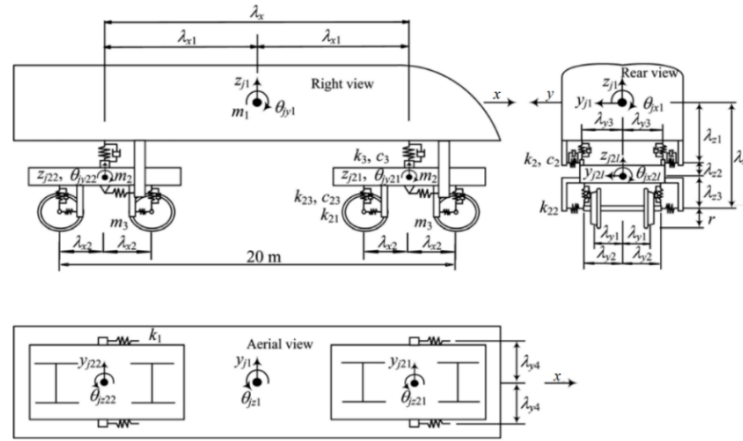


Figure 2-4. Tradition train system modeled by He et al., [13].

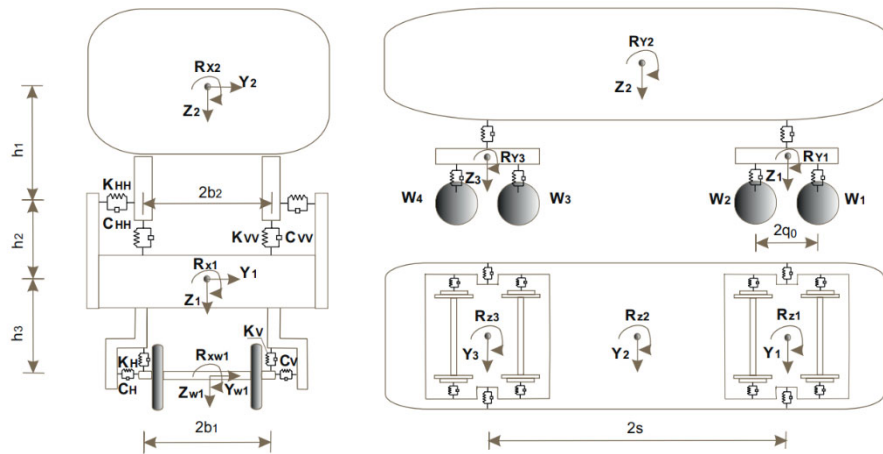


Figure 2-5. Traditional train system modeled by Liu et al., [24].

2.1.2. Articulated Vehicle System

For articulated vehicle systems, each passenger car no longer behaves independently, and the behavior of each bogie will be affected by the dynamic behavior of the fore and rear car-bodies. Aside from the coupling of intermediate passenger cars, the modeling procedure of articulated vehicle systems are similar to the traditional vehicle system. The model by Kwark et al., [19] individually modeled the car-bodies, the bogie in between, and the wheels with DOFs as shown in Figure 2-6. Additional damping due to a central elastic hinge in-between adjacent car-bodies was modeled by transverse springs and dampers, also seen in the model by Xia et al., [42]. Another method is to model the fore and rear car-body behavior as a single joint directly above the articulated bogie. In Song et al., [36] study, the bouncing, swaying, pitching and yawing motions are considered for the non-articulated power cars and these motions were condensed into two DOFs by the bouncing motion and swaying motion at the joint for the articulated vehicles, as shown in Figure 2-7. The bogie considered the bouncing, sliding, swaying, pitching, rolling, and yawing motion, so each car had a total of 16 DOFs. The car-body masses are lumped at the joints and the bogies are connected through rigid bodies with masses. This method was also followed by Rocha et al., [35].

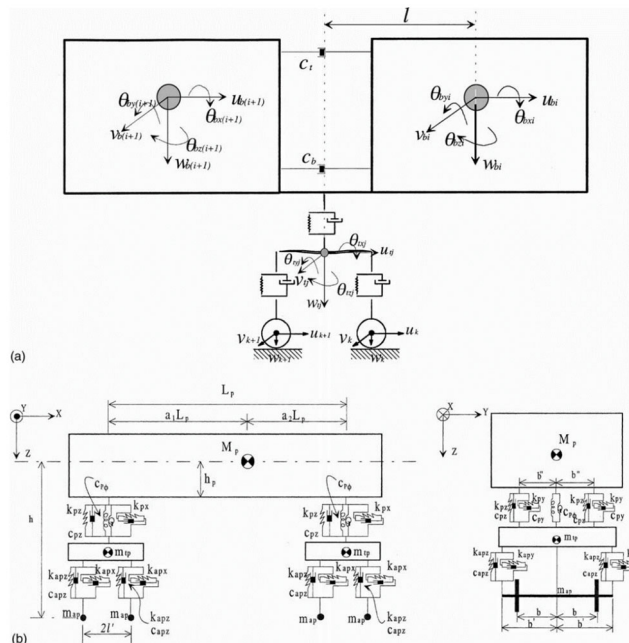


Figure 2-6. Articulated train system modeled by Kwark et al., [19].

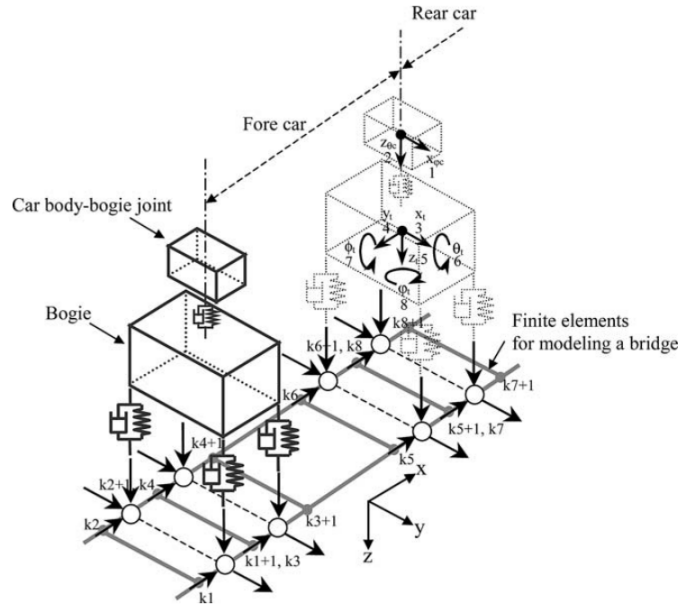


Figure 2-7. Bogie–bridge interaction system in an articulated train system modeled by Song et al., [36].

2.2. Modeling of Railway Track Systems

2.2.1. Rail

Rails in HSR systems mainly rest on two types of foundations: ballasted foundations and ballastless foundations. For both systems, a single track consists of two rails that are designed to behave elastically as a capacity protected element. Therefore, they are modeled as a series of linear elastic beam-column elements, and this method is consistent throughout numerous research studies investigated for this report [22, 23, 24, 50]. If bridge abutments are being modeled, the rail elements should be extended past the abutments to the embankments to correctly represent the transition zone [23, 29].

When the train system is being modeled as a moving load, rail irregularity is commonly considered to simulate the complex time-varying random dynamic behavior that occurs when a high-speed train crosses over a bridge. Safety, stability, comfort, service-life of train and track components, as well as the environmental noise of the train is influenced by irregularity in the rails [25]. Vertical irregularity considers roughness of the rail surface, elastic deformation, inelastic deformation, inconsistency of gap components, and uneven subsidence of track foundations. Rail irregularities are approximately represented as stationary and ergodic processes in space due to its random nature and is most frequently characterized by power spectral density (PSD) functions [30, 35, 36, 49]. The PSD functions are adjusted based on the characteristics of the rails used in each country.

2.2.2. Ballasted Track System

For ballasted track systems, rails rest on an elastic foundation composed of track ballast and railroad ties (Figure 2-8). Ballast is the crushed material placed on the top layer of a bridge superstructure to allow the embedment and support of railroad ties, also known as sleepers. The ballast is traditionally made of interlocking sharp-edged hard stone to stabilize the track system. Rails are fixed to railroad sleepers by fasteners. Rail pads are placed between the rail and tie to act

as a damper that reduces fatigue cracking of fasteners due to impact. Rail ties are rectangular wood or reinforced concrete supports placed transverse to the rail and maintains correct gauge spacing between the rails.

A ballasted track system modeled by Song et al., [36] is shown in Figure 2-9. The figure demonstrates a simple model with rails and sleepers as beam elements and ballast as Winkler springs to idealize a two-parameter elastic foundation that models the interaction between the track and the bridge deck. Ties were modeled as beam elements and lay on the ballast, modeled similar to the Winkler foundation consisting of infinite closely spaced linear springs. It is noted that the traditional Winkler foundation, based on the Winkler hypothesis, does not consider interaction of springs. On the contrary, the additional second parameter suggested by Zhaohua and Cook, [51] considers the effects of the interaction between the linear spring-dampers which accurately represents characteristics of practical foundations.

The ballasted track system modeled by Montenegro et al., [29] similarly modeled rails and sleepers as beam elements (Figure 2-10). The stiffness and damping of the rail pads/fasteners are combined and modeled as linear spring-dampers to simulate the dynamic behavior of this layer. The ballast and non-structural elements such as safeguard and edge beams of the deck were modeled as point mass elements. Spring-dampers are also used to idealize the stiffness and damping of the ballast layer in the longitudinal, transversal, and vertical directions.

Guo et al., [11] modeled both the sleepers and ballast as point mass elements at an interval. The sleepers were connected to the rail through distributed spring-dampers simulating the dynamic behavior of rail pads. The vertical and horizontal stiffness and damping of the ballast were idealized with spring-dampers which also connect the ballast layer to the sleepers. Shear stiffness of the ballast layer was also explicitly modeled as spring-dampers, and rigid arms connected the ballast to the bridge deck (Figure 2-11).

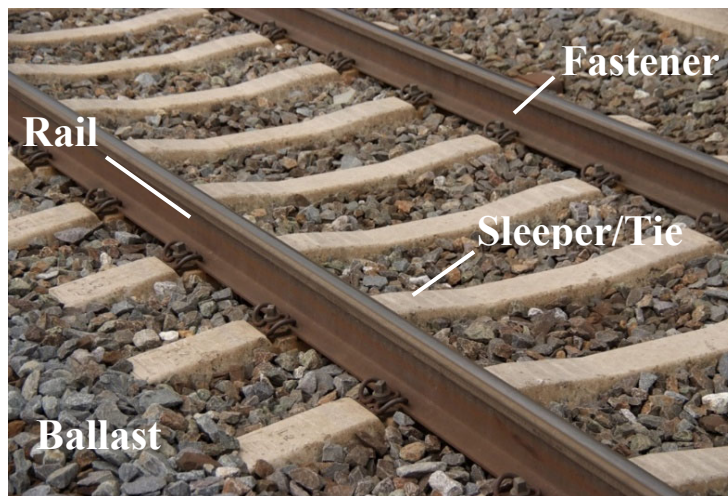


Figure 2-8. Photo of ballasted track system [33].

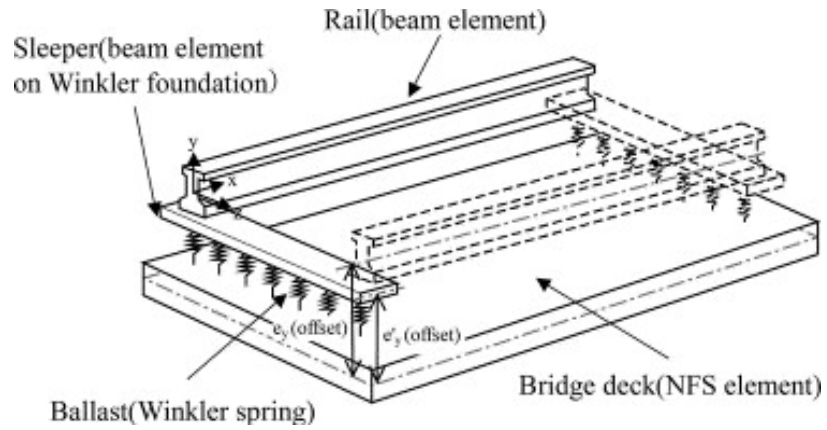


Figure 2-9. Ballasted track system modeled by Song et al., [36].

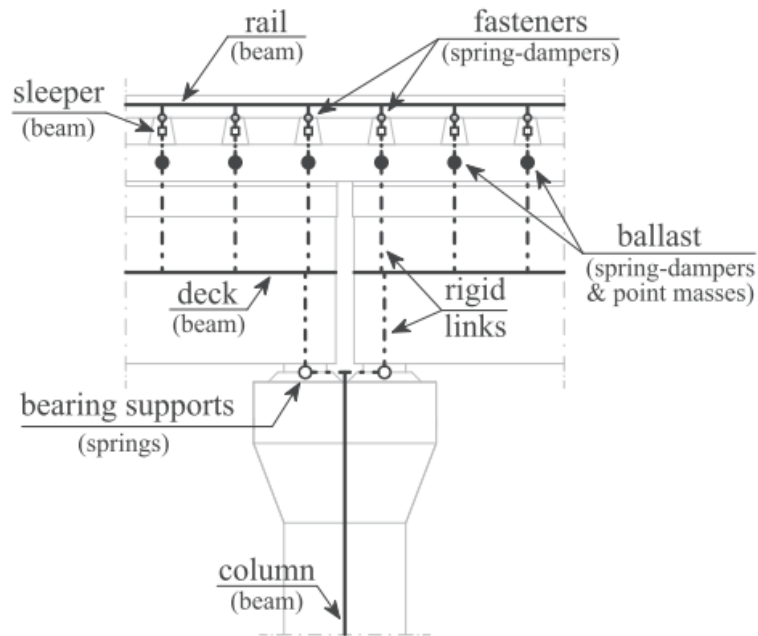


Figure 2-10. Ballasted track system modeled by Montenegro et al., [29].

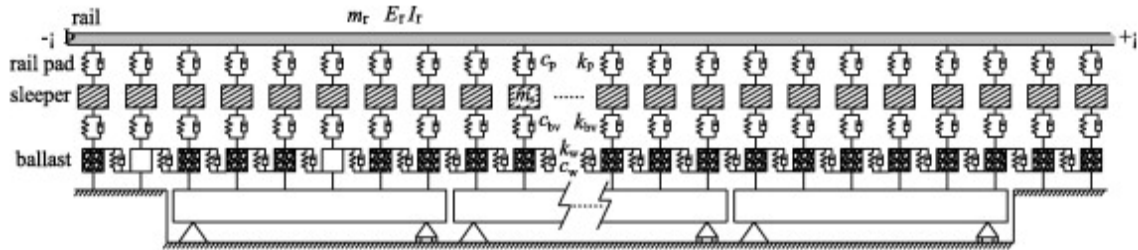


Figure 2-11. Ballasted track system modeled by Guo et al., [11].

2.2.3. Ballastless Track System

As the name suggests, ballastless track systems utilize slabs instead of ballast (Figure 2-12). The typical design includes continuous welded rails, track plates, base plates, and connecting members [22, 23]. Connecting members can vary depending on regional design standards. In the study by Li et al., [22], the China Railway Track System (CRTS) II ballastless track was adopted and includes sliding layers, shear cogging, concrete asphalt (CA) mortar layers, shear reinforcement, fasteners, and lateral blocks as connection members. Similarly, the Japanese reinforced concrete roadbed system (RCRS) slab track utilizes fasteners, track slabs and CA mortar (Figure 2-13). The study by Li and Conte, [23] for the California High Speed Rail (CHSR) Authority adopted connecting members of direct fixation fasteners for rail-track slab attachment and cylinder bollards as shear reinforcement to anchor the track slab to the concrete base plate. Figure 2-14(a) demonstrates the modeling schematic of a CHSR ballastless track system by Li and Conte, [23]. The rails were connected to the rigid deck through direct fixation fasteners modeled as a series of three elastic and inelastic springs to represent the behavior between the rails and track base.

To represent the rail-structure interaction, linear springs were used to model the vertical and transverse stiffness, and an elastic–perfectly–plastic (EPP) spring was used to model the resistance of the track base against the relative longitudinal displacement of the rail track. Additionally, longitudinal boundary springs were modeled at each rail end because of the finite length modeling of the rail extensions to accurately capture seismic response performance. A nonlinear spring model, defined as a single element, denoted as series-parallel (S-P) spring model, was developed to represent the longitudinal boundary spring. A mechanical model was developed to calibrate and validate the rail boundary spring model, and the cyclic hysteresis behavior of the mechanical and S-P model is shown in Figure 2-14(b). The closeness of the behavior validates the S-P model.

In the China Railway Track System (CRTS) study by Li et al., [22], the track plate and base plate were modeled using linear elastic beam-column elements with their respective cross-section parameters because they are designed to behave elastically as capacity protected elements (Figure 2-15). The connection components consisting of the sliding layer, CA mortar layer, fastener, shear reinforcement, and lateral block are simulated using nonlinear zero-length elements.



Figure 2-12. Photo of ballastless track system [39].

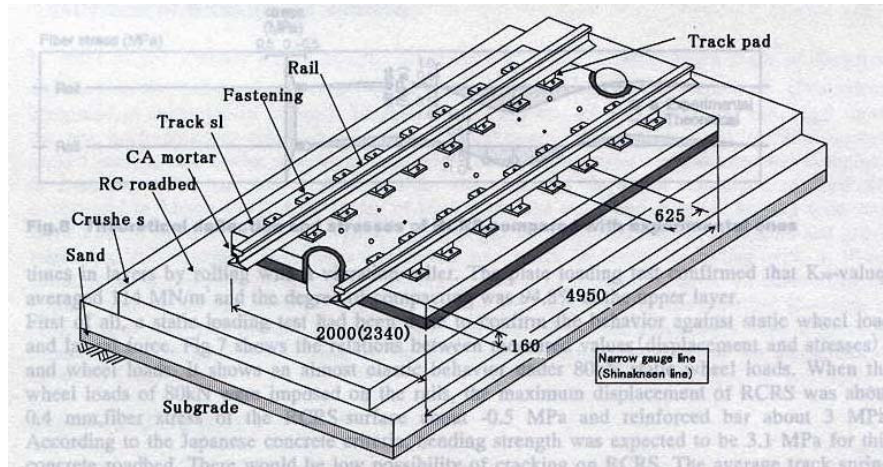


Figure 2-13. Japanese type RCRS slab track on grade [38].

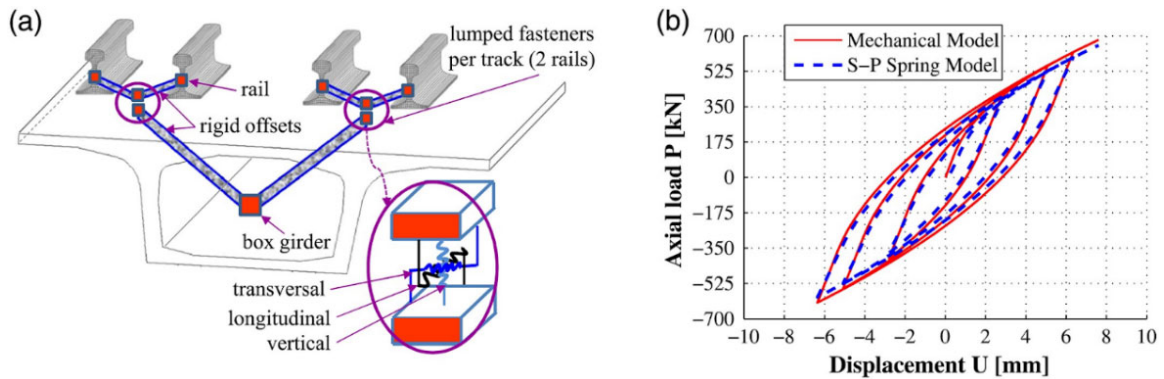


Figure 2-14. Track system scheme with fasteners (a) and longitudinal boundary spring hysteresis loop (b) by Li and Conte, [23].

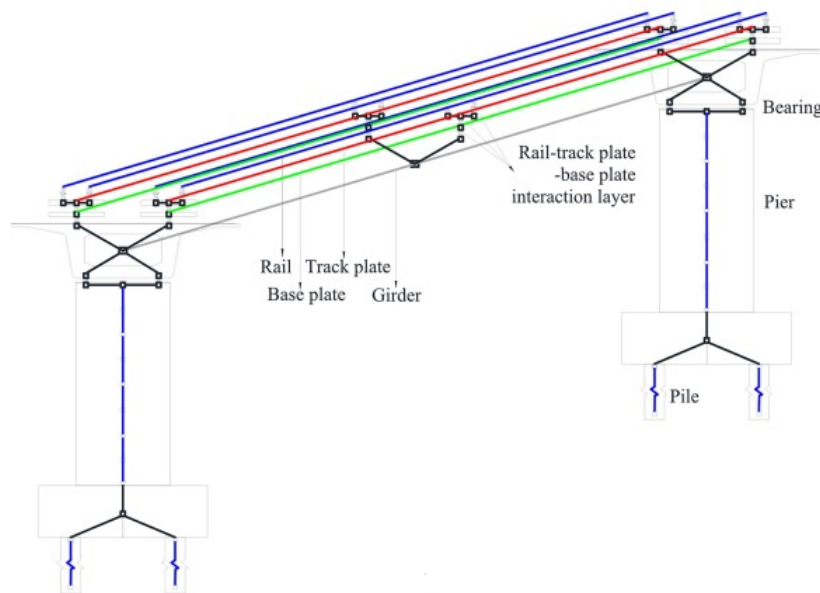


Figure 2-15. Modeling schematic of ballastless track system modeled by Li et al., [22].

2.3. Modeling of Bridge Systems

2.3.1. Deck and Girder

Concrete box girder bridges were found to be the common bridge type used in HSR systems. Such type is commonly modeled using three-dimensional linear elastic beam-column elements, even when representing bridges in highly seismic areas, since they are structurally designed to be capacity protected elements that need to remain essentially elastic [19, 22, 23, 29]. Figure 2-16 and Figure 2-17 schematically show example box-girder bridge idealization and modeling as relates to the track modeling for HSR systems from two previous studies. As shown in the figures, bridge spans are discretized into several nodal increments to allow for the representation of different section properties at the ends of each spans and to accommodate the rail track-to-deck connections and deck-to-bearing connections. Each increment was connected using linear elastic beam-column elements defined by the cross-sectional characteristics of the actual bridge being modeled, and rigid arms were used to connect the bridge girder to the rail and bearing systems. The increment lengths should be adjusted relative to the actual bridge span dimensions and based on the desired accuracy of bridge response values. Bridges have also been modeled as an assemblage of three-dimensional beam elements in the elastic domain with six DOFs at each node as illustrated in Figure 2-18 and Figure 2-19 [13, 22].

Three-dimensional shell elements have also been used to idealize bridges. Song et al., [36] utilized nonconforming flat shell elements (NFS-series) formulated by a linear combination of the nonconforming membrane element with drilling DOF (NMD-series) and the nonconforming plate bending element (NPB-series). NFS elements with six DOFs per node are used to model the box-girder structure as shown in Figure 2-20. In-plane and out of-plane deformations are coupled and the consistent mass matrix of the NFS element is lumped at the element joints using the HRZ lumping scheme [36]. When the superstructure and track system are modeled using NFS elements, consisting of four nodes with six DOFs per node, it is common engineering practice to use a relatively fine finite element grid in areas of high stress gradients due to abrupt geometrical changes or concentrated loading and a course finite element grid in areas of uniform stress gradients. Transition zones between the fine and coarse grids are modeled using variable-node NFS elements [36].

In another study, a combination of flat plate elements and beam elements were used to model a steel plate girder bridge. In Kim et al., [18] study, a steel girder bridge was idealized by modeling the concrete decks as flat plate elements with four nodes and the steel girders, cross beams, and guard rails of the bridge as linear elastic beam elements with six DOF nodes. As a similar steel bridge, a steel box girder bridge has been idealized by modeling the concrete deck as a solid element and the steel box as shell elements [24]. Headed shear studs that connect the concrete deck to the steel boxes are modeled as linear spring elements in the longitudinal direction and coupled in other directions [34].

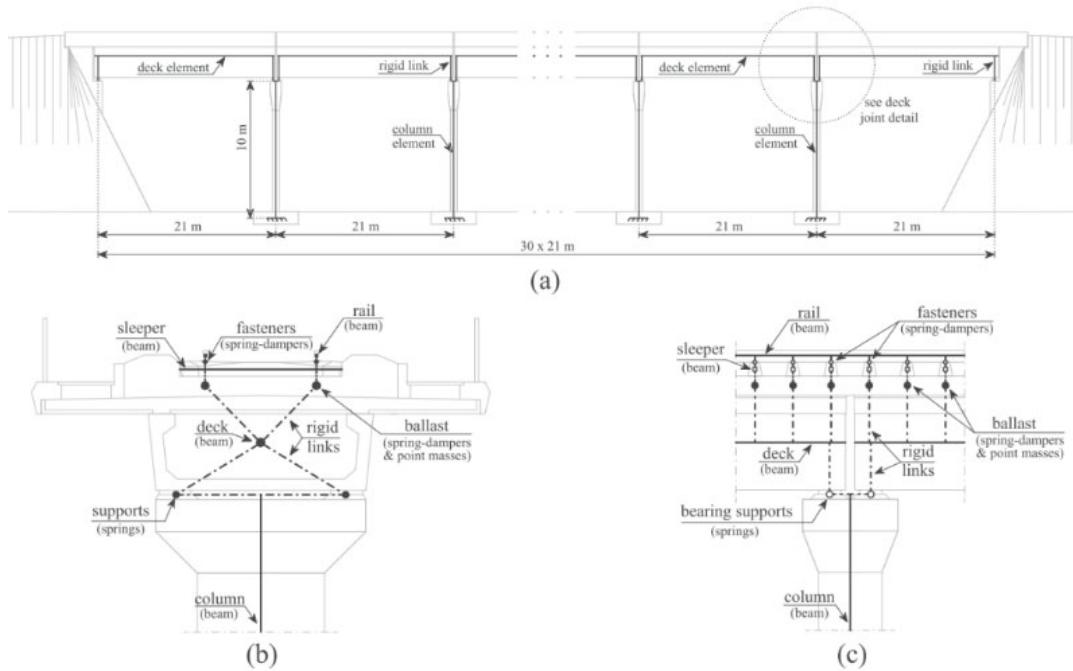


Figure 2-16. Modeling schematic of track-bridge system by Montenegro et al., [29].

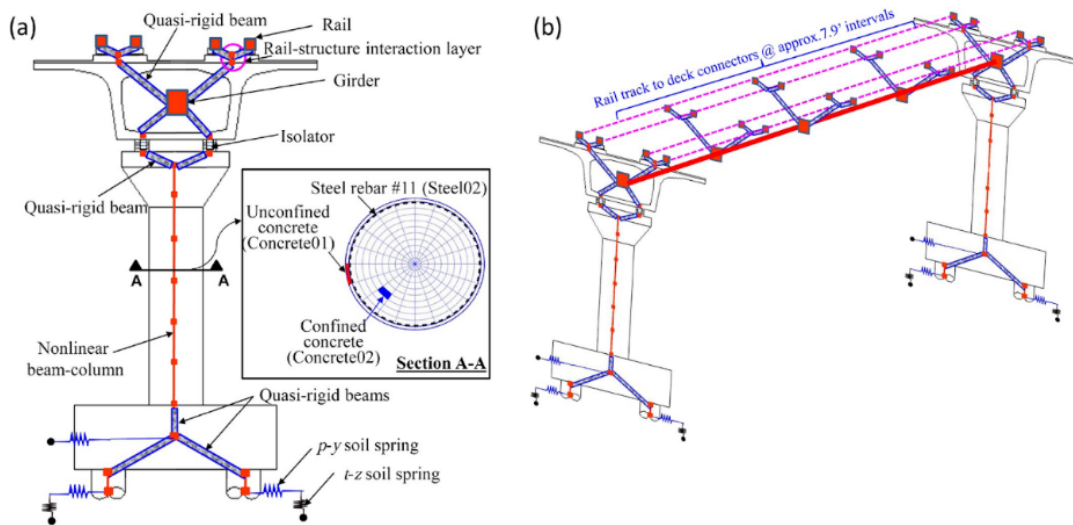


Figure 2-17. Modeling schematic of track-bridge system by Li and Conte, [23].

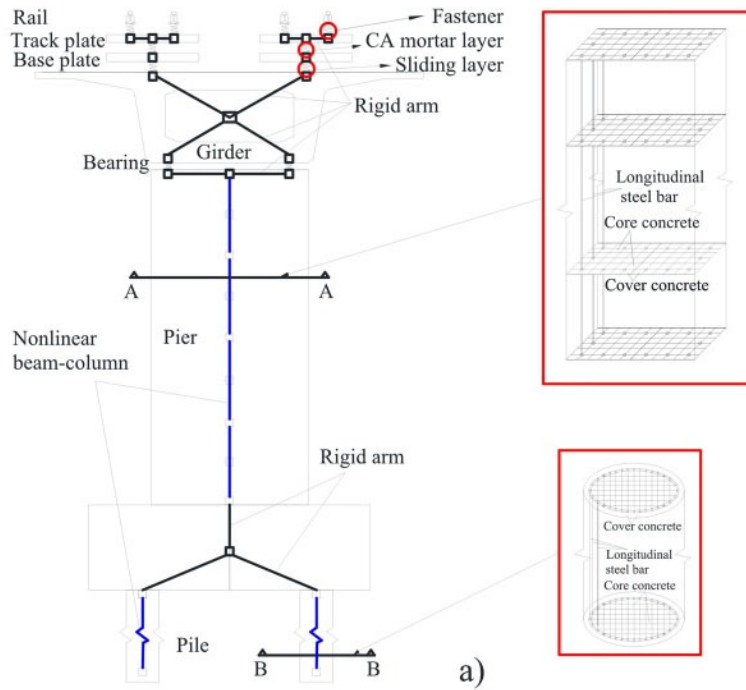


Figure 2-18. Modeling schematic of bridge system by Li et al., [22].

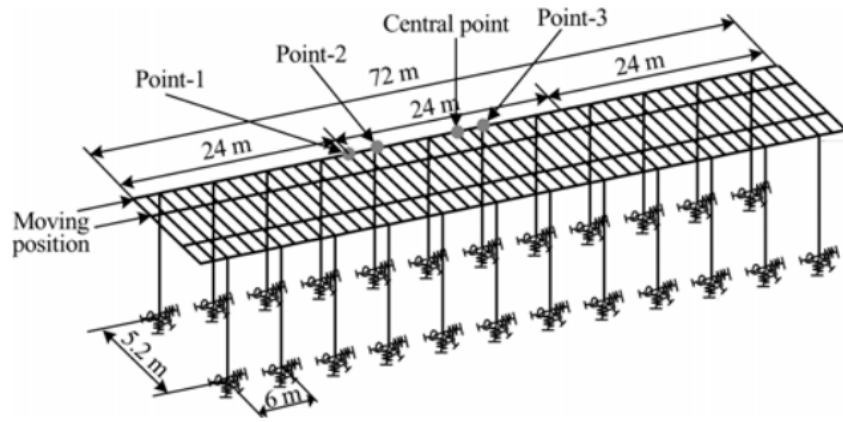


Figure 2-19. Modeling schematic of bridge system by He et al., [13].

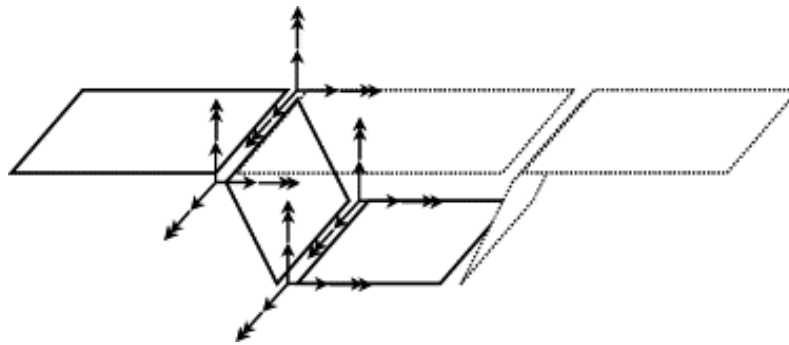


Figure 2-20. Concrete box girder modeled using shell elements by Song et al., [36].

2.3.2. Pier Column

Pier columns can be modeled using a number of fiber-based elements such as displacement-based fiber-section beam-column elements [23], fiber-based force-based beam finite elements [17], and three-dimensional elastoplastic fiber elements [22]. Fiber based elements account for material nonlinearity, geometric nonlinearity, and bond slip effect of anchoring steel in joints, making it an accurate plastic hinge representation. Integration points are placed along the length of the element in each column to allow for inelastic behavior at every point. Column cross sections are discretized into fibers in polar coordinates as shown in the Section A-A examples in Figures 2-17, 2-18, and 2-21, with a specific nonlinear uniaxial material model assigned to each fiber, i.e. unconfined concrete, confined concrete, and steel rebar [17, 22, 23]. To obtain the behavior of the nonlinear column section, the fiber behavior over the column cross-section is integrated. Potential plastic hinge regions (bottom of column for seismically isolated bridges, and both top and bottom of column for non-isolated bridges) are modeled using a single element with length equal to the plastic hinge length, approximated as half the column diameter, to ensure mesh objectivity of the finite element response prediction. The portion of the column-bent embedded in the superstructure was modeled as a rigid element attached to the top of the nonlinear beam-column element, and the length of this rigid element is set equal to the distance between the top of the column and the centroid of the soffit-flange of the box-girder.

If a bridge is being modeled to observe the response under moderate earthquakes, the columns may be modeled with a linear elastic behavior, because unlike highway bridges, the HSR bridge columns generally do not experience significant damage in this case. An alternate methodology by Montenegro et al., [29] estimated the effective stiffness of the columns performed in the elastic domain, considering reduction in stiffness due to cracking. The material behavior of the columns should be decided based on the magnitude of the excitation applied to the structural model and the overall purpose of the model. A number of studies have completely omitted the modeling of bridge piers and limited their model to the train, track, and deck/girder system [11].

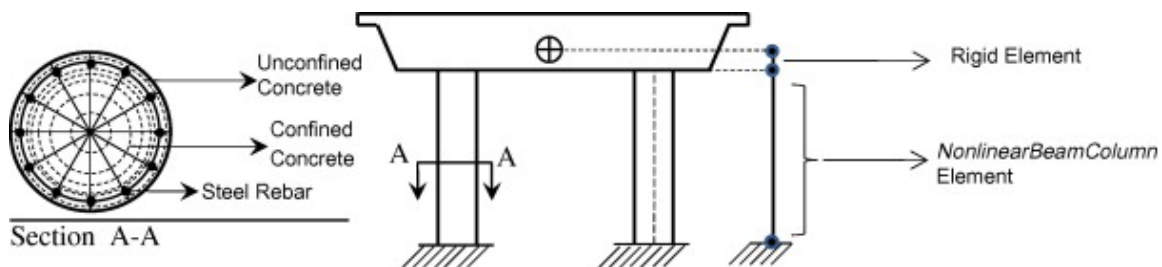


Figure 2-21. Modeling schematic of bridge pier columns using fiber-based elements by Kaviani et al., [17].

2.3.3. Pier Column Foundation

Column supports can be modeled with a variety of complexities depending on the intended study or analysis emphasis on soil-structure interaction. If the focus of the model is to analyze the train-track-structure interactions, the soil-structure interaction can be simplified to a few springs modeled between the fixed base and the bottom of the column footing elements. He et al., [13] modeled the elastic effects of column footings, pile structures and the surrounding soil by placing longitudinal and transversal ground springs at the bottom of each column.

Li and Conte, [23] have extensively modeled HSR bridge deep pile foundations using a variety of elements. The schematic from their study is shown in Figure 2-22, along with the geometric and material properties that represent the bridge site considered in their study. The well-established p-y approach was used in modeling the pile foundations and each pile was modeled through displacement-based nonlinear fiber-section beam-column elements. These piles were supported by a series of springs distributed along the length of the pile representing the resistance of the surrounding soil, p-y springs for horizontal resistance and t-z springs for vertical resistance. These springs represented the horizontal and vertical resistance of the surrounding soil, and Q-z springs were placed at the pile tips to represent the vertical soil end-bearing. Pile caps were considered essentially rigid and rigidly connected to the top of each pile, thus modeled as quasi-rigid beam elements to capture the various geometric offsets. Hyperbolic p-y springs were attached to the pile caps to represent the lateral soil resistance. Similarly, Li et al., [22] have modeled pile foundations as three-dimensional elastoplastic fiber elements. The fiber elements were divided into 1 m intervals and connected to the soil through three translational and three rotational springs with constant spring values to simulate the pile-soil interaction (Figure 2-18).

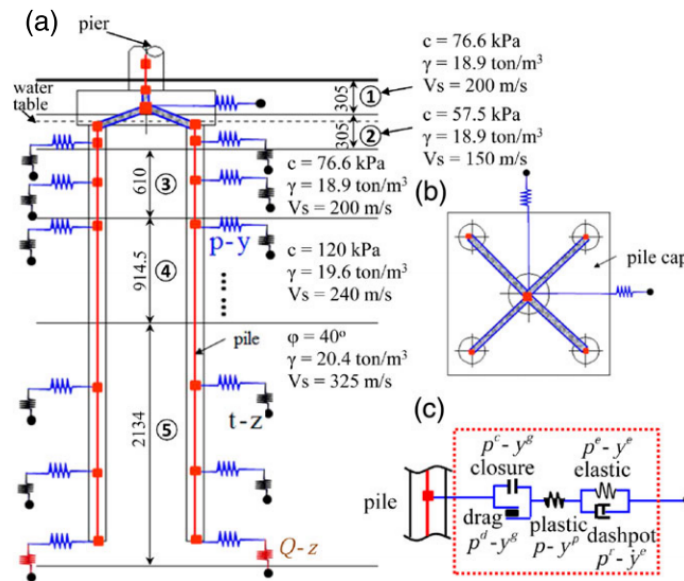


Figure 2-22. Pile foundation model using dynamic p-y approach: (a) schematic view of the FE model, (b) pile cap mode [23].

2.3.4. Isolation Bearing

A bridge bearing is a component of the bridge placed between the bridge superstructure girders and substructure pier/bent. Bearings transfer deck loads to piers or bents and allow specific movements and rotations of the superstructure. Studies that include bearings are limited but explicitly modeling bearings allows the user to capture the interaction between bridge decks and columns. Li and Conte, [23] idealized a generic seismic isolation device with a material of bilinear inelastic force-deformation behavior. Each bearing is modeled as a zero-length element combined with two uncoupled bilinear inelastic materials for the horizontal behavior: one in the longitudinal direction and the other in the transverse direction of the bridge. Li et al., [22] similarly idealized bearings as zero-length nonlinear connection elements. Each girder span was supported by four steel bearings, with alternation between fixed and spherical bearings to minimize torsional effects.

An elastic-perfectly-plastic force-deformation material behavior was used to model the nonlinear characteristics of the bearings. Linear spring-dampers were used to idealize bearing supports in a study by Montenegro et al., [29] for moderate earthquakes.

2.4. General Modeling Procedures

2.4.1. Rigid Connection Arm

Connections between bridge and track elements are commonly modeled using a type of rigid arm or element. The use of rigid arms allows the user to simplify structural components connecting these elements to each other and allow load transfer throughout the structure. For this study, rigid arms are used to connect the centroid of bridge girders to the track system and bridge girder supports in a similar way to what have been adopted in previous studies and illustrated in Figure 2-16, Figure 2-17, Figure 2-18, Figure 2-22, and Figure 2-23.

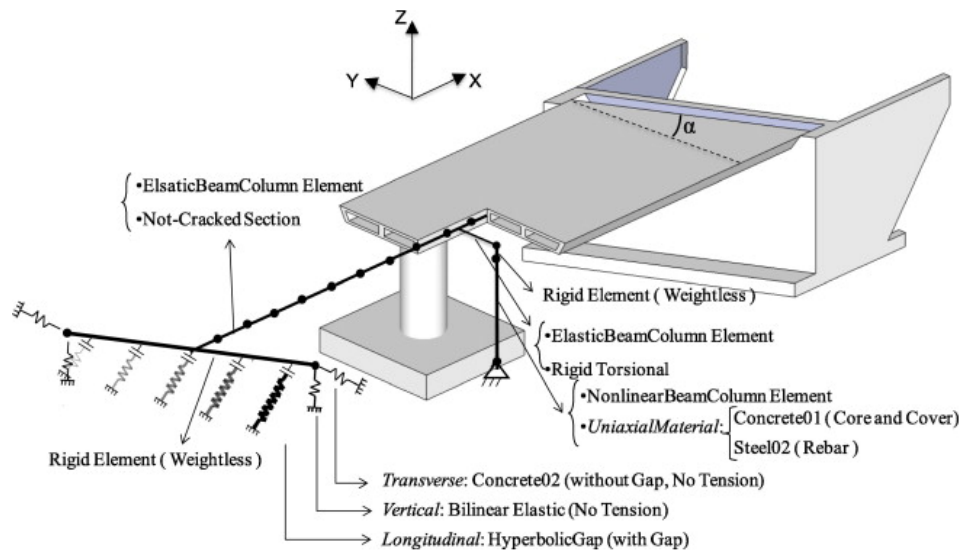


Figure 2-23. Modeling schematic of rigid connections by Kaviani et al., [17].

Linear elastic beam-column elements assigned with exceedingly stiff properties, referred to as quasi-rigid objects, can be used to represent the rigid offset between respective element nodes such as the rail and deck. Quasi-rigid objects allow the user to extract the internal forces between the two nodes in connection. The finite element model scheme utilizing quasi-rigid beam elements by Li and Conte, [23] is displayed in Figure 2-17. The figure illustrates the use of quasi-rigid beam elements to connect the centroidal axis of the box girder deck to the track system along a single span. The rigid element also connects the isolation system to the column substructure and box girder deck at the ends of each bridge span.

Another method for modeling rigid arms is to use rigid links. A rigid link is an explicit command in different analysis platforms such as OpenSees that allows the user to constrain DOFs between a master node and slave node. The command offers two types: bar/rod and beam. The bar/rod type rigid link constrains only the translational DOFs of the slave node to be the exactly the same as those at the master node. The beam type rigid link constrains both the translational and rotational DOFs of the slave node to the master node. The advantage of using rigid links is the simplification of the element stiffness matrix. Rigid links reduce computational effort but does not allow the user

to extract the internal forces between the two nodes connected by the rigid link. A modeling schematic by Montenegro et al., [29], utilizing rigid links, is shown in Figure 2-16. The placement and use of rigid links are almost identical to quasi-rigid objects discussed previously.

2.4.2. *Viscous Damping*

Energy dissipation can be idealized in finite element models through inelastic materials applied to elements, as mentioned in previous sections, and a method of viscous damping. Although the hysteretic damping included within the elements with nonlinear behavior can dissipate the majority of energy introduced by a seismic load, energy dissipation due to inherent non-hysteretic damping must be accounted for through the application of viscous damping to obtain a realistic result. A Rayleigh damping scheme with a specified damping ratio at two selected modes is commonly used to idealize such damping due to vibration, and applies to all structural components of the bridge model that are not highly nonlinear elements [10, 20, 21, 40, 50]. The Rayleigh damping scheme forms the damping matrix through a linear combination of the stiffness and mass matrices of the numerical model, and a damping ratio of 2% has been commonly used for HSR bridges [23, 29, 36]. Higher values of 3% and 5% have also been reported and used in other studies [13, 48]. The damping coefficients are usually estimated based on the dominant transverse and longitudinal vibration modes, which are estimated from an eigenvalue analysis that uses the tangent stiffness matrix of the bridge system after application of the gravity loads through static analysis.

Chapter 3. HSR BRIDGE SYSTEM NUMERICAL MODEL: SELECTION OF PROTOTYPE SYSTEM AND MODELING PROCEDURE

This chapter presents the process of formulating a sophisticated train-track-structure interaction model of a prototype HSR system. A prototype bridge, track, and train system were selected from the studies researched in the literature search. The prototype track-bridge system was selected based on the completeness of the design guideline provided in the reference study, such as bridge dimensions and cross-sectional properties. Assumptions were made where information was omitted in the reference study. This was not a major issue because the purpose of this study was to demonstrate how to model an HSR system as opposed to discuss or assessing the viability of a certain design. Similarly, the prototype train system was selected from a reference study that explicitly stated the masses of the various train components, as well as the stiffness and damping properties of the primary and secondary suspension systems, which are critical to accurately simulating the dynamic behavior of an HSR system.

3.1. Selection of Prototype HSR System

3.1.1. Train System Prototype

The prototype train system selected for this study is the KTX-Sancheon high-speed train which is shown in Figure 3-1. Formerly known as the KTX-II, the KTX-Sancheon is the second commercial high-speed train operated in South Korea as part of the Korea Train eXpress (KTX), making its debut in 2010 [6]. The KTX-Sancheon consists of two power cars at both ends and an articulated set of eight intermediate passenger cars in-between. As mentioned previously, an articulated bogie system couples a passenger car with the fore and rear passenger car, improving riding conditions of the train. As can be seen in Figure 3-1, the power cars have two standard bogies, and the extreme intermediate passenger cars have a standard bogie and an articulated bogie coupling them with the intermediate passenger cars.



Figure 3-1. Photo of KTX-Sancheon [6].

3.1.2. Track and Bridge System Prototype

The prototype track-bridge system selected for this study is a ballastless track prestressed concrete double-track simply supported girder bridge used in a publication by Li et al., [22]. The track-bridge system is from the Beijing to Xuzhou section of the Beijing-Shanghai high-speed railway. The bridge has 10 equal spans of 31.95 m with a total length of 319.5 m. The bridge superstructure is made of C50 concrete and is 13.40 m wide at the top, 5.74 m wide at the bottom, and 3.09 m deep from the top to bottom surface. Each girder end is supported by two spherical steel bearings that rest on the 11 single column bents of 13.5 m height, made of C50 concrete and HRB335 steel bars. The bridge properties and overview as obtained from the reference study is shown in Figure 3-2.

The CRTS II slab ballastless track was adopted for the track system and comprises of base plates, track plates, rails and connecting members. The connecting members include sliding layers, shear cogging, CA layers, shear reinforcement, fasteners, and lateral blocks. The CHN60 rails are fixed to the base plate through WJ-8C fasteners. The track plate is made of C55 concrete and has a width and thickness of 2.55 m and 0.20 m, respectively. The track plate is connected to the C30 concrete base plate of 2.95 m width and 0.19 m thickness through the CA layer. Shear reinforcement bars are placed at the girder ends in the CA layer to withstand the deformation caused by rotation, and the sliding layer is arranged between the bridge deck and the base plate. The sliding layer, CA layer and fasteners allow for longitudinal slippage relative to the bridge and the lateral blocking provides support in the transverse direction relative to the bridge. The layout of the connection layers is shown in Figure 3-2(b) and Figure 3-3.

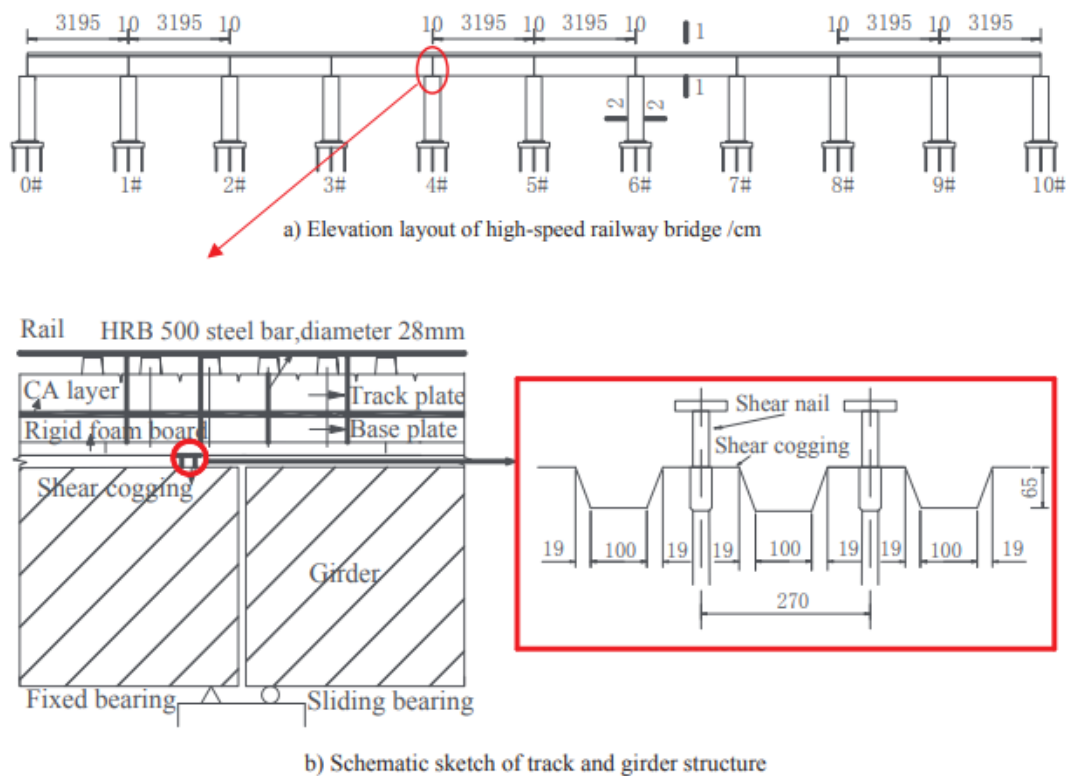


Figure 3-2. Schematic of the prototype bridge: a) Elevation layout of high-speed railway bridge/cm, b) Schematic sketch of track and girder structure [22].

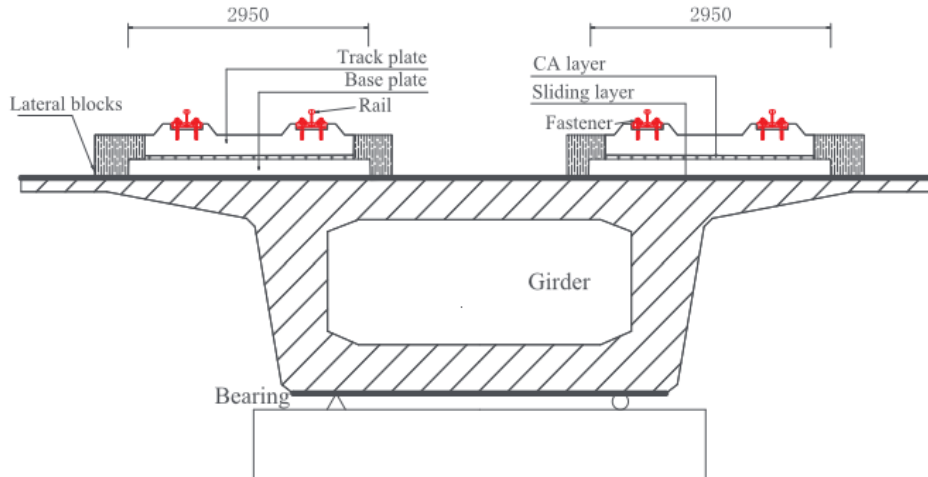


Figure 3-3. Schematic of the prototype bridge typical cross-section of track and girder structure [22].

3.2. Numerical Model in OpenSees

OpenSees is an object-oriented, open source software framework that allows users to create both serial and parallel finite element computer applications for simulating the response of structural and geotechnical systems subjected to earthquakes and other hazards [32]. OpenSees allows the user to build a structural model by using the numerous commands available in the program. The commands used in the model for this study are discussed in this section. For the convenience of the reader, the syntax and input parameter of the key OpenSees commands or functions used throughout this study are presented via series of screenshots provided in Appendix A. Moreover, sample scripts that represent or form the main sections of a typical HSR bridge model in OpenSees are provided in Appendix B. In the discussion presented in this section as well as the next chapter, specific figures from both Appendix A and Appendix B are explicitly referenced in the text for completeness and convenience. Figures from Appendix A and Appendix B use a numbering sequence that starts with A or B, respectively, such as Figure A-5 or Figure B-11 for instance.

3.2.1. Basic Model Definitions

To start a model, the user must define the spatial dimensions (1, 2, or 3) and the number of DOFs (1, 3, or 6) at each node, using the model command shown in Figure A-1. Since a three-dimensional model was created for this study, the spatial dimension was specified as 3 and the DOF at each node was specified as 6 to account for all translational and rotational movement. The user can then construct numerous nodes which will be used to construct the framework of the structure. The node command requires a unique tag number and the x, y, and z-coordinates to define the location (Figure A-2). OpenSees uses the numbers 1, 2, 3, 4, 5, and 6 to define the three translational and three rotational DOFs, respectively. For this specific model, the x-coordinates were modeled in direction 1, the y-coordinates in direction 2, and the z-coordinates in direction 3.

Single-point (SP) homogeneous boundary constraints can be implemented using the *fix* command, and multi-point (MP) constraint between nodes can be defined using the *equalDOF* command (Figure A-3 and Figure A-4). The *fix* command is typically used at the base of the structure and was used at the foundation in this model. The *equalDOF* command was used to maintain structural stability between zero-length elements where stiffness was not defined for every DOF. The way

in which the local coordinates of the elements correlate to the global coordinates of the model is defined using the *geomTransf* command (Figure A-5). This command defines how OpenSees transforms the stiffness and resisting forces of the beam element from the local system to the global-coordinate system. Specifically, the basic linear geometric transformation method was selected for this study. Careful attention should be given towards assigning the vector orientations for elements since this could result in element cross-section properties such as inertia in the local y and z axis to be flipped if defined incorrectly. A very helpful visual demonstration is provided in the OpenSeesWiki, [32] which should be referred to.

The next step is to define material properties used in the model. OpenSees has a wide variety of uniaxial materials, including steel and concrete materials. The *uniaxialMaterial* command is used to construct a material object which represents uniaxial stress-strain relationships [32]. *Steel01*, *Steel02*, *Concrete02*, *ViscousDamper* and *Elastic* material commands were used in this study to model the nonlinear behavior of the train, track, and bridge system components (Figure A-6 through Figure A-10). The *Steel01* material was used to simulate the behavior of bearings and the connection layers in the track system. *Steel02*, *Concrete02* and *Elastic* materials were used to simulate the pier columns, and *ViscousDamper* materials were used to model the train suspension system. These materials were then specified as a parameter for the construction of elements.

Three types of elements were used in the model: elastic beam-column elements, displacement-based beam-column elements, zero-length elements, and two-node links (Figure A-11 through Figure A-14). The elastic beam-column elements were used to model the elastic capacity protected elements like the bridge girder. This element command requires the section properties and not the material behavior because they remain elastic. Displacement-based beam-column elements were used to model the pier column. To accurately model the behavior of the columns, the cross-section must be modeled using the *section fiber* command (Figure A-15). The *patch* and *layer* commands allow the construction of several fibers within a predefined cross-section to model the behavior of cover concrete, core concrete, and steel reinforcement with the material properties that were defined (Figure A-16 and Figure A-17). The specific details will be explained later in Section 3.3.4.3. The fiber section can then be aggregated into an existing elastic material using the *section aggregator* command (Figure A-18). The new aggregated material can then be used as the material parameter for the displacement-based beam-column elements. *zeroLength* element were used together with the *Steel01* material to simulate the bridge bearings and track connection layers. *twoNodeLink* elements were used together with the *ViscousDamper* material to simulate the damping in the train suspension system, and the stiffness in the train suspension system was simulated using an elastic material. A complete list of elements and materials used in the prototype model is presented in Table 3-1.

The mass of each component in the model can be defined using the *mass* command in OpenSees (Figure A-19). The mass command allows the user to set the nodal mass values corresponding to each DOF. Defining masses allows the user to perform modal and dynamic analyses but is not required for static analysis. For this study, analysis of the modal and dynamic behavior of the structure was of interest, so the mass command was used to set translational and rotational mass values at every appropriate node. Mass values were applied at the nodes representing the centroid of the train system components and bridge footings, and the masses of the rest of the track-bridge system components were distributed at every node along the entire length of the rails, track and base plates, bridge girder, and pier columns.

Table 3-1. Prototype HSR Model Element and Material.

Components	Material	Element
Bridge		
Main Girder	Elastic	elasticBeamColumn
Footing	Rigid	elasticBeamColumn
Column-fiber Section	Concrete02	dispBeamColumn
	Steel02	
Foundation Springs	Elastic	zeroLength
Fixed Bearing	Steel 01	zeroLength
Sliding Bearing	Steel 01	zeroLength
Track		
Base Plate	Elastic	elasticBeamColumn
Track Plate	Elastic	elasticBeamColumn
Rail	Elastic	elasticBeamColumn
Sliding Layer	Steel 01	zeroLength
CA Mortar Layer	Steel 01	zeroLength
Fasteners	Steel 01	zeroLength
Shear Reinforcement	Steel 01	zeroLength
Lateral Blocking	Steel 01	zeroLength
Train		
Car Body	Rigid	elasticBeamColumn
Bogie	Rigid	elasticBeamColumn
Axle	Rigid	elasticBeamColumn
Axle Box Suspension	ViscousDamper	twoNodeLink
Secondary Suspension	ViscousDamper	twoNodeLink

3.2.2. Train System Model

To model the KTX-Sancheon, a study by Kwark et al., [19] was used as a reference due to the similarity of the train prototype selected. The train selected by Kwark et al., [19] is a Korean High-Speed Train (KHST) with an articulated bogie system. Based on the train configuration described in the study and the year the paper was published, the prototype train system selected by Kwark et al., [19] was assumed to be the KTX-I, which is the first set of trains used by the Korea Train eXpress (KTX). The 20-car formation (380.15 m long) of the high-speed train entered service in 2004 and is optimized for high capacity. In comparison, the KTX-Sancheon is the second commercial high-speed train operated in South Korea and was created as a shorter companion to the KTX-I. Initially, the same train prototype was considered for this study; however, the train was exceptionally long (20 cars with a total length of 380.15 m) and was conceived as unfit for the prototype bridge selected. The transition was made to the KTX-Sancheon which has similar car-body and bogie systems with roughly half the total length (193.15 m). The configuration and numerical model discretization of the prototype train model used in this study is shown in Figure 3-4.

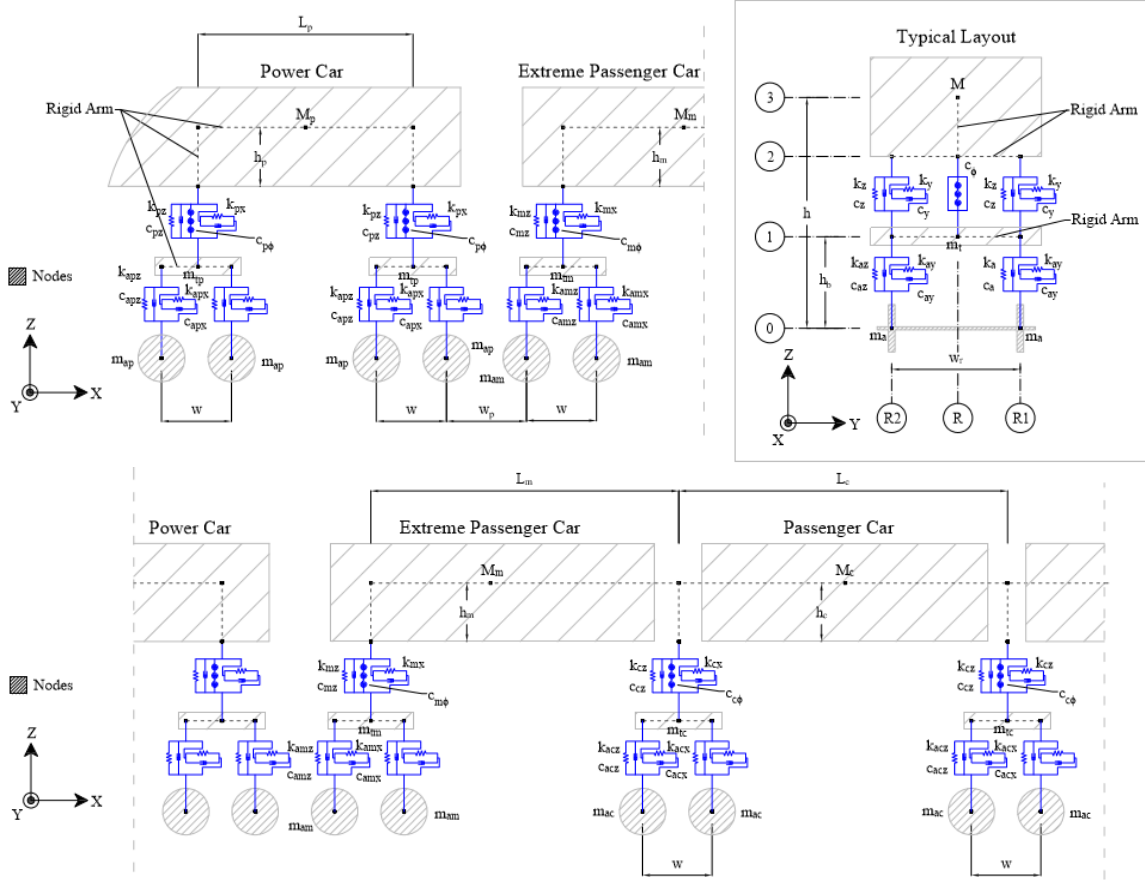


Figure 3-4. Schematic drawing for the numerical modeling of train system (Top: Cross-section, Bot: Elevation).

3.2.2.1. Train System Model Geometry

Before defining the train nodes, lateral and vertical distances for the general location and geometric design of the train system were predefined to simplify the modeling process and allow for easy modification when necessary. As mentioned before, the track system of the prototype HSR bridge selected is a double-track, which means there is a right (*R*) and left (*L*) track relative to the center of the bridge. From here onwards the right and left tracks will be referred to as tracks 1 and 2, respectively. Train dimensions retrieved from the reference study by Kwarck et al., [19] were used to define the train nodes. The train axle wheels are 3 m apart in the x-direction (w) and 2 m apart in the y-direction (w_r), so the rails for track system 1 were defined as R1 and R2 and are 1 m to the right and left of the track center line, respectively. Similarly, the rails for track system 2 were defined as R3 and R4. As previously mentioned, Appendix B provides scripts from the developed OpenSees model input file for completeness and step-by-step guidance. Figure B-1 in Appendix B is the first screenshot in the series of model definition figures which shows the predefined geometric locations for train nodes. The lateral lengths of the power car (L_p), extreme passenger car (L_m), and intermediate passenger car (L_c) were defined respectively as 14.0 m, 18.7 m, 18.7 m, as well as the total length of the bridge system (L_T) as 193.15 m. The distance between the axle wheels of the power car and extreme passenger car is 3.275 m (w_p) [19].

Various height parameters for the train system were also predefined. The rail height (h_r) was defined as 16.59 m, which is the sum of the column height (13.5 m) and girder depth (3.09 m).

The height of centroid for the bogies (h_b) were defined as 0.56 m and the height of centroid for the power and passenger car-bodies (h) were defined as 1.72 m and 1.627 m, respectively. These values were retrieved from a study by Song et al., [36] who similarly modeled a Korean high-speed train assumed to be the KTX-I based on the dynamic properties of the mass constituent elements. The vertical distance between the bottom of the car-body and center-of-mass of the power car (h_p), extreme passenger car (h_m), and intermediate passenger car (h_c) were defined respectively as 0.605 m, 0.420 m, and 0.508 m. These values were taken from the reference study by Kwark et al., [19]. To expedite the process of shifting the train system along the length of the bridge, all train nodes were defined with an initial variable (x), which is the x-coordinate of the last wheel assuming the train is moving in the positive x-direction. This practice was beneficial to analyze various train load cases as part of the seismic analysis conducted in Chapter 5 and is recommended for future studies. The value (x) is adjusted depending on the load case being analyzed. Figure B-1 shows how the aforementioned parameters were defined and the “ x ” value shown in the snippet is for the load case where the train is loading the second to seventh spans of the bridge. A summary of all the parameters used for the train system is shown in Table 3-2.

Table 3-2. Dynamic Characteristics of Train Model [19].

Property	Power Car	Extreme Passenger Car	Intermediate Passenger Car
Mass of car-body (kg) [M]	54960	26000	26000
Primary sprung mass per bogie (kg) [m_i]	2420	2514	3050
Unsprung mass per axle (kg) [m_a]	2050	2050	2000
Primary stiffness per axle box (kN/m) [k_x, k_y, k_z]	40000, 9000, 1250	40000, 9000, 1250	55000, 11000, 800
Secondary stiffness per bogie side (kN/m) [k_{ax}, k_{ay}, k_{az}]	303, 303, 1270	100, 150, 370	100, 170, 303
Primary damper per axle box (kN-s/m) [c_x, c_y, c_z, c_ϕ]	0, 0, 10, 4230	0, 0, 10, 4230	0, 0, 6, 240
Secondary damper per bogie side (kN/m) [c_{ax}, c_{ay}, c_{az}]	0, 100, 20	0, 30, 20	0, 0, 0
Moment of inertia of car-body ($Mg\text{-m}^2$) [I_x, I_y, I_z]	59.4, 1132.8, 1112.9	33.94, 971.81, 971.81	33.94, 971.81, 971.81
Moment of inertia of bogie ($Mg\text{-m}^2$) [I_{tx}, I_{ty}, I_{tz}]	1.645, 2.593, 3.068	2.07, 3.26, 3.86	2.03, 3.20, 3.79
Moment of inertia of wheel ($Mg\text{-m}^2$) [I_{ax}, I_{ay}, I_{az}]	1.03, 0.0008, 1.03	1.03, 0.0008, 1.03	1.03, 0.0008, 1.03
Length of car-body (m) [L_p, L_m, L_c]	14.0	18.7	18.7
Height of centroid (m) [h, h_b]	1.72, 0.56	1.627, 0.56	1.627, 0.56
Height from secondary suspension arm to centroid (m) [h_p, h_m, h_c]	0.605	0.420	0.508

3.2.2.2. Train System Nodes

Train nodes are created by defining the parameters specified for the *node* command (Figure A-2). For large scale structural models for an OpenSees model to be filled with thousands of nodes, which can be very confusing if the node tags (*NodeTags*) are not organized. Since this study is modeling the train system running on track 1, the train node tags were organized where any tag starting with a 7 specified an alignment on the right side of the train over R1 (rail 1), a 8 specified an alignment on the left side of the train over R2 (rail 2), and a 6 specified an alignment on the

centerline of track 1 (R). This can be seen in the y-coordinate for the nodes defined in Figure B-2, Figure B-3, and Figure B-4. These figures in Appendix B are snippets of the rear power car, rear extreme passenger car, and first intermediate passenger car to demonstrate how they are defined in OpenSees. The second value of the node tag specifies the vertical grid of the train system as can be seen in the train model schematic (Figure 3-4). The value 0 is for the wheel nodes, 1 is for the bogie nodes, 2 is for the primary suspension nodes, and 3 is for the car-body nodes. The second to last number in the node tag specifies the bogie that the wheel, bogie, or suspension node is associated with, and the last number further specifies the location of the node within axle (1 or 2), bogie (1 to 3), or suspension system (1 to 3). For example, *NodeTag* 70042 designates the node for wheel 2 on the right side of bogie 4, and *NodeTag* 71052 designates the node for bogie 5's center node. This trend is not followed for the car bodies. Instead, the last digit of the car-body node tags ranges from 1 to 23. Each car-body is constituted by three nodes and car-bodies for the articulated system share a node as can be seen in Figure 3-4.

All coordinates are defined using the predefined parameters as discussed in Section 3.2.2.1 above. This allows for simple adjustment of the train dimensions in the case of a parametric study or adjustment to a potential design. For the intermediate passenger cars, a value " n " was set to represent the respective number of the 6 intermediate passenger cars. A value of 1 was set for the first intermediate passenger car which was used to define the x-coordinates of the nodes, and each successive intermediate passenger car nodes were defined by increasing the n value by 1. The variable " x " previously defined and shown in Figure B-1 is included in the x-coordinates of every train node to shift the location of the entire train system along the length of the bridge. The z-coordinates were defined with the predefined train system heights as shown in Figure 3-4. Wheel nodes were modeled at the same height as rail nodes under the assumption of perfect contact and the height of the bogie nodes were modeled as the sum of the rail height and bogie height relative to the rail. The z-coordinate of car-bodies were defined as the sum of the height of their center-of-mass (h) assumed in Section 3.3.2.1 and the height of the rail (h_r). and the top node of the secondary suspension system as the sum of car-body height (h) and the height of the rail (h_r), minus the respective cars vertical distance between the car-body center of mass to the bottom of the car-body. The node set up for the rear power car, rear intermediate passenger car, and first intermediate passenger car are illustrated in Appendix B in Figure B-2, Figure B-3, and Figure B-4.

3.2.2.3. *Train System Rigid Connections*

The car-body and bogie are modeled as elastic beam-column elements with exceedingly stiff properties. The cross-sectional area, Young's modulus, shear modulus, torsional moment of inertia of the cross-section, and second moment of area about the local z and y-axis were assigned exceptionally large values to create a rigid element. Exceptionally stiff elements can potentially cause convergence issues depending on the type of convergence test type for analysis, so the values should be defined accordingly. The cross-section values used for this study as defined in Figure B-5, which were determined to provide appropriate stiffness relative to the rest of the elements in the model. Examples of the rigid elastic beam-column elements defined for the bogies are shown in Figure B-5 and Figure B-6. Similarly, Figure B-7 and Figure B-8 demonstrate the rigid elements for the primary suspension system. Since the KTX-Sancheon has an articulated bogie system, the passenger cars act as a coupled unit. The car-bodies for the extreme and intermediate passenger cars are modeled as rigid beam-column elements in series; however, the power cars are disconnected from the rest of the system. This is demonstrated in Figure B-9 where Node 63003 of the power car is not connected to Node 63004 of the extreme passenger car.

3.2.2.4. *Train System Suspensions*

Flexibility is provided in the train system through the primary suspensions system between the axles and bogies, and the secondary suspension system between the bogies and car-bodies. The primary and secondary suspension system of the train were modeled using the *twoNodeLink* link element command in OpenSees. This command allows the user to construct a zero or non-zero length element defined by two nodes and apply material behavior to any transverse or rotational DOFs for a three-dimensional model. Uniaxial elastic materials were used to model the stiffness in the translational DOFs, and uniaxial viscous damper materials were used to model the vertical damping within the suspension system. Stiffness and damping coefficients for the suspension system of the power car, extreme passenger car, and intermediate passenger car were defined as given in the reference study [19]. The *parallel* material command was used to combine the stiffness and damping material in the z-direction to a single material. These materials were then used as the material parameters for the two-node link elements. The i-nodes shown are the bogie nodes and the j-nodes are the axle wheel nodes. The materials defined were applied in their respective directions and the *orient* command was used to manually instruct OpenSees of the element vector components. Since the primary suspension system only applies stiffness in the three translational DOFs, the *equalDOF* command was used to constrain the remaining DOFs between the bogie and axle nodes. Figure B-10 and Figure B-11 demonstrates how the primary suspension system of the power cars were modeled.

Similar process was performed for the secondary suspension systems; however, damping for the z-rotational DOF was also applied in addition to any translational damping (Figure B-12). As shown in the train model schematic in cross-section of the train model in Figure 3-4, the secondary suspension system has three layers: left, middle, and right. The left and right layers supply stiffness and damping in the translational DOFs and the middle layer supplies damping in the z-rotational DOF. Due to this DOF not having any stiffness, the DOF must be constrained for the stability of the model. However, if the displacement between the two-nodes constituting the middle layer of the secondary suspension system were constrained using the *equalDOF* command, the z-rotational damping would not activate due to the lack of displacement (x). Therefore, a relatively small stiffness value (1 kN/m) was applied in the z-rotational DOF to allow for the activation of the damping, and the rest of the DOFs were constrained using the *equalDOF* command (Figure B-13).

3.2.2.5. *Train System Masses*

The train masses were modeled using the values given in the reference study [19], included in Table 3-3. Since the extreme passenger car for the KTX-Sancheon is not motorized, unlike the KTX-I in the reference study, the translational mass and inertial mass values for the intermediate passenger car were used for the extreme passenger car as well. The masses were defined at the center-of-mass nodes for each car-body and bogie. The masses for the wheels are defined at every wheel node. Figure B-14 through Figure B-17 demonstrate how the car-body, bogie, and axle masses were defined in OpenSees. The inertial masses were used to define the rotational nodal masses.

Table 3-3. Masses for Track-Bridge System.

	Mass (Mg/node)	Moment of Inertia 1 (Mg-m ²)	Moment of Inertia 2 (Mg-m ²)	Moment of Inertia 3 (Mg-m ²)
Girder	63.7359	159.1817	61.1692	189.1868
Column	7.9940	27.2587	11.7515	23.8342
Footing	629.7408	7859.6900	7859.6900	14122.9870
Rail	0.1693	0.0025	0.1459	0.1446
Track Plate	3.5878	1.9561	3.0640	4.9961
Base Plate	3.9466	2.8739	3.3691	6.2193

3.2.3. Train System Model

The track system comprises of rails, track plates, base plates, and the connection layers in between these components. The rails, track plates, and base plates were modeled as *elasticBeamColumn* elements and the connection layers were modeled as *zeroLength* elements. The rails, track plates, and base plates were discretized into equal intervals of 3.195 m and the connection layers were modeled at the end nodes of each interval. The train-track interaction was modeled by including and connecting the train wheel nodes as a member of the series of nodes creating the rail elements. This directly transfers the train loads to the track system, which then transfers the loads down to the bridge system through rigid arms connecting the track system to the bridge girder. The bridge girder was also discretized into equal increments of 3.195 m, which allowed for the track-bridge interaction to occur at an equal distribution along the entirety of the bridge length. A general schematic of the track system is shown in Figure 3-5 and Figure 3-6. The steps taken to model the track system nodes, elements, and masses are further discussed in detail in this chapter.

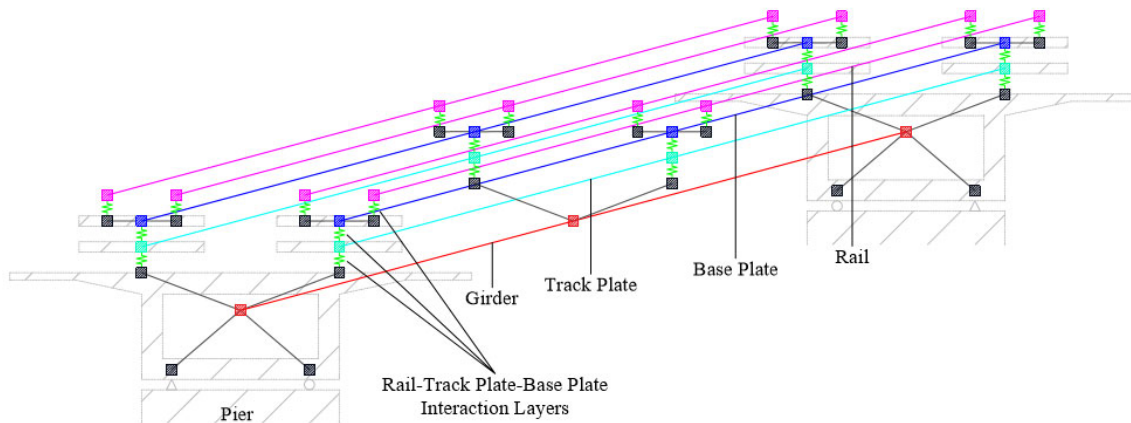


Figure 3-5. Schematic of track system.

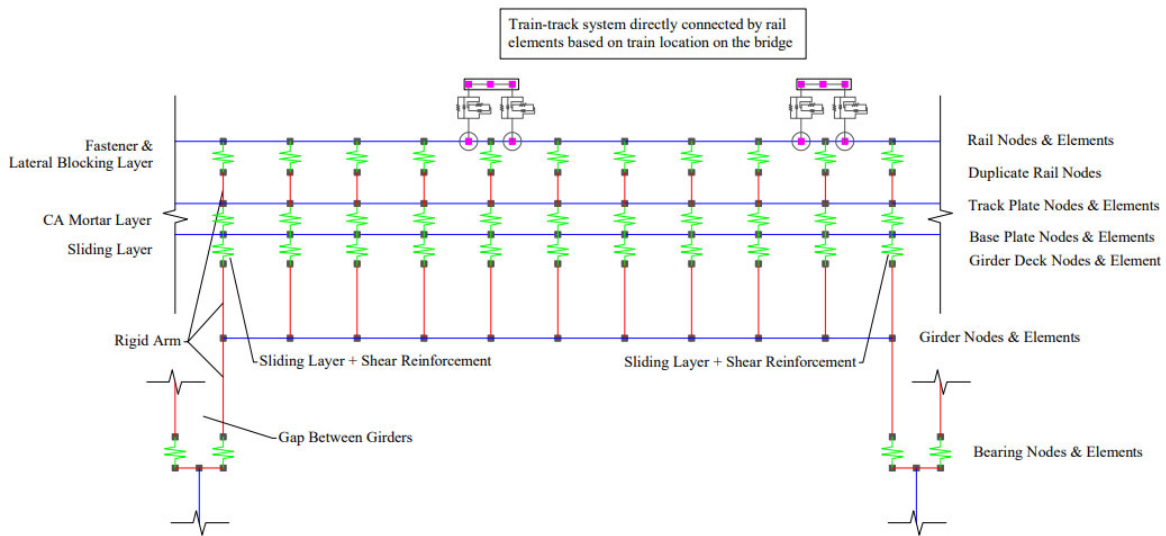


Figure 3-6. Schematic of track-bridge system.

3.2.3.1. Track System Elastic Elements

The rails, track plate, and base plate were modeled as linear elastic beam-column elements because they are all designed to remain elastic as capacity protected elements. The location of the track plate and base plate nodes are the same, and rail nodes are located to the right and left of the track plate/base plate nodes by half the transverse train wheel spacing, defined earlier as R1 and R2 for track 1 and L1 and L2 for track 2, respectively. Figures B-18, B-19, and B-20 in Appendix B show sample node setup for rail, base plate, and track plate of one of the tracks, respectively. The elements were assigned cross section parameters as given in the study by Li et al., [22]. The rail, track plate, and base plate elements span the entirety of the bridge length. The process of modeling rail, track plate, and base plate elements are shown in Figure B-21, B-22, and Figure B-23, respectively.

To connect the train system to the track system, wheel nodes of the train were connected to neighboring rail nodes using the same linear elastic beam-column elements used for the rails. Since the train was placed on track 1 consisting of rails 1 and 2, the wheel nodes were modeled at the same y and z-coordinates as the rail nodes. The sequential order of the wheel nodes and rail nodes were organized offline and defined in OpenSees accordingly. This was done under the assumption that the train wheels are always in contact with the rails, as researched in Chapter 2 to be a common assumption.

3.2.3.2. Track System Connection Layers

Zero-length elements were used to simulate the nonlinear behavior of the sliding layer, CA layer, shear reinforcement, lateral blocking, and fasteners. The nonlinear material behavior was assigned to the zero-length elements using the *Steel01* material in OpenSees. The yield strengths were assigned as given by Li et al., [22] and the initial elastic tangent was found by a quotient of the yield strength and relative displacement. The strain hardening ratio was assigned a value of zero to mirror the perfectly elastic-plastic behavioral graph from the reference study. Figure 3-7 first shows the generalized elastic-plastic behavior along with the parameters of the different zero-length connection elements in the track-bridge system as adopted from Li et al., [22]. Next,

dedicated plots were generated to demonstrate the behavior of five of those connection component in track systems and shown in Figure 3-8. Fasteners and lateral blocking were modeled between the duplicate rail nodes as demonstrated in Figure B-24 and Figure B-25 in Appendix B, respectively. The CA mortar layer was modeled between the track plate and base plate (Figure B-26), and the sliding layer was modeled between the base plate and rigid arm connecting the track system to the bridge girder (Figure B-27). Sample shear reinforcement definition is also shown in Figure B-28. The fasteners, CA mortar layer, and sliding layer allow for longitudinal slipperly relative to the bridge length. Multi-point constraints were used to constrain the remaining DOFs of the connection layer nodes that stiffness was not applied to through zero-length elements. For example, stiffness was applied in the longitudinal direction for the sliding layer to allow for movement based on the behavior of the material, so the *equalDOF* command was used to constrain the remaining 5 DOFs (Figure B-29).

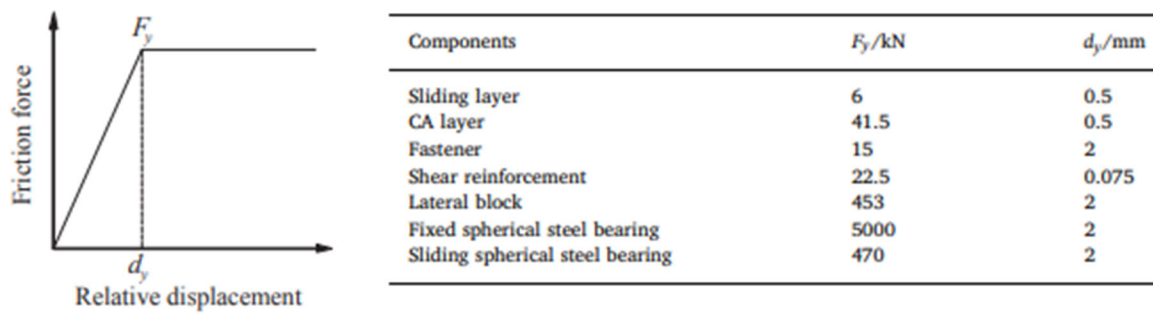


Figure 3-7. Parameters of zero-length connection elements in the track-bridge system as adopted from Li et al., [22].

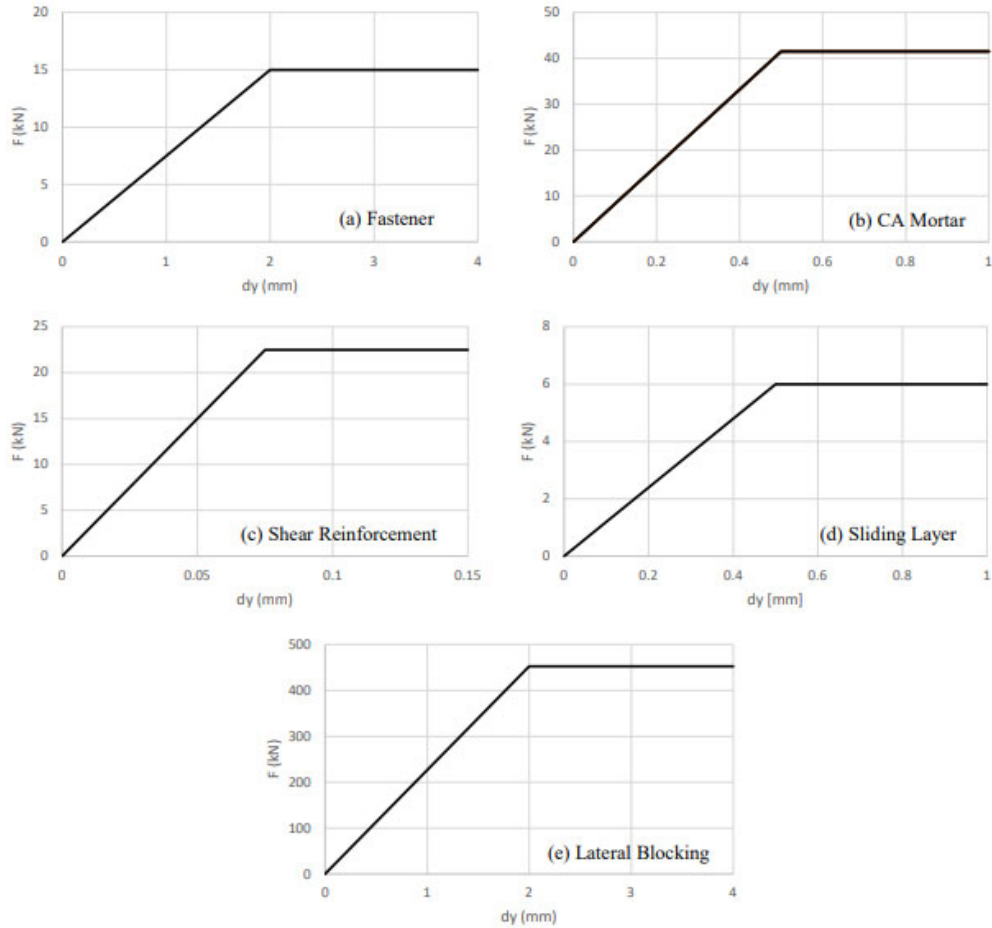


Figure 3-8. Force-deformation behavior of track system connection layers: (a) Fastener, (b) CA mortar, (c) Shear reinforcement, (d) Sliding layer, and (e) Lateral blocking

3.2.3.3. Track System Rigid Connections

Rigid elements were used in the track system to connect the track plate nodes to the rails. Specifically, the rigid arms branch out from each track plate node to duplicate rail nodes that were not used to model the rail elements. The rigid section properties to model rigid arms out of elastic beam-column elements were kept the same as what was used for the train system rigid bodies. Rigid arms were modeled at 3.195 m intervals for both tracks 1 and 2, which is the same intervals as the track system nodes. The location of the rigid arms can be seen in Figure 3-9.

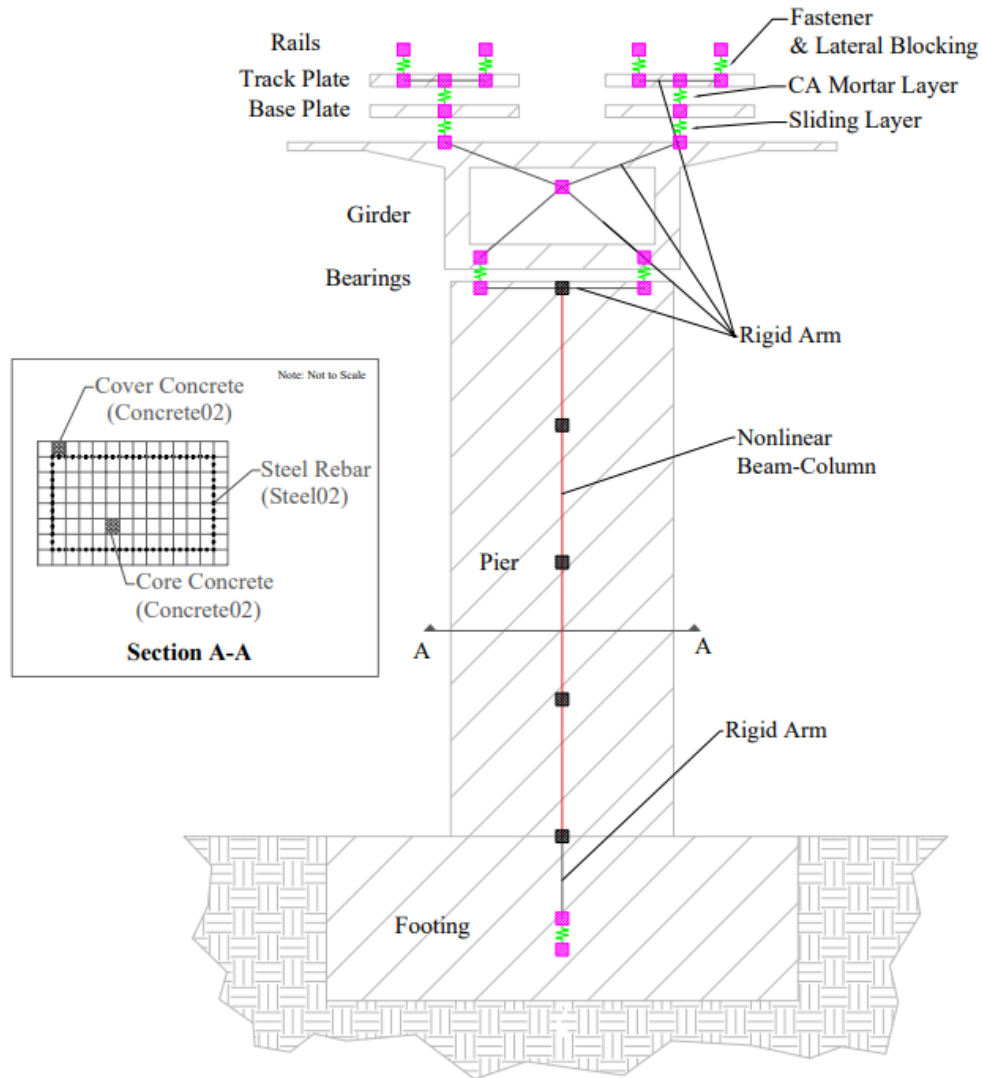


Figure 3-9. Schematic of track-bridge system.

3.2.3.4. Track System Rigid Masses

The masses for the rails, track plates, and base plates were assumed using approximate densities of steel and concrete. The steel rails were assumed to have a density of $7,700 \text{ kg/m}^3$, and the concrete track plate and base plate were assumed to have a density of $2,400 \text{ kg/m}^3$. These are very generic values and accurate densities should be utilized to accurately model the dynamic performance of HSR systems because the mass matrix is one of the key components of solving the equation-of-motion of the model. Mass per node was found by dividing the product of the given cross-sectional area and the length of the bridge by the number of nodes constituting the entire length (110 nodes). General mass moment of inertia equations for rectangular sections were used to solve for the moment of inertia in the three rotational DOFs. The masses used for the track system in this study is shown in Table 3-3. The mass per node was used for the nodal mass value in the translational DOFs and the inertial masses were used for the rotational DOFs (Figure B-30).

3.2.4. Bridge System Model

The bridge system comprises of girders, bearings, pier columns, and footings. Girders were modeled as elastic beam-column elements, and bearings were modeled as zero-length elements. Pier columns were modeled as displacement based elastoplastic fiber elements and columns footings were modeled as rigid elements. Rigid arms were used to connect each bridge component to one another as illustrated in the track-bridge system schematic shown in Figure 3-9.

3.2.4.1. Train System Girder

The prestressed concrete box-girder bridge is designed to be elastic, i.e. capacity protected component for seismic considerations, so linear elastic beam-column elements with equivalent section characteristics were used to model the superstructure. Each span was discretized into 10 equivalent lengths of 3.195 m by creating 11 nodes per girder span. Figure B-31 demonstrates how the nodes for the first two bridge girder spans were defined. A 0.05 m gap was created between each bridge girder span to simulate the isolated movement allowed to each girder span by four steel bearings, two fixed and two sliding. The cross-sectional area, Young's modulus, shear modulus, torsional moment of inertia of the cross-section, and second moment of area about the local z and y-axis were assigned the values given by Li et al., [22] and shown in Table 3-4. To simulate the process of bridge design, the Young's Modulus was decreased from $3.45e7$ kN/m² to $2.45e7$ kN/m² and the moment of inertia values were reduced by 30% to account for the reduction in concrete stiffness due to cracking. The process of modeling the first span of the bridge girder is shown in Figure B-32. For the first girder span, Node 90001 to Node 90011 were modeled in series with the elastic beam-column element, using predefined cross-sectional parameters. The distance between Node 90011 and Node 90012 demonstrate the gap between girders, so these nodes are not connected using the elastic element.

Table 3-4. Section parameters of elastic beam elements in track-bridge system as adopted from Li et al., [22].

	Sectional area/m ²	Elastic modulus /kN/m ²	Shear modulus /kN/m ²	Torque /kN m	Inertia moment 1/m ⁴	Inertia moment 2 /m ⁴
Main girder	9.06	3.45×10^7	1.44×10^7	2.26×10^3	1.10×10^3	9.48×10^3
Base plate	5.61×10^{-1}	3.00×10^7	1.25×10^7	6.74×10^{-3}	1.69×10^{-3}	4.06×10^{-1}
Track plate	5.10×10^{-1}	3.55×10^7	1.48×10^7	6.80×10^{-3}	1.70×10^{-3}	2.76×10^{-1}
Rail	7.75×10^{-3}	2.06×10^8	8.05×10^6	2.00×10^{-6}	3.20×10^{-5}	5.00×10^{-6}

3.2.4.2. Bridge System Bearings

The spherical steel bearings were modeled using zero-length elements. To use zero-length elements, the OpenSees user must create two nodes with the same coordinates, hence the zero-length. Since the bearings are located at the ends of each bridge span, two-sets of nodes were created accordingly. The fixed and sliding bearings were assumed to be 4 m apart, based on the box-girder dimensions, in the direction transverse to the bridge at the top of the 13.5 m tall pier columns. The nodes for the bearings supporting the first bridge span are shown in Figure B-33. One set of the bearing nodes were used to connect the bearing system to the bridge girder, and the other set of nodes were used to connect the bearings to the top of the pier columns, both through rigid arms.

The OpenSees material command *Steel01* was used to define the bilinear behavior of the steel bearings within the zero-length elements. The required parameters for the zero-length elements for the steel bearings are shown in Figure 3-7. The yield strength was defined as given by the reference study in Figure 3-7 with a value of 5000 kN for the fixed bearing and 470 kN for the sliding

bearing, and the elastic tangent or slope of the elastic region was found by a quotient of the yield strength and relative displacement also given in Figure 3-7. As previously mentioned, the strain-hardening ratio was set as 0 and the uniaxial material was applied into directions 1 and 2 to apply stiffness in the lateral translational DOFs. The behavior of the fixed and sliding bearing is shown in Figure 3-10. The fixed and sliding bearings were alternated as shown in Figure 3-11 to mirror the design of the actual bridge.

As previously mentioned, stiffness was only applied in the longitudinal and transverse DOFs, so the vertical DOF and the three rotational DOFs were constrained for structural stability. The high stiffness value for the fixed bearing idealizes the resistance it provides to constrain movement and the low value for the sliding bearing idealizes the slight resistance it provides despite allowing movement. The fixed and sliding bearings modeled to support the first span of the bridge are shown as examples in Appendix B in Figure B-34 and Figure B-35, respectively. For this study, the *equalDOF* command was used to constrain the rest of the DOFs and make sure duplicate bearing nodes will have the same movement (Figure B-36).

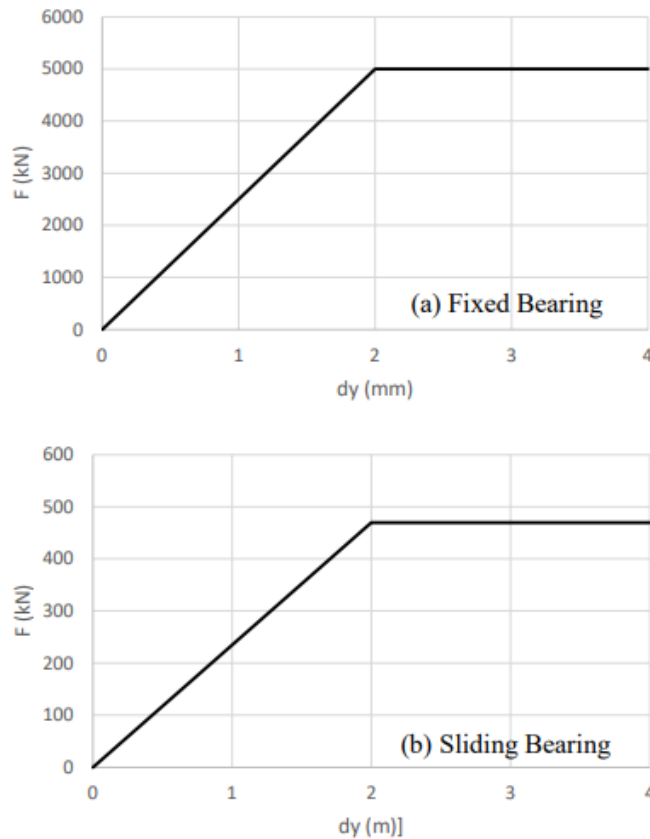


Figure 3-10. Force-deformation behavior of bridge bearings: (a) Fixed bearing, (b) Sliding bearing.

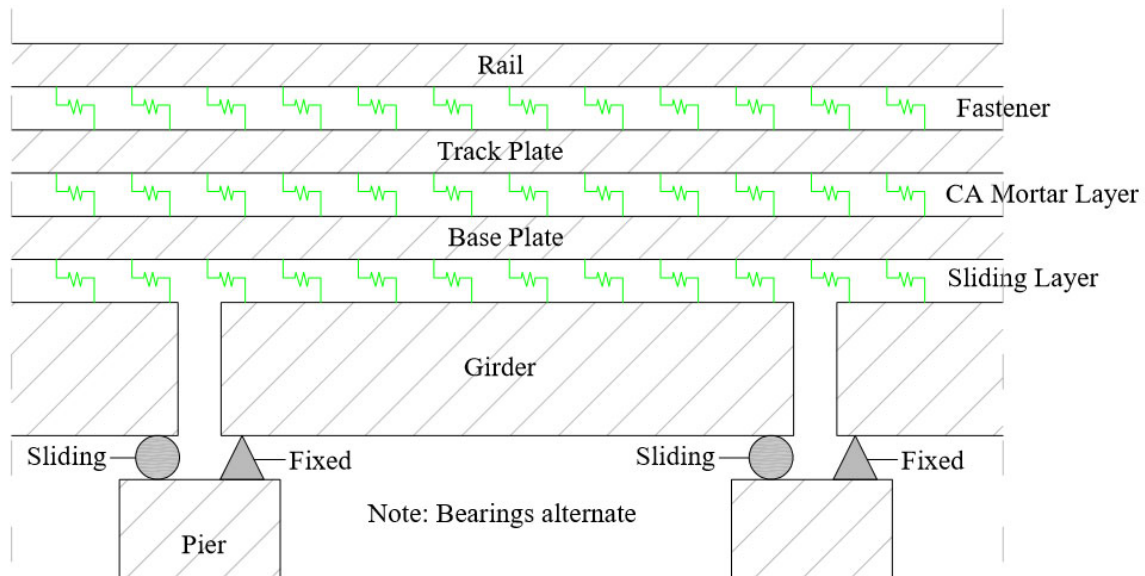


Figure 3-11. Finite element model of bridge.

3.2.4.3. Bridge System Pier Columns

Materials for the pier column cross-section were defined using uniaxial materials available within OpenSees and material strengths were input as parameters. The core concrete, cover concrete, and reinforcing steel strength assumptions were adopted from a sample code provided by the OpenSeesWiki, [32] since the design guideline for the selected prototype HSR bridge used herein did not provide sufficient information on specific material specifications for the bridge columns. The assumptions used for the concrete and reinforcing steel properties and input parameters are shown in Figure B-37. The cover and core concrete were modeled using the *Concrete02* material and the longitudinal reinforcement was modeled using the *Steel02* material in OpenSees; a typical modeling practice for bridge elements that has been adopted in many of the reviewed studies such as the one Li and Conte, [23]. For the *Steel02* command, the R0, cR1, and cR2 parameters were defined as 15, 0.925, and 0.15, respectively, as recommended for general reinforcing bar by the OpenSeesWiki.

The pier cross-section was created using the *fiber section* command (Figure B-38). The cover and core concrete were defined within the section using the *patch rect* command to generate fibers over a rectangular cross-sectional area. The reinforcing steel was defined using *layer straight* commands to generate fibers along a straight line for the four sides of the rectangular cross-section. The material tag (*matTag*) for these commands reflect what was defined for the cover, core, and reinforcing steel materials.

The geometry of cross-section design, as well as the coordinates required in the command parameters to create the cross-section were predefined as shown in Figure B-39. A reinforcement ratio of 1.30% was assumed for the cross-section and this led to a preliminary design of 176- #11 bars, split into 60 bars on the long face and 28 bars on the short face of the cross-section. Transverse reinforcement was assumed as #4 bars and a clear cover of 0.04 m was also assumed. The design used for the cross-section does not reflect the actual design of the pier columns, but since the details are unknown, a general design was done based on engineering judgement. The design specified in the *section Fiber* command was then aggregated into a uniaxial elastic material section using the *section Aggregator* command to create a single section force-deformation model. The torsion

force-deformation (T) was selected as the force-deformation quantity parameter to be modeled by the section object.

The rectangular bridge pier columns were modeled as a series of four three-dimensional displacement based elastoplastic fiber elements using the *dispBeamColumn* command with the nonlinear fiber cross-section that was defined. Each pier was constituted by five nodes with equal 3.375 m intervals with five integration points each (Figure B-40). Integration of fiber characteristics over the pier cross-section allowed for the obtainment of nonlinear section characteristics. The process of modeling the first pier column is shown in Figure B-41.

3.2.4.4. *Bridge System Column Footings and Soil*

Column footing dimensions of the prototype bridge selected were not explicitly noted in the reference study, so generic dimensions of 4 m for the depth and 11 m for the width were assumed. The nodes were defined at -2 m to create nodes at the centroid of the footings. The column footings were modeled as rigid elements via the same method for all other rigid elements to connect the column base nodes to the footing nodes. Figure B-42 in Appendix B shows a sample for footing nodes and ground.

Due to the focus of the study being the dynamic interactions between the train-track-bridge systems, a simplistic method was used to model the interaction between the bridge and soil. Since California is projected to be the home of the largest HSR system in the United States, soil spring constants from a study by Abbasi, [1] were used to simulate the general soil properties of California. Since multi-column box-girder bridges in California typically have the pinned connection details in the foundation, there are no rotational stiffness defined at the column footings. Abbasi, [1] considered a wide range of soil profiles and foundation systems over the state of California and determined the stiffness of translational springs to be 115 MN/m. However, adjustments were made to accommodate the single column bent design of the bridge piers. Single column bents typically utilize fixed-base connections to provide stability to the cantilevered system. Accordingly, the footing nodes were fixed in the non-translational DOFs and the foundation nodes were fixed in all 6 DOFs to create a base for the entire model (Figure B-43).

The structure-soil interaction was simplified in-part due to the lack of information regarding the soil spring constants required to model the pile-soil interaction and the focus of the study being the train-track-structure interaction. If this information is available, a sophisticated soil-structure interaction model is recommended by explicitly modeling the piles as displacement based elastoplastic fiber elements, as done by Li et al., [22] and Li and Conte, [23]. The process of modeling the column footings and the interaction with the soil for the model in place is shown in Figure B-43 and Figure B-44.

3.2.4.5. *Bridge System Rigid Connections*

Rigid elements are used in the bridge system to connect the bridge girder, bearing, pier column, and footing to one another. For the model in-place, the track system is connected to the bridge girder through two diagonal arms at an interval of 3.195 m, along the entire bridge length. Additionally, two diagonal rigid arms connected the bridge girder to the steel bearings isolating the bridge girder from the pier columns, meaning the two nodes defining the ends of each bridge girder span had a total of four rigid arms. The bearings are connected to the pier columns through two horizontal arms in the y-direction at the top of the pier columns, and the column footings are idealized as a rigid arm. The location of rigid arms is shown in the track-bridge system schematic

in Figure 3-9. The same rigid section properties were used as the rigid arms in the train and track system. Examples of all the rigid elastic beam-column elements used in the bridge system are shown in Figure B-45 through Figure B-48.

3.2.4.6. *Bridge System Masses*

For the dynamic equation of motion, masses for the concrete deck, pier column, and footing were assumed using a standard density of $2,400 \text{ kg/m}^3$. General mass moment of inertia equations for rectangular sections were used to solve for the very approximate mass moment of inertia in the three rotational DOFs. The masses of the bridge girder were distributed along the 10 spans, consisting of 11 nodes each. The masses of each pier column were distributed along the five nodes constituting the entire column. The masses were applied at the center-of-mass node for each footing. The masses for the bridge system in this study is shown in Table 3-3 as previously mentioned. Moreover, the process of applying the masses for sample different bridge components, i.e. box-girder, columns, and footings, are shown in Figure B-49, Figure B-50, and Figure B-51, respectively.

Chapter 4. DEMONSTRATION OF GRAVITY, MODAL, AND SEISMIC ANALYSIS OF HSR BRIDGE SYSTEM

In OpenSees, an analysis is performed through the aggregation of component objects. The component objects define the type of analysis that is performed on the model and consists of the following: constraints handler, DOF numberer, integrator, solution algorithm, system-of-equation constructor and solver, and convergence test. This chapter will discuss the component objects defined for the gravity load static analysis and the seismic load dynamic analysis, as well as how the modal analysis was performed. Static and dynamic analysis were performed for a load case without the train and an example load case with the train. The recorded data was analyzed to verify and observe the responses within the HSR bridge. This chapter serves to demonstrate the selection of analyses component objects for the prototype HSR model and present example studies that can be performed to understand the behavior of the model under various loading.

4.1. Gravity Load Analysis

4.1.1. Gravity Load Analysis Setup

To perform a linear or nonlinear static gravity load analysis, loads must be applied to represent the self-weight of each structural component. Masses do not have to be defined for static analysis because inertial and damping effects are neglected. The masses defined in Section 3 were instead converted into forces (kN) and applied as vertical loads at the same nodes as the masses. This was done through the *pattern plain* command which allows the user to apply loads to specific nodes and elements. Train system car-body, bogie, and axle wheel and bridge foundation dead loads were applied at their center-of-mass nodes, and track-bridge system rail, track plate, base plate, bridge girder, and pier column dead loads were distributed to each node formulating their respective elements. The train system, track system, and bridge system had a total weight of 3,989 kN, 16,992 kN, and 184,230 kN, respectively, with a total static weight of 205,211 kN. The static weights of the train-track-bridge system were used to verify the load transfer within the HSR model through comparison with column base reactions. As previously mentioned and shown in Chapter 3, the step-by-step type of model and analysis definition demonstration is provided in Appendix B. As part of Appendix of B, Figure B-52 through Figure B-60 demonstrate the process of applying dead loads to each component of the HSR bridge system.

The *constraints* command handles how the constraint equations are enforced in the analysis. Constraint equations enforce a specified value for a DOF, or a relationship between DOFs [31]. The type of constraint selected should depend on the type of constraints implemented in the user's model, homogeneous single-point constraints or non-homogenous single-point constraints. For this study, multi-point constraints were used (*equalDOF*), so the *Transformation* command was used to enforce the constraints using the transformation method.

The *numberer* command determines the mapping between equation numbers and DOF, and how DOF are numbered. The use of the plain numberer is recommended mostly for very small problems and for the sparse matrix solvers which provide their own numbering scheme. For this study, the *RCM* option was used for the numberer in the case of this large-scale system model. The RCM (Reverse Cuthill-McKee) algorithm optimizes node numbering to reduce bandwidth using a numbering graph, and outputs a warning when the structure is disconnected. The *system* command constructs the linear system-of-equations and solver objects to store and solve the linear system-

of-equations ($K \cdot u = R$), and each solver is tailored to a specific matrix topology. The *UmfPack* command was used to construct a large sparse system-of-equations object which will be factored and solved during the analysis using the UmfPack solver.

To perform nonlinear analysis, the user must define how OpenSees will deem whether the model has converged to the correct solution. The *test* command is used to select convergence test to determine if convergence has been achieved at the end of an iteration step. The command parameters allow the user to define the convergence tolerance, the maximum number of iterations that will be performed before OpenSees returns “failure to converge”, and a flag to instruct OpenSees on how to print information on convergence. The *NormDispIncr* test type selected in this study uses the norm of the left-hand side solution vector of the matrix equation to determine if convergence has been reached. The test returns positive for convergence if the displacement increment in the linear system-of-equation is less than the specified tolerance. For this model, a tolerance of 1.0×10^{-6} and a maximum number of iterations of 100 was deemed reasonable. A flag value of 1 was selected to instruct OpenSees to print convergence information on each step to monitor whether the model was operating correctly, but this does not affect the actual analysis.

The next step is to define a solution algorithm to instruct OpenSees on the sequence of steps to take to solve the nonlinear equation. The *Newton* command was used to solve the nonlinear residual equation using the Newton-Raphson algorithm, which is the most widely used robust method for solving nonlinear algebraic equations [31]. The *integrator* command is used to determine the predictive time step for the analysis, specify the tangent matrix and residual vector at any iteration, and determine the corrective time step based on the displacement increment. The *LoadControl* integrator type was selected and an initial load-increment factor (pseudo-time step) was defined as 0.1 to apply a tenth of the dead loads defined earlier at each step. The gravity load was applied through 10 loading steps to avoid convergence issues that might have happened if the large gravity loads is applied in one step.

Finally, the *analysis* command was used to specify a static analysis and the *analyze* command was used with the number of load steps parameter, to slowly apply the gravitational loads in 10 steps. The *loadConst* command was used to instruct OpenSees to maintain constant gravity loads and reset the time to zero before the transient analysis. This entire process of setting up the gravity analysis parameters then performing the analysis is demonstrated in Figure B-61 and Figure B-62, respectively.

4.1.2. Gravity Load Analysis Results

Sample studies were performed to demonstrate behavioral analysis that can be performed using the gravity analysis results obtained from the model. In high seismic areas, the main design considerations for HSR bridges are usually dictated by resonance and seismic forces. Nonetheless, the static analysis was performed as a precursor to the dynamic analysis and for verification of load transfer within the structure. Several loading scenarios could be considered for analyzing the HSR bridge system with respect to train position on the bridge as the train approaches and crosses the bridge. A list of 16 different scenarios that could be considered for the system in hand is provided in Table 4-1 as an example. Only few selected cases are included in this research, but the list is still provided to highlight and indicate how train position over the bridge can be represented. For gravity load analysis, two load cases from Table 4-1 were considered for the demonstration purposes as sample studies: (1) Load Case 1 where the train is not on the bridge, and Load Case 8 where the train is loading spans 2 through 7. The load cases are illustrated in Figure 4-1. For Load

Case 1, the train model and train model gravity loads were completely omitted, leaving just the track and bridge model, along with their respective gravity loads. For Load Case 8, the very first train wheel was determined to be located 30.815 m along the bridge, the train system was connected to the track system accordingly.

The first exercise performed with the static analysis results was the verification of load transfer within the HSR system. Since loads were applied within the track and bridge subsystems, an error within either subsystem could cause the loads to incorrectly transfer through the structure. To perform this exercise, node recorders were used to extract the reactions at the column bases under Load Case 1 without the train and Load Case 8 with the train. The column base reactions in the vertical direction were tabulated in Table 4-2 for both load cases, and the distribution and sum of the reactions were observed to check for any red flags regarding the incorrect transfer loads. The sum of column base reactions in both load cases were found to be equal to the total loads applied for each load case, described in Section 4.2.1, which indicates all the loads were able to transfer to the column bases. The distribution of the interior column base reactions for Load Case 1, to the left and right of the center pier column #6, was symmetrical. The exterior columns had a difference of 33 kN which is not exceptionally large considering the scale of the reactions. For Load Case 8, an increase in the reactions for columns #2 through #8 were observed. This behavior verifies that the train loading over bridge girder spans #2 through #7 was properly supported by the pier columns supporting those respective spans. The rest of the pier columns maintained the same reactions as Load Case 1 since they were not affected by the static loading of the train.

As a verification of static behavior of the model, vertical displacements of the bridge box-girder were analyzed for both load cases. Node recorders were used to output vertical nodal displacements along the entire bridge length. The recorded values were post-processed using Matlab to organize the data and plot a graph demonstrating the deformed shape of the bridge girder under gravity loads. An exaggerated view of the deflection in each bridge span under the loading scenarios of Load Case 1 and Load Case 8 is shown in Figure 4-2. The bridge span displacements were nearly identical among all the spans for Load Case 1. A maximum vertical displacement for the bridge was recorded at -0.408 mm at the center node of each span. For Load Case 8, an increase in vertical displacements for the spans loaded by the train was visibly apparent in the graph. Larger displacements were recorded at span 2 and span 7, which is due to these spans supporting the fore and rear power cars of the KTX-Sancheon model. The maximum vertical displacement for the bridge under Load Case 8 was recorded at -0.452 m at spans #2 and #7. As seen in Figure 4-2, the mass of the power cars is greater than two times that of the passenger cars, so the displacement trend observed from Load Case 8 were deemed reasonable.

Table 4-1. Example HSR bridge system load cases based on the train position above the bridge (the cases represent instances of the train crossing the bridge).

Case Number	Train Load Cases	x (m)
1	No train on bridge	NA
2	Train on entire bridge span 1	-161.155
3	Train on entire bridge spans 1-2	-129.16
4	Train on entire bridge spans 1-3	-97.165
5	Train on entire bridge spans 1-4	-65.17
6	Train on entire bridge spans 1-5	-33.175
7	Train on entire bridge spans 1-6	-1.18
8	Train on entire bridge spans 2-7	30.815
9	Train on entire bridge spans 3-8	62.81
10	Train on entire bridge spans 4-9	94.805
11	Train on entire bridge spans 5-10	126.8
12	Train on entire bridge spans 6-10	158.795
13	Train on entire bridge spans 7-10	190.79
14	Train on entire bridge spans 8-10	222.785
15	Train on entire bridge spans 9-10	254.78
16	Train on entire bridge span 10	286.775

* Train moving in the positive x direction

Table 4-2. Column Base Reactions (kN) in Direction 3 from Static Analysis.

Column	Column Base Reactions (kN)	
	Load Case 1	Load Case 8
1	14528.6	14520.8
2	19132.7	19790.2
3	19071.1	19758.7
4	19072.6	19506.9
5	19072.6	19530.6
6	19072.6	19534.3
7	19072.6	19766.4
8	19072.6	19681.1
9	19071.6	19066.3
10	19115.3	19115.4
11	14939.0	14939.1
Total	201221.3	205209.8

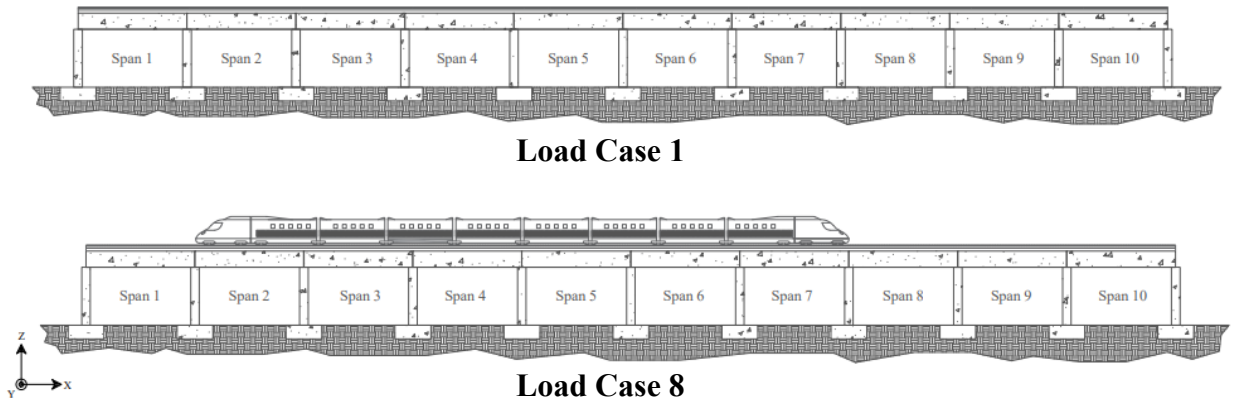


Figure 4-1. Train load cases used for Chapter 4.

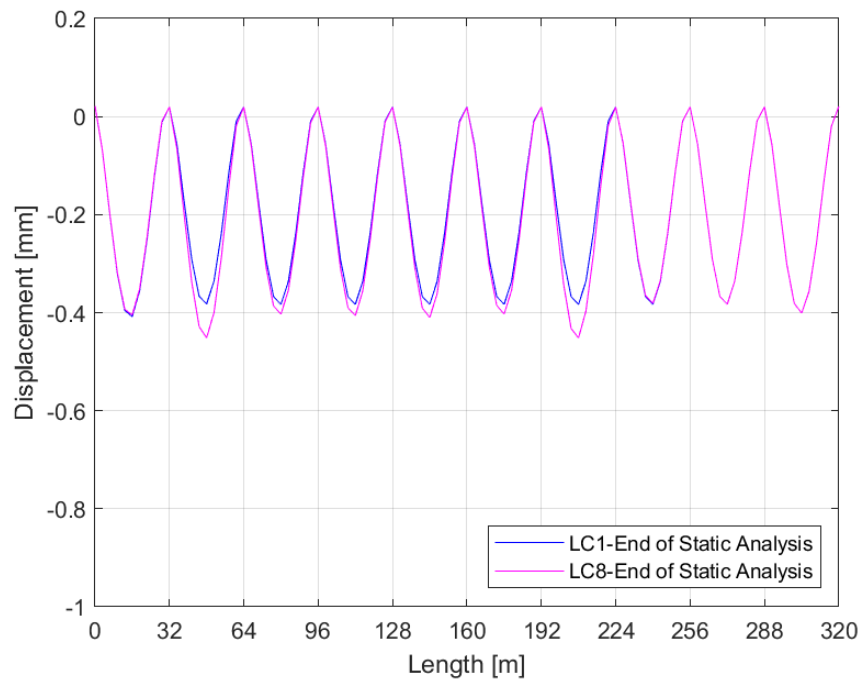


Figure 4-2. Vertical bridge girder displacements under static analysis for both load cases.

4.2. Modal Load Analysis

Analyzing modal characteristics is imperative to designing HSR bridges for seismic stability and riding comfort by minimizing resonance within the structure. Modal analysis of the bridge system was performed by using the *eigen* command which uses the overall mass and stiffness of the structure to determine the various vibration frequencies (or periods) along with mode shapes. The *eigen* command performs a generalized eigenvalue problem to determine a user specified number of eigenvalues and eigenvectors. For this study, the parameter for number of eigenvalues (λ) was defined as 10, for the first 10 modes which were then used to solve for the periods (T) of the structural model (Figure A-20). An open vector for the periods and the value for pi (π) were defined. The tcl commands *foreach* and *lappend* were used to instruct OpenSees to take each eigenvalue from the lambda index and solve for periods using equations (1) and (2) below. An output file was then specified and a tcl command, *open*, was used to open the output file and the *foreach* and *puts* commands were used to record the periods that were solved. The output file was then closed using the tcl command, *close*, to allow OpenSees to continue with the rest of the analyses.

$$\omega = \sqrt{\lambda} \quad (1)$$

$$T = \frac{2\pi}{\omega} \quad (2)$$

The modal analysis process covered in this section is demonstrated for a step-by-step procedure in Appendix B in Figure B-63. The first 10 periods obtained for the bridge system under the two sample load cases, i.e. without the train and with the train covering spans 2 through 7 of the bridge, are tabulated in Table 4-3. The values shown in the table show that the first two modes are likely the dominant bridge modes in the transverse and longitudinal direction that are not sensitive to the train loading. Higher modes varied slightly which is attributed to the added train mass and specific train-track-bridge system vibration modes.

Table 4-3. Periods for first 10 modes.

Mode	Period (seconds)	
	Load Case 1	Load Case 8
1	0.691	0.704
2	0.691	0.699
3	0.560	0.662
4	0.407	0.594
5	0.349	0.561
6	0.264	0.546
7	0.209	0.537
8	0.204	0.513
9	0.170	0.504
10	0.147	0.463

4.3. Seismic Load Analysis

4.3.1. Seismic Load Analysis Setup

To start off the set up for the seismic analysis, structural damping must be applied first to model the inherent damping and energy dissipation mechanisms within the structure. The *Rayleigh* command was used to apply classical Rayleigh damping, i.e. viscous damping proportional to a linear combination of mass and stiffness, to all previously-defined elements and nodes in the structural model as demonstrated in Figure B-64. Due to the nature of the bridge system and model, the natural frequencies of the first and sixth modes were selected to solve the alpha and beta parameters for the *Rayleigh* command as defined from the OpenSees syntax shown in Appendix A in Figure A-21. A typical damping ratio of 2% was used for this study.

The set up for the seismic load analysis is overall similar to the gravity load analysis, with some differences to accommodate the transition from static analysis to transient analysis as depicted in Figure B-65. For the constraint handler, the transformation method was used again due to the use of multi-point constraints in the model. The RCM algorithm was also used as the DOF numberer to optimize node numbering and reduce bandwidth, and the Newton-Raphson method was used to advance the analysis to the next time step. The convergence test type was changed to the energy increment test which uses the dot product of the solution vector and norm of the right-hand side of the matrix equation to determine if convergence has been reached. The test returns positive for convergence if one half of the inner-product of the unbalanced load and displacement increments at the current iteration is less than the specified tolerance. The tolerance was decreased to 1.0e-8 to increase accuracy of the analysis and the maximum number of iterations was increased to 1000 to raise the chances of the model correctly converging. The OpenSees Manual does not recommend a type of convergence test for static or dynamic analysis, but this is one area where informed user input is needed to properly obtain correct convergence. The same linear equation solver, UmfPack, was used to store and solve the system-of-equations in the analysis.

For the transient analysis, a numerical integrator is needed to solve the dynamic equation of motion that is needed to account for inertial and damping effects. For this study, the classical Newmark method was used to perform the numerical integration. The Newmark method is a two-parameter time-stepping method developed by Nathan M. Newmark. The gamma (γ) and beta (β) parameter values depend on whether the average acceleration method or linear acceleration method is selected. For this study, the average acceleration method was selected because it is unconditionally stable, i.e. independent of the analysis time step, and the gamma = 0.5 and beta = 0.25 values were defined accordingly. Dynamic analyses could use any of several explicit or implicit integrator types as per the list provided in the OpenSeesWiki or OpenSees Manual, and users could select from the available methods based on the application or so. The analysis command was then used to instruct OpenSees to conduct a transient analysis with the parameters defined above.

Once the specifics of the transient analysis were defined, the ground motions to be used as the transient loads were defined. The ground motion selected for the sample transient analysis is from the 1994 Northridge earthquake recorded at the LA-Sepulveda VA Hospital. The acceleration time-history was retrieved from the Pacific Earthquake Engineering Research Center (PEER) ground motion database provided by the University of California, Berkeley. The downloaded acceleration time-history file was placed in the same OpenSees bin folder as the tcl file of the structural model to allow the code to call out the ground motion. The *ReadSMDFile*, available on the OpenSeesManual, [31] and OpenSeesWiki, [32] online, was sourced to convert the PEER

ground motion to a format readable by OpenSees. The sourced file removes the header text in the PEER ground motion file and converts the file extension from AT2 to g3. This process can be seen in Figure B-66. The analysis time-step (Δt) and total number of steps (N_{step}) were defined as 0.005 seconds and 9557, respectively, with maximum duration of the ground motion being 47.785 seconds.

Using the converted acceleration time-history file and the ground motion parameters defined, the *timeSeries path* command was used to define the time-series information for both ground motions (see Figure A-22 in Appendix A for OpenSees command details). A gravitational acceleration value of 9.81 m/s^2 was applied as the factor to retrieve the acceleration time-history values from the multiples of [g] format. The factor can be further increased if amplification of the ground motion is of interest. Unique load tags were created for each excitation, and the ground motions were then applied to the model using the *UniformExcitation* pattern command. The parameters required in the *UniformExcitation* pattern command are shown in Figure A-23. The respective unique pattern tag (*patternTag*), ground motion direction, and time-series information for each excitation defined earlier were used in the command. The process of applying the ground motion in both directions is shown in Figure B-67.

After completing the definition of dynamic analysis parameters and the transient loads, the *analyze* command was used to instruct OpenSees to perform the dynamic analysis with the time-stepping parameters previously defined for the ground motion. Figure B-68 demonstrates a loop function created to run the dynamic analysis and engage additional algorithms and convergence test types if the initial dynamic analysis parameters are incapable of converging the model. The *analyze* command set to return “*ok = 0*” if the analysis at a time-step successfully converged to a solution. The loop command is set to start if “*ok != 0*”, which means that the “*ok*” value is not 0. While the current time-step is less than the maximum duration of the ground motion, the loop attempts to converge the model using a norm displacement increment convergence test and the Newton-Raphson algorithm with initial stiffness iterations, the Broyden algorithm, and the Newton-Raphson algorithm with line search, in order.

4.3.2. Seismic Load Analysis Results

After the gravity load analysis was completed and damping was applied, dynamic analysis of the model was performed. The same two load cases were considered for the dynamic analysis: (1) Load Case 1 where the train is not on the bridge, and (2) Load Case 8 where the train is loading spans 2 through 7. Several sample exercises were conducted using the results from the two load cases to analyze the maximum forces and moments experienced by the prototype HSR bridge and observe the sensitivity of the results with and without train loading. This section aims to demonstrate the variety of studies that can be performed using the data output by OpenSees and the sample results presented shall not be taken as a reference for design.

As an extension to the exercise done for the static analysis, the vertical displacements of the bridge girders under seismic loading were plotted for both load cases. The maximum vertical displacement was recorded as -0.657 mm at girder spans #1 and #10 for Load Case 1. The bridge girder displacements at the end of the static analysis (start of dynamic analysis) and at a time-step of 4.185 seconds during the dynamic analysis, when the maximum displacement was recorded for Load Case 1, were plotted in Figure 4-3 as sample. For Load Case 8, the maximum vertical displacement of -0.636 mm was recorded at girder spans #2 and #7. The bridge girder displacements at the end of the static analysis and at a time-step of 3.915 seconds during the

dynamic analysis, where the maximum displacement for Load Case 8 was observed, were also plotted as samples and shown in Figure 4-4. The vertical displacement trends for both load cases under seismic loading were found to be very similar to that of the static analysis. This behavior is understandable because only the two horizontal components of the ground motion were considered (which excites the lateral directions of the bridge) and the vertical excitation component was neglected. The box-girder is also designed to be a capacity protected element, meaning inelastic deformation is not expected to be caused by the ground motions. The minor increase in displacements are most likely caused by rotations at each girder-span end above the pier. It is noted that the box-girder is not continuously supported over the pier and the gap between each two successive girder spans allow for some minor rotation.

The second exercise conducted was the observation of transverse bridge displacement trends, which are crucial for seismic performance assessment. To observe the displacements experienced by the bridge during the ground motion, the transverse displacements were analyzed at the time-step at which the bridge experienced the largest transverse displacement between both load cases and the final time-step of the ground motion to see whether any residual displacements were observed. The maximum displacement during the ground motion between both load cases occurred at a time-step of 4.735 seconds for Load Case 1, with an absolute value of 291.7 mm. The maximum transverse displacement recorded for Load Case 2 was 282.2 mm at a time-step of 4.750 seconds. The transverse displacements at the end of the ground motion were also analyzed to observe the residual displacements caused by the nonlinear effects of dynamic loading, and plastic damage, if any. The prototype HSR bridge under Load Case 1 had a residual displacement of 111.2 mm and Load Case 8 had a residual displacement of 116.6 mm. The displaced shapes of the bridge for the selected time steps mentioned above is shown in Figure 4-5 for Load Case 1 and Figure 4-6 for Load Case 8.

Similar to the previous displacement exercises, time-histories of pier column and girder end displacements were plotted to better understand the bridge behavior with and without train loading. The time-history graphs compare the relative drift between girder ends and the supporting columns and indicate whether residual displacements were observed due to nonlinear/plastic deformations induced by the cyclic loading of the ground motions. Four pier columns and their respective girder ends were considered in the shown sample time-history analysis: #2, #6, #8, and #11, to observe the magnitudes of drift along the bridge. Pier column displacements were recorded by outputting the transverse and longitudinal displacements of the top nodes and their histories were plotted through the total duration of the ground motion. Similarly, the translational displacements of the nodes defining the ends of each girder span were recorded and plotted. The displacement time-histories from the four piers are shown in Figure 4-7 through Figure 4-10 for Load Case 1 and Figure 4-11 through Figure 4-14 for Load Case 8. The figures include two sub-plots, which are designated as “a” and “b” to represent the displacement trends in the longitudinal and transverse direction, respectively. Based on the longitudinal displacement trends, the shapes are nearly identical between both load cases with Load Case 8 showing slightly larger drift between the column and girder for columns #6 and #8. From the displacement time-histories for the transverse direction shown in Figure 4-8(b), Figure 4-9(b), Figure 4-12(b), and Figure 4-13(b), all four columns showed similar trends within each load case. Comparing the displacement trend between the load cases, Load Case 1 had larger displacements in the 8 to 15 second range, and Load Case 8 had larger displacements in the 15 to 20 second range and showed larger oscillations throughout the rest of the ground motion which can be a result of additional mass due to train loading.

To further demonstrate other seismic performance metrics, hysteresis loops for the pier columns as obtained from force-displacement relationships were plotted. The same four columns (#2, #6, #8, and #11) were selected from the displacement time-history analysis and were analyzed under both load cases. Column forces were extracted from OpenSees by assigning element recorders with the force parameter for the fiber-based column element that was modeling the bottom of the pier columns. The shear force-displacement relationships from the two load cases were plotted in the two lateral directions 1 and 2, i.e. longitudinal and transverse directions, in Figure 4-15 and Figure 4-16, respectively. The main objective of graphing the force-displacement behavior of the pier columns was to identify extent of nonlinearity and damage in the columns. The nonlinearity is observed by observing whether the loading and unloading behavior follows a similar slope which signifies the column remains within the elastic region. From the hysteresis loops provided, the force-displacement behavior can be observed to be relatively linear for the four columns under both load cases with the transverse direction showing slight instances of nonlinearity. The residual displacements previously shown are also indicators of nonlinear behavior. Given the observed residual displacements, this might be attributed to other components yielding or damage (e.g. bearings). However, it is beyond the scope of this study to interpret or assess the seismic behavior especially that no proper design was conducted for the bridge components and only demonstration is desired here.

As the last exercise in this part of the study, the internal forces and moments within the bridge girders were observed by plotting shear force and bending moment diagrams. Girder straining actions are usually more important for gravity load checks and design. However, for better demonstrations selected cases of girder straining actions are shown under the seismic loading as it accounts for gravity loads already in addition to any extra demands from the seismic loading. Forces in the bridge girder elements were recorded by assigning element recorders to all 100-elastic beam-column elements used to model the bridge with the force parameter. The recorders export the axial force, and shear forces and moments in the local y and z-axis of the element cross-section. The forces and moments were plotted along the length of the bridge for each load case at an arbitrary time-step of 4.600 seconds during the peak of the Northridge ground motion. The shear force diagrams and bending moment diagrams for Load Case 1 and Load Case 8 are shown in Figure 4-17 through Figure 4-22, and Figure 4-23 through Figure 4-28, respectively. Again, analyzing the obtained shear and bending moment values is not the goal here.

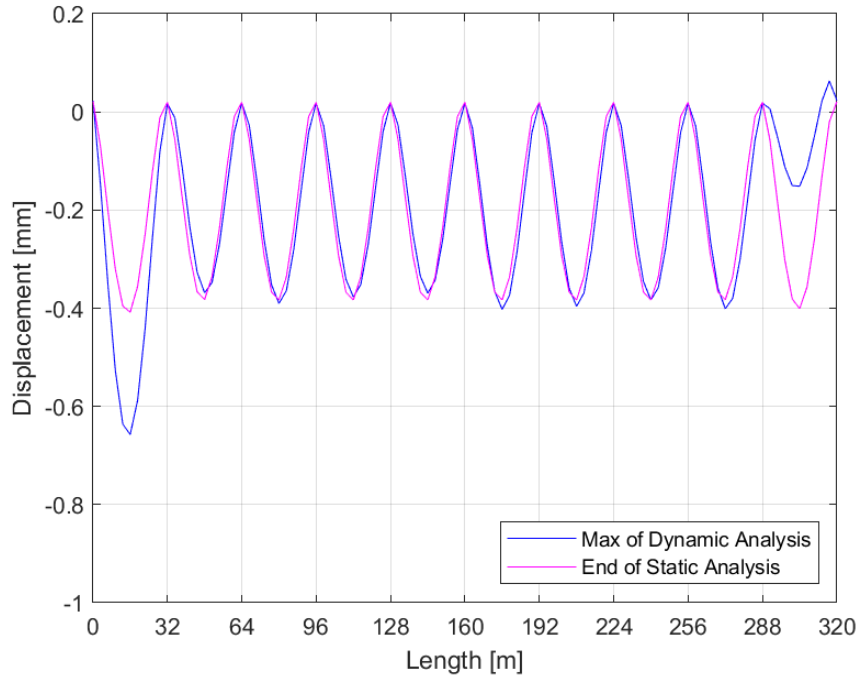


Figure 4-3. Vertical bridge girder displacements under Load Case 1.

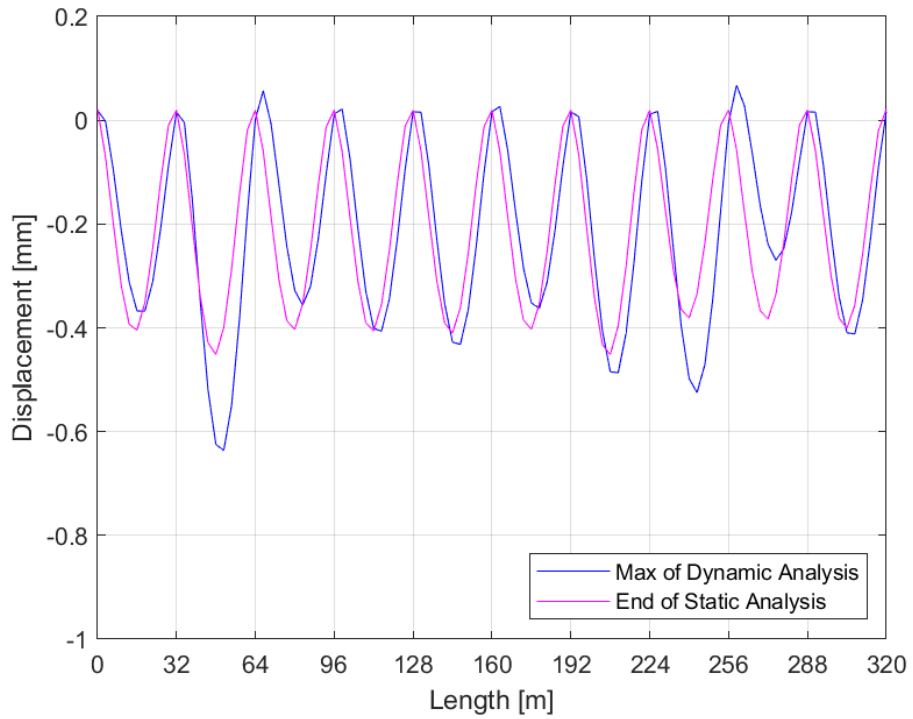


Figure 4-4. Vertical bridge girder displacements under for Load Case 8.

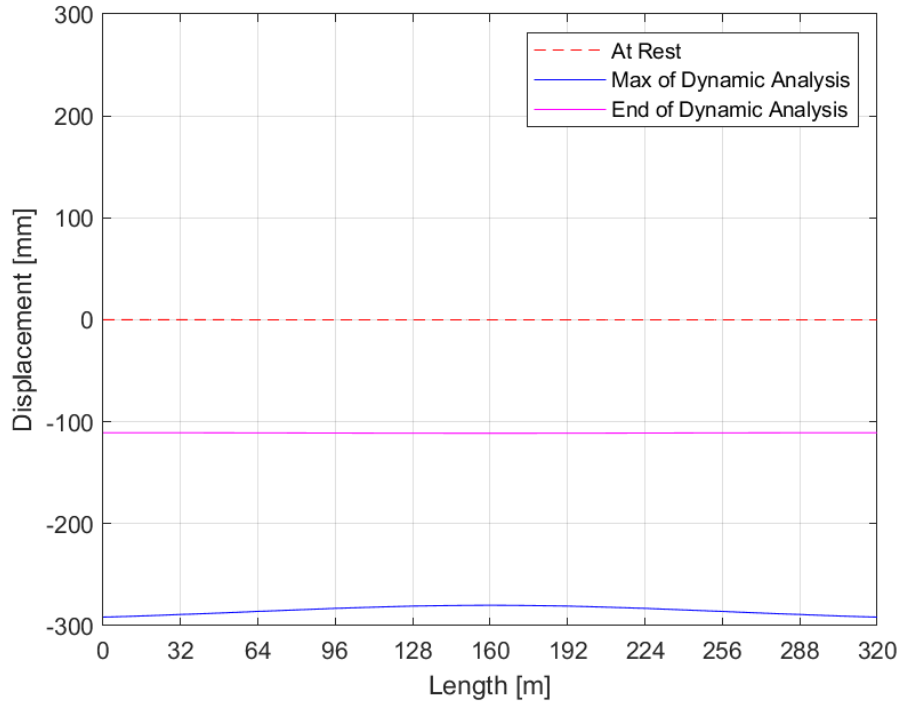


Figure 4-5. Transverse bridge girder displacements under Load Case 1.

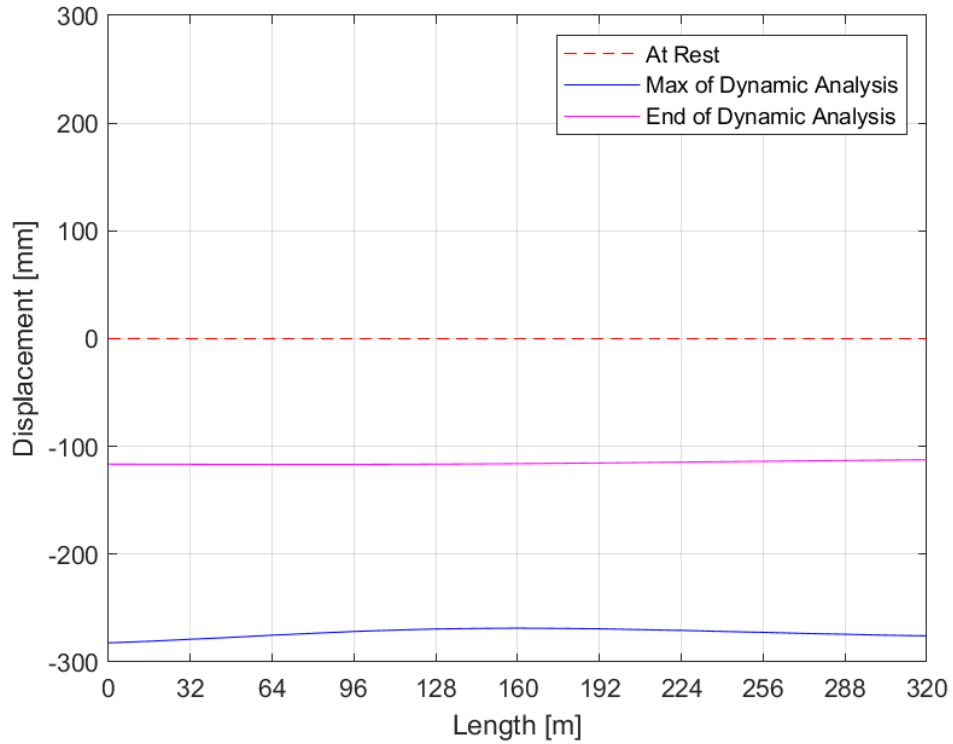
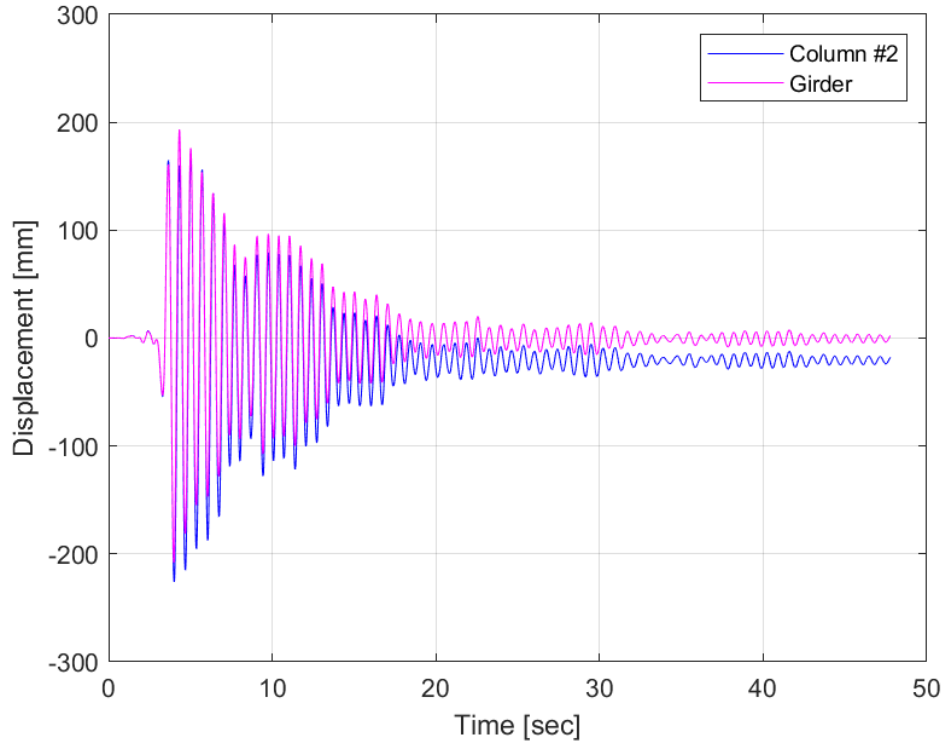
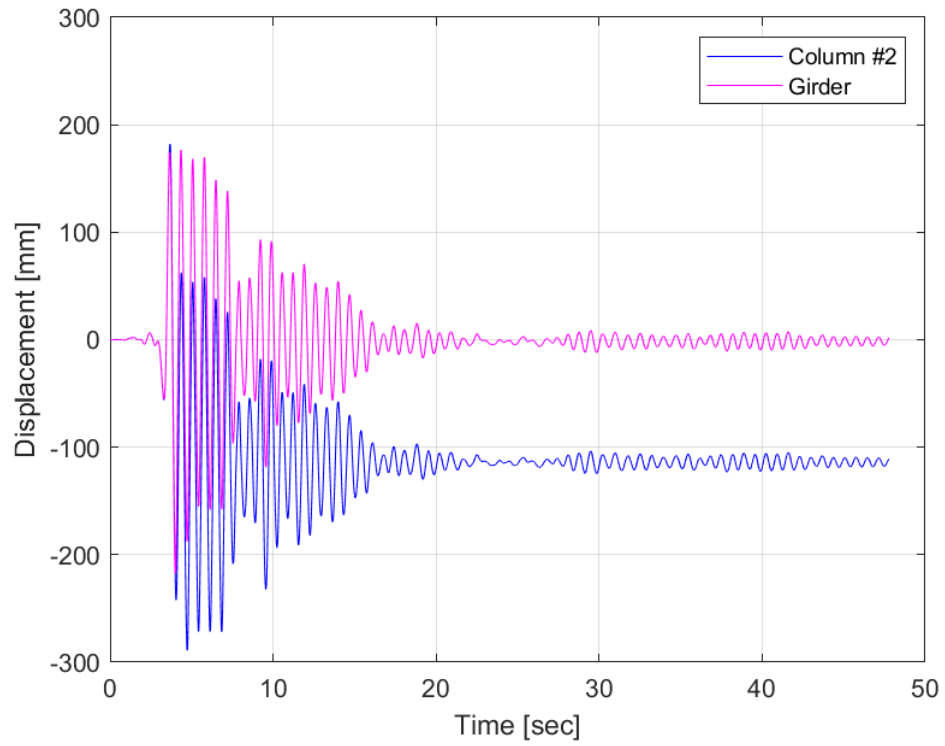


Figure 4-6. Transverse bridge girder displacements under Load Case 8.



(a)



(b)

Figure 4-7. Displacement time-history of column #2 under Load Case 1 in:
 (a) Longitudinal, (b) Transverse directions.

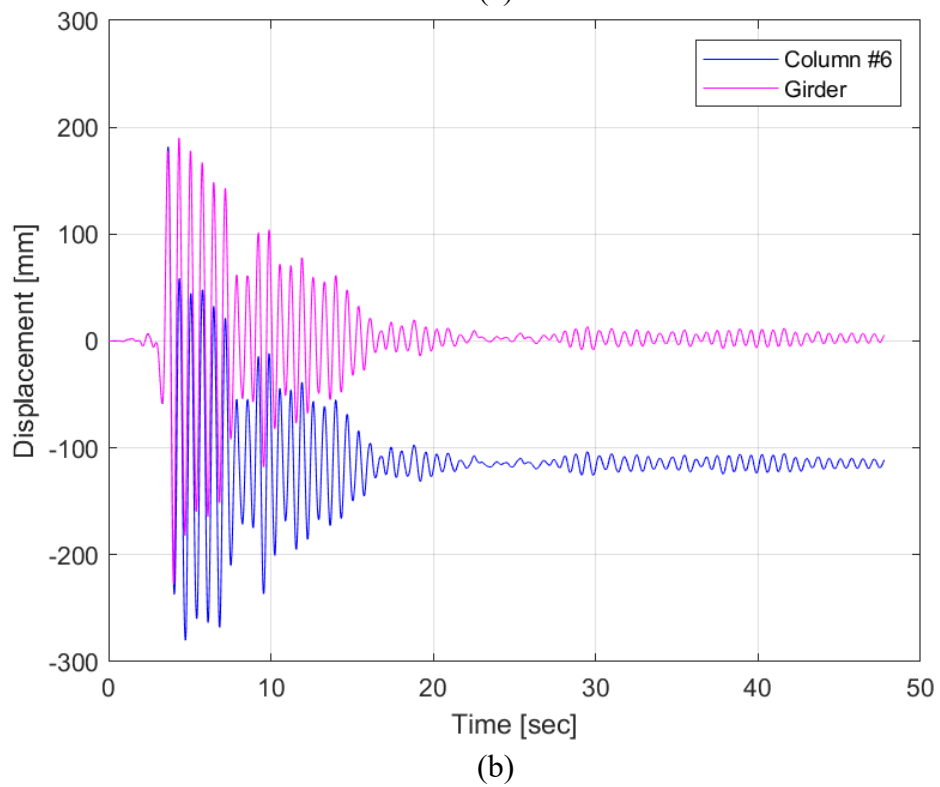
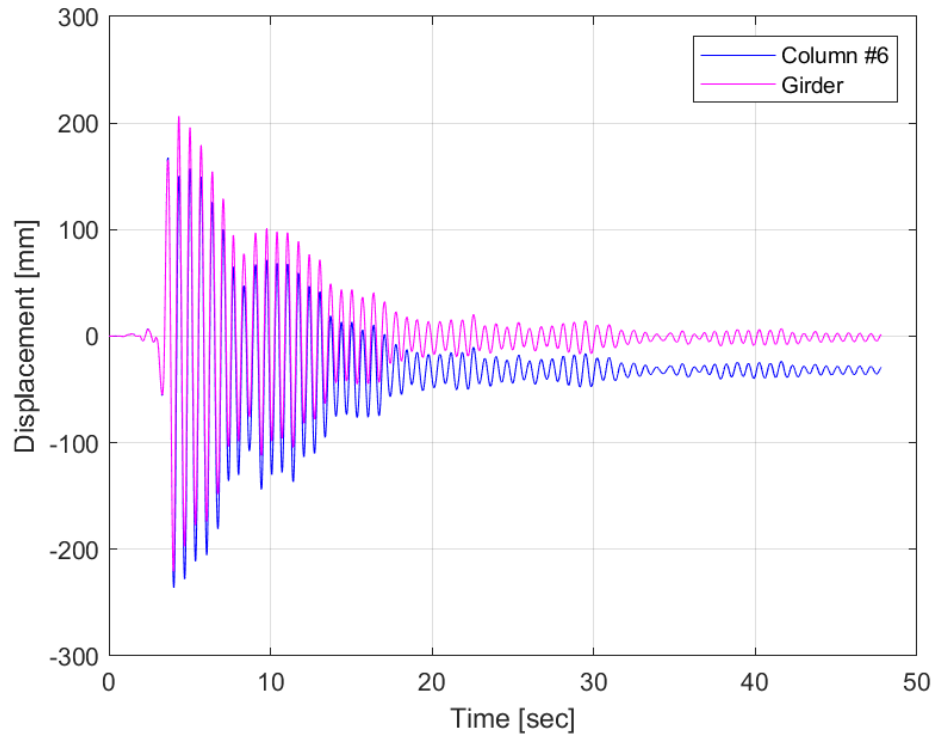
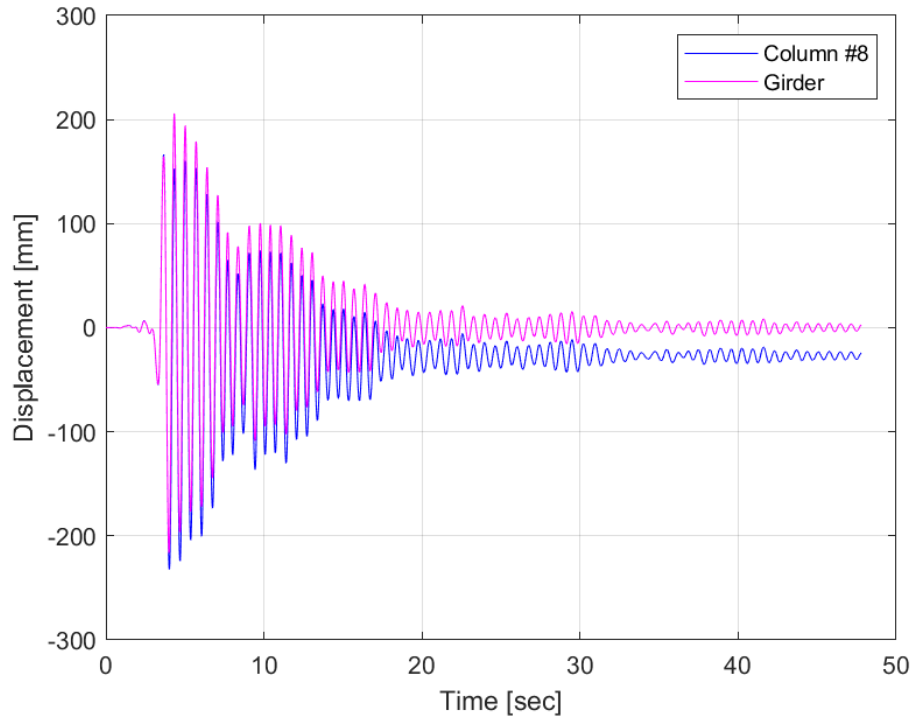
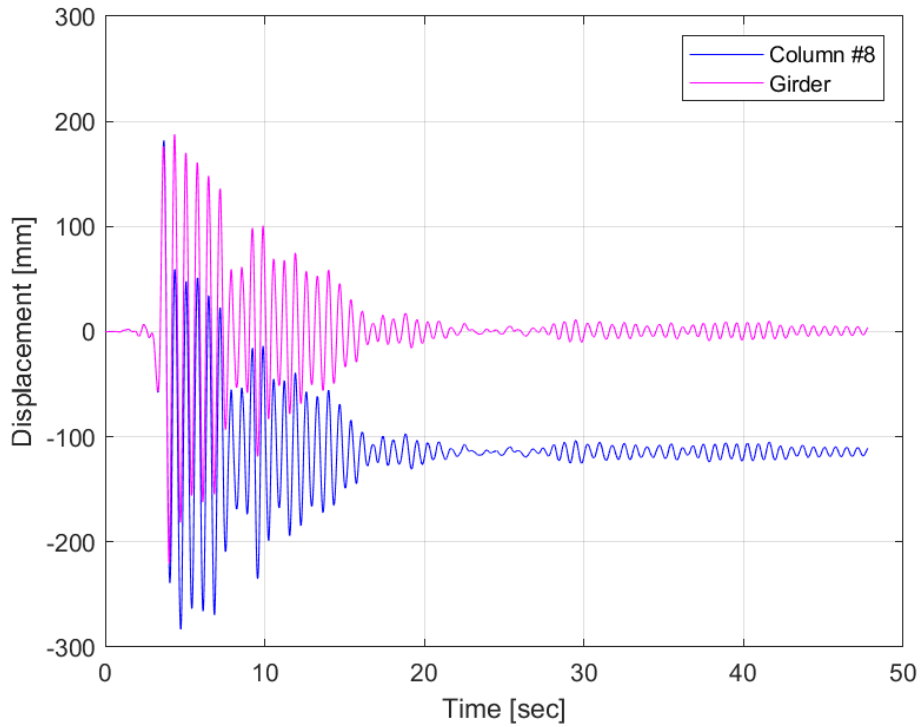


Figure 4-8. Displacement time-history of column #6 under Load Case 1 in:
 (a) Longitudinal, (b) Transverse directions.

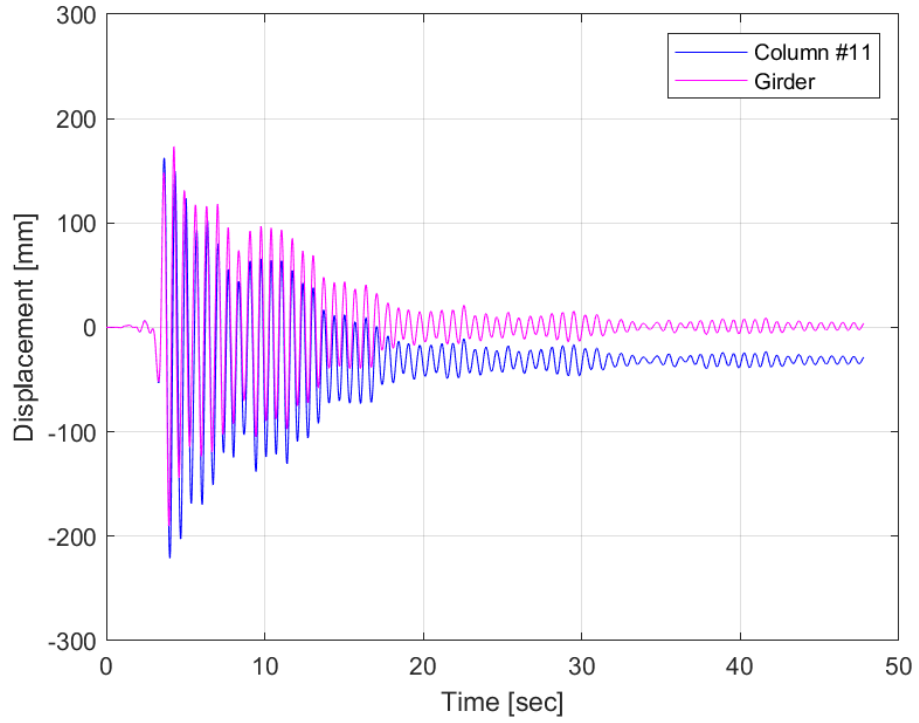


(a)

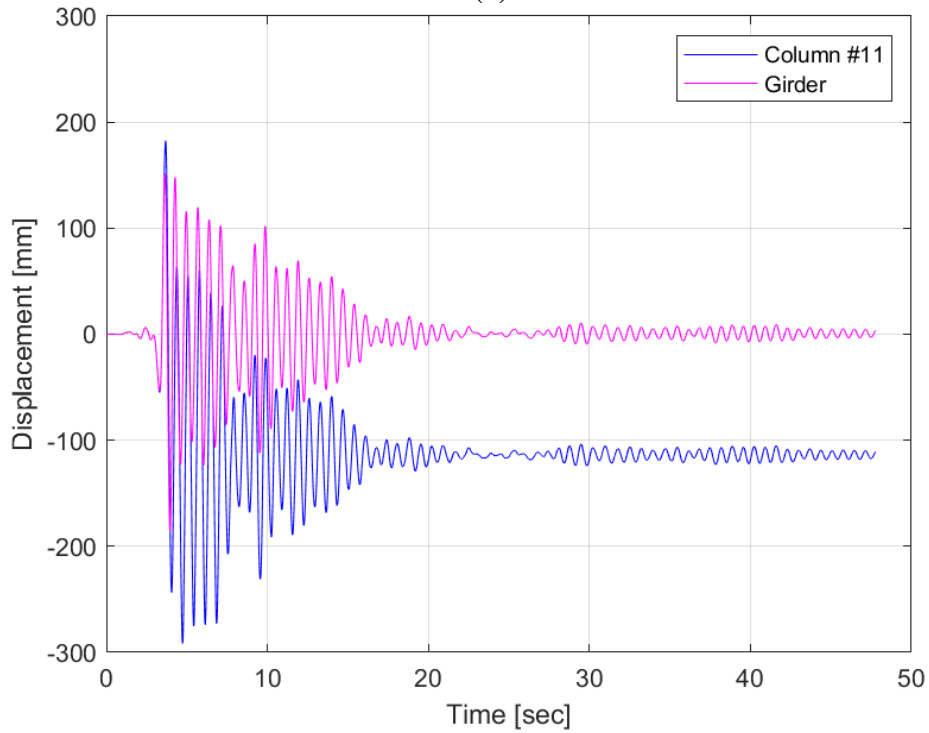


(b)

Figure 4-9. Displacement time-history of column #8 under Load Case 1 in:
 (a) Longitudinal, (b) Transverse directions.

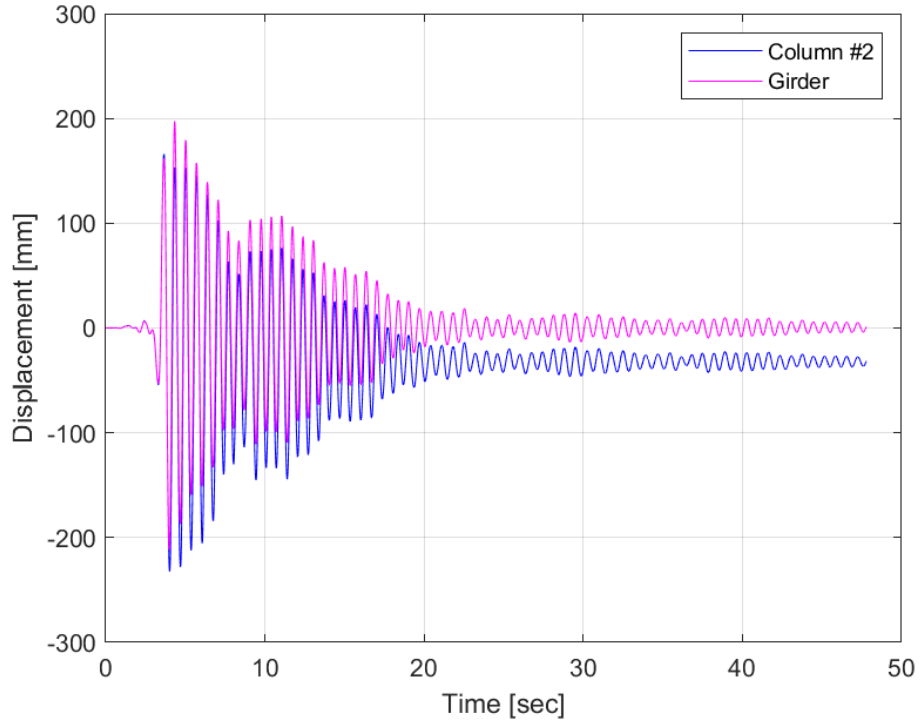


(a)

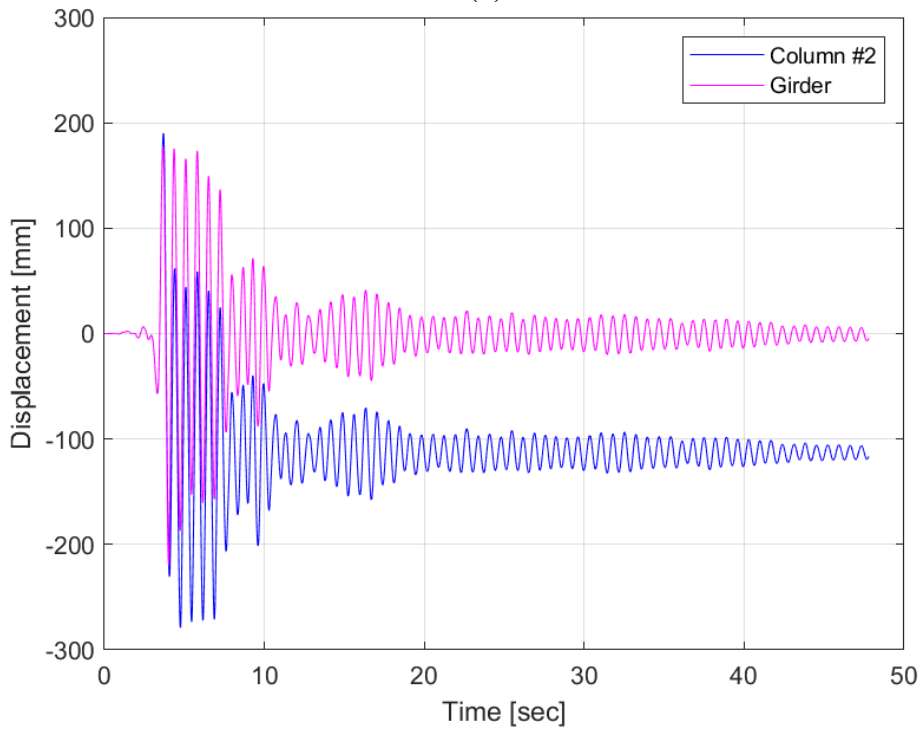


(b)

Figure 4-10. Displacement time-history of column #11 under Load Case 1 in:
 (a) Longitudinal, (b) Transverse directions.

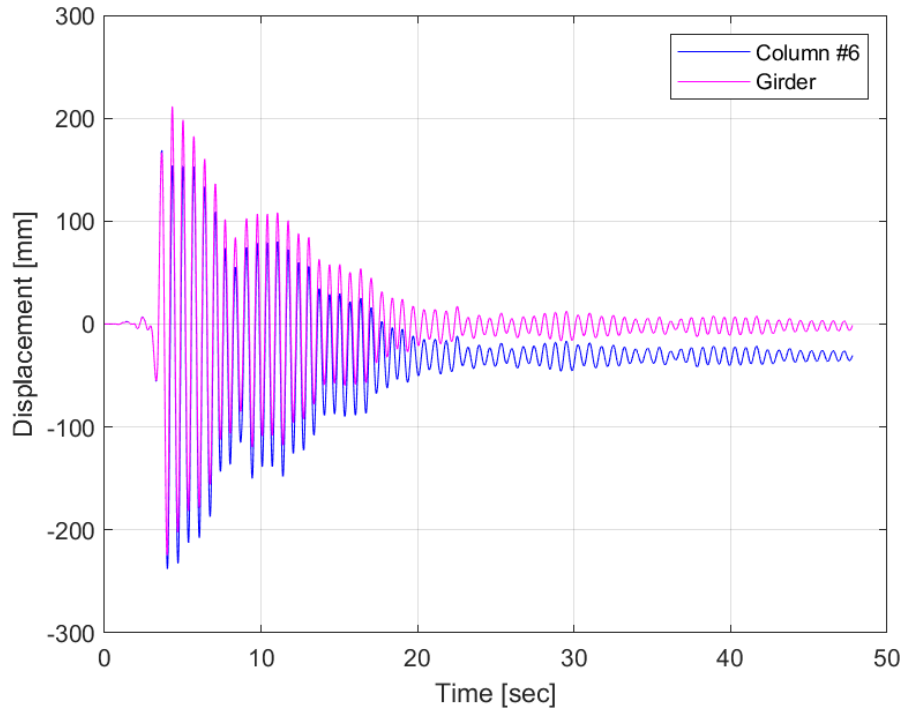


(a)

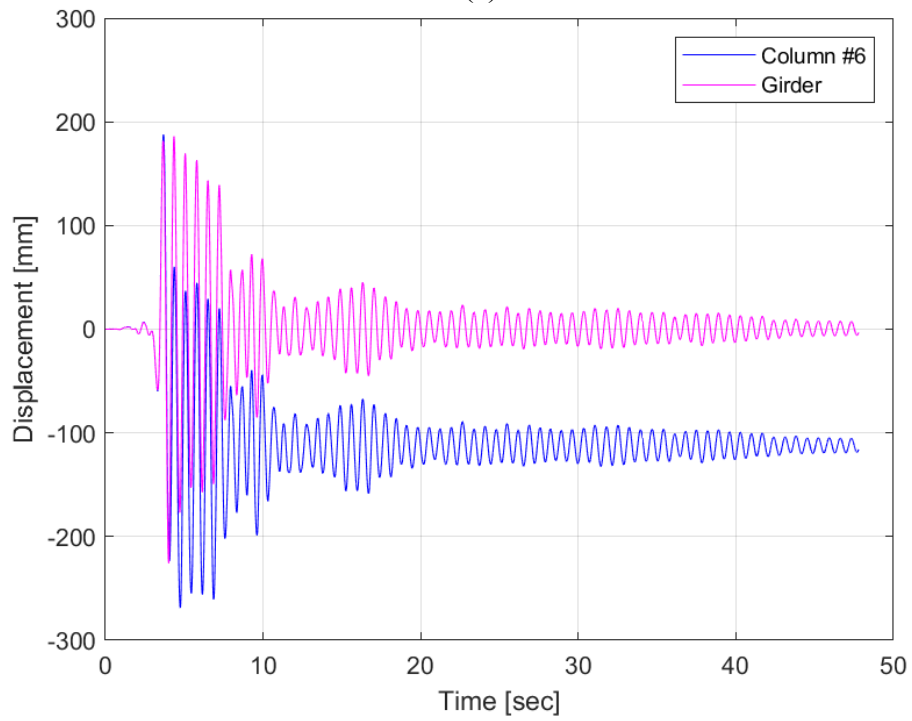


(b)

Figure 4-11. Displacement time-history of column #2 under Load Case 8 in:
 (a) Longitudinal, (b) Transverse directions.

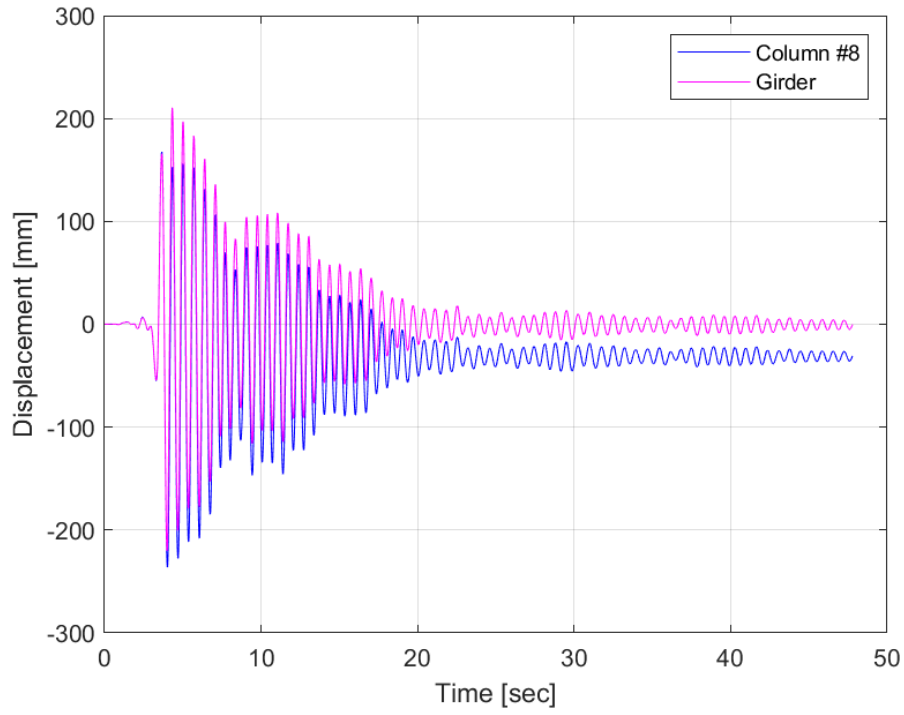


(a)

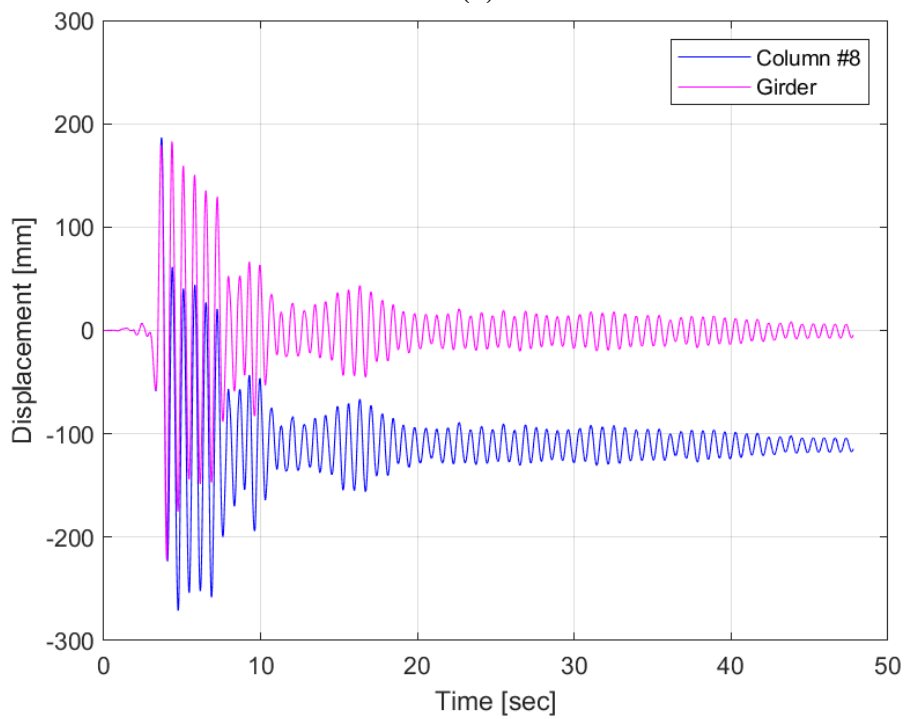


(b)

Figure 4-12. Displacement time-history of column #6 under Load Case 8 in:
 (a) Longitudinal, (b) Transverse directions.

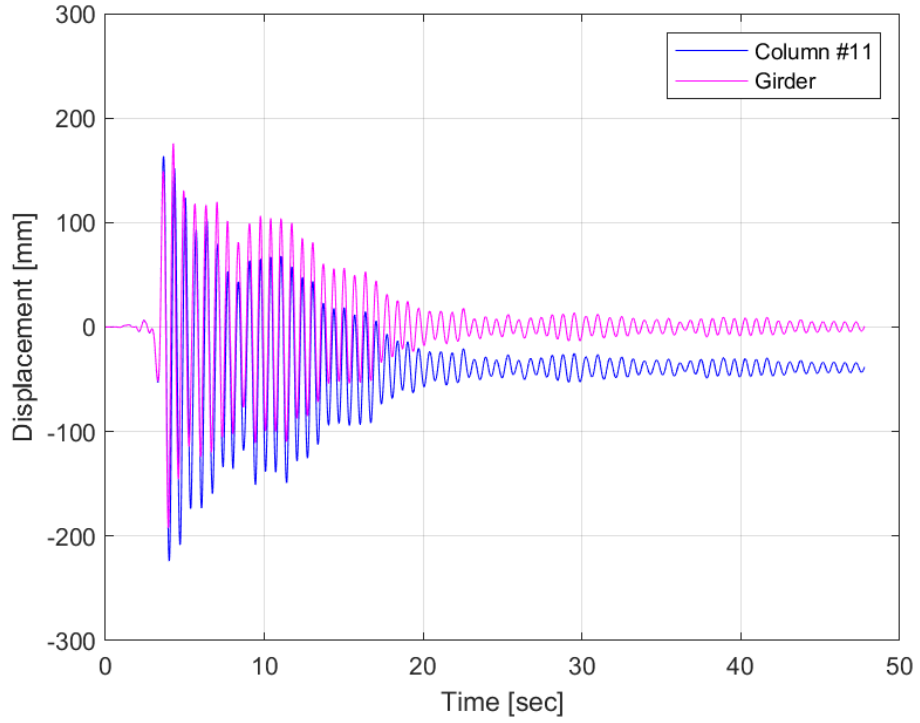


(a)

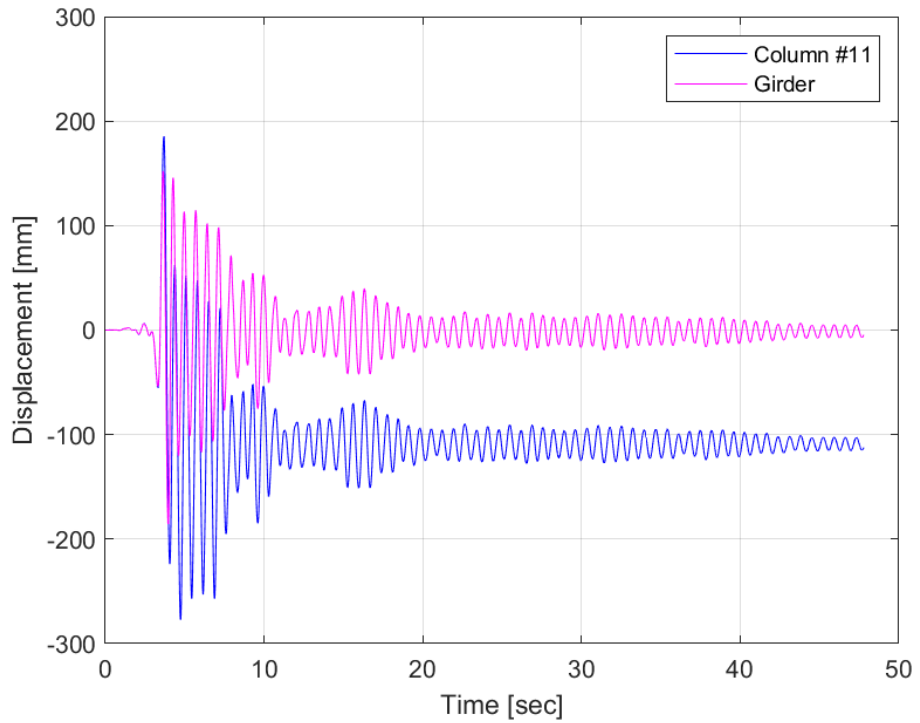


(b)

Figure 4-13. Displacement time-history of column #8 under Load Case 8 in:
 (a) Longitudinal, (b) Transverse directions.

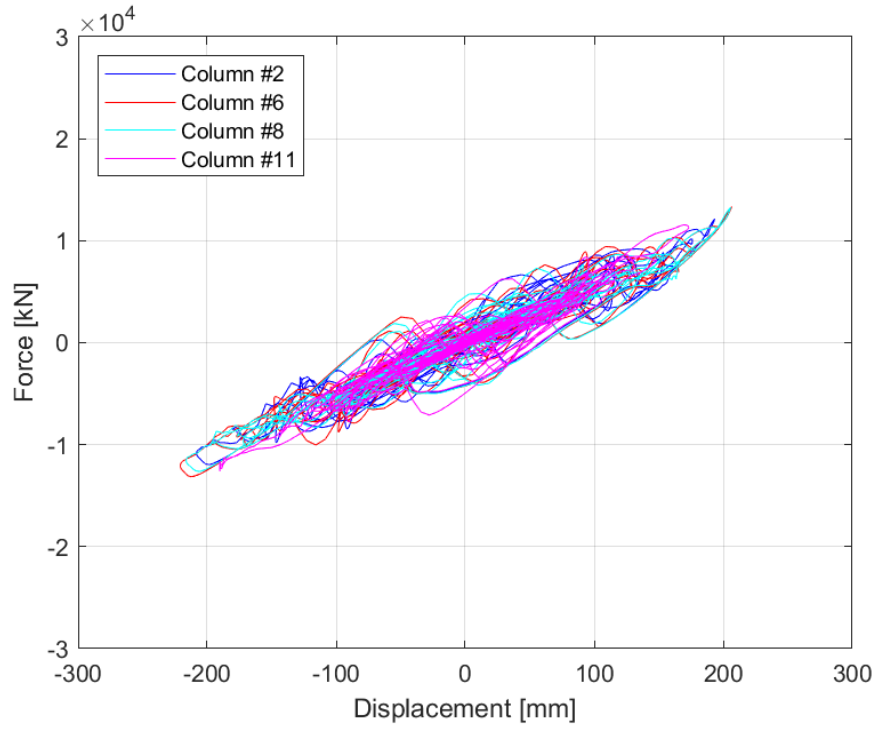


(a)

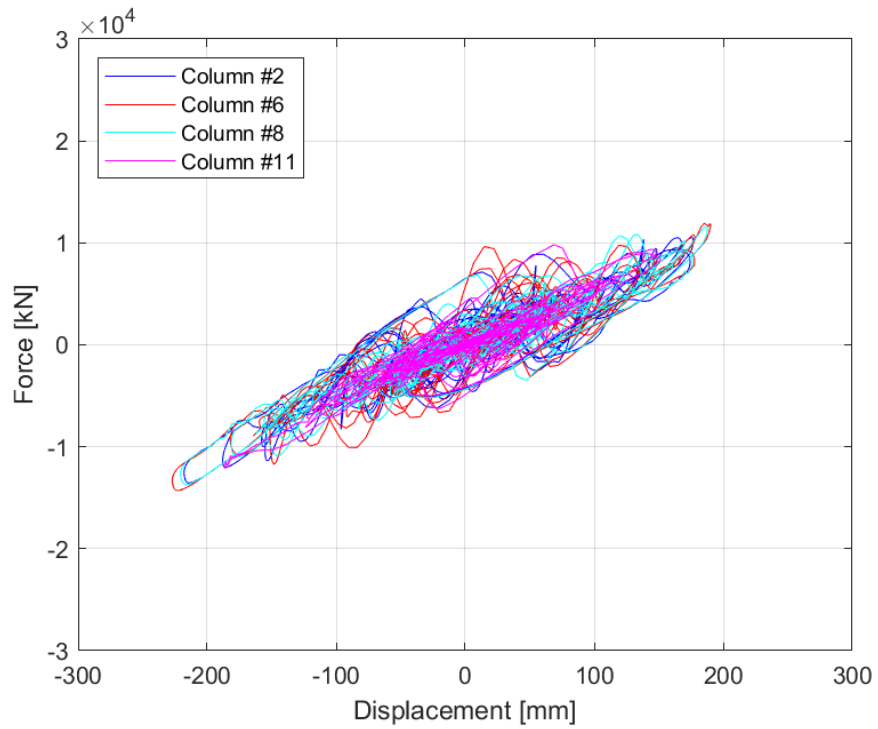


(b)

Figure 4-14. Displacement time-history of column #11 under Load Case 8 in:
 (a) Longitudinal, (b) Transverse directions.

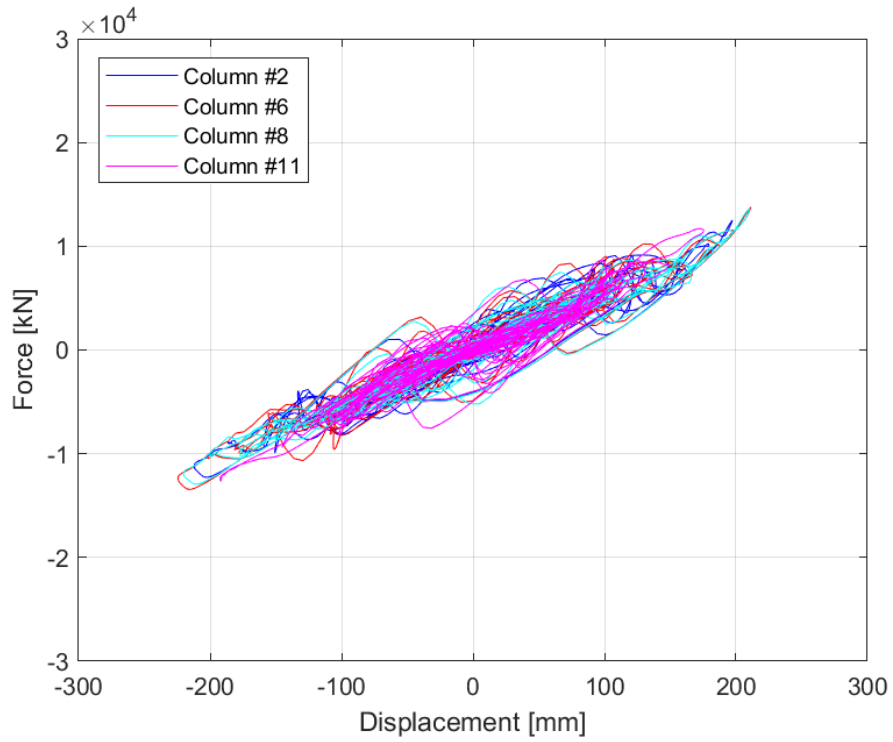


(a)

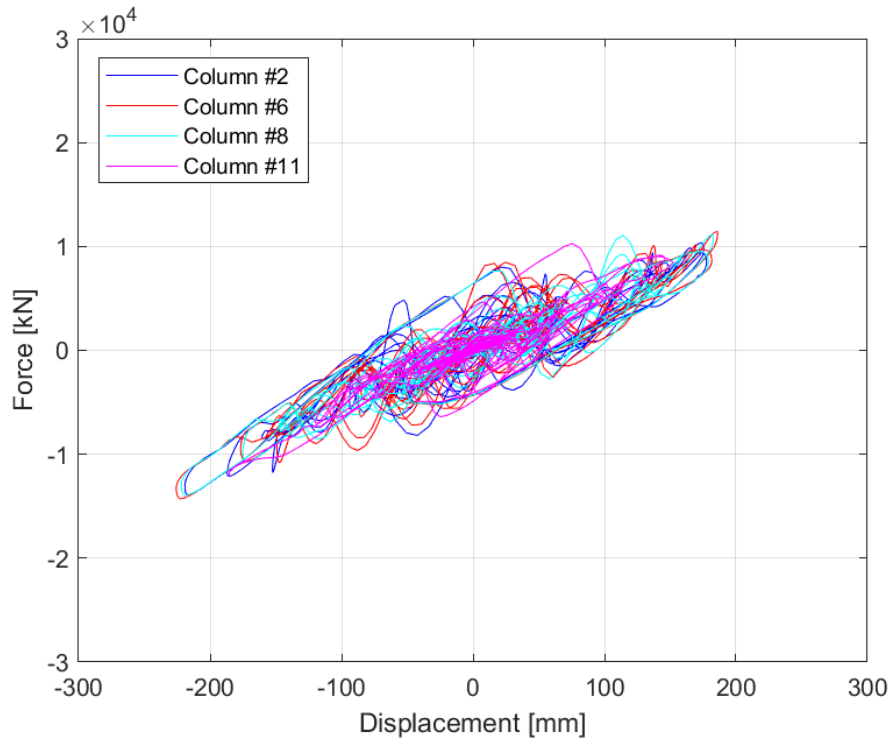


(b)

Figure 4-15. Force-displacement relationship of column #2, #6, #8, and #11 in the longitudinal direction for: (a) Load Case 1, (b) Load Case 8.



(a)



(b)

Figure 4-16. Force-displacement relationship of column #2, #6, #8, and #11 in the transverse direction for: (a) Load Case 1, (b) Load Case 8.

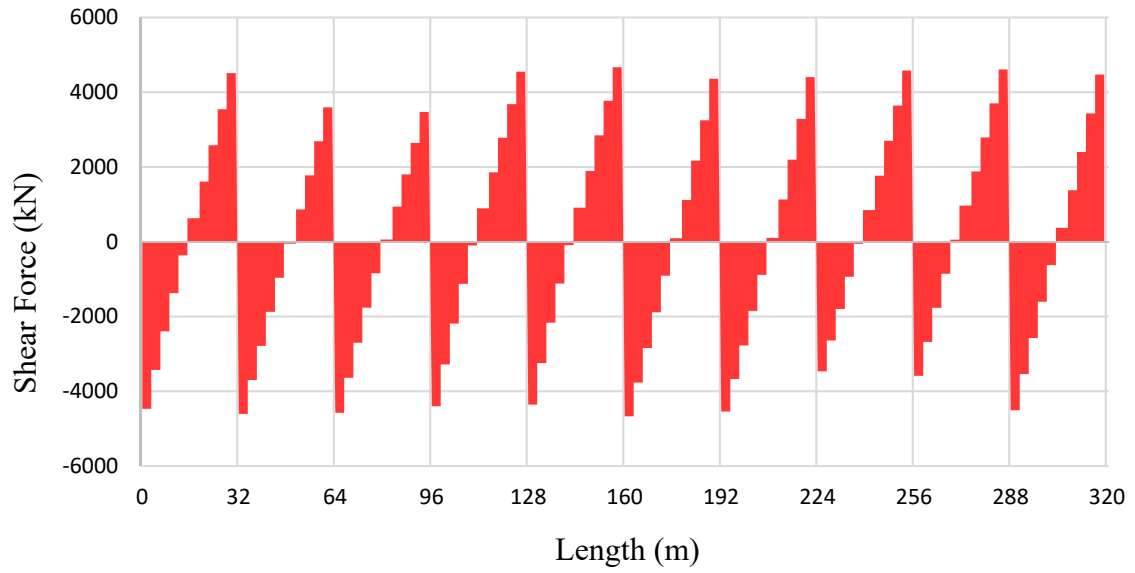


Figure 4-17. Bridge girder shear in the longitudinal direction (V_x) for Load Case 1.

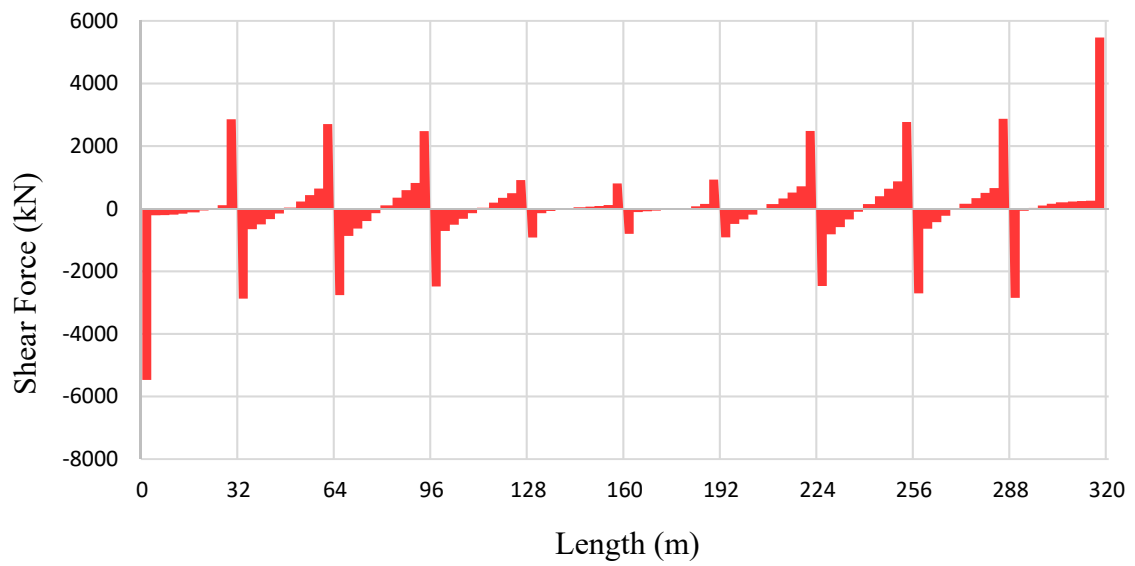


Figure 4-18. Bridge girder shear in the transverse direction (V_y) for Load Case 1.

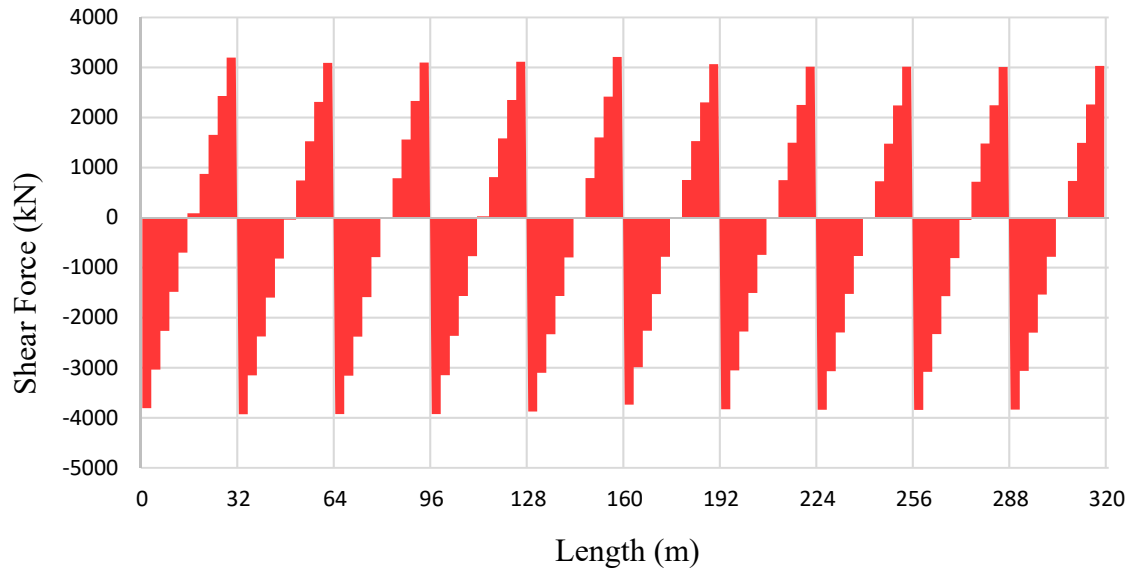


Figure 4-19. Bridge girder shear in the vertical direction (V_z) for Load Case 1.

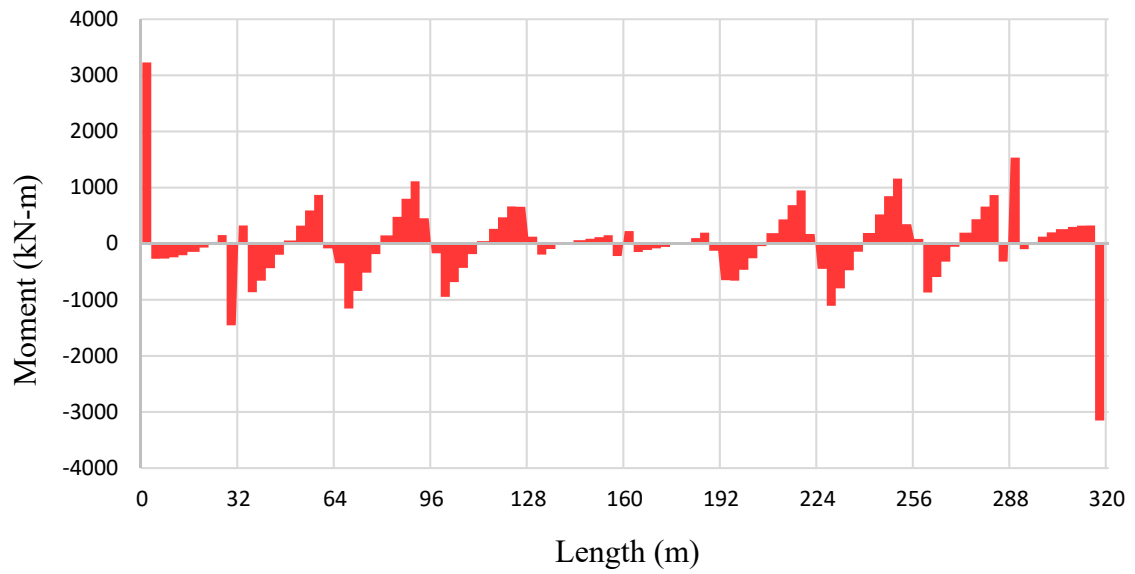


Figure 4-20. Bridge girder moment in the longitudinal direction (M_x) for Load Case 1.

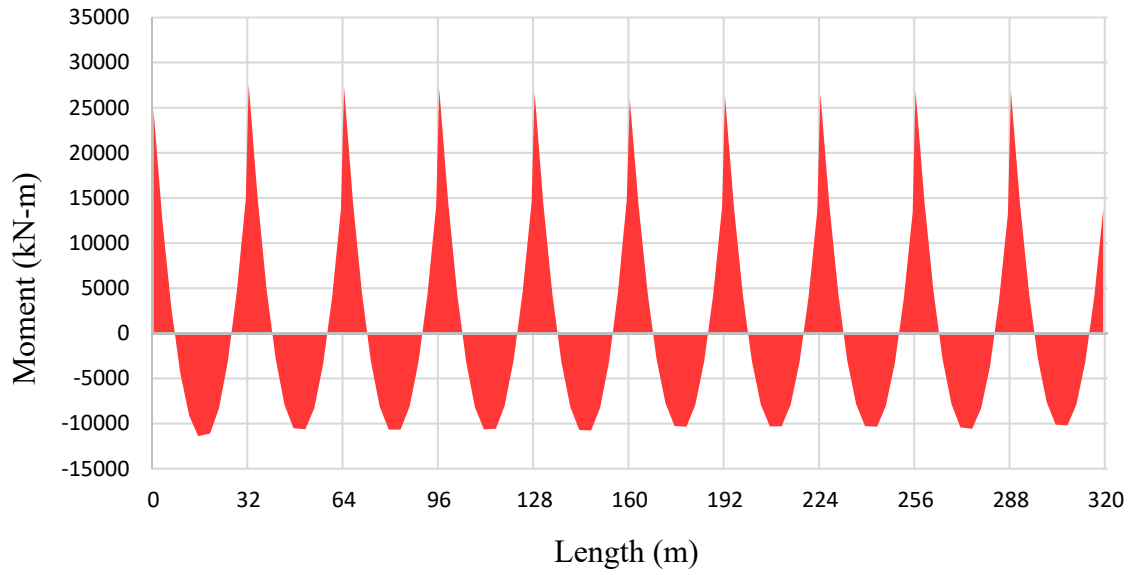


Figure 4-21. Bridge girder moment in the transverse direction (M_y) for Load Case 1.

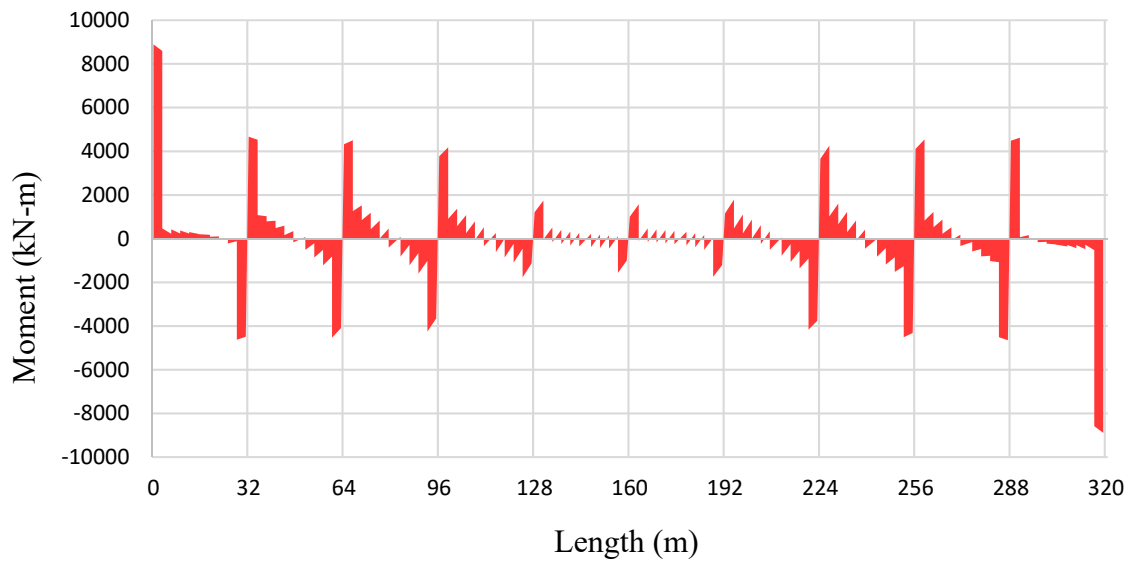


Figure 4-22. Bridge girder moment in the vertical direction (M_z) for Load Case 1.

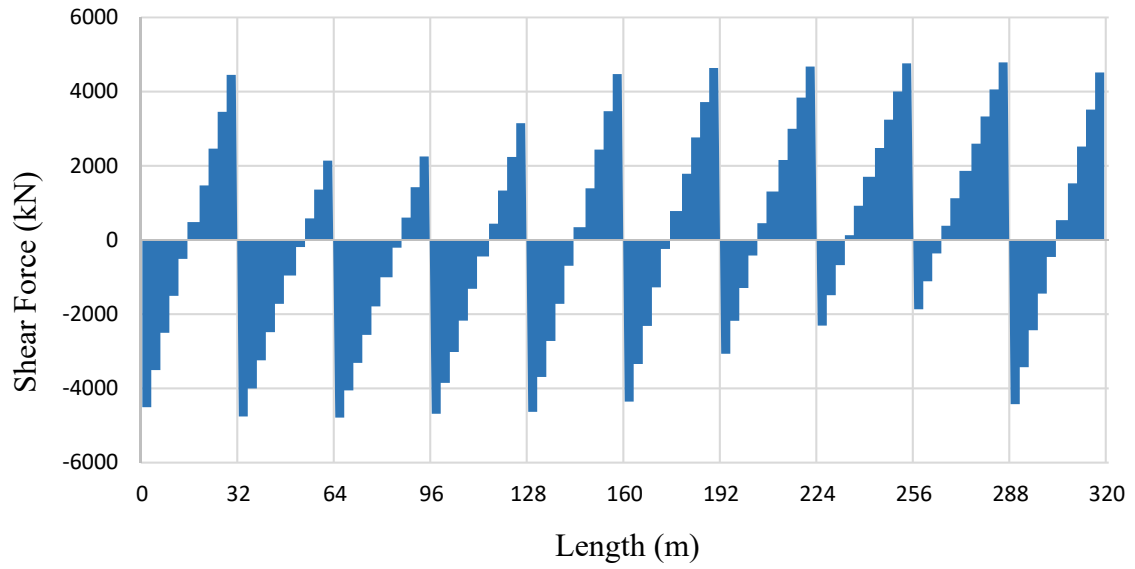


Figure 4-23. Bridge girder shear in the longitudinal direction (V_x) for Load Case 8.

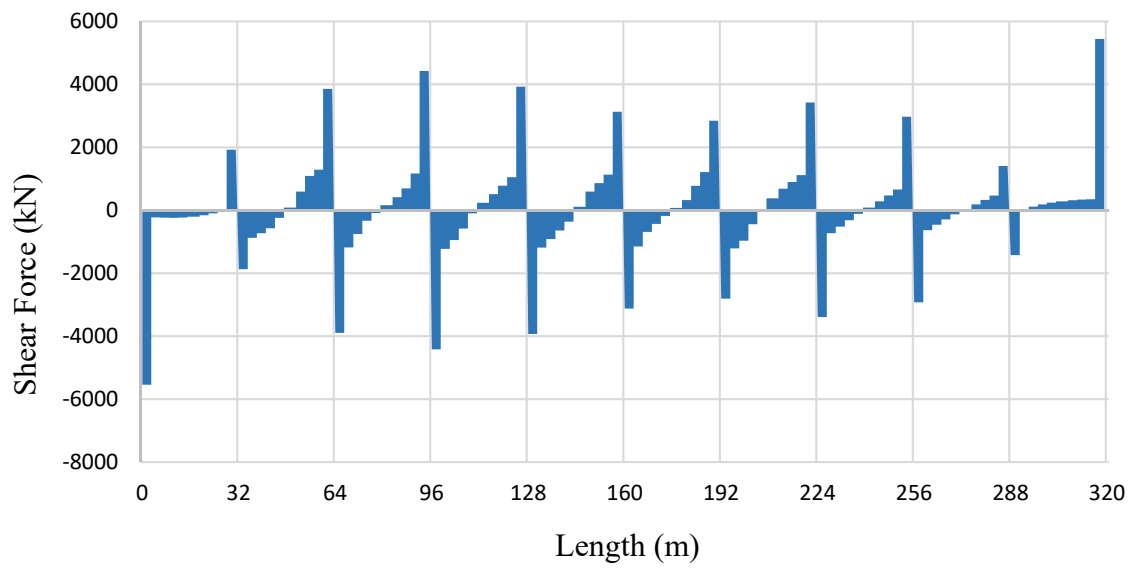


Figure 4-24. Bridge girder shear in the transverse direction (V_y) for Load Case 8.

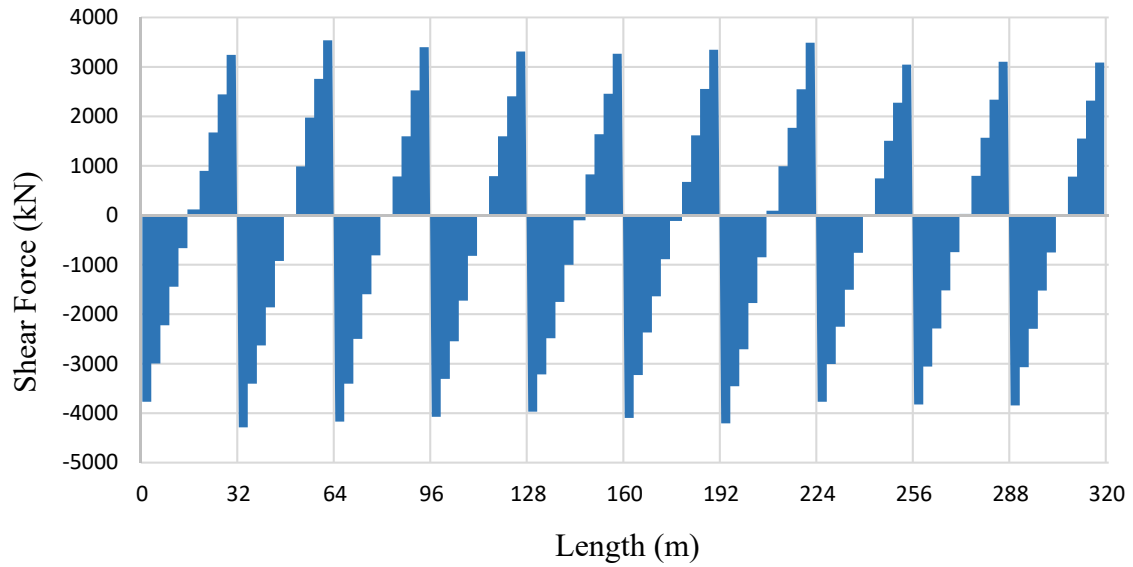


Figure 4-25. Bridge girder shear in the vertical direction (V_z) for Load Case 8.

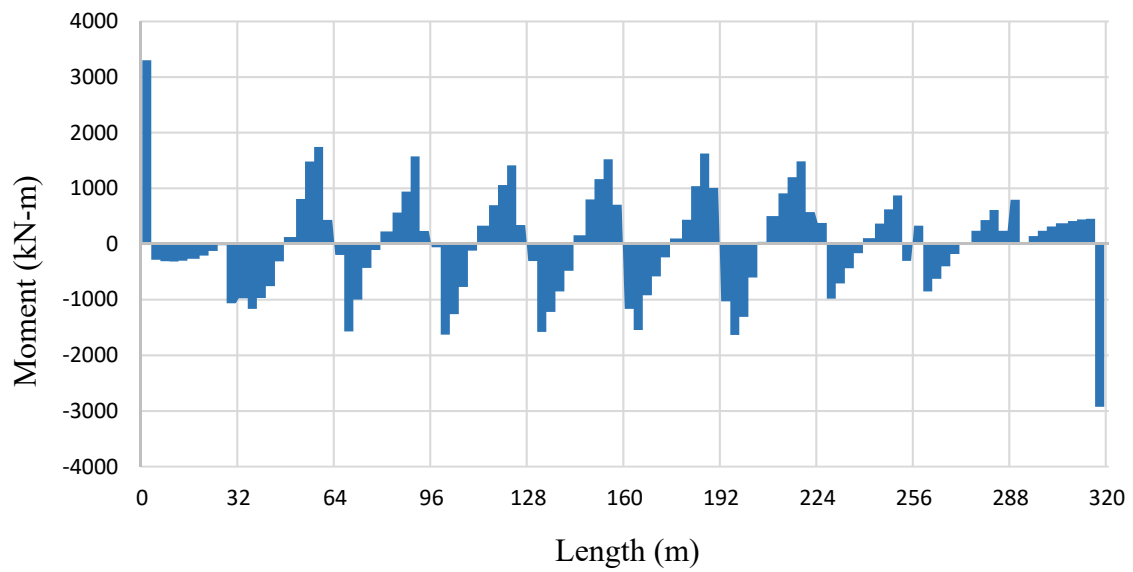


Figure 4-26. Bridge girder moment in the longitudinal direction (M_x) for Load Case 8.

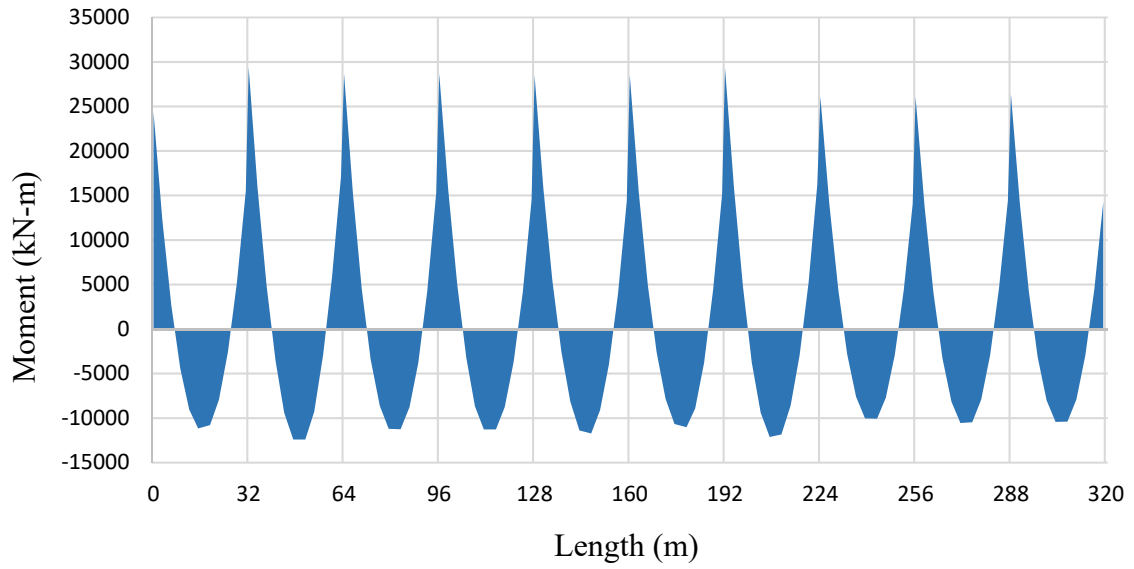


Figure 4-27. Bridge girder moment in the transverse direction (M_y) for Load Case 8.

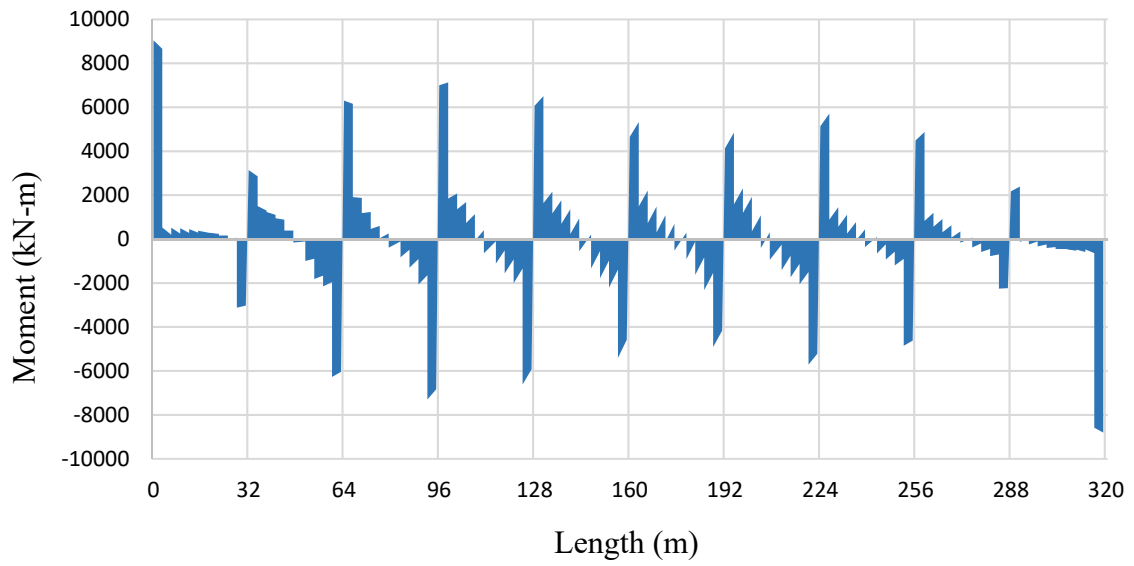


Figure 4-28. Bridge girder moment in the vertical direction (M_z) for Load Case 8.

Chapter 5. SEISMIC RESPONSE OF PROTOTYPE HSR BRIDGE SYSTEM: MORE IN-DEPTH DEMONSTRATION

Seismic loads pose a great threat to the stability of HSR bridges that can be built in high seismic regions, such as California in the United States. A proper design guideline and code are required to assess the seismic performance of an HSR bridge, which is not fully mature and developed for the United States yet. Nonetheless, this chapter further extends the brief seismic analysis presented in Section 4.4 by providing a more in-depth demonstration of the attributes of a comprehensive analysis of the structural behavior of HSR system with focus on bridge components. The more in-depth demonstration of nonlinear time history analysis of HSR bridge systems performed in this chapter considered three load cases and three ground motions applied with various intensities. The seismic analysis was performed under earthquakes applied biaxially in the longitudinal and transverse directions and applied as identical support excitations. Although the train was modeled to be stationary during the seismic loading, this simulates a scenario where a train would be called to a stop after notice of an earthquake early warning.

The three load cases were again selected from the 16 sample cases previously outlined in Table 4-1 for the selected train and bridge prototypes used in this study. These are Load Case 1, Load Case 6, and Load Case 9. Load Case 1 was selected similar to the sample analysis conducted in Chapter 4 to demonstrate the HSR bridge response without any loading from the train. Load cases 6 and 9 were selected to demonstrate the prototype HSR bridge behavior under partial and full train loading. The load cases are illustrated in Figure 5-1. The prototype HSR bridge model under each of these load cases was subjected to three ground motions sourced from the PEER Ground Motion Database by the University of California, Berkeley. The acceleration time histories of the three selected ground motions are shown in Figure 5-2. The first record is the same 1994 Northridge earthquake record from the Sepulveda VA Hospital station as used before in Chapter 4. The two additional ground motions include one from the 1995 Kobe earthquake recorded at the Takatori station, and another one from the 1989 Loma Prieta earthquake recorded at the LGPC station. Each of the three ground motions were applied with two intensity levels at 100% and 200% scale of the original record. An additional analysis was performed for the Northridge record scaled at 300% to explore the seismic response of the HSR bridge at higher seismic demands.

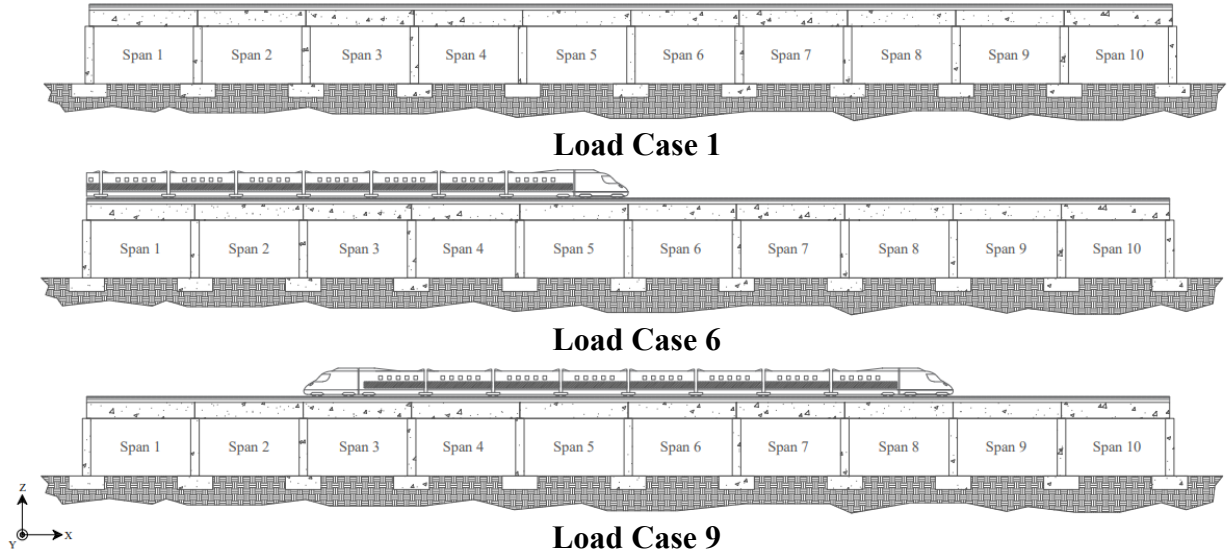


Figure 5-1. Train load cases used in the seismic analysis in Chapter 5.

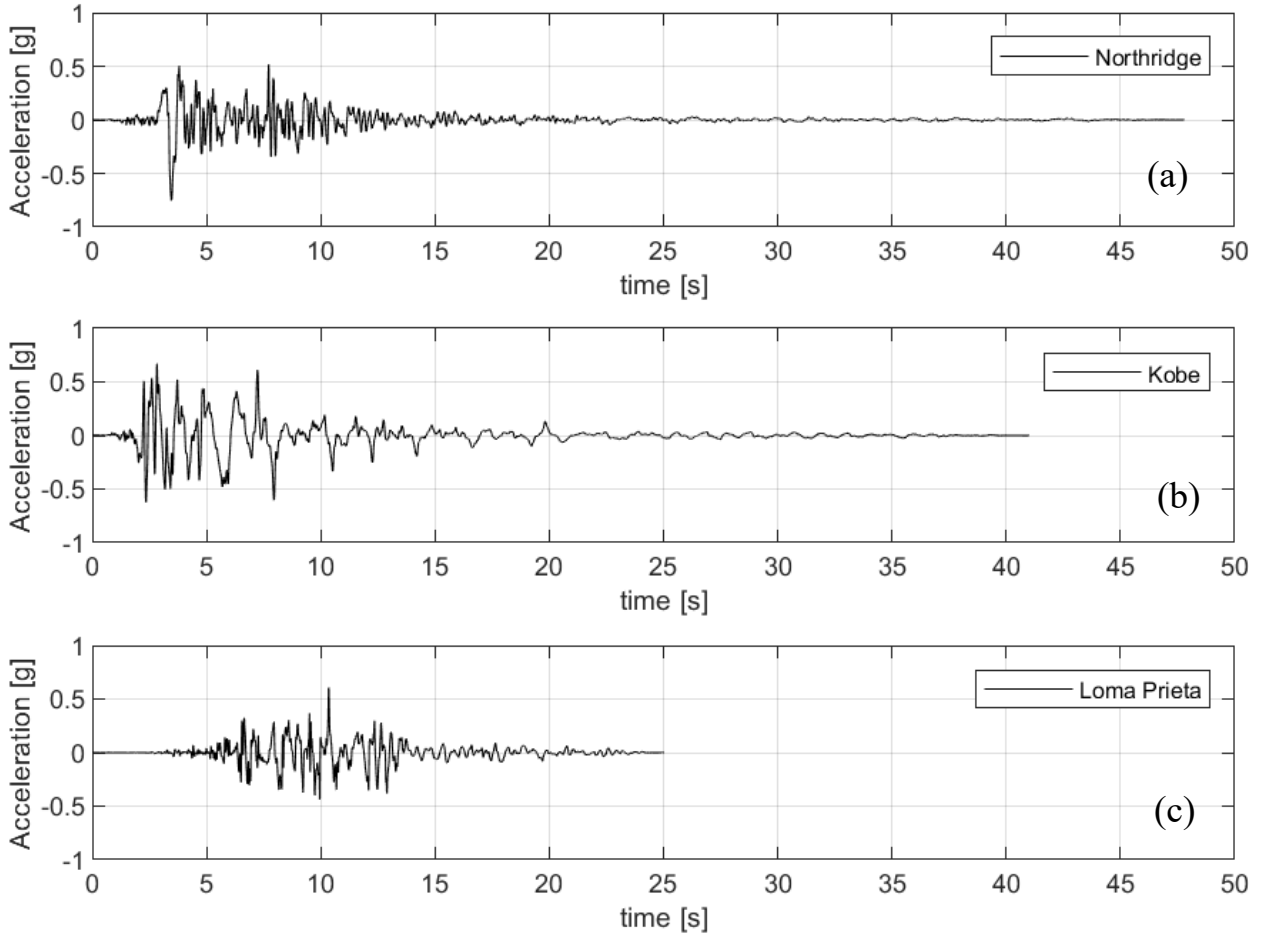


Figure 5-2. PEER database ground motions used for the seismic performance assessment: (a) Northridge, (b) Kobe, and (c) Loma Prieta.

In addition to what was presented in Chapter 4 as sample seismic analysis, this chapter provides a deeper look at both global and local behavior of selected bridge components from the 100% and 200% scale ground motion runs. A comprehensive summary of the maximum selected local and global responses of the HSR bridge are tabulated and provided here. Additional displacement time-histories, force-displacement relationships, and moment-curvature relationships are plotted to compare the effect of ground motion intensity and train loading scenarios on the HSR bridge. Moreover, results from the 300% scale Northridge record to assess the extent of nonlinear and inelastic behavior of the HSR bridge columns as well as the force-deformation behavior of selected track-bridge interaction zero-length elements to observe the load transfer within the system during seismic events.

5.1. Maximum Response Tables

The behavior of the prototype HSR bridge was analyzed by tabulating the maximum responses under the various loading scenarios. A total of 12 tables were created to analyze the maximum responses of the prototype HSR bridge. The local maximum responses of the pier columns and bridge girder spans under each load case (1, 6, and 9) were tabulated for the three ground motions at an amplification of 100% and 200%, resulting in 6 tables. The shear, moment, and curvature in the transverse and the longitudinal directions were recorded for the pier columns. However, only the longitudinal shear and moment for the bridge box-girder spans were recorded at each end of the spans since the in-plane responses were not of interest. The other 6 tables demonstrate the global maximum displacement and acceleration of the bridge girder nodes directly above the pier columns for the same load variations. The values in the tables represent the absolute maximum responses (positive or negative) and the maximum response within each category was highlighted to help visualize the trends under each load case.

Observing the tabulated maximum local responses of the pier columns and girder spans presented in Table 5-1 through Table 5-6, there is an obvious increase in magnitude for all presented values when comparing the maximum response under the original 100% scaled ground motion to the 200% scaled ground motion. The columns experienced a significant increase due to the larger seismic forces applied at the base of the model connected to the column footings through translational springs. Column shear, moment, and curvature showed an average increase of 70%, 28%, and 32% about the longitudinal axis, and an average increase of 56%, 19%, and 30% about the transverse axis. The box-girder sections were assumed to be less affected by the earthquake intensity because they are capacity protected elements and should not see higher demands beyond what is dictated by the columns' capacity.

The magnitude of the maximum local responses for Load Case 1, 6, and 9 were compared among all of the considered loading scenarios to identify the impact of train loading. The Load Case 6 train loading is heavily shifted to one side of the bridge and imposes less total weight of the train on the bridge, relative to full train load in Load Case 9, due to a portion of the train not being on the bridge. Yet, the bridge seismic response due to both load cases with partial and full train load on top of the bridge were similar. Comparing the average responses between Load Case 1 with no train loading to Load Cases 6 and 9 with train loading, the most notable change was in the maximum longitudinal moment response where an average increase of 10% and 12% was observed for Load Case 6 and 9, respectively. The maximum column shear response showed small increases of less than 2% and the maximum transverse column moment increased by 4% for both load cases. Load Case 9 showed 6% increase for the maximum column curvature in both directions and Load

Case 6 increased by 4% for both directions. The in-plane girder shear and moment also increased by 5% for Load Case 6 and 6% for Load Case 9. When comparing the two load cases with train loading, Load Case 9 had slightly larger responses on average when compared against Load Case 6.

The maximum global response in terms of the displacement and acceleration measured at the girder nodes directly above the respective pier columns were obtained under the three different ground motions and are tabulated in Table 5-7 through Table 5-12. Each table compares results from the three selected load cases. Thus, the six tables represent the six ground motion scenarios: 3 different records \times 2 different seismic intensities. On average, the higher intensity ground motions at 200% scale increased the longitudinal and transverse maximum global displacements by 111% and 87%, respectively, as well as the longitudinal and transverse maximum global accelerations by 54% and 55%, respectively. When comparing Load Case 1 to Load Case 6 and 9, the most notable change was increase in the average maximum longitudinal displacement by 4% for both load cases. The maximum transverse displacement increased by 3% for Load Case 6 but did not change for Load Case 9. The increase in maximum acceleration for either load case was insignificant with less than 1% increase and the transverse acceleration for Load Case 9 even decreased by 3%. The minimal increase in the longitudinal acceleration and decrease in the transverse acceleration for the load cases with train loading can be assumed to follow the fundamental concept of Newton's Second Law of Motion. The addition of train loading increases the mass and in-turn decreases the acceleration of the bridge to maintain force equilibrium; however, this is assuming a perfectly linear system which is not the case for this study since inelastic material behavior have been modeled. Seismic response of the prototype HSR bridge will vary as the stiffness of the structure changes throughout the cyclic loading of the seismic forces and the overall mass changes based on the load case. Ultimately, the lack of major change in local and global response due to additional train loading could be a result of the inherent conservative design nature of HSR bridges. Compared to similar highway bridges, HSR bridge columns are designed to be much stiffer to minimize lateral deformations to improve the train and track stability as well as the riding comfort of passengers. HSR bridges feature massive columns with larger force and moment capacities, relative to equivalent highway bridges, which indirectly result in HSR bridges withstanding larger earthquake forces before failure.

Table 5-1. Maximum Local Responses – Northridge 100% Scale.

Member ID	LC1						LC6						LC9					
	Shear Long (kN)	Shear Trans (kN)	Moment Long (kN-m)	Moment Trans (kN-m)	Curvature Long (1/m*10^-6)	Curvature Trans (1/m*10^-6)	Shear Long (kN)	Shear Trans (kN)	Moment Long (kN-m)	Moment Trans (kN-m)	Curvature Long (1/m*10^-6)	Curvature Trans (1/m*10^-6)	Shear Long (kN)	Shear Trans (kN)	Moment Long (kN-m)	Moment Trans (kN-m)	Curvature Long (1/m*10^-6)	Curvature Trans (1/m*10^-6)
Columns																		
1	12275	11907	151849	150935	5.41115	3.6981	12422.8	11944.4	153028	150033	5.41941	3.89747	12437.9	11843	152118	150278	5.40287	3.73938
2	12139.6	13550	209734	232044	7.36617	5.66054	12476.7	14063	210456	240450	7.01737	5.4112	12490.1	13728.8	215793	235574	7.50425	5.75906
3	12859.2	13708.3	210118	234453	7.02843	5.30174	13339.3	14352.7	232814	244012	7.84353	5.97026	13356.1	13954.6	234245	243050	7.94912	6.03848
4	13258.3	13721.5	210939	234834	7.0626	5.27189	13610.6	14203.3	210842	244499	7.11357	5.50165	13663.2	14021.5	213835	243314	7.08676	5.48557
5	13365.7	14047.6	210939	235179	7.1229	5.50255	13770.8	14229.3	212045	239368	7.16862	5.38151	13801.5	14184.5	212137	245451	7.13918	5.49617
6	13320.8	14309.5	211007	236872	7.15251	5.43494	13717	14242.9	214807	244416	7.1018	5.49007	13753.1	14291.9	212750	245455	7.1478	5.5029
7	13368.2	14046.1	211333	235138	7.12706	5.5076	13778.5	14021.2	212103	242456	7.13283	5.48129	13797.5	14184.6	212081	245393	7.1431	5.5019
8	13259.2	13725.8	211147	234877	7.06274	5.27728	13612.9	13716.5	213501	237046	7.06994	5.40843	13658.2	14037.6	211293	245531	7.14937	5.51575
9	12858.1	13707	210541	234440	7.02732	5.30118	13236.6	13547.9	238736	244999	7.7545	5.83619	13345.7	13981.1	238770	244187	8.08671	6.11182
10	12139.3	13550.6	208201	232096	7.34406	5.6722	12461.5	13285.8	208189	230721	6.96425	5.33878	12485.6	13766.2	209233	232733	6.98815	5.43353
11	12603.9	12169.3	169872	155746	5.48013	4.30796	12450.1	11857.8	167967	165218	5.57852	4.34042	12659.2	12042.6	168648	165987	5.5765	4.34327
Long. Girder																		
S1-L	4249.26	NR	28142.2	NR	NR	NR	4720	NR	30867	NR	NR	NR	4366.01	NR	29280.2	NR	NR	NR
S1-R	4523.86	NR	35581.7	NR	NR	NR	4777.25	NR	37026.6	NR	NR	NR	4414.67	NR	35350.4	NR	NR	NR
S2-L	4528.71	NR	31278.9	NR	NR	NR	4763.85	NR	34406.5	NR	NR	NR	4601.22	NR	33261.9	NR	NR	NR
S2-R	4607.31	NR	36807.2	NR	NR	NR	4810.39	NR	38131.5	NR	NR	NR	4615.77	NR	37201	NR	NR	NR
S3-L	4628.05	NR	33189.6	NR	NR	NR	4480.13	NR	32922	NR	NR	NR	4845.49	NR	35341.8	NR	NR	NR
S3-R	4559.36	NR	36821.6	NR	NR	NR	4708.54	NR	37941	NR	NR	NR	4960.25	NR	39749.2	NR	NR	NR
S4-L	4448.05	NR	31915.9	NR	NR	NR	4600.01	NR	32157.7	NR	NR	NR	4451.39	NR	32485.1	NR	NR	NR
S4-R	4624.44	NR	37117.6	NR	NR	NR	4749.83	NR	37766.3	NR	NR	NR	4810.66	NR	37964.9	NR	NR	NR
S5-L	4359.03	NR	30665.4	NR	NR	NR	4671.02	NR	34922.3	NR	NR	NR	4377.22	NR	31865.1	NR	NR	NR
S5-R	4559.82	NR	36634.2	NR	NR	NR	4962.56	NR	39008.5	NR	NR	NR	4721.4	NR	37513	NR	NR	NR
S6-L	4275.74	NR	30736.7	NR	NR	NR	4294.8	NR	31305.1	NR	NR	NR	4356.86	NR	32199.1	NR	NR	NR
S6-R	4580.36	NR	18128.6	NR	NR	NR	4352.85	NR	17954	NR	NR	NR	4503.42	NR	18078	NR	NR	NR
S7-L	3770.44	NR	18106.6	NR	NR	NR	3561.85	NR	17938.3	NR	NR	NR	3597.58	NR	18060.6	NR	NR	NR
S7-R	4611.25	NR	36843.4	NR	NR	NR	4560.33	NR	36621.6	NR	NR	NR	4792.65	NR	38123.6	NR	NR	NR
S8-L	4582.72	NR	32888.4	NR	NR	NR	4622.42	NR	34322.2	NR	NR	NR	4996.97	NR	36406.6	NR	NR	NR
S8-R	4565.15	NR	36635.2	NR	NR	NR	4498.31	NR	36489.8	NR	NR	NR	5001.73	NR	39461	NR	NR	NR
S9-L	4545	NR	31721.5	NR	NR	NR	4442.28	NR	31360.8	NR	NR	NR	4495.7	NR	32748.1	NR	NR	NR
S9-R	4682.04	NR	36740	NR	NR	NR	4515.52	NR	36560.9	NR	NR	NR	4596.1	NR	36596.3	NR	NR	NR
S10-L	4319.29	NR	30788.8	NR	NR	NR	4184.43	NR	29786.8	NR	NR	NR	4229.61	NR	30970.6	NR	NR	NR
S10-R	4463.03	NR	33056.3	NR	NR	NR	4329.4	NR	32397.5	NR	NR	NR	4387.44	NR	32682.7	NR	NR	NR

Table 5-2. Maximum Local Responses – Northridge 200% Scale.

Member ID	LC1						LC6						LC9					
	Shear Long (kN)	Shear Trans (kN)	Moment Long (kN-m)	Moment Trans (kN-m)	Curvature Long (1/m*10 ⁻⁶)	Curvature Trans (1/m*10 ⁻⁶)	Shear Long (kN)	Shear Trans (kN)	Moment Long (kN-m)	Moment Trans (kN-m)	Curvature Long (1/m*10 ⁻⁶)	Curvature Trans (1/m*10 ⁻⁶)	Shear Long (kN)	Shear Trans (kN)	Moment Long (kN-m)	Moment Trans (kN-m)	Curvature Long (1/m*10 ⁻⁶)	Curvature Trans (1/m*10 ⁻⁶)
Columns																		
1	20152.7	22146.5	190602	209865	7.00727	5.2734	20719.5	23078.4	194594	232675	7.33951	5.85553	20754.9	23545.4	204927	231068	7.25686	5.69594
2	17084.8	22655.5	243403	278781	9.62929	7.44995	17206.6	23525.9	266737	302135	9.13953	7.03529	17196.8	23922.4	274384	295901	9.35216	7.1118
3	17342	22319.8	241642	289519	9.46651	7.191	17469.2	23374.2	264985	299544	9.25183	7.10208	17492.6	23773	279593	303647	9.45321	7.25856
4	17572.4	22504.2	242350	292998	9.53332	7.27315	17763.4	23652.1	263819	304077	9.30209	7.16542	17752	24083.2	273577	305148	9.19906	7.10607
5	17750.7	22863	242633	295158	9.56806	7.30668	17966.1	24118.1	261716	306859	9.31858	7.20032	17988.5	24531.5	264792	306115	9.15409	6.97717
6	17758.1	22949.9	242890	289233	9.55678	7.29323	17957.7	24194	265034	306437	9.40173	7.24145	17969.9	24647.3	265440	305918	9.13021	6.99337
7	17753	22863.7	242731	295133	9.56814	7.30742	17970.8	24029.8	262488	303768	9.36128	7.23338	17961.5	24515.6	264656	306256	9.14575	7.01521
8	17569.4	22527	242354	293030	9.53566	7.27484	17731.6	23528.2	264075	299540	9.31224	7.17816	17744.8	24025.9	257955	303791	9.15903	7.0545
9	17335.8	22337.5	242211	289532	9.46736	7.1919	17478.5	23227.2	270904	299456	9.49071	7.32262	17473.3	23713.4	265271	300861	9.21683	7.04442
10	17115.9	22667.2	243626	279916	9.60255	7.44459	17214.1	23496.5	275967	292447	9.37865	7.14331	17196.7	23963.2	273211	290999	9.34182	7.11047
11	20151.2	22146.5	204065	198594	6.21755	4.81196	20731.2	23338.4	205219	207401	6.1281	4.74792	20753.6	23473.3	206101	211862	6.29587	4.86896
Long. Girder																		
S1-L	4755.73	NR	31968.1	NR	NR	NR	5105.45	NR	34369.3	NR	NR	NR	4732.45	NR	33582	NR	NR	NR
S1-R	4984.97	NR	39200.6	NR	NR	NR	5063.32	NR	39513.3	NR	NR	NR	4820.44	NR	38117.7	NR	NR	NR
S2-L	4707.7	NR	33866.7	NR	NR	NR	4639.89	NR	37186.1	NR	NR	NR	4718.67	NR	35394.5	NR	NR	NR
S2-R	5080.08	NR	39799.6	NR	NR	NR	5087.51	NR	40304.3	NR	NR	NR	4866.94	NR	39247.4	NR	NR	NR
S3-L	4721.37	NR	33973.9	NR	NR	NR	4588.66	NR	34632.5	NR	NR	NR	5007.36	NR	36144.7	NR	NR	NR
S3-R	4699.26	NR	39007.7	NR	NR	NR	4827.88	NR	40302.1	NR	NR	NR	5060.25	NR	41989.4	NR	NR	NR
S4-L	4661.32	NR	34143.5	NR	NR	NR	4796.73	NR	34920	NR	NR	NR	4985.45	NR	35965.6	NR	NR	NR
S4-R	4678.83	NR	39119.8	NR	NR	NR	4880.98	NR	40475.7	NR	NR	NR	4932.37	NR	40444	NR	NR	NR
S5-L	4709.23	NR	34120	NR	NR	NR	4953.79	NR	36820	NR	NR	NR	4577.62	NR	35729.8	NR	NR	NR
S5-R	4693.49	NR	38791	NR	NR	NR	5077.49	NR	41572.7	NR	NR	NR	4838.41	NR	39848	NR	NR	NR
S6-L	4746.34	NR	34234.2	NR	NR	NR	4559.8	NR	34167.5	NR	NR	NR	4524.27	NR	35732.3	NR	NR	NR
S6-R	4771.79	NR	21583.3	NR	NR	NR	4548.78	NR	21200.3	NR	NR	NR	4643.89	NR	21687.8	NR	NR	NR
S7-L	3878.25	NR	21613	NR	NR	NR	3710.37	NR	21220.2	NR	NR	NR	3746.69	NR	21690.8	NR	NR	NR
S7-R	4720.16	NR	38911.3	NR	NR	NR	4676.62	NR	38957.6	NR	NR	NR	4898.65	NR	40469.3	NR	NR	NR
S8-L	4696.16	NR	34334.8	NR	NR	NR	4428.73	NR	34009	NR	NR	NR	4900.96	NR	37247	NR	NR	NR
S8-R	4699.85	NR	38752.3	NR	NR	NR	4673.45	NR	39024.1	NR	NR	NR	5105.31	NR	41558.5	NR	NR	NR
S9-L	4535.27	NR	33654.1	NR	NR	NR	4595.69	NR	36013.1	NR	NR	NR	4710.92	NR	35935	NR	NR	NR
S9-R	4931.36	NR	39146.5	NR	NR	NR	4705.11	NR	39190.6	NR	NR	NR	4688.15	NR	39323.2	NR	NR	NR
S10-L	4777.57	NR	37057.4	NR	NR	NR	4706.12	NR	35888.4	NR	NR	NR	4705.99	NR	36483.7	NR	NR	NR
S10-R	5081.84	NR	37999.3	NR	NR	NR	5008.66	NR	37477.6	NR	NR	NR	4987.95	NR	37372.5	NR	NR	NR

Table 5-3. Maximum Local Responses – Kobe 100% Scale.

Member ID	LC1						LC6						LC9					
	Shear Long (kN)	Shear Trans (kN)	Moment Long (kN-m)	Moment Trans (kN-m)	Curvature Long (1/m*10 ⁻⁶)	Curvature Trans (1/m*10 ⁻⁶)	Shear Long (kN)	Shear Trans (kN)	Moment Long (kN-m)	Moment Trans (kN-m)	Curvature Long (1/m*10 ⁻⁶)	Curvature Trans (1/m*10 ⁻⁶)	Shear Long (kN)	Shear Trans (kN)	Moment Long (kN-m)	Moment Trans (kN-m)	Curvature Long (1/m*10 ⁻⁶)	Curvature Trans (1/m*10 ⁻⁶)
Columns																		
1	6842.45	8109.37	127960	133318	4.87947	3.4002	7285.29	7692.3	130692	132320	4.90077	3.41558	7330.79	7719.35	129415	132523	4.86118	3.39022
2	6481.78	9435.41	152482	206944	5.68237	4.54798	6689.65	9978.51	159062	212987	5.69277	4.6711	6531.22	9931.94	155022	207516	5.53066	4.48544
3	6583.86	7942.98	147228	206859	5.61823	4.28045	6678.79	8183.46	149464	211335	5.49168	4.30567	6764.32	8076.88	150264	211354	5.49097	4.27324
4	6553.46	7554.41	149248	207191	5.3409	4.43362	6781.09	7790.09	157674	211460	5.66492	4.42625	6841.63	7479.63	164509	211277	5.36275	4.23135
5	6734.85	7237.97	149619	214377	5.93882	4.88066	6927.39	7898.16	144733	213947	5.76678	4.43761	6980.66	7764.29	154784	211400	5.65427	4.39664
6	7354.78	8085.57	145059	209173	5.80052	4.50659	7239.29	8238.39	151609	213804	5.89383	4.42065	7335.8	8353.99	150737	213228	5.94126	4.42391
7	6710.87	7271.82	149848	208405	5.6074	4.48985	6925.32	7351.16	151601	208066	5.61963	4.27139	6934.52	7756.07	155475	211070	5.67654	4.40343
8	6546.59	7534.98	149336	207586	5.32395	4.41378	6808.99	7187.21	161465	206112	5.37757	4.32048	6784.16	7432.73	161450	211116	5.44874	4.23418
9	6626.4	7901.77	147301	207481	5.57534	4.26632	6730.05	7693.34	149645	204934	5.4075	4.28778	6794.6	8046.95	154950	210508	5.42327	4.21701
10	6503.19	9430.09	152067	200593	5.71556	4.56559	6634.11	9634.42	152469	196778	5.50469	4.35323	6534.2	9875.7	153508	196050	5.72868	4.67844
11	6839.1	8105.63	138042	133431	5.64877	4.48034	7289.2	7794.25	143808	141281	5.42658	4.34666	7337.27	7781.06	140961	140867	5.39112	4.32932
Long. Girder																		
S1-L	3975.21	NR	25144.1	NR	NR	NR	4255.66	NR	27520.9	NR	NR	NR	4073.83	NR	26104.7	NR	NR	NR
S1-R	4309	NR	33374.2	NR	NR	NR	4628.39	NR	35081.5	NR	NR	NR	4288.96	NR	33332.9	NR	NR	NR
S2-L	3971.04	NR	26913.8	NR	NR	NR	4239.29	NR	29739.1	NR	NR	NR	4018.86	NR	27379.5	NR	NR	NR
S2-R	4381.58	NR	33736.3	NR	NR	NR	4581.46	NR	34980.6	NR	NR	NR	4370.93	NR	33602.3	NR	NR	NR
S3-L	4071.31	NR	27761.1	NR	NR	NR	4068	NR	29053	NR	NR	NR	4386.35	NR	30572.5	NR	NR	NR
S3-R	4318.78	NR	33099.9	NR	NR	NR	4469.12	NR	34692.3	NR	NR	NR	4691.63	NR	36032.5	NR	NR	NR
S4-L	4061.79	NR	27603.8	NR	NR	NR	4233.91	NR	28521.1	NR	NR	NR	4191.64	NR	28645.4	NR	NR	NR
S4-R	4286.46	NR	33089.7	NR	NR	NR	4550.09	NR	35109.9	NR	NR	NR	4567.19	NR	34606.4	NR	NR	NR
S5-L	4099.45	NR	28170.5	NR	NR	NR	4438.85	NR	30919.7	NR	NR	NR	4154.84	NR	28790.2	NR	NR	NR
S5-R	4304.81	NR	33645.1	NR	NR	NR	4751.93	NR	36420.6	NR	NR	NR	4540.2	NR	34856.8	NR	NR	NR
S6-L	4130.95	NR	28267.3	NR	NR	NR	4009.89	NR	27632.1	NR	NR	NR	4078.52	NR	28269.2	NR	NR	NR
S6-R	4070.1	NR	14421	NR	NR	NR	3965.1	NR	14615.6	NR	NR	NR	4224.2	NR	14525.9	NR	NR	NR
S7-L	3273.88	NR	14433.8	NR	NR	NR	3184.54	NR	14623.3	NR	NR	NR	3319.56	NR	14534.6	NR	NR	NR
S7-R	4319.93	NR	33041.1	NR	NR	NR	4275.36	NR	33031.7	NR	NR	NR	4556.21	NR	34853.8	NR	NR	NR
S8-L	4048.41	NR	28091.1	NR	NR	NR	4035.02	NR	28624.8	NR	NR	NR	4489.57	NR	31457.9	NR	NR	NR
S8-R	4325.47	NR	33449.3	NR	NR	NR	4254.86	NR	32863.8	NR	NR	NR	4708.34	NR	35710.3	NR	NR	NR
S9-L	4097.17	NR	27315	NR	NR	NR	4054.86	NR	27225.2	NR	NR	NR	4031.02	NR	27390.9	NR	NR	NR
S9-R	4357.47	NR	33600.7	NR	NR	NR	4318.24	NR	33535.1	NR	NR	NR	4301.59	NR	33269.4	NR	NR	NR
S10-L	4215.23	NR	27443	NR	NR	NR	3954.54	NR	27187.8	NR	NR	NR	3952.54	NR	27243.4	NR	NR	NR
S10-R	4262.95	NR	31549.7	NR	NR	NR	4223.26	NR	31072.6	NR	NR	NR	4224.54	NR	31223.5	NR	NR	NR

Table 5-4. Maximum Local Responses – Kobe 200% Scale.

Member ID	LC1						LC6						LC9					
	Shear Long (kN)	Shear Trans (kN)	Moment Long (kN-m)	Moment Trans (kN-m)	Curvature Long (1/m*10 ⁻⁶)	Curvature Trans (1/m*10 ⁻⁶)	Shear Long (kN)	Shear Trans (kN)	Moment Long (kN-m)	Moment Trans (kN-m)	Curvature Long (1/m*10 ⁻⁶)	Curvature Trans (1/m*10 ⁻⁶)	Shear Long (kN)	Shear Trans (kN)	Moment Long (kN-m)	Moment Trans (kN-m)	Curvature Long (1/m*10 ⁻⁶)	Curvature Trans (1/m*10 ⁻⁶)
Columns																		
1	13716.3	12749	149482	144193	5.27707	3.58005	13921	14125.1	149748	144340	5.2799	3.57615	13943.6	13961.9	148665	143423	5.24562	3.55812
2	13422.4	14302.9	208222	233769	7.49649	5.69571	13403.4	14061	209223	238697	7.19138	5.34883	13474.3	13674.2	209502	234145	7.51944	5.7105
3	11992.3	12894.7	209583	233683	7.67266	5.83275	12069.2	13393.6	210916	237778	7.7646	5.90552	11954.3	13159.2	208154	237203	7.74261	5.84001
4	12291.3	12865.4	211518	234634	7.24206	5.56671	12112.1	12874.6	230850	249906	8.83907	6.84503	12497.4	13016.5	214639	239571	7.70273	5.88979
5	12986.2	12674.2	212410	234179	7.29024	5.6256	13417.1	12741.2	212563	236406	7.3021	5.63304	13503.9	12899.5	236359	248338	9.02336	6.92826
6	12152.8	12610.5	213599	233568	7.28118	5.61594	12801.9	12626.8	241418	251446	9.1849	7.03165	12319.6	13012.2	238505	248224	9.06442	6.94811
7	12992.4	12673.4	212404	234148	7.28743	5.61305	13491.3	12419.3	213743	233147	7.27847	5.61632	13572.5	12922.8	214488	236729	7.26236	5.60993
8	12268.3	12872.6	211513	234509	7.23472	5.58531	12535.4	12374.9	227362	246263	8.79005	6.79716	12550.3	13138.5	229051	247450	8.66734	6.71856
9	12002	12897.5	210450	233683	7.66997	5.85466	11968.5	13019.3	225467	250427	8.79389	6.82875	11980	13084.5	213370	245759	7.631	5.81854
10	13413.9	14306.3	208258	234168	8.17172	6.13608	13317.9	14082.4	225780	250207	8.7294	6.78618	13351	13497.5	208537	233973	7.61943	5.82539
11	13716.4	12743.6	160327	145102	5.59314	4.45932	13864	12841.2	161418	142795	5.36289	4.32393	13913.5	13825.1	161653	144242	5.38167	4.34128
Long. Girder																		
S1-L	4226.03	NR	27795.7	NR	NR	NR	4377.69	NR	28588.9	NR	NR	NR	4125.19	NR	27588.6	NR	NR	NR
S1-R	4478.98	NR	35831.9	NR	NR	NR	4775.86	NR	37249.1	NR	NR	NR	4451.8	NR	35752.1	NR	NR	NR
S2-L	4407.42	NR	31814.9	NR	NR	NR	4497.64	NR	32479.5	NR	NR	NR	4392.12	NR	32113.5	NR	NR	NR
S2-R	4632.74	NR	37258.8	NR	NR	NR	4766.05	NR	38054.7	NR	NR	NR	4601	NR	37111.5	NR	NR	NR
S3-L	4320.26	NR	31254.8	NR	NR	NR	4554.22	NR	33712	NR	NR	NR	4757.83	NR	34140.9	NR	NR	NR
S3-R	4562.08	NR	36603.5	NR	NR	NR	4694.15	NR	38092.9	NR	NR	NR	4986.02	NR	40205.3	NR	NR	NR
S4-L	4307.38	NR	31231.7	NR	NR	NR	4574.54	NR	33256.7	NR	NR	NR	4476.65	NR	32908.8	NR	NR	NR
S4-R	4611.87	NR	37127.6	NR	NR	NR	4757.13	NR	38166.7	NR	NR	NR	4825.82	NR	38211.5	NR	NR	NR
S5-L	4348.48	NR	31386.2	NR	NR	NR	4691.34	NR	34647.4	NR	NR	NR	4495.87	NR	34563.2	NR	NR	NR
S5-R	4672.97	NR	37416.7	NR	NR	NR	4989.26	NR	39650	NR	NR	NR	4772.22	NR	37986.8	NR	NR	NR
S6-L	4302.84	NR	31195.9	NR	NR	NR	4310.07	NR	32372.1	NR	NR	NR	4396.99	NR	33204.1	NR	NR	NR
S6-R	4339.42	NR	17537.2	NR	NR	NR	4293.02	NR	17962	NR	NR	NR	4553.17	NR	18332.2	NR	NR	NR
S7-L	3529.41	NR	17509.1	NR	NR	NR	3505.91	NR	17948.1	NR	NR	NR	3643.5	NR	18329	NR	NR	NR
S7-R	4583.08	NR	37017.3	NR	NR	NR	4566.1	NR	36805.4	NR	NR	NR	4794.28	NR	38181.5	NR	NR	NR
S8-L	4423.87	NR	31812.3	NR	NR	NR	4337.7	NR	32997.6	NR	NR	NR	4715.96	NR	35681.2	NR	NR	NR
S8-R	4527.46	NR	36818.9	NR	NR	NR	4500.57	NR	36546.3	NR	NR	NR	4943.07	NR	39369.2	NR	NR	NR
S9-L	4336.16	NR	31686.5	NR	NR	NR	4279.28	NR	33077.4	NR	NR	NR	4405.32	NR	32413.8	NR	NR	NR
S9-R	4626.66	NR	37728.1	NR	NR	NR	4520.3	NR	36870.5	NR	NR	NR	4553.61	NR	37056.6	NR	NR	NR
S10-L	4185.51	NR	30762.5	NR	NR	NR	4237.82	NR	32213.2	NR	NR	NR	4194.21	NR	30462.3	NR	NR	NR
S10-R	4372.06	NR	32576.7	NR	NR	NR	4328.48	NR	32365.3	NR	NR	NR	4340.75	NR	32532.5	NR	NR	NR

Table 5-5. Maximum Local Responses – Loma Prieta 100% Scale.

Member ID	LC1						LC6						LC9					
	Shear Long (kN)	Shear Trans (kN)	Moment Long (kN-m)	Moment Trans (kN-m)	Curvature Long (1/m*10^-6)	Curvature Trans (1/m*10^-6)	Shear Long (kN)	Shear Trans (kN)	Moment Long (kN-m)	Moment Trans (kN-m)	Curvature Long (1/m*10^-6)	Curvature Trans (1/m*10^-6)	Shear Long (kN)	Shear Trans (kN)	Moment Long (kN-m)	Moment Trans (kN-m)	Curvature Long (1/m*10^-6)	Curvature Trans (1/m*10^-6)
Columns																		
1	18090.3	17832.4	164586	169323	6.17969	4.56933	18371.3	17455.8	166636	178540	6.29184	4.66569	18377.1	17132.1	165050	176353	6.24588	4.61246
2	16081	16619.4	261783	265299	9.39466	7.21671	16266.1	17074.8	227660	260074	8.0638	6.25632	16267.6	16262.7	227321	244129	7.49701	5.74717
3	17865.4	16149.3	262337	273088	9.45647	7.29856	18006.7	16484.6	227950	268104	7.97688	6.12987	18001	15949.5	225390	268975	8.01144	6.1399
4	18190.1	16317.4	261967	271696	9.45463	7.30875	18585.7	16420.9	228535	241843	7.54876	5.71088	18612.1	15978.6	230277	241309	7.51171	5.69014
5	18816.4	16905.2	262771	264270	9.28755	7.15381	19247.4	17031.7	227535	268825	8.09598	6.19242	19264.5	16671.9	230478	242194	7.61735	5.7205
6	18737.3	17212.7	259179	260556	9.19193	7.06837	19191.5	17021.1	231792	252511	7.82044	6.02074	19203.1	16992.4	272540	276239	9.08128	6.90757
7	18816.5	16893.4	266148	269914	9.38724	7.17197	19251.3	16476.6	228634	245295	7.59148	5.68077	19264.1	16709.1	229791	242830	7.59818	5.72358
8	18190.1	16317.3	262716	281712	9.34399	7.31966	18599.7	15877.7	228366	243601	7.55562	5.71659	18611.6	16071.9	227104	240894	7.60195	5.7456
9	17865.4	16149.3	263859	275056	9.4392	7.28442	18004	15787.2	227543	242109	7.46174	5.71401	18012.3	15952.5	231866	258731	7.88486	6.02266
10	16009.3	16614.4	259004	263083	9.1868	7.09524	16232.4	16199.6	226313	243698	7.52181	5.77986	16254.9	16471.3	270091	279718	9.02614	6.81032
11	17982.1	17804.2	180699	161837	5.57519	4.31428	18246.3	17425.3	181121	164967	5.50602	4.269	18302.6	17404.2	181250	166101	5.45412	4.22745
Long. Girder																		
S1-L	4570.9	NR	30467.4	NR	NR	NR	4576.52	NR	30361.2	NR	NR	NR	4280.99	NR	28825.7	NR	NR	NR
S1-R	4587.57	NR	36808.4	NR	NR	NR	4820.43	NR	37936.3	NR	NR	NR	4492.72	NR	36370.3	NR	NR	NR
S2-L	4566.76	NR	33468.1	NR	NR	NR	4519.04	NR	34720.3	NR	NR	NR	4289.43	NR	33399.5	NR	NR	NR
S2-R	4764.7	NR	38077.3	NR	NR	NR	4868.81	NR	38914.4	NR	NR	NR	4643.47	NR	37883.7	NR	NR	NR
S3-L	4847.43	NR	34474	NR	NR	NR	4460.22	NR	34690.6	NR	NR	NR	4765.03	NR	36291.9	NR	NR	NR
S3-R	4634.89	NR	37473.2	NR	NR	NR	4737.63	NR	38558	NR	NR	NR	5024.07	NR	40431.5	NR	NR	NR
S4-L	4577.96	NR	33654.4	NR	NR	NR	4687.38	NR	33943.3	NR	NR	NR	4671.77	NR	33364.5	NR	NR	NR
S4-R	4652.22	NR	37243.8	NR	NR	NR	4802.48	NR	38741.8	NR	NR	NR	4864.24	NR	38454.5	NR	NR	NR
S5-L	4720.05	NR	35298.8	NR	NR	NR	4827.54	NR	34980.8	NR	NR	NR	4609.41	NR	34241.7	NR	NR	NR
S5-R	4758.32	NR	37840.4	NR	NR	NR	5000.92	NR	39668.2	NR	NR	NR	4805.48	NR	38383.4	NR	NR	NR
S6-L	4744.11	NR	34435.6	NR	NR	NR	4344.72	NR	32975.5	NR	NR	NR	4440.88	NR	33934.9	NR	NR	NR
S6-R	4678.54	NR	19763.4	NR	NR	NR	4348.49	NR	19178.4	NR	NR	NR	4602.33	NR	19737.6	NR	NR	NR
S7-L	3901.85	NR	19751.9	NR	NR	NR	3575.32	NR	19161.9	NR	NR	NR	3702.69	NR	19725.2	NR	NR	NR
S7-R	4606.92	NR	37075.9	NR	NR	NR	4575.35	NR	37009	NR	NR	NR	4782.66	NR	38419.5	NR	NR	NR
S8-L	4551.16	NR	33239.8	NR	NR	NR	4208.02	NR	32117.1	NR	NR	NR	4802.79	NR	36417.7	NR	NR	NR
S8-R	4749.99	NR	37743.9	NR	NR	NR	4648.75	NR	37235	NR	NR	NR	5099.81	NR	40443.3	NR	NR	NR
S9-L	4644.09	NR	34045.8	NR	NR	NR	4414.33	NR	31729.8	NR	NR	NR	4525.49	NR	34106.8	NR	NR	NR
S9-R	4784.92	NR	38203.2	NR	NR	NR	4637.13	NR	37391.4	NR	NR	NR	4614.36	NR	37525.6	NR	NR	NR
S10-L	4539.52	NR	33100.4	NR	NR	NR	4315.75	NR	31373.9	NR	NR	NR	4301.34	NR	31641.1	NR	NR	NR
S10-R	4585.58	NR	34549.2	NR	NR	NR	4424.55	NR	33518.6	NR	NR	NR	4384.02	NR	33416.5	NR	NR	NR

Table 5-6. Maximum Local Responses – Loma Prieta 200% Scale.

Member ID	LC1						LC6						LC9					
	Shear Long (kN)	Shear Trans (kN)	Moment Long (kN-m)	Moment Trans (kN-m)	Curvature Long (1/m*10 ⁻⁶)	Curvature Trans (1/m*10 ⁻⁶)	Shear Long (kN)	Shear Trans (kN)	Moment Long (kN-m)	Moment Trans (kN-m)	Curvature Long (1/m*10 ⁻⁶)	Curvature Trans (1/m*10 ⁻⁶)	Shear Long (kN)	Shear Trans (kN)	Moment Long (kN-m)	Moment Trans (kN-m)	Curvature Long (1/m*10 ⁻⁶)	Curvature Trans (1/m*10 ⁻⁶)
Columns																		
1	11039.9	10544.1	135087	140500	5.11384	3.81802	11305.2	11474.3	138647	146522	5.2021	3.88601	11336.9	11792.1	137200	146071	5.11743	3.81271
2	9217.77	9975.57	163239	207450	5.84277	4.33635	10080.1	10715.6	172205	207610	5.96079	4.46486	10003.5	9647.59	169645	207322	5.99219	4.38254
3	10197	8599.32	165228	210016	5.65301	4.33877	10649	9333.28	205387	236119	7.25016	5.62403	10741.7	9352.97	205407	234324	7.22202	5.6023
4	9636.05	9588.47	169382	210595	5.75228	4.39446	9661.1	9978.15	206843	239960	7.23388	5.64704	9709.17	10345.2	206611	235611	7.21229	5.58597
5	10438.3	9052.15	181871	209318	5.90334	4.3139	10676.4	9788.66	185150	210743	6.01122	4.44738	10709.6	9986.87	182819	210623	5.92948	4.36553
6	11409.9	10587.3	183095	218731	6.75596	5.2808	11052.3	10477.7	189745	211515	5.86136	4.39481	11015.7	10703.9	188377	210965	5.84681	4.46908
7	10444.9	9058.73	180419	209269	5.90949	4.31781	10633.9	9619.61	220075	234284	7.37663	5.64273	10673.5	9903.76	221710	244823	7.56149	5.80688
8	9634.6	9588.12	169381	210572	5.7305	4.40536	9720.39	9873.2	213394	240924	7.2062	5.62137	9724.77	9959.28	207770	236367	7.36674	5.72358
9	10195.4	8598.25	167180	209951	5.63985	4.33742	10633.8	9023.38	210641	238619	7.2221	5.61405	10720.3	9013.87	209664	234911	7.2859	5.62821
10	9187.01	9990.2	161952	207631	5.85199	4.34094	10071.4	9425.46	167786	206890	5.9542	4.36225	10006.6	9417.3	170362	207614	6.00885	4.38921
11	11039.7	10542.9	157986	148487	5.64344	4.37684	11319.1	11444.8	164824	157860	5.49628	4.27008	11343.3	11281.5	167561	159726	5.53455	4.28566
Long. Girder																		
S1-L	4250.15	NR	26733.9	NR	NR	NR	4350.67	NR	27643.7	NR	NR	NR	4020.73	NR	25793.5	NR	NR	NR
S1-R	4335.4	NR	33574	NR	NR	NR	4659.17	NR	35384.8	NR	NR	NR	4300.83	NR	33400.8	NR	NR	NR
S2-L	4304.55	NR	29791.6	NR	NR	NR	4432.43	NR	31755.6	NR	NR	NR	4238.88	NR	31061	NR	NR	NR
S2-R	4369.46	NR	33278.6	NR	NR	NR	4629.46	NR	34991.8	NR	NR	NR	4421.39	NR	33926.7	NR	NR	NR
S3-L	4414.68	NR	30501.2	NR	NR	NR	4499.63	NR	32464.9	NR	NR	NR	4570.18	NR	34532.5	NR	NR	NR
S3-R	4311.09	NR	33595.5	NR	NR	NR	4479.39	NR	35027.5	NR	NR	NR	4731.2	NR	36740.1	NR	NR	NR
S4-L	4178.14	NR	29519.5	NR	NR	NR	4628.78	NR	32375.1	NR	NR	NR	4537.59	NR	32164.8	NR	NR	NR
S4-R	4304.15	NR	33305.9	NR	NR	NR	4553.26	NR	35232.7	NR	NR	NR	4620.82	NR	35182.5	NR	NR	NR
S5-L	4488.74	NR	31948.3	NR	NR	NR	4767.62	NR	35595.6	NR	NR	NR	4536.66	NR	33955.1	NR	NR	NR
S5-R	4373.2	NR	35128	NR	NR	NR	4737.1	NR	36519	NR	NR	NR	4522.89	NR	34869.6	NR	NR	NR
S6-L	4428.07	NR	30998.6	NR	NR	NR	4339.99	NR	31534.5	NR	NR	NR	4469.16	NR	33180.4	NR	NR	NR
S6-R	4114.69	NR	16532	NR	NR	NR	4301.54	NR	19004.5	NR	NR	NR	4584.82	NR	18552.6	NR	NR	NR
S7-L	3402.83	NR	16541.3	NR	NR	NR	3527.87	NR	19001.7	NR	NR	NR	3663	NR	18561.4	NR	NR	NR
S7-R	4330.45	NR	33233.7	NR	NR	NR	4332.01	NR	33915.3	NR	NR	NR	4590.55	NR	33539.9	NR	NR	NR
S8-L	4309.83	NR	28752	NR	NR	NR	4353.25	NR	33146.4	NR	NR	NR	4753.57	NR	34902.7	NR	NR	NR
S8-R	4309.83	NR	33301.9	NR	NR	NR	4308.07	NR	33607.5	NR	NR	NR	4758.58	NR	36250.9	NR	NR	NR
S9-L	4318.04	NR	29812.7	NR	NR	NR	4294.22	NR	30476.6	NR	NR	NR	4332.22	NR	30671.5	NR	NR	NR
S9-R	4353.26	NR	33767.9	NR	NR	NR	4337.66	NR	33660.5	NR	NR	NR	4340.04	NR	33699.5	NR	NR	NR
S10-L	4207.2	NR	29001.9	NR	NR	NR	4137.79	NR	28556.2	NR	NR	NR	4144.47	NR	28549.6	NR	NR	NR
S10-R	4282.96	NR	31674.7	NR	NR	NR	4259.17	NR	31511	NR	NR	NR	4265.45	NR	31581.1	NR	NR	NR

Table 5-7. Maximum Global Responses – Northridge 100% Scale.

Node	LC1				LC6				LC9			
	Displacement (mm)		Acceleration (m/s ²)		Displacement (mm)		Acceleration (m/s ²)		Displacement (mm)		Acceleration (m/s ²)	
	long.	trans.	long.	trans.	long.	trans.	long.	trans.	long.	trans.	long.	trans.
1	220.173	291.638	18.1297	20.7431	224.07	283.923	18.106	21.7147	224.291	274.967	18.1087	20.2731
2	226.489	289.063	17.9711	17.7602	230.575	281.393	18.1384	17.0194	230.771	272.699	18.1432	16.8891
3	230.808	286.113	18.0509	18.176	236.204	278.63	18.1385	16.3869	236.351	270.187	18.1435	16.0106
4	230.928	283.275	18.0482	17.5288	235.722	276.194	18.1384	16.9118	235.793	267.833	18.1434	16.1048
5	234.024	281.201	18.0472	17.9692	239.76	274.362	18.1353	19.5949	239.985	266.171	18.1398	16.684
6	234.013	280.436	18.0561	24.6424	239.69	273.54	18.1349	18.2082	240.004	265.658	18.1393	21.5007
7	230.932	281.198	18.0549	17.8171	235.485	273.957	18.1399	16.0272	235.808	266.396	18.1439	16.5026
8	230.816	283.277	18.0587	17.5404	235.87	275.447	18.1394	15.7514	236.362	268.144	18.1439	16.2389
9	226.518	286.131	17.9451	18.1577	231.274	277.687	18.1378	16.0623	230.801	270.513	18.1444	16.0502
10	220.184	289.104	18.0018	17.7816	224.196	279.945	18.1004	17.026	224.278	272.921	18.1095	16.868
11	220.18	291.704	18.1302	20.7981	224.195	282.021	18.1067	20.276	224.277	275.002	18.1083	20.3591

Table 5-8. Maximum Global Responses – Northridge 200% Scale.

Node	LC1				LC6				LC9			
	Displacement (mm)		Acceleration (m/s ²)		Displacement (mm)		Acceleration (m/s ²)		Displacement (mm)		Acceleration (m/s ²)	
	long.	trans.	long.	trans.	long.	trans.	long.	trans.	long.	trans.	long.	trans.
1	422.714	517.01	24.7193	23.6438	427.985	551.491	24.8429	27.0323	427.782	543.11	24.8501	22.0936
2	426.462	517.437	24.7217	21.3772	431.459	550.132	24.8443	22.0753	431.767	543.835	24.8518	20.7823
3	429.899	517.826	24.7251	22.58	435.35	548.392	24.8469	22.4465	434.763	544.538	24.8537	21.6196
4	431.001	518.226	24.7259	22.9845	436.201	546.241	24.8473	22.4698	436.986	545.091	24.8553	22.1671
5	432.085	518.566	24.7284	22.7514	437.257	543.647	24.8488	24.1219	437.664	545.463	24.8563	22.2856
6	432.34	518.698	24.7279	26.4511	436.941	540.621	24.8485	22.0339	438.063	545.639	24.8567	24.5155
7	430.778	518.548	24.7258	22.7452	436.581	537.316	24.8478	21.9863	437.229	545.547	24.8556	22.2459
8	429.592	518.194	24.7248	22.9748	434.913	534.079	24.8467	21.9043	435.606	545.25	24.8546	22.1465
9	426.417	517.781	24.7227	22.5685	432.408	531.195	24.8454	21.4894	432.068	544.76	24.8522	21.7005
10	422.676	517.384	24.7209	21.3646	427.834	528.818	24.843	20.6958	428.194	544.113	24.8505	20.8681
11	422.675	516.948	24.7191	23.6489	427.834	526.734	24.843	21.9246	428.194	543.457	24.8505	23.3678

Table 5-9. Maximum Global Responses – Kobe 100% Scale.

Node	LC1				LC6				LC9			
	Displacement (mm)		Acceleration (m/s ²)		Displacement (mm)		Acceleration (m/s ²)		Displacement (mm)		Acceleration (m/s ²)	
	long.	trans.	long.	trans.	long.	trans.	long.	trans.	long.	trans.	long.	trans.
1	220.77	336.095	20.5924	28.031	218.571	334.959	20.7562	26.1702	220.43	341.439	20.7711	26.0713
2	265.195	333.987	19.2497	21.8164	284.984	331.812	19.7819	21.6328	283.869	339.63	19.2868	23.3982
3	261.045	331.542	20.888	21.072	304.214	328.245	21.2213	20.5624	303.634	337.526	21.6827	20.069
4	266.3	329.193	19.7873	20.0552	305.785	324.813	20.5616	19.3183	301.246	335.384	20.0416	17.9761
5	284.246	327.52	21.0722	19.0784	317.917	322.511	21.543	19.5075	319.615	333.621	22.3597	17.1697
6	284.63	326.994	20.5083	20.0989	315.635	321.47	20.98	18.1445	320.202	332.723	22.0692	17.5461
7	266.145	327.522	19.8137	19.0643	304.331	321.284	21.2745	17.872	302.896	332.603	21.0173	18.1102
8	261.039	329.2	20.4293	20.0061	300.956	321.428	21.0604	18.3273	302.355	333.759	20.462	19.9144
9	264.922	331.55	19.6444	21.127	283.654	322.202	19.183	20.3455	283.181	335.751	19.3969	21.1202
10	221.159	333.997	22.4902	21.9048	219.418	323.187	21.4383	22.3114	220.248	338.034	21.1615	22.3699
11	220.861	336.09	20.5787	27.9978	219.414	324.035	20.6994	23.9808	220.248	340.086	20.5854	23.4458

Table 5-10. Maximum Global Responses – Kobe 200% Scale

Node	LC1				LC6				LC9			
	Displacement (mm)		Acceleration (m/s ²)		Displacement (mm)		Acceleration (m/s ²)		Displacement (mm)		Acceleration (m/s ²)	
	long.	trans.	long.	trans.	long.	trans.	long.	trans.	long.	trans.	long.	trans.
1	122.818	158.586	10.9737	13.9866	127.837	170.99	11.5296	15.9968	128.317	160.334	11.1577	15.8894
2	125.143	158.688	10.4641	12.224	129.559	169.513	11.4144	12.5048	130.079	161.024	11.3599	12.9179
3	126.474	158.63	10.9184	12.1794	130.327	167.648	11.0288	12.6313	130.736	161.468	11.0676	12.5226
4	129.241	158.469	11.0576	11.6836	133.414	165.437	11.7255	12.3095	133.757	161.519	11.693	12.0023
5	129.764	158.666	10.7749	12.5503	134.135	162.715	10.8223	12.6439	134.403	161.526	10.7358	12.4405
6	129.83	158.814	10.767	12.9141	134.155	160.065	10.91	12.7983	134.438	161.537	10.9568	12.7415
7	129.376	158.677	11.0974	12.5843	133.636	157.312	11.2486	12.2959	133.834	161.63	11.1822	12.4268
8	126.642	158.498	10.8513	11.7487	130.469	154.814	11.0251	11.5919	130.803	161.665	11.0176	11.9377
9	125.33	158.652	10.4747	12.216	129.638	152.685	10.9823	11.8426	130.149	161.561	11.3729	12.4574
10	122.97	158.691	10.3778	12.2146	128.211	150.865	10.7215	12.7505	128.506	161.01	10.6466	12.897
11	122.723	158.567	10.9395	13.9902	128.095	149.171	11.1773	14.8811	128.386	160.245	11.0822	15.7895

Table 5-11. Maximum Global Responses – Loma Prieta 100% Scale.

Node	LC1				LC6				LC9			
	Displacement (mm)		Acceleration (m/s ²)		Displacement (mm)		Acceleration (m/s ²)		Displacement (mm)		Acceleration (m/s ²)	
	long.	trans.	long.	trans.	long.	trans.	long.	trans.	long.	trans.	long.	trans.
1	145.243	165.033	15.4967	16.2067	147.999	171.773	16.5199	16.9416	148.238	164.692	16.2405	16.4247
2	147.687	164.9	16.8363	15.0463	150.913	170.721	17.8373	14.8667	151.083	164.78	17.6233	14.6924
3	149.406	165.036	18.0338	14.5144	152.698	169.797	17.7442	15.5009	152.79	165.145	17.8242	16.0599
4	152.098	165.553	16.0938	15.2267	155.435	169.131	16.4774	16.6474	155.655	165.751	16.4812	17.0599
5	153.403	166.022	17.6241	14.3871	156.941	168.396	17.6083	16.1842	157.053	166.228	17.3691	16.4378
6	153.426	166.201	17.3278	14.7155	156.952	167.286	17.4853	16.4443	157.073	166.462	17.6411	16.9073
7	152.098	166.019	16.1601	14.3982	155.448	165.776	15.9866	15.7566	155.662	166.333	16.023	16.1117
8	149.513	165.557	17.1067	15.3135	152.758	164.043	17.2487	16.4158	152.888	165.841	17.2617	16.5182
9	147.807	165.056	16.1149	14.571	151.021	162.236	16.6822	15.356	151.137	165.114	16.6537	15.3428
10	145.28	164.929	15.3265	15.0201	148.161	160.729	15.9113	14.3049	148.277	164.606	15.8868	14.6136
11	145.154	165.04	15.5009	16.2427	148.022	159.622	16.3261	15.6704	148.143	164.325	16.2378	16.204

Table 5-12. Maximum Global Responses – Loma Prieta 200% Scale.

Node	LC1				LC6				LC9			
	Displacement (mm)		Acceleration (m/s ²)		Displacement (mm)		Acceleration (m/s ²)		Displacement (mm)		Acceleration (m/s ²)	
	long.	trans.	long.	trans.	long.	trans.	long.	trans.	long.	trans.	long.	trans.
1	264.389	272.622	23.4207	26.5507	276.593	280.476	23.8302	24.9355	275.791	268.434	23.8784	23.8155
2	315.641	273.261	23.7626	19.2035	325.263	279.987	22.3963	19.5038	323.419	269.462	22.4035	18.7076
3	330.49	273.86	23.0078	21.3331	332.701	279.209	22.4536	19.0579	329.384	270.481	22.4447	20.0264
4	321.998	274.318	22.4954	23.6247	330.335	278.018	22.4823	20.1828	327.975	271.388	22.4813	20.6076
5	332.32	274.529	22.5585	23.4402	340.503	276.263	22.4869	23.7959	338.808	271.916	22.4878	22.5551
6	332.264	274.591	22.4913	30.9524	340.029	274.003	22.5093	28.6083	338.049	272.225	22.5041	27.0224
7	321.941	274.556	22.6067	24.0565	328.535	271.505	22.5194	24.1969	328.366	272.349	22.5146	22.2059
8	330.567	274.363	23.0276	23.4175	333.045	268.845	22.5375	21.5324	331.101	272.164	22.552	21.9325
9	315.708	273.914	23.2407	21.3233	320.775	266.129	22.5934	20.1864	322.911	271.551	22.5981	20.4836
10	264.261	273.324	22.7976	19.2562	274.668	263.473	22.3295	20.4392	276.248	270.599	22.3201	18.9951
11	264.229	272.697	23.4237	26.5554	274.616	261.065	23.859	23.844	276.18	269.704	23.8413	23.4235

5.2. Seismic Behavioral Graphs

The behavioral graphs plotted for the additional seismic analysis conducted in this chapter include displacement time-histories, force-displacement relationships, and moment-curvature relationships of selected columns in the longitudinal and transverse directions. The displacement time-history graphs demonstrated the displacement amplitudes and trends along with residual displacements at the end of the ground motion duration. The force-displacement and moment-curvature relationships graphs serve to demonstrate the full range of response of the prototype HSR bridge system throughout the course of the ground motions whether it remains linear elastic or started getting nonlinear. The graphs were plotted for the data retrieved from the prototype HSR bridge response under the three earthquakes at 100% and 200% amplification.

Displacement time-histories for Load Cases 1, 6, and 9 under all three ground motions are shown in Figure 5-3 through Figure 5-6 for the transverse and longitudinal directions and at 100% and 200% seismic intensity. Each of the four figures provides nine subplots where each subplot compares the displacement at the girder end node above columns #3, #6, and #11 to visually assess the displacement trends of the interior and exterior columns. The nine subplots represent the three different ground motion records \times the three train loading cases. Observing the figures for the 100% scale, the time-histories for the Kobe and Loma Prieta earthquakes oscillated about the 0 mm displacement mark for both directions, i.e. no residual displacements were observed to indicate the columns among other components stayed linear throughout the ground motion duration. The time-histories for the Northridge earthquake were shifted to oscillate about the 40 mm mark for the longitudinal direction and about the 110 mm mark for the transverse direction. These are residual displacements, i.e. plastic damage, which indicate that either the columns underwent nonlinear inelastic behavior or other components simulating the train-track-superstructure-substructure interaction might have yielded. This was previously noted in Chapter 4. However, given that the 200% run of the Northridge record rendered higher force demands in the columns, the columns were obviously well below their capacities as a result of the 100% run. Therefore, the residual displacements observed in the 100% or 200% Northridge earthquake cases are not likely associated with the columns, which motivated an additional analysis case at 300% as discussed later in this chapter. It is also noted from the Figures 5.2 through 5.5 that the overall displacement trends for the three load cases were nearly identical between Load Case 1, 6, and 9 for each direction barring any apparent variations in the displacement amplitudes after the 8 second mark.

For the 200% scale, larger residual drift between the interior and exterior columns become apparent for all three ground motions in the longitudinal direction. The relative drift stayed similar between the three load cases for the Northridge and Loma Prieta earthquakes, and showed a slight increase for the load cases with train loading for the Kobe earthquake. The transverse displacements heavily increased for the Northridge earthquake, oscillating about the 240 mm line for the load cases with train loading and the 140 mm line for the load case with no train loading. In comparison, the Kobe and Loma Prieta earthquakes had small residual transverse displacements which were nearly consistent among the load cases.

Based on the displacement time-history graphs for both scales, the addition of train loading had higher influence towards the displacement trends for ground motions scaled at 200%. The displacement trends under the Loma Prieta earthquake lacked any variation among the load cases for either scale, but the Northridge and Kobe earthquakes showed definite signs of increased

residual displacement for the load cases with train loading under the 200% earthquakes. Displacement time-histories for Load Case 6 and 9 also oscillate at a larger magnitude towards the middle to end of the ground motion for the transverse direction which proves the addition of train loading does increase the magnitude of bridge vibration despite the peak displacement values being relatively similar for all the load cases.

Similar to the displacement time-history graphs, the force-displacement and moment-curvature behavioral graphs were compiled in four figures, with each figure presenting a respective direction and ground motion scale. Observing the force-displacement relationships shown in Figure 5-7 and Figure 5-9 for columns #6, #8, and #11 and the moment-curvature relationships shown in Figure 5-11 and Figure 5-13 for columns #1, #6, and #10, the columns showed glimpses of inelastic response but stayed relatively linear elastic. However, the columns clearly demonstrate signs of nonlinearity under the 200% scale Northridge earthquake in the force-displacement graphs for both directions, shown in Figure 5-8 and Figure 5-10, where larger or fatter hysteresis loops were recorded. The moment-curvature graphs for the 200% scale ground motions presented in Figure 5-12 and Figure 5-14 also showed instances of large nonlinearity for all of the ground motions. In comparison to the transverse moment-curvature graphs, the longitudinal moment-curvature relationship behaved along a lower slope. This can be assumed to be a result of the geometric orientation of the rectangular pier columns providing higher resistance to rotation in the transverse direction compared to the longitudinal direction.

Although the force-displacement behaviors were similar among the three load cases, the moment-curvature behaviors showed that the columns experienced larger responses for Load Cases 6 and 9 for the ground motions scaled at 200%, which was an observation also seen in the displacement time-histories. In general, the influence of train loading becomes more apparent when the columns start to experience some nonlinearity due to large seismic loading. This can be tied to the inherent design of HSR bridges being very stiff and high capacity, which results in a bridge that can behave consistently regardless of various loading scenarios but only up to a certain seismic demand level. However, further research is necessary to fully validate this observation and tie it to proper seismic design and assessment framework.

Regardless of the onset of nonlinear column behavior shown under the 200% scale runs, it is not conclusive whether any of the columns reached its ultimate capacity already. Thus, it was of interest to pick the most damaging ground motion out of the three utilized ones, i.e. the Northridge record, and apply it at 300% scale. This mainly aimed at understanding whether the residual displacements observed at least at the 200% scale were related to the column's nonlinear behavior. It was also desired to confirm whether the column reached its capacity during the 200% run or still had more capacity that can be rendered at an even larger seismic intensity. The displacement time-history, force-displacement, and moment-curvature relationships are shown in both the transverse and longitudinal directions under the 300% Northridge record in Figure 5-15 through Figure 5-20. Observing the displacement time-histories, it can be confirmed that the columns approached their capacity and might have failed under excessive nonlinear demands that reached about 1400 mm as suggested by the residual displacement values that surpassed 500 mm for both directions. Unlike the response at 100% and 200% scales, no other bridge component is likely to lead to 500 mm residual displacements except the main lateral support system, i.e. columns.

The force-displacement and moment-curvature graphs for both directions confirm the large nonlinear response and inelasticity within the columns as demonstrated through the large hysteresis loops that stray from the core elastic behavior. Analyzing the seismic performance of

the prototype HSR bridge under the 300% scale further supports the perspective that a by-product of the HSR bridge column's large stiffness requirement is the large force and moment capacity that can help the columns remain almost linear elastic under moderate seismic intensities. In other words, the large column nonlinearities were not observed until the 300% intensity where the force and moment values suggest that these are at the capacity of the analyzed columns. A formal design guideline and code would be necessary in the near future to do a proper seismic assessment of HSR bridge behavior under simultaneous train and seismic loading, which is a future work that can stem from the research presented in this study.

Finally, the force-deformation behavior of selected track-bridge interaction elements for the prototype HSR bridge were obtained and plotted under the Northridge record scaled at 300% and under the same train loading cases. Force and deformation were output for the zero-length elements idealizing the fasteners, CA layers, and sliding layers at locations directly above columns #4 and #6, which were selected arbitrarily. The force-deformation behavior for fasteners supporting rail 1 and rail 2 of track 1 is shown in Figure 5-21 and Figure 5-22 respectively. Similarly, the force-deformation behavior for the CA layers supporting track 1, and the sliding layers supporting track 1 at the locations indicated above are plotted in Figure 5-23 and Figure 5-24, respectively. These graphs compare the demand and performance of the interaction elements under three levels of seismic intensity.

From this brief analysis, it is apparent that the fasteners and CA layers operate within its elastic capacities which were defined as part of the modeling of the material behaviors (see Figure 3-7 and Figure 3-8 in Chapter 3). Contrarily, the sliding layer has clearly exceeded its yield capacity and is deforming heavily due to the lack of capacity. The sliding layer in a ballastless track system connects the track system to the bridge deck and is prone to be firstly damaged under earthquakes. The sliding layer is also implemented in ballastless track systems to effectively dissipate seismic energy through the damage of the layer [12]. However, the damage observed in the sliding layer for this study is excessive and does raise some concern. An obvious issue could be the lack of resistance provided in the interaction layers of the track system due to the large sub-spans or intervals used to model elements and springs along the length of the bridge. The reference study that the prototype track-bridge system was based off modeled each girder span as 50 elements of identical lengths opposed to the 10 elements used for this study, which was a limitation to expedite the modeling process given the overall goal that the model in-place is for demonstration purposes. This modeling limitation significantly decreased the amount of springs modeled per interaction layer because the springs were modeled at intervals five times larger than that of the reference study for instance. Nonetheless, it is again noted that the provided analysis in this chapter or previous ones were intended to only demonstrate the capabilities associated with the developed HSR bridge system model, and touch on the potential response metrics that could be assessed against a formal future design framework.

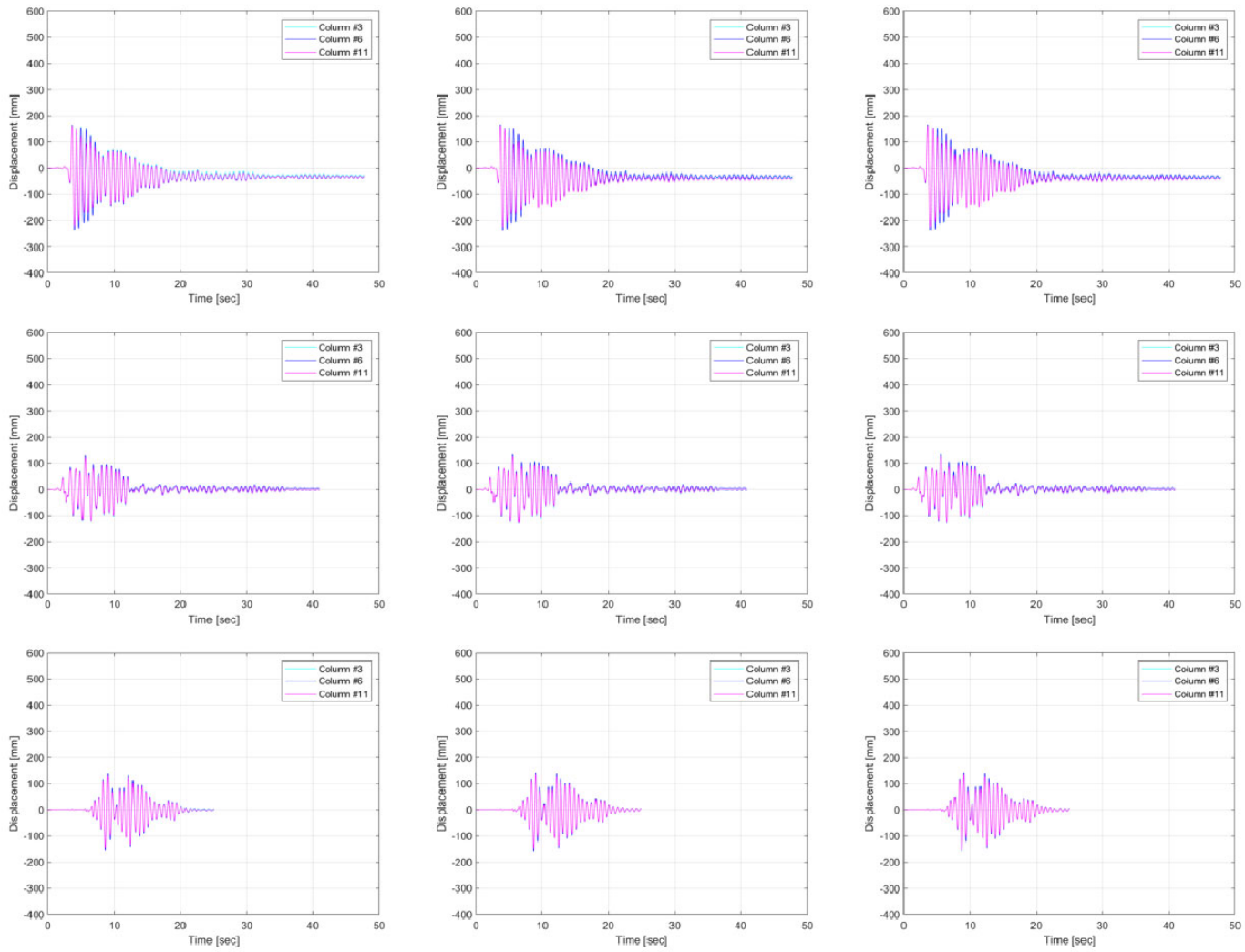


Figure 5-3. Longitudinal displacement time-history for columns #3, #6, and #11 at 100% – (Row: (1) Northridge, (2) Kobe, and (3) Loma Prieta, Column: (1) Load Case 1, (2) Load Case 6, and (3) Load Case 9).

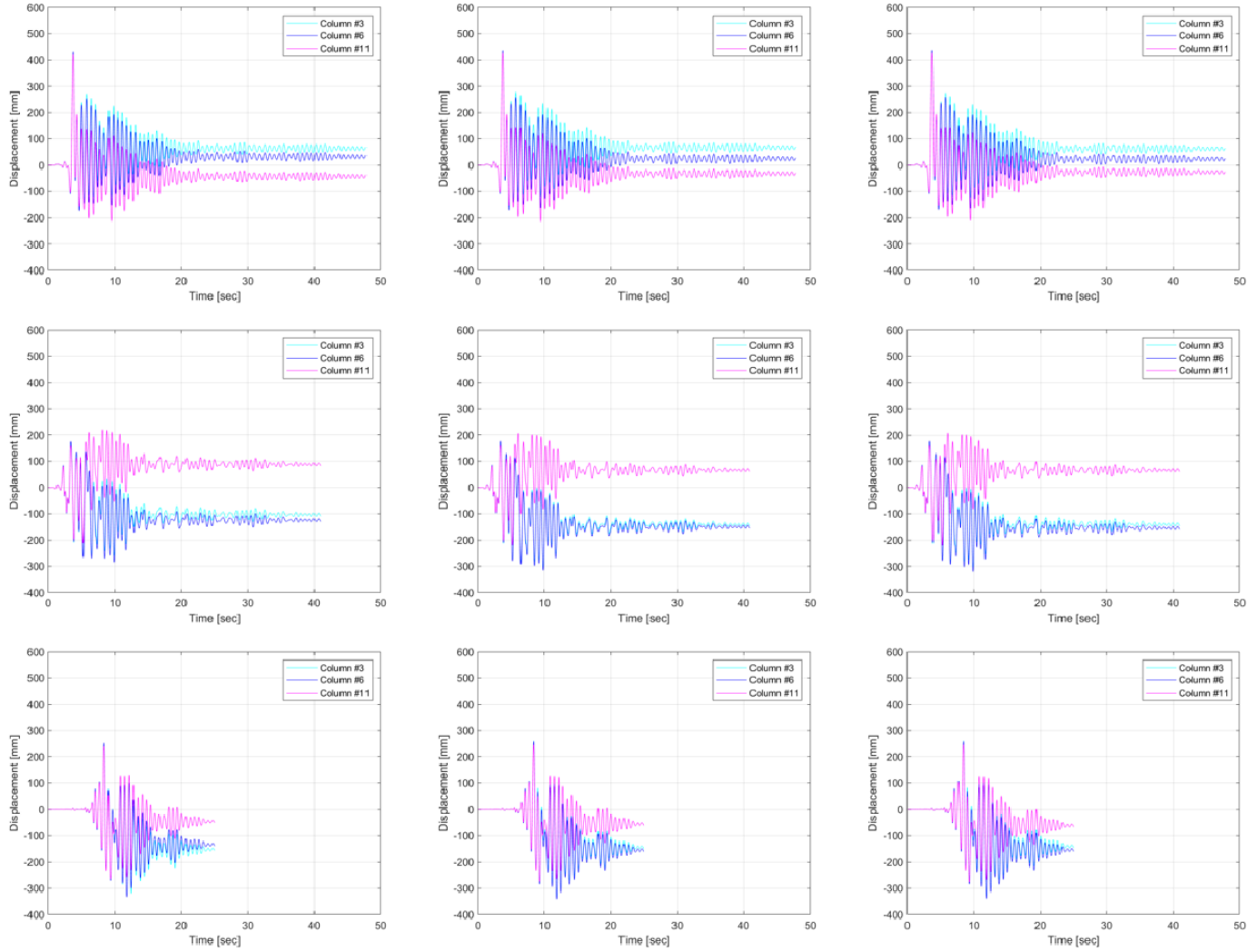


Figure 5-4. Longitudinal displacement time-history for columns #3, #6, and #11 at 200% – (Row: (1) Northridge, (2) Kobe, and (3) Loma Prieta, Column: (1) Load Case 1, (2) Load Case 6, and (3) Load Case 9).

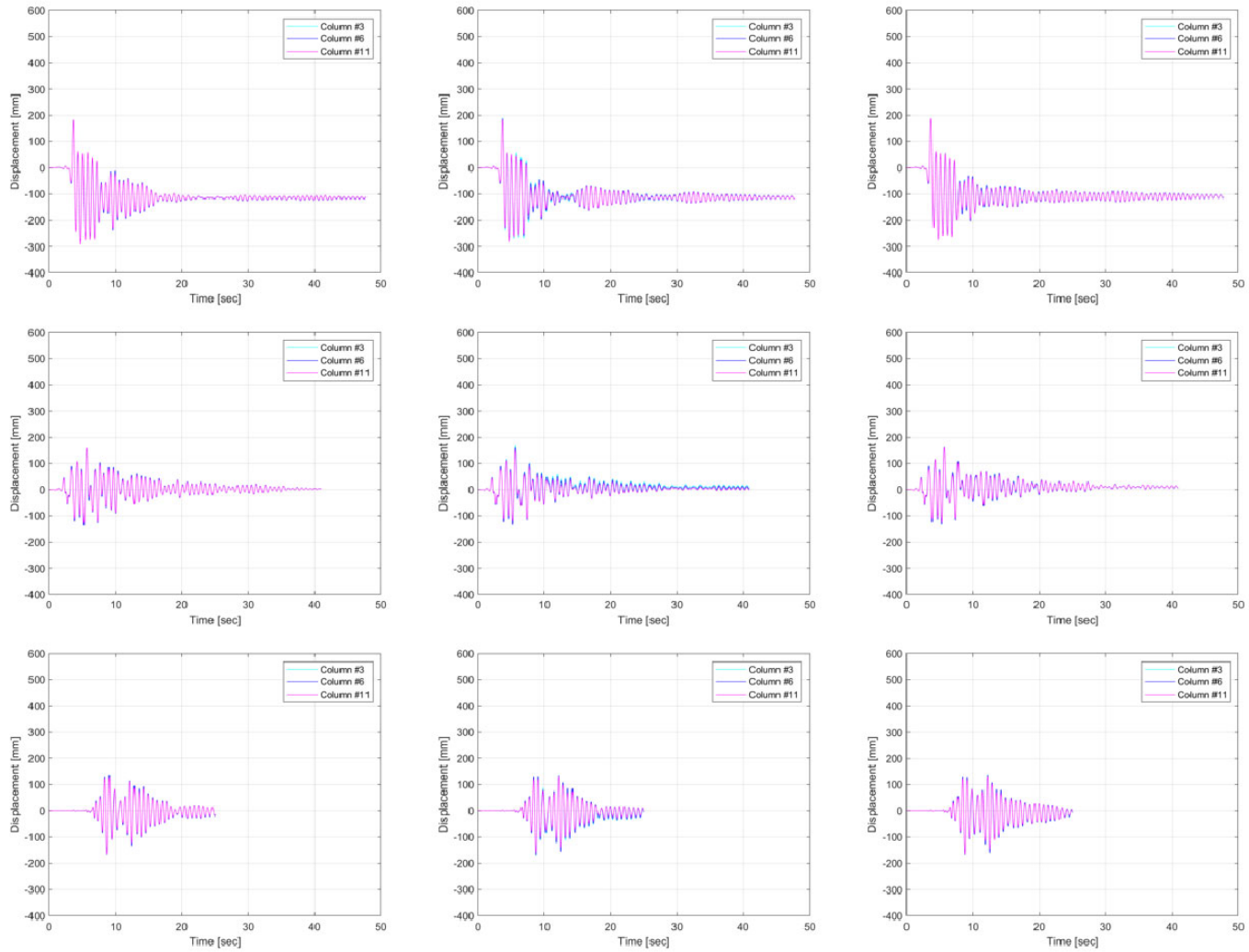


Figure 5-5. Transverse displacement time-history for columns #3, #6, and #11 at 100% – (Row: (1) Northridge, (2) Kobe, and (3) Loma Prieta, Column: (1) Load Case 1, (2) Load Case 6, and (3) Load Case 9).

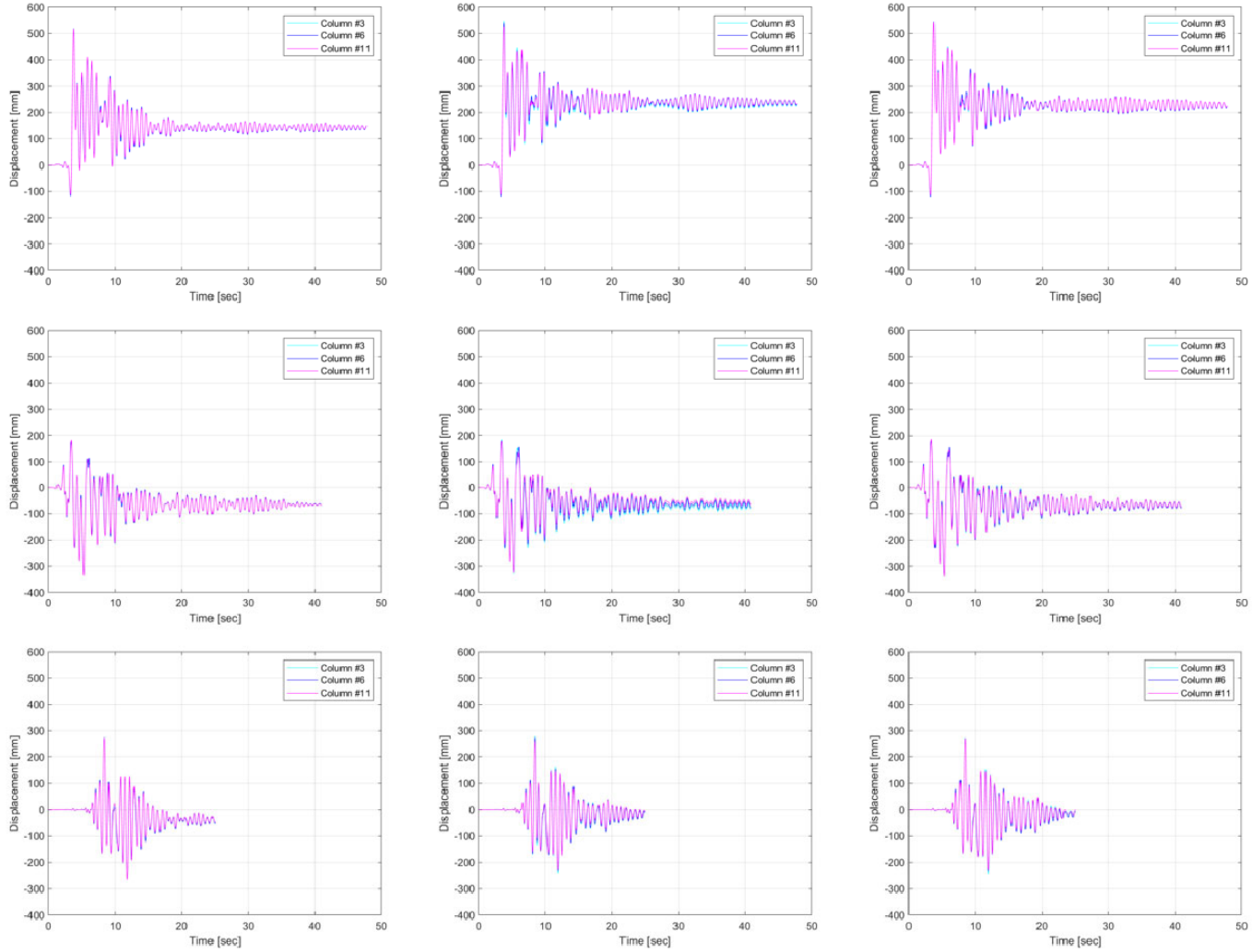


Figure 5-6. Transverse displacement time-history for columns #3, #6, and #11 at 200% – (Row: (1) Northridge, (2) Kobe, and (3) Loma Prieta, Column: (1) Load Case 1, (2) Load Case 6, and (3) Load Case 9).

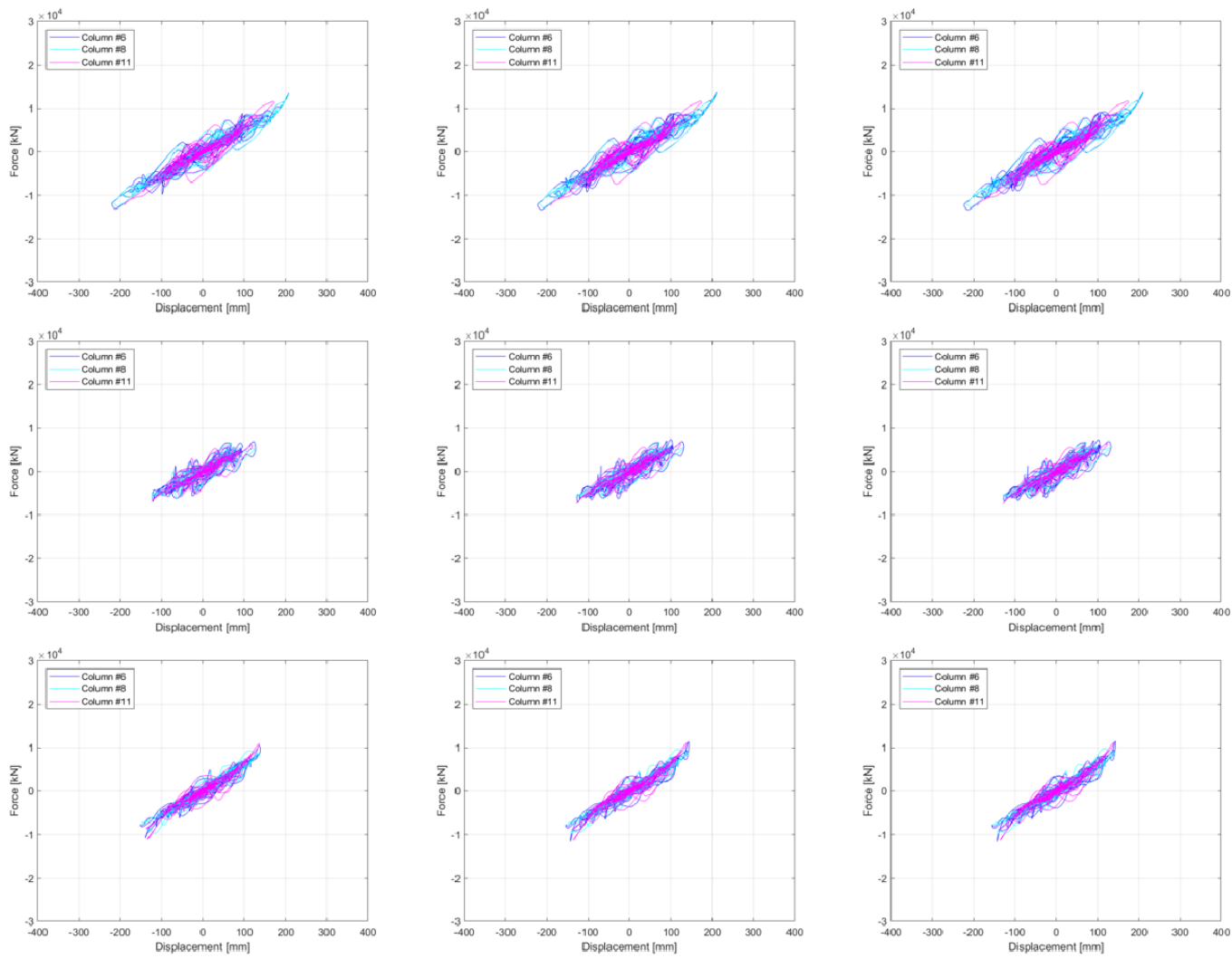


Figure 5-7. Longitudinal force-displacement relationship for columns #6, #8, and #11 at 100% – (Row: (1) Northridge, (2) Kobe, and (3) Loma Prieta, Column: (1) Load Case 1, (2) Load Case 6, and (3) Load Case 9).

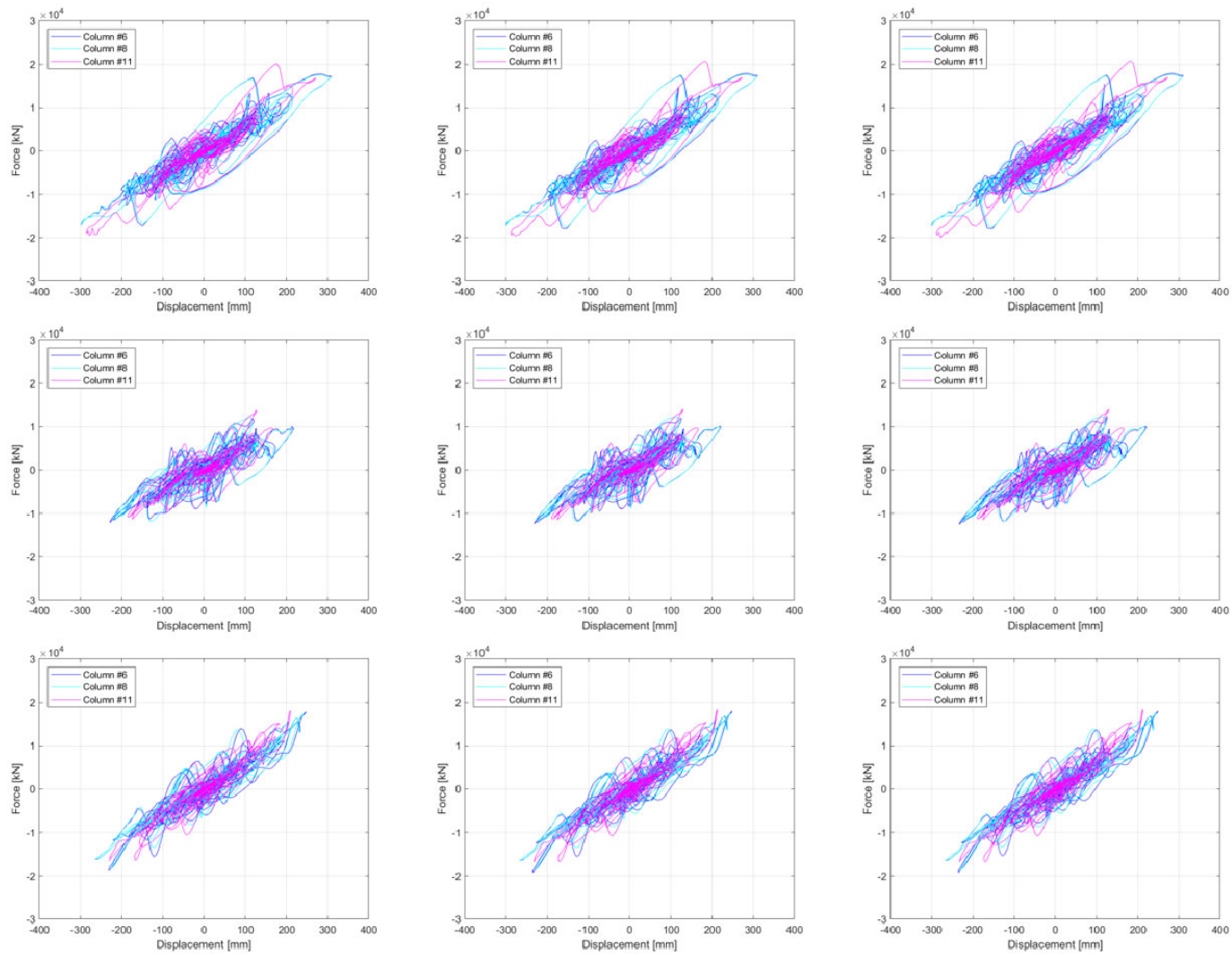


Figure 5-8. Longitudinal force-displacement relationship for columns #6, #8, and #11 at 200% – (Row: (1) Northridge, (2) Kobe, and (3) Loma Prieta, Column: (1) Load Case 1, (2) Load Case 6, and (3) Load Case 9).

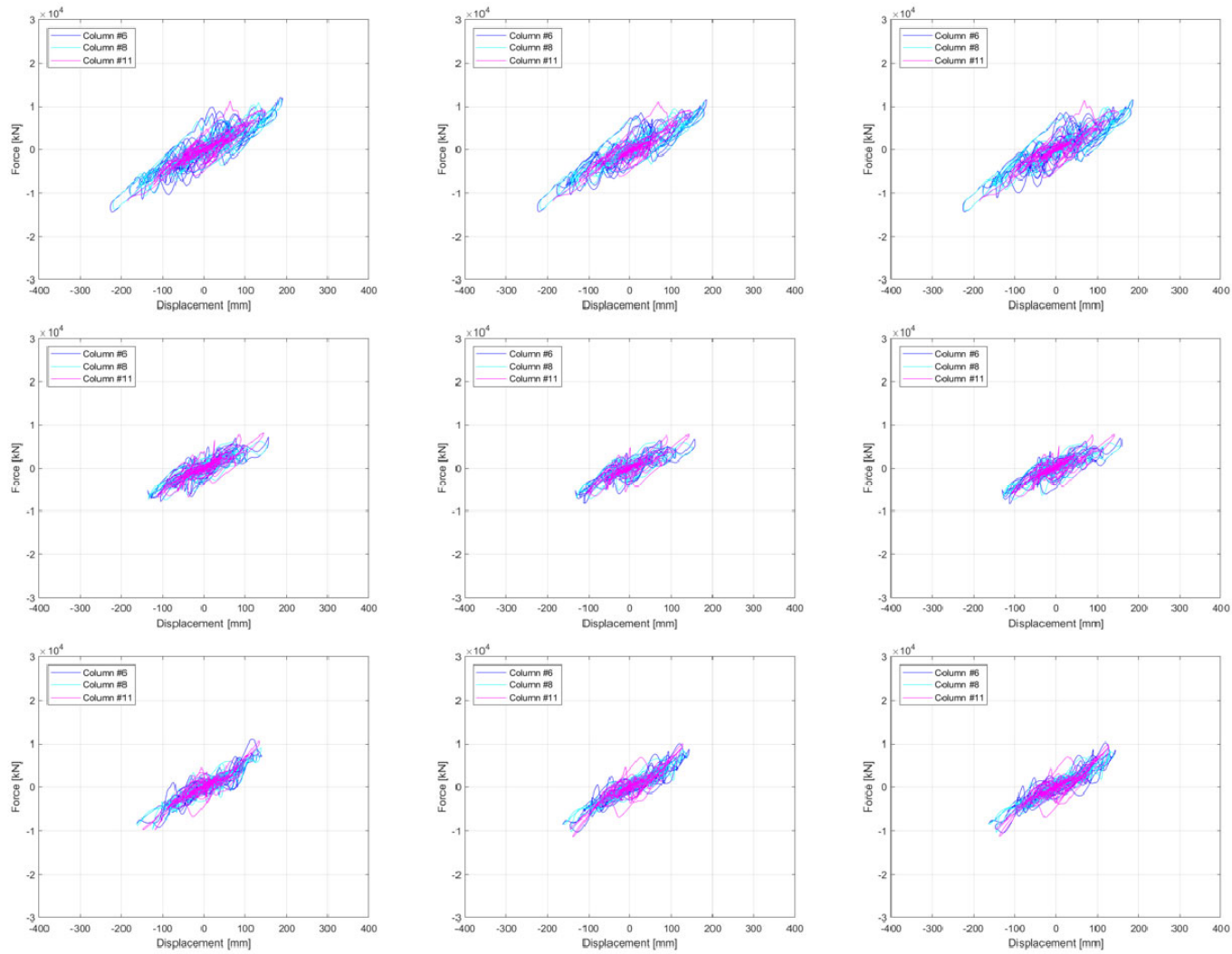


Figure 5-9. Transverse force-displacement relationship for columns #6, #8, and #11 at 100% – (Row: (1) Northridge, (2) Kobe, and (3) Loma Prieta, Column: (1) Load Case 1, (2) Load Case 6, and (3) Load Case 9).

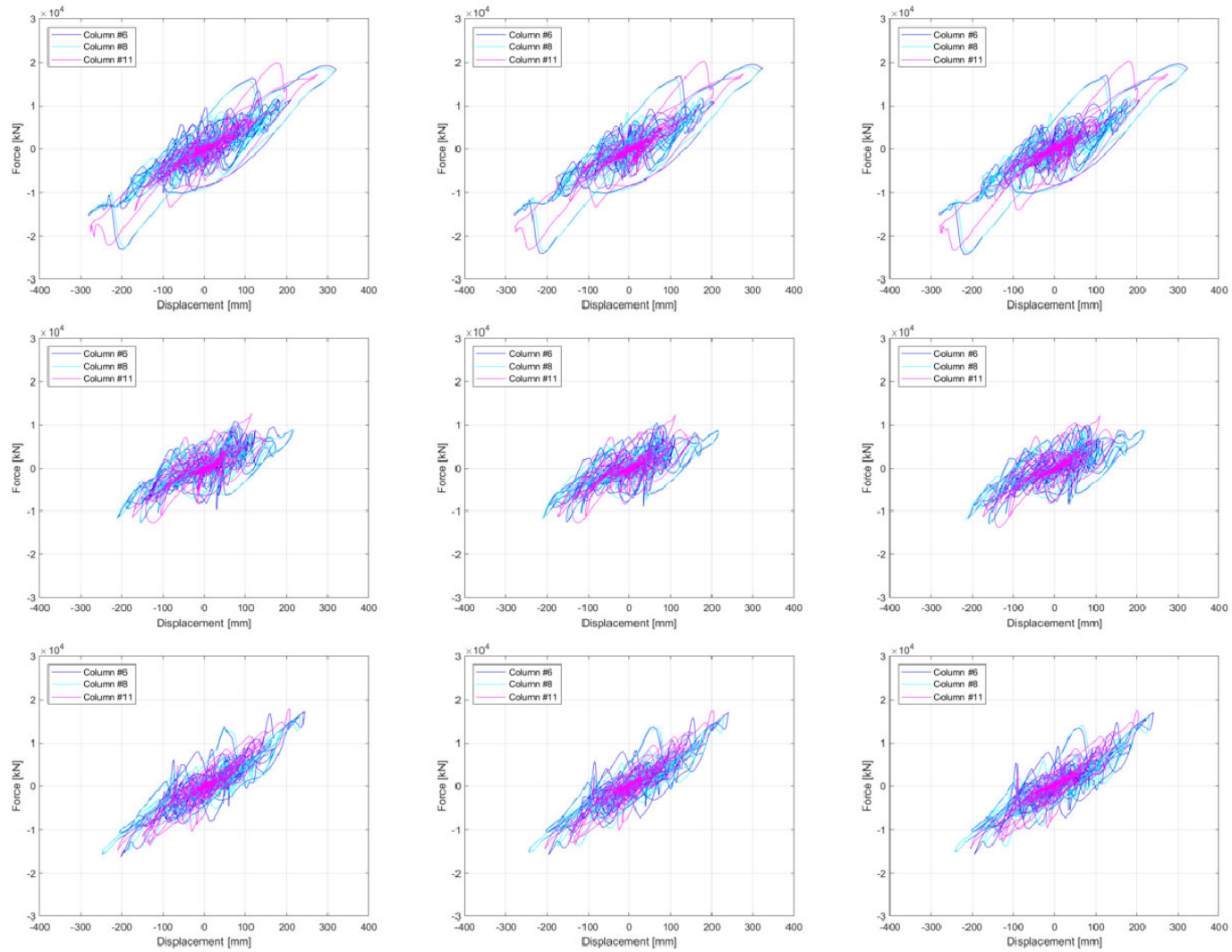


Figure 5-10. Transverse force-displacement relationship for columns #6, #8, and #11 at 200% – (Row: (1) Northridge, (2) Kobe, and (3) Loma Prieta, Column: (1) Load Case 1, (2) Load Case 6, and (3) Load Case 9).

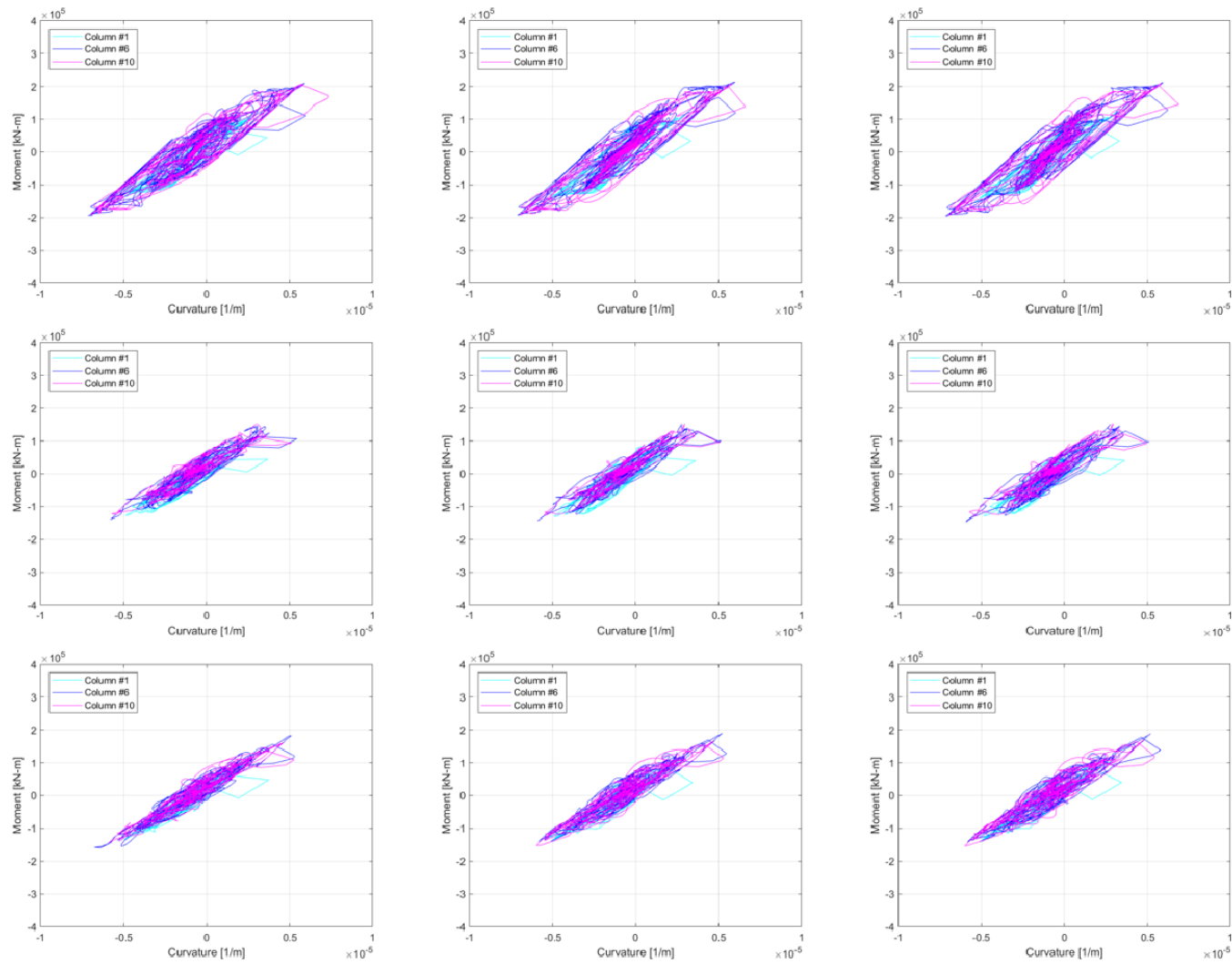


Figure 5-11. Longitudinal moment-curvature relationship for columns #1, #6, and #10 at 100% – (Row: (1) Northridge, (2) Kobe, and (3) Loma Prieta, Column: (1) Load Case 1, (2) Load Case 6, and (3) Load Case 9).

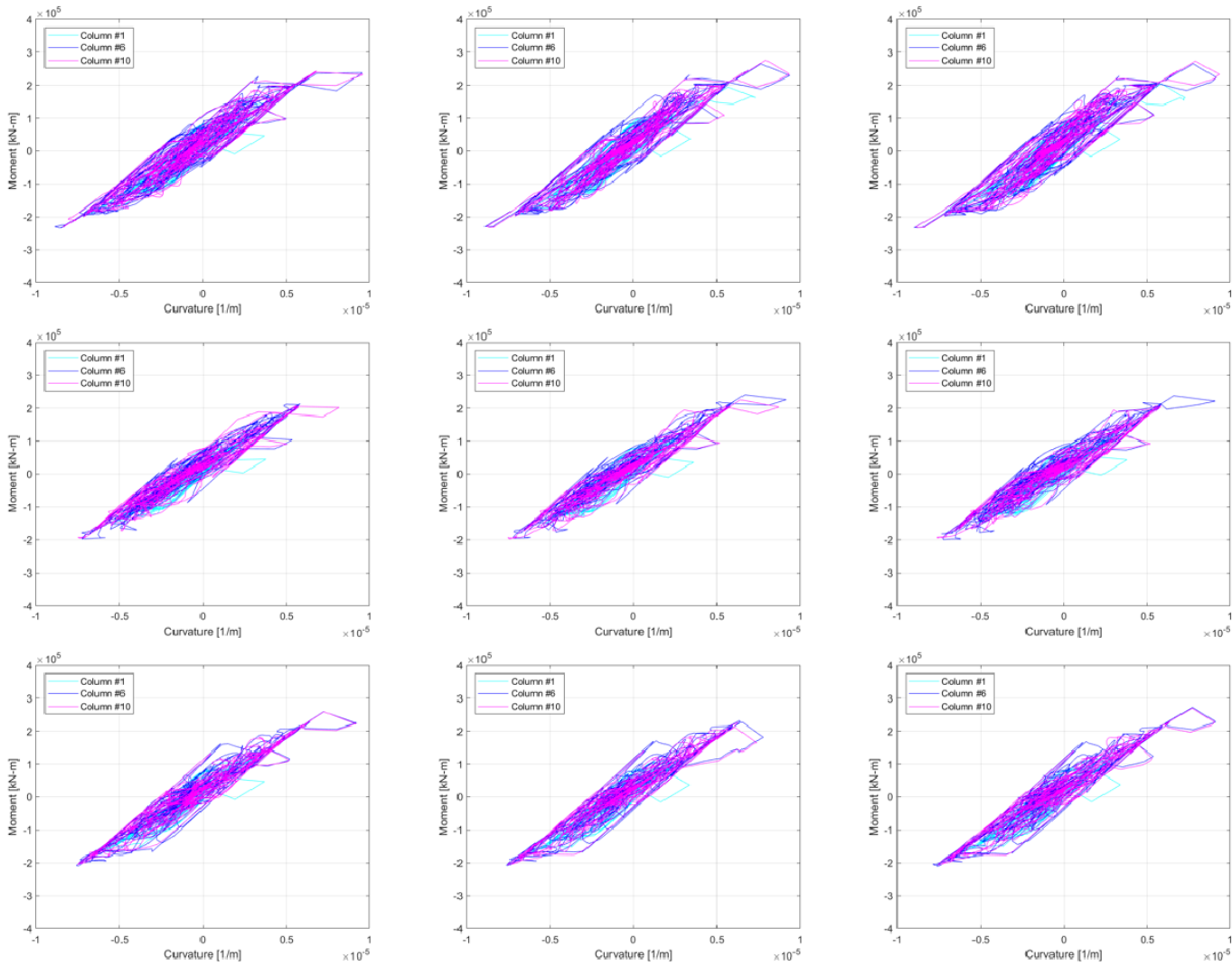


Figure 5-12. Longitudinal moment-curvature relationship for columns #1, #6, and #10 at 200% – (Row: (1) Northridge, (2) Kobe, and (3) Loma Prieta, Column: (1) Load Case 1, (2) Load Case 6, and (3) Load Case 9).

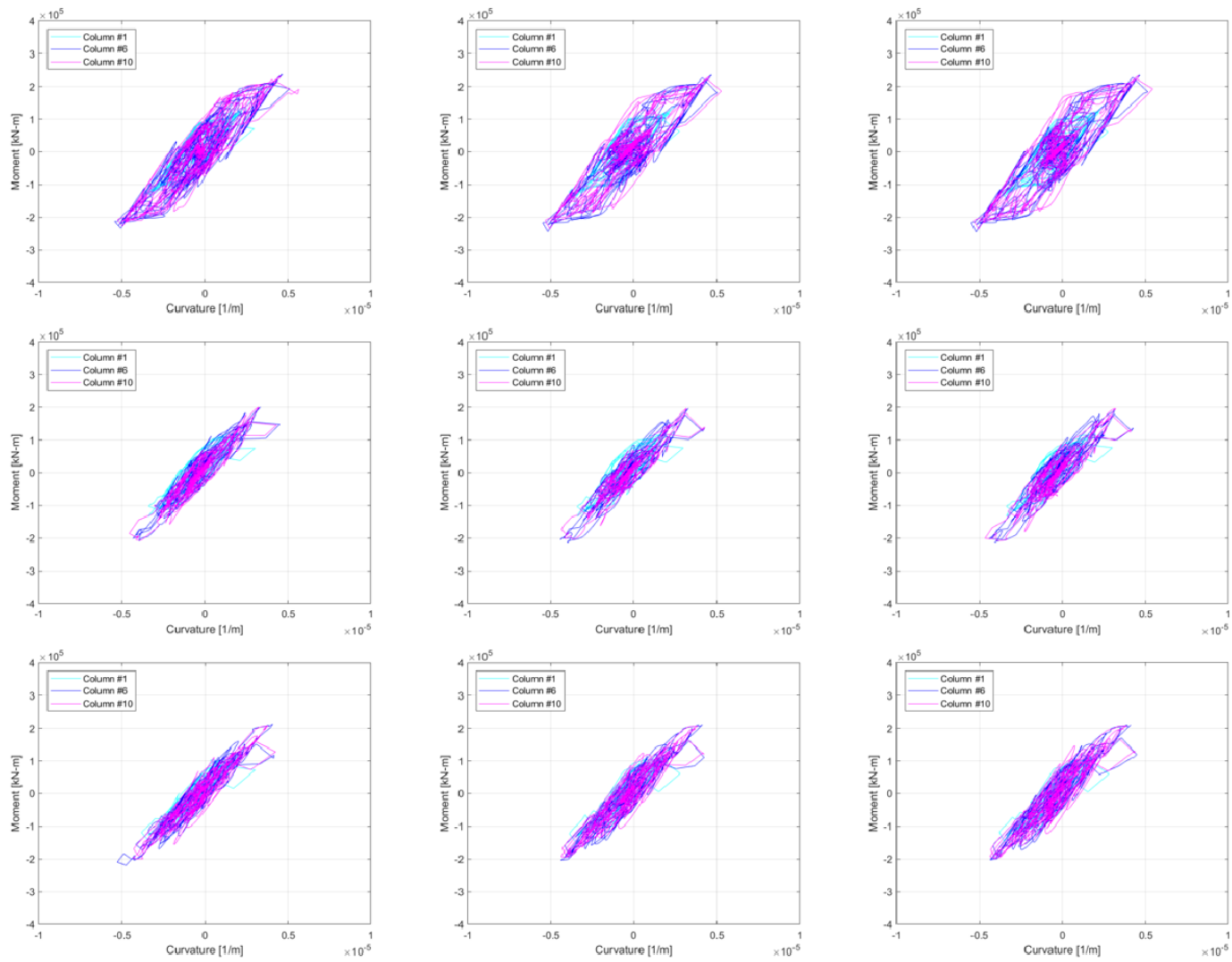


Figure 5-13. Transverse moment-curvature relationship for columns #1, #6, and #10 at 100% – (Row: (1) Northridge, (2) Kobe, and (3) Loma Prieta, Column: (1) Load Case 1, (2) Load Case 6, and (3) Load Case 9).

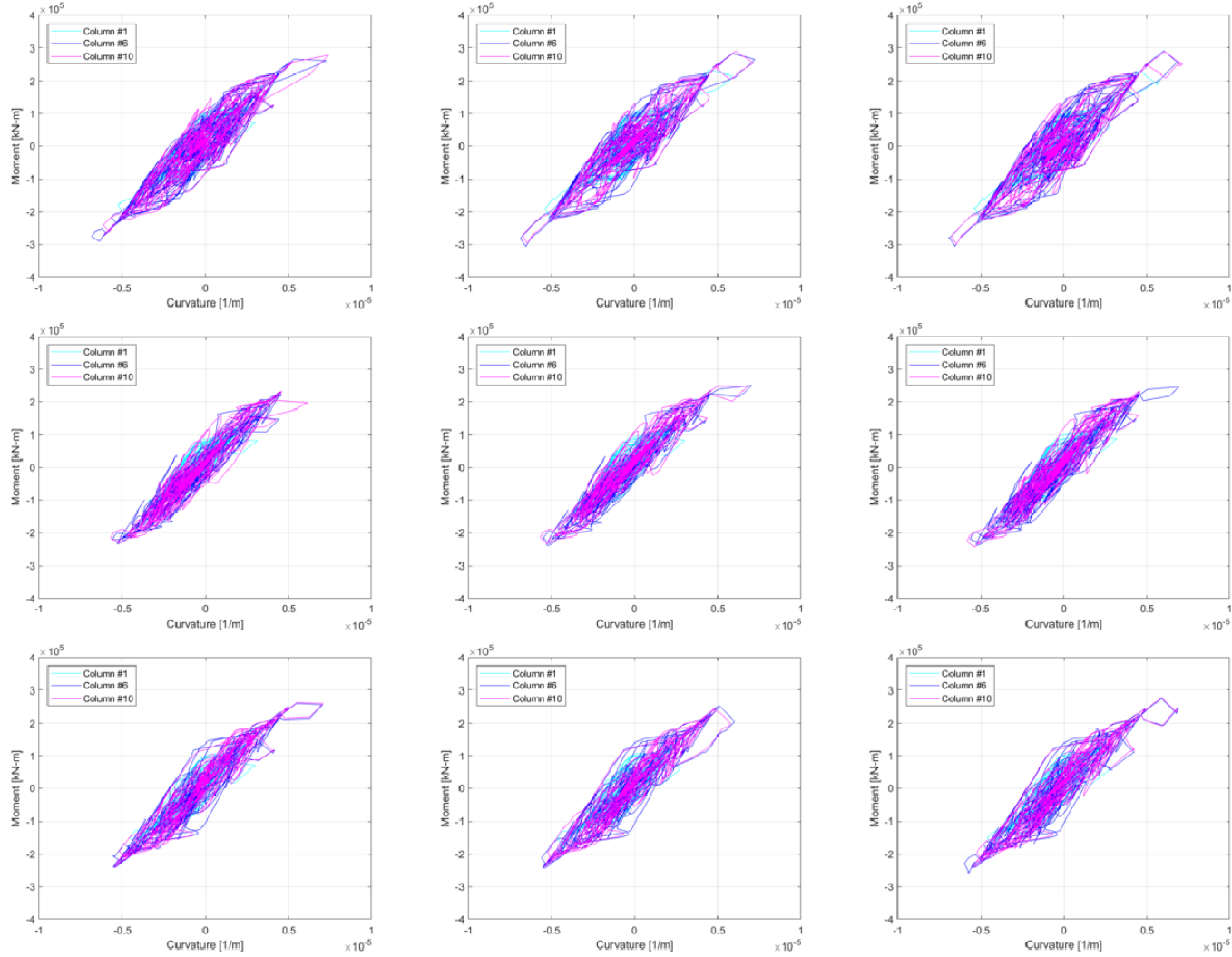


Figure 5-14. Transverse moment-curvature relationship for columns #1, #6, and #10 at 200% – (Row: (1) Northridge, (2) Kobe, and (3) Loma Prieta, Column: (1) Load Case 1, (2) Load Case 6, and (3) Load Case 9).

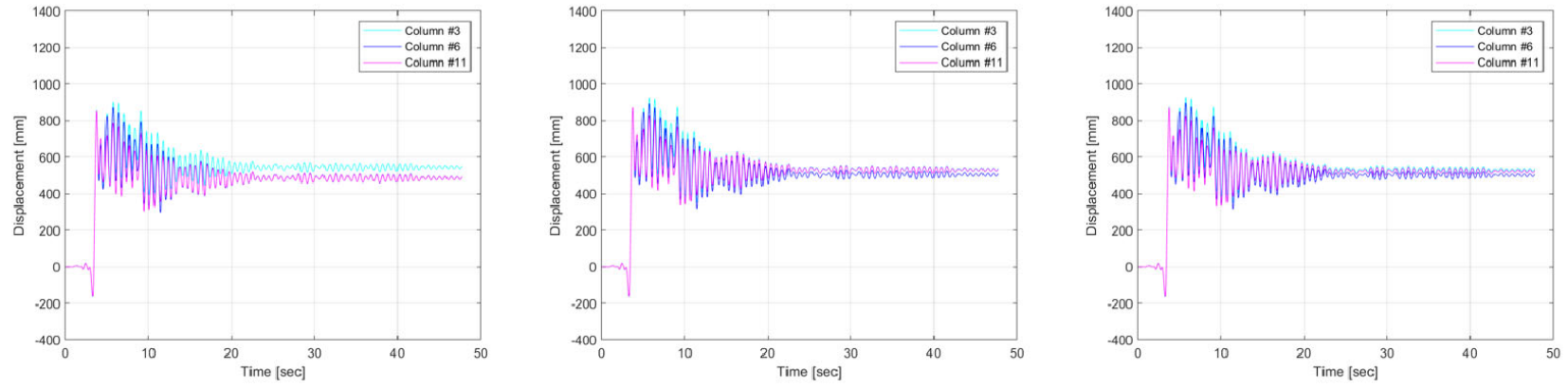


Figure 5-15. Longitudinal displacement time-history for columns #3, #6, and #11 at Northridge 300% – (Left: Load Case 1, Middle: Load Case 6, Right: Load Case 9).

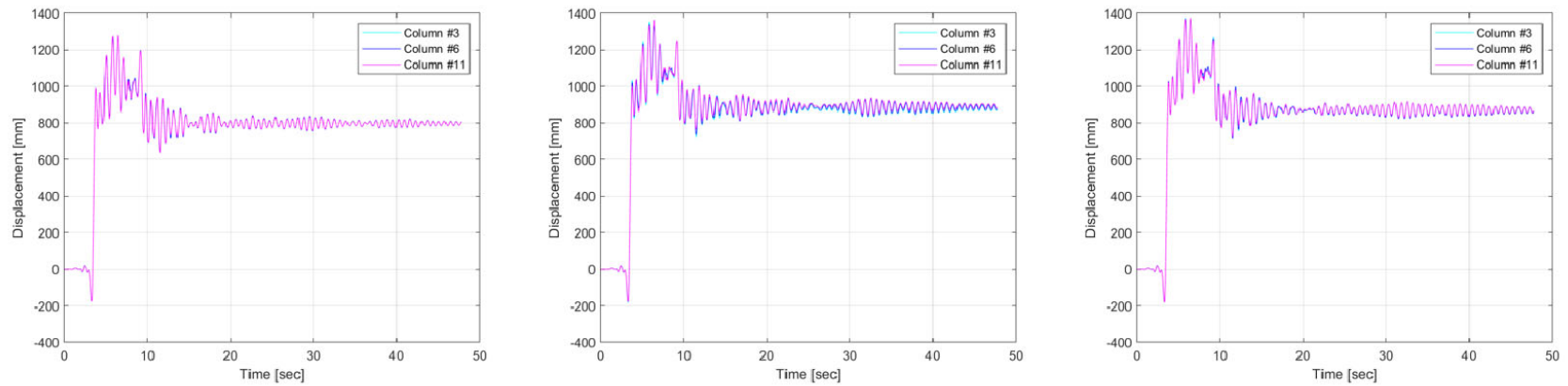


Figure 5-16. Transverse displacement time-history for columns #3, #6, and #11 at Northridge 300% – (Left: Load Case 1, Middle: Load Case 6, Right: Load Case 9).

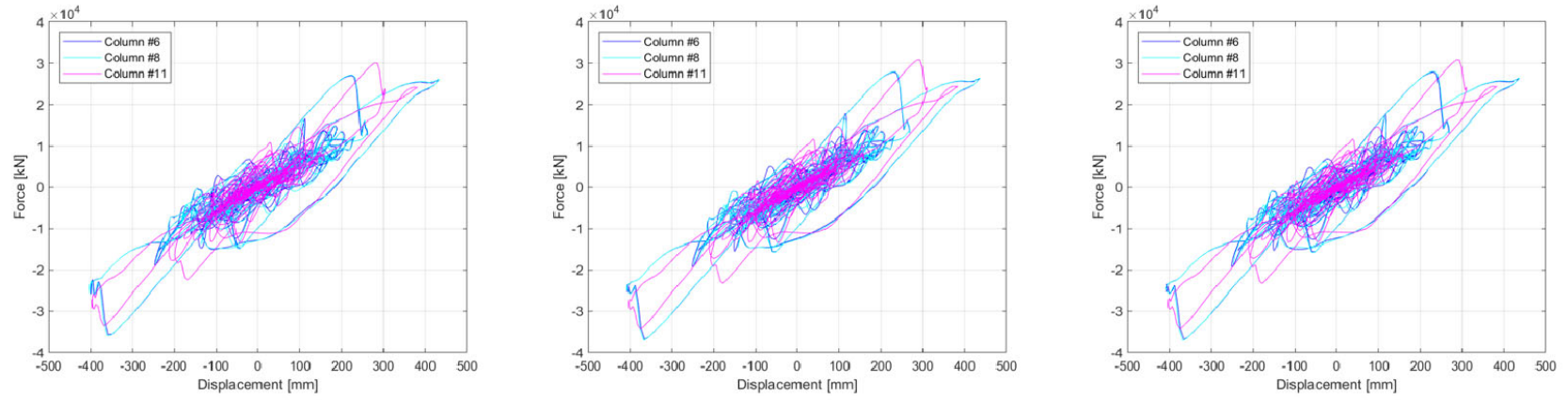


Figure 5-17. Longitudinal force-displacement relationship for columns #6, #8, and #11 at Northridge 300% – (Left: Load Case 1, Middle: Load Case 6, Right: Load Case 9).

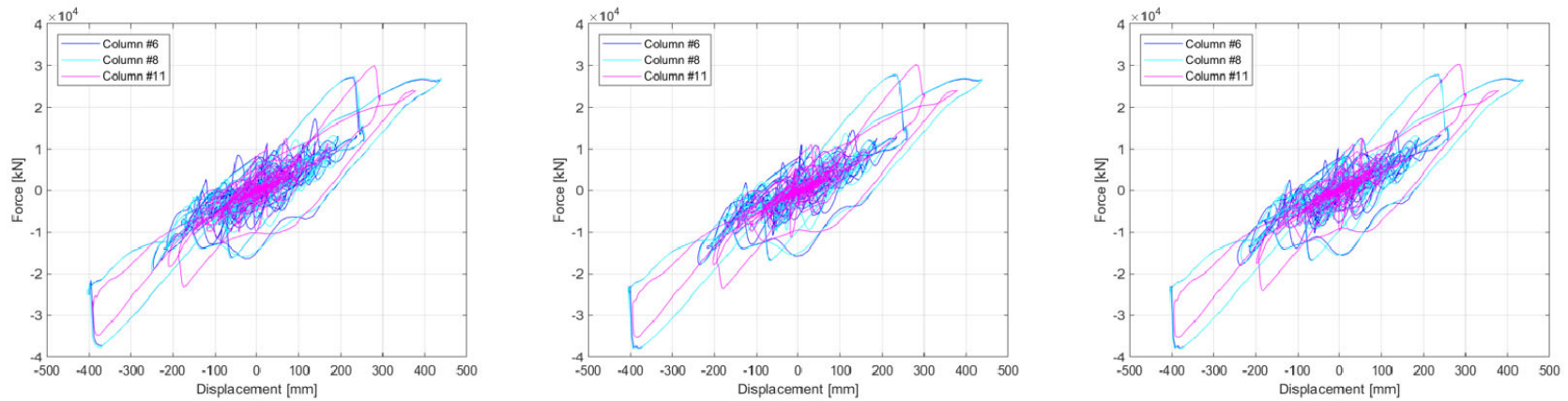


Figure 5-18. Transverse force-displacement relationship for columns #6, #8, and #11 at Northridge 300% – (Left: Load Case 1, Middle: Load Case 6, Right: Load Case 9).

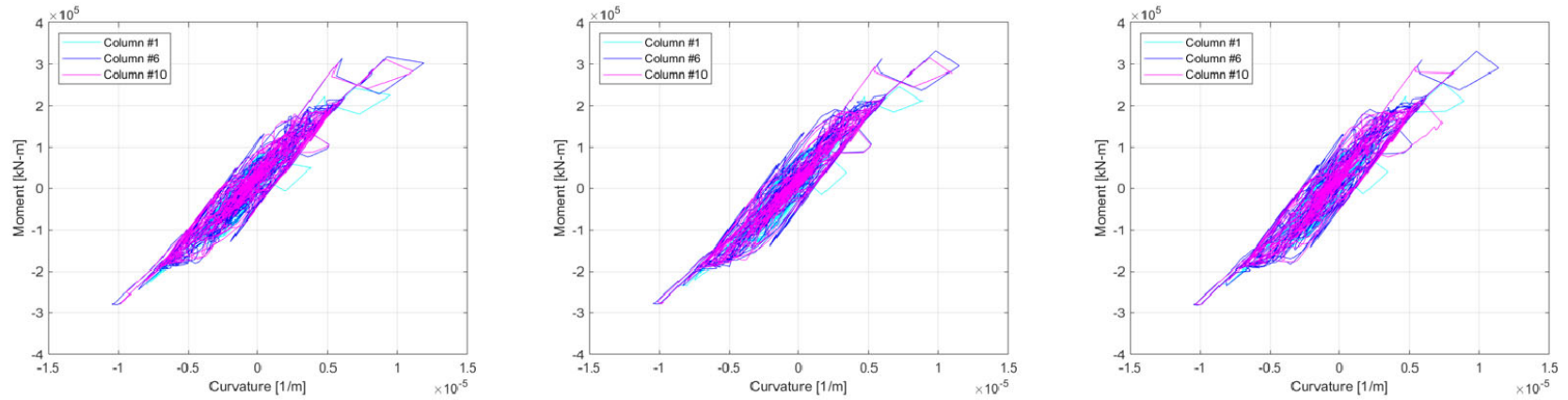


Figure 5-19. Longitudinal moment-curvature relationship for columns #1, #6, and #10 at Northridge 300% – (Left: Load Case 1, Middle: Load Case 6, Right: Load Case 9).

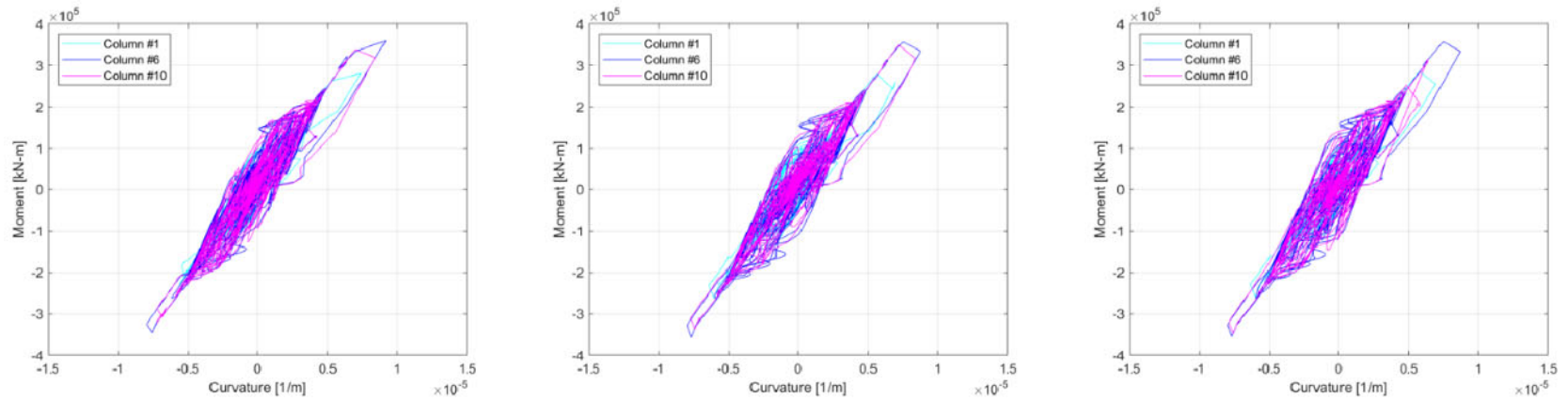


Figure 5-20. Transverse moment-curvature relationship for columns #1, #6, and #10 at Northridge 300% – (Left: Load Case 1, Middle: Load Case 6, Right: Load Case 9).

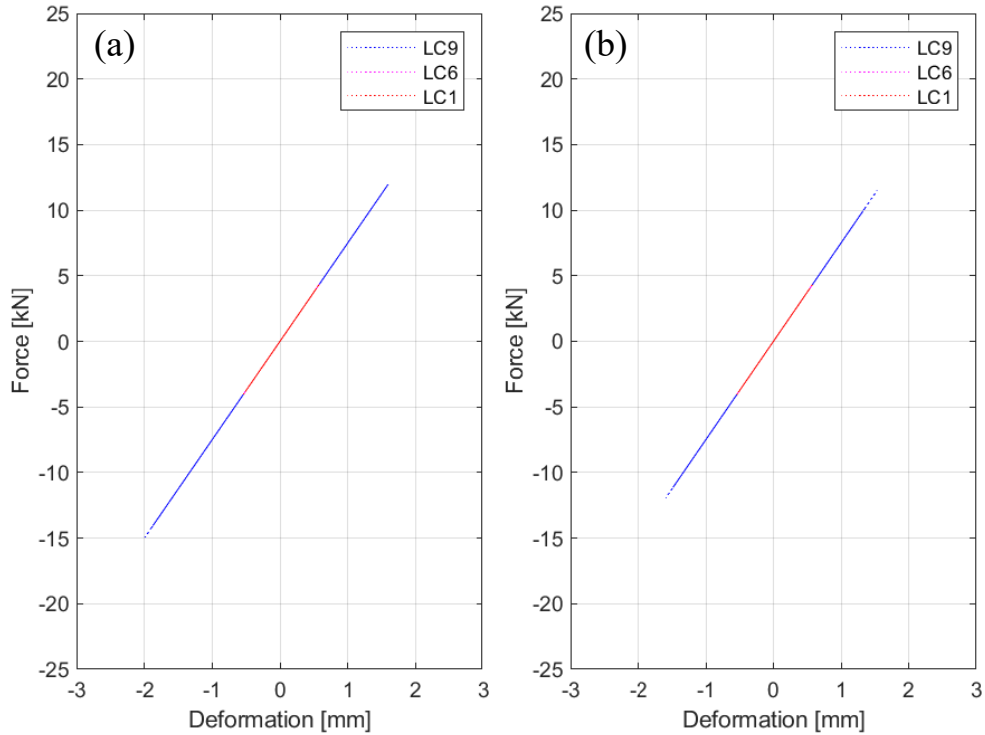


Figure 5-21. Force-deformation relationship of fasteners supporting rail 1 under Northridge 300%: (a) Above column #4, (b) Above column #6.

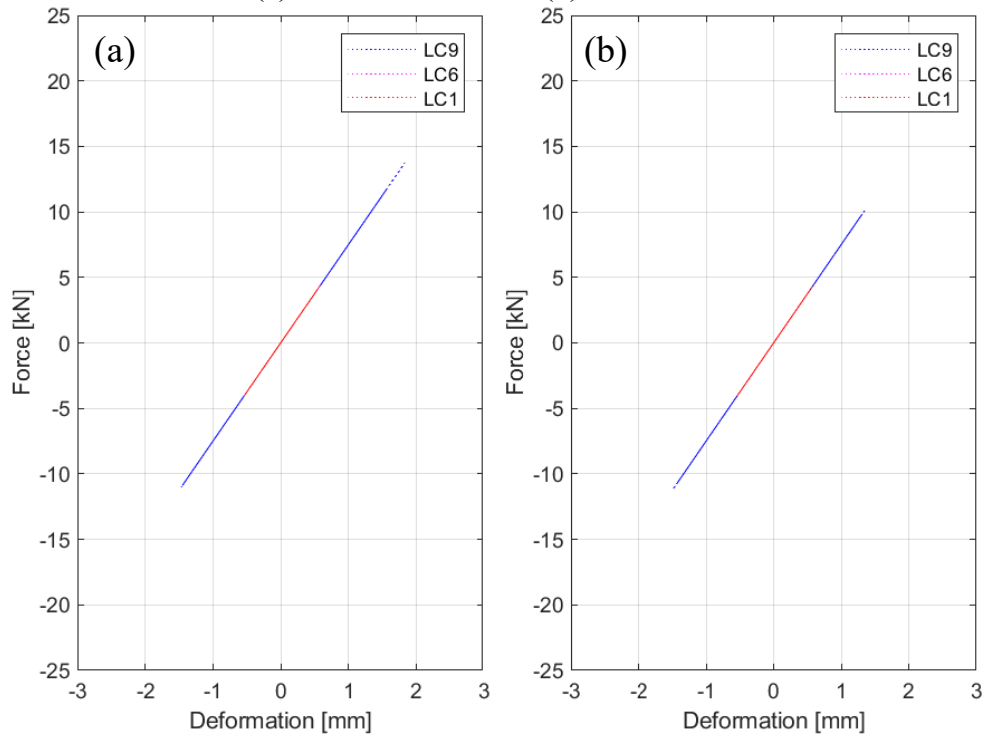


Figure 5-22. Force-deformation relationship of fasteners supporting rail 2 under Northridge 300%: (a) Above column #4, (b) Above column #6.

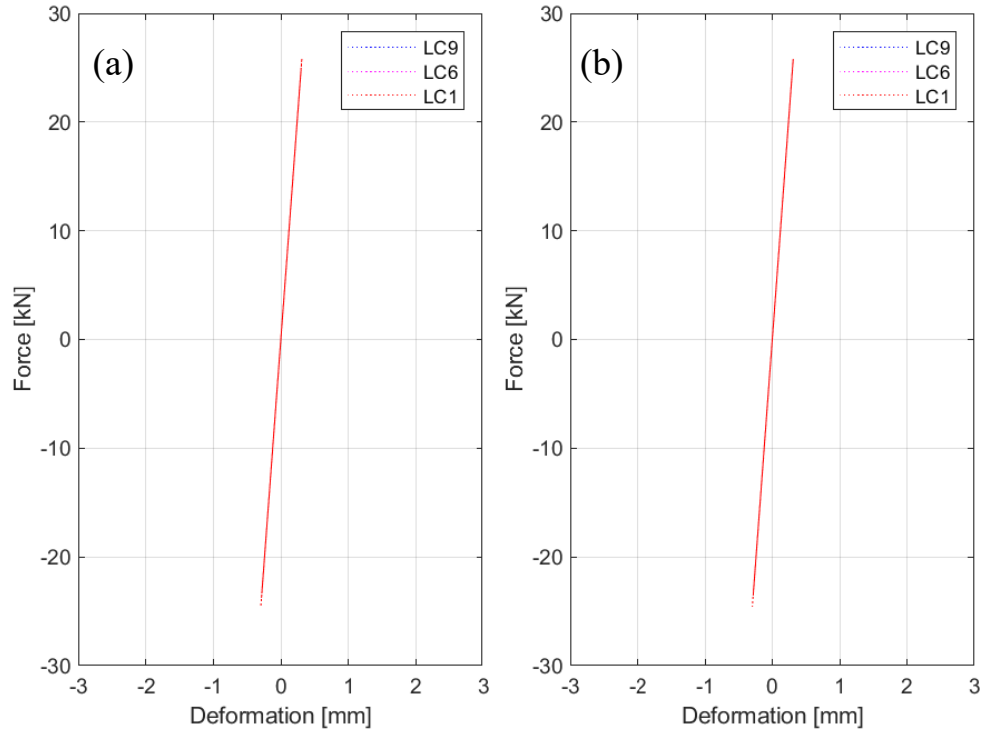


Figure 5-23. Force-deformation relationship of CA mortar layers supporting track 1 under Northridge 300%: (a) Above column #4, (b) Above column #6.

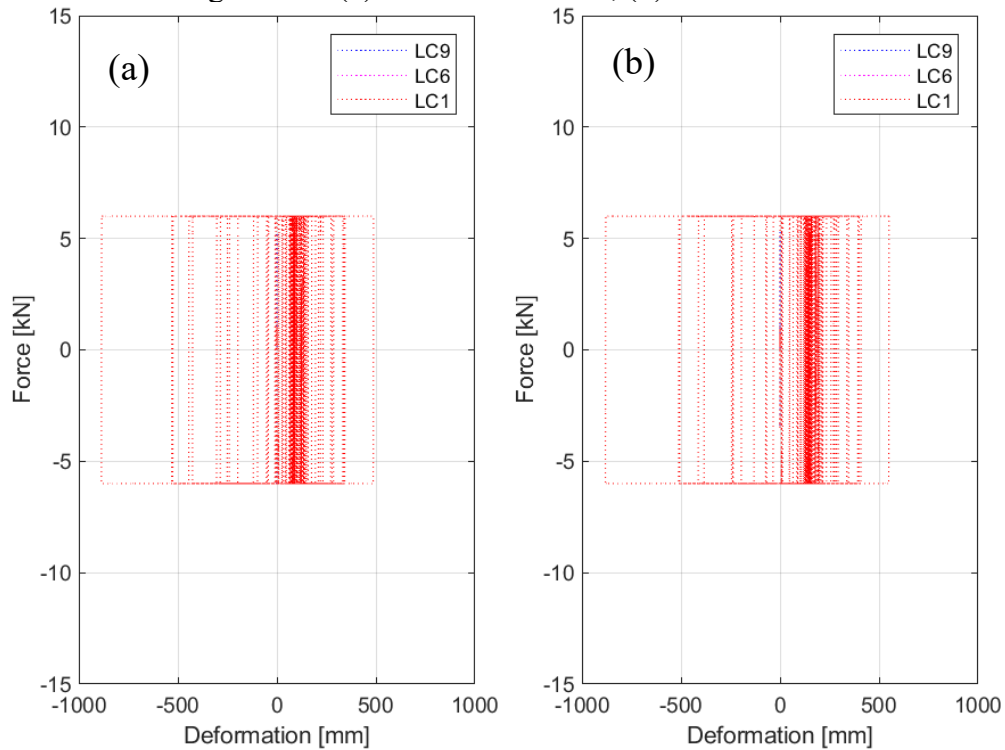


Figure 5-24. Force-deformation relationship of sliding layers supporting track 1 under Northridge 300%: (a) Above column #4, (b) Above column #6.

Chapter 6. SEISMIC RESPONSE OF PROTOTYPE HSR BRIDGE SYSTEM: MORE IN-DEPTH DEMONSTRATION

6.1. Summary

High-speed rail (HSR) is a complex system that involves critical infrastructure components such as bridges, that in turn, poses several design challenges unique to the nature of the HSR systems. With the requirements for deflections, rotations, and natural frequencies of bridge spans, comprehensive understanding of the HSR dynamic interactions among train-track-bridge structures is a topic of great importance. Accordingly, national and international research studies have focused on such dynamic interaction through sophisticated structural models. The main objective of this study was to synthesize existing knowledge to create a comprehensive modeling guideline for HSR bridge systems. To do so, an extensive literature search was performed to compile the modeling techniques for various HSR systems and identify common modeling practices. A prototype HSR system model was constructed using the modeling methods researched and a follow through of the steps taken to create a detailed model in OpenSees was documented and discussed sequentially. Due to the lack of a complete design guideline for a full HSR model, a train system, train-track system, and soil properties from separate studies were combined under the assumption that they are compatible. Sample static and dynamic analyses were performed for a variety of train loading scenarios, and the data was used to analyze the behavior of the HSR superstructure. The analysis aimed to showcase some of the capabilities associated with the developed OpenSees model. A more elaborate summary of the different components of this study are provided in the next few paragraphs.

A thorough literature review was conducted to synthesize the various methods of numerical modeling techniques used to model HSR systems. Literature published from national and international sources were reviewed and compiled to demonstrate and how the individual components within a train system, track system, or bridge system have been modeled in previous studies and the similarities and differences regarding the finite element modeling techniques. Doing so, the reader can gain insight on how to model different types of train, track, and bridge systems and apply this knowledge to the formulation of their own HSR system model. This task also aided the selection of the prototype train-track-bridge system modeled to demonstrate the application of the modeling techniques highlighted in the literature search.

Based on the studies analyzed in the literature search, a prototype train system and track-bridge system were selected to construct an example HSR model. The prototypes were selected based on available information regarding design. Although the model is for demonstration purposes, a realistic design would produce results that can be comprehended and allows for easier identification of any errors in the formulation of the model. The modeling procedures for each component of the HSR model in-place followed the methods presented in their respective studies. Any information that was not stated in the reference study was assumed using knowledge gained from the literature search. A step-by-step guide of the process of formulating the model and analysis parameters from start to finish were documented, accompanied by snapshots from the OpenSees model in-place for visual demonstration.

To exemplify potential data analysis with the variety of data that can be output by OpenSees, sample static and dynamic analyses were performed with a load case without train loading on the HSR bridge and with train loading on the HSR bridge. Additionally, a more in-depth set of

nonlinear seismic analyses were performed to set the stage for potential future seismic performance assessment. The analyses used three ground motions retrieved from the PEER Ground Motion Database and scaled at 100% and 200%. Three different load cases with no, partial, and full train loading were considered to observe the sensitivity of seismic response of the bridge with respect to the train loading scenarios. Although the train was modeled to be stationary during the seismic loading, this simulates a scenario where a train would be called to a stop after notice of an earthquake early warning. Local and global response of the prototype HSR bridge was presented through maximum response tables and behavioral graphs including displacement time-history, force-displacement, and moment-curvature, and a comparative seismic assessment for the response was conducted.

6.2. Conclusions

The focal point of this report was the presentation of numerical modeling methods of HSR bridge systems including train-track-structure interaction. The modeling details provided in Chapter 3 along with the complementary step-by-step procedure and scripts provided from an example OpenSees input file in Appendix B are the main outcome of this research study. Thus, the impact is more of a product as opposed to set of conclusions based on analytical studies. Nonetheless, the study provided a demonstration of the seismic response of HSR bridges through a prototype HSR model created based off previous studies. The analysis results presented in that part of the study are based on a prototype HSR bridge system assumption that were generously assumed to be applicable to one another. However, general conclusions can be still drawn from the performance of the prototype HSR bridge from a broad perspective, which at least could serve as a foundation for future research, as provided next.

Based on the seismic performance of the model in-place, the location of train loading for Load Case 6 and 9 did increase the local and global response within the bridge girders and columns. The maximum longitudinal moment response in the bridge columns under train loading experienced an average 10% and 13% increase throughout the three ground motions scaled to a 100% and 200% for Load Case 6 and Load Case 9, respectively. Column curvature also increased in the longitudinal and transverse directions by 4% and 6% on average for Load Case 6 and Load Case 9, respectively, and the maximum transverse moments in the columns showed an average increase of 5% for both of the load cases with train loading. The columns did not experience a significant increase in maximum shear forces due to additional train loading with less than 2% increase on average due to train loading. As for the global responses, bridge girders under Load Case 6 and Load Case 9 had an average increase of 4% for the maximum longitudinal displacement. Acceleration at the girder level for either direction experienced insignificant effects, even decreasing by 3% for the acceleration under Load Case 9 in the transverse direction.

Although the maximum response of the HSR bridge experienced variation due to the addition of train loading, the behavioral trends documented in the force-displacement and moment-curvature graphs were nearly identical with and without train loading for the original scale of the ground motions and showed slight instances of increased nonlinear loading-unloading loops for the 200% scale. Increase in displacements throughout the course of the ground motion were observed at the bridge girder level in the transverse displacement time-histories. Exceptionally large nonlinearities were not observed until analyzing the HSR bridge under the Northridge earthquake at 300% scale where apparent inelastic behavior was observed in all of the behavioral graphs plotted for Load Case 9.

The similarities in the seismic performance of the HSR columns between the load cases may be attributed to the intrinsic design, where force and moment capacities are much higher compared to typical railway or highway bridges; a by-product of the desired excessively large stiffness for HSR systems. In other words, the HSR bridge started to show response variation due to static train loading when the linear elastic limit had been exceeded. However, the inherent design complications for HSR bridges may be influenced largely by the dynamic loading of the train system which was not included in this study. To fully understand and design for the operation of HSR systems under the paramount safety, future studies are recommended to analyze the seismic performance of HSR bridges under the dual loading of dynamic train loading and dynamic seismic loading.

The overall performance of the prototype HSR bridge was well as it showed its ability to behave within its linear capacity. The performance was particularly good under the original scale of the ground motions. The HSR bridge columns were able to behave within its elastic capacity and showed slight nonlinearities when analyzed under the 200% scaled ground motions. Thus, at moderate ground motion intensities, it is safe to say the HSR bridge columns behaved essentially linearly or at least did not get into a large range of nonlinearities and were not at their force and moment capacities as well.

6.3. Research Impact

The work presented in this report is critical and timely as the implementation of HSR as a major mode of transportation in the United States is coming into fruition. Due to the recent advances in HSR research, national studies regarding this topic are still very limited and heavily rely on the publications from researchers abroad in Europe and East Asia where HSR systems are widely used as a major method of transportation. This study resulted in the following new and important contributions:

- The main contribution of this study is the walk-through of the processes of modeling a prototype HSR system, including the train-track-bridge system in high detail. This guide will allow future students and researchers with minimal experience in numerical modeling or modeling in OpenSees to formulate their own HSR model. This report can also be of benefit to researchers or designers who may need some guidance, as existing publications regarding this topic focus mainly on the analysis and results rather than the specific methods that were used to model each sub-system.
- Sub-systems of HSR have evolved over the years as technological advancements continue to improve the safety and efficiency of HSR. The extensive literature search presented in this study synthesizes the modeling methods that have been used by national and international researchers to idealize variety of train, track, and bridge systems. Future researchers can access this study to understand how specific HSR sub-systems are modeled and can pursue the publications referenced within this study for further details since.
- The design and analysis of HSR bridges presents many challenges in comparison to the design of highway bridges and conventional railway bridges. Consequently, this study demonstrates a variety of potential methods for analyzing the seismic performance of an HSR bridge through post-processing OpenSees output which would allow the verification of design. Although the seismic performance assessment demonstrated in this study is not meant to prove the soundness of the prototype HSR bridge modeled, future work can be built off of the research presented to formulate a national code and design guideline for HSR bridges.

6.4. Validities and Limitations

For completeness, a statement on the validities and limitations of this study are presented here and discussed to provide points of future recommendations and improvements. Due to the recent emphasis on implementing HSR systems as a mode of transportation in the United States, the literature available is heavily limited to a few national studies and foreign studies that have been translated to English and published to journals. This results in limitation of reference studies that can be researched for the purpose of understanding the methods of numerical modeling of HSR systems.

Another issue is the validity of the prototype model analysis results due to the lack of available design information regarding the prototype train, track, or bridge system that have been selected from the reference studies. This is mainly due to the limitation of content that can be included in such journal papers which could lead to the omission of detail that is not the emphasis of the respective study. To combat this, many assumptions were made when formulating the prototype model as discussed in Chapter 3. A design assumption example being the cross-sectional design and strength of concrete and reinforcing steel of the pier columns for the prototype bridge from the Beijing to Xuzhou section of the Beijing-Shanghai high-speed railway. Although the cross-sectional area and height of the pier columns were specified, the reinforcement layout and strength design were omitted so generic assumptions were made regarding reinforcement ratio and strength of core concrete.

For this study, the train-track-structure interaction was the focus of the model. Accordingly, soil-structure interaction was simplified to a few springs between the column bases and the fixed boundaries of the model as discussed in Chapter 3. Future studies should elaborate on the modeling of soil-structure interaction by creating a sophisticated footing model with pile-soil interaction and abutments at bridge ends. In addition, elements were not discretized as precisely as recommended for a study focusing on analysis results, since the focus is to demonstrate the process of modeling and analyzing a prototype model. The prototype HSR bridge model in place is a primitive design combining a train system from Korea, a track-bridge system from China, and general soil properties from California under the assumption that they are all compatible for the sake of demonstrating a model.

A proper seismic analysis of any structural system requires a design guideline and code that acts a standard for the performance of the structural design. Since there is no such standards in-place for HSR bridges in the United States as of yet, the performance of the prototype HSR bridge was based on engineering judgement and preexisting knowledge based on highway bridges. The analysis presented should not be taken as a recommendation for design, but as a demonstration of potential seismic analysis that can be conducted with a formal design guideline and code.

The seismic analysis presented was performed under earthquakes applied biaxially in the longitudinal and transverse directions and applied as identical support excitations. Although this is a common assumption when conducting seismic analysis of structures, there are limitations to the validity of the analysis. Vertical excitations can impact the response of girders with large spans, and multi-support excitations might be considered to accurately analyze the response of multi-support structures under incoherent ground motions. Future research is recommended to consider such limitations to expand the comprehensive understanding of HSR bridge performance.

REFERENCES

- [1] Abbasi, Mohammad. Seismic Vulnerability Assessment of As-Built and Retrofitted Multi-Frame Box-Girder Bridges. Diss. 2018.
- [2] Du, X. T., Y. L. Xu, and H. Xia. "Dynamic interaction of bridge–train system under non-uniform seismic ground motion." *Earthquake Engineering & Structural Dynamics* 41.1 (2012): 139-157.
- [3] Connolly, D., A. Giannopoulos, and M. C. Forde. "Numerical modelling of ground borne vibrations from high-speed rail lines on embankments." *Soil Dynamics and Earthquake Engineering* 46 (2013): 13-19.
- [4] En.wikipedia.org. 2020. Acela. [online] Available at: <<https://en.wikipedia.org/wiki/Acela>> [Accessed 25 July 2020].
- [5] En.wikipedia.org. 2020. High-Speed Rail In The United States. [online] Available at: <https://en.wikipedia.org/wiki/High-speed_rail_in_the_United_States> [Accessed 23 July 2020].
- [6] En.wikipedia.org. 2020. KTX-Sancheon. [online] Available at: <<https://en.wikipedia.org/wiki/KTX-Sancheon>> [Accessed 27 May 2020].
- [7] En.wikipedia.org. 2020. Texas Central Railway. [online] Available at: <https://en.wikipedia.org/wiki/Texas_Central_Railway> [Accessed 25 July 2020].
- [8] En.wikipedia.org. 2020. Xpresswest. [online] Available at: <<https://en.wikipedia.org/wiki/XpressWest>> [Accessed 25 July 2020].
- [9] Garg, Vijay. *Dynamics of railway vehicle systems*. Elsevier, 2012.
- [10] González, Arturo, Eugene J. OBrien, and P. J. McGetrick. "Identification of damping in a bridge using a moving instrumented vehicle." *Journal of Sound and Vibration* 331.18 (2012): 4115-4131.
- [11] Guo, W. W., et al. "Integral model for train-track-bridge interaction on the Sesia viaduct: Dynamic simulation and critical assessment." *Computers & Structures* 112 (2012): 205-216.
- [12] Guo, Wei, et al. "Simplified seismic model of CRTS II ballastless track structure on high-speed railway bridges in China." *Engineering Structures* 211 (2020): 110453.
- [13] He, Xingwen, et al. "Numerical analysis on seismic response of Shinkansen bridge-train interaction system under moderate earthquakes." *Earthquake engineering and engineering vibration* 10.1 (2011): 85-97.
- [14] Hurty, Walter C., and Moshe F. Rubinstein. *Dynamics of structures (Text on response of structures to large variety of dynamic excitations)*. ENGLEWOOD CLIFFS, N. J., PRENTICE-HALL, INC., 1964. 455 P (1964).
- [15] Hutton, S. G., and Y. K. Cheung. "Dynamic response of single span highway bridges." *Earthquake Engineering & Structural Dynamics* 7.6 (1979): 543-553.
- [16] Hsr.ca.gov. 2018. 2018 Business Plan. [online] Available at: <https://hsr.ca.gov/docs/about/business_plans/2018_BusinessPlan.pdf> [Accessed 23 July 2020].

- [17] Kaviani, Peyman, Farzin Zareian, and Ertugrul Taciroglu. "Seismic behavior of reinforced concrete bridges with skew-angled seat-type abutments." *Engineering Structures* 45 (2012): 137-150.
- [18] Kim, Chul Woo, Mitsuo Kawatani, and Ki Bong Kim. "Three-dimensional dynamic analysis for bridge-vehicle interaction with roadway roughness." *Computers & structures* 83.19-20 (2005): 1627-1645.
- [19] Kwark, J. W., et al. "Dynamic behavior of two-span continuous concrete bridges under moving high-speed train." *Computers & structures* 82.4-5 (2004): 463-474.
- [20] Lee, Chang Hun, et al. "Dynamic response analysis of monorail bridges under moving trains and riding comfort of trains." *Engineering Structures* 27.14 (2005): 1999-2013.
- [21] Lee, Chang Hun, et al. "Dynamic response of a monorail steel bridge under a moving train." *Journal of Sound and Vibration* 294.3 (2006): 562-579.
- [22] Li, Haiyan, et al. "Nonlinear random seismic analysis of 3D high-speed railway track-bridge system based on OpenSees." *Structures*. Vol. 24. Elsevier, 2020.
- [23] Li, Yong, and Joel P. Conte. "Effects of seismic isolation on the seismic response of a California high-speed rail prototype bridge with soil-structure and track-structure interactions." *Earthquake Engineering & Structural Dynamics* 45.15 (2016): 2415-2434.
- [24] Liu, Kai, et al. "Experimental and numerical analysis of a composite bridge for high-speed trains." *Journal of Sound and Vibration* 320.1-2 (2009): 201-220.
- [25] Lu, Dan, Futian Wang, and Suliang Chang. "The research of irregularity power spectral density of Beijing subway." *Urban Rail Transit* 1.3 (2015): 159-163.
- [26] Mao, Jianfeng, et al. "Random dynamic analysis of a train-bridge coupled system involving random system parameters based on probability density evolution method." *Probabilistic Engineering Mechanics* 46 (2016): 48-61.
- [27] Matsuura, Akio. "A study of dynamic behavior of bridge girder for high speed railway." *Proceedings of the Japan Society of Civil Engineers*. Vol. 1976. No. 256. Japan Society of Civil Engineers, 1976.
- [28] McCarthy, N., 2020. Infographic: The World's Longest High-Speed Rail Networks. [online] Statista Infographics. Available at: <<https://www.statista.com/chart/17093/miles-of-high-speed-rail-track-in-operation-by-country/>> [Accessed 23 July 2020].
- [29] Montenegro, P. A., et l. "Running safety assessment of trains moving over bridges subjected to moderate earthquakes." *Earthquake Engineering & Structural Dynamics* 45.3 (2016): 483-504.
- [30] Nguyen, Dinh-Van, Ki-Du Kim, and Pennung Warnitchai. "Simulation procedure for vehicle-substructure dynamic interactions and wheel movements using linearized wheel-rail interfaces." *Finite Elements in Analysis and Design* 45.5 (2009): 341-356.

- [31] Opensees.berkeley.edu. 2020. Opensees User Manual. [online] Available at: <<https://opensees.berkeley.edu/OpenSees/manuals/comparisonManual/1417.htm>> [Accessed 6 August 2020].
- [32] Opensees.berkeley.edu. 2020. Openseeswiki. [online] Available at: <https://opensees.berkeley.edu/wiki/index.php/Main_Page> [Accessed 6 August 2020].
- [33] Plasseramerican.com. 2020. Plasser American - Machines & Systems - Ballast Bed Cleaning. [online] Available at: <<http://www.plasseramerican.com/en/machines-systems/ballast-bed-cleaning.html>> [Accessed 23 July 2020].
- [34] Queiroz, F. D., P. C. G. S. Vellasco, and D. A. Nethercot. "Finite element modelling of composite beams with full and partial shear connection." *Journal of Constructional Steel Research* 63.4 (2007): 505-521.
- [35] Rocha, J. M., A. A. Henriques, and R. Calçada. "Probabilistic safety assessment of a short span high-speed railway bridge." *Engineering Structures* 71 (2014): 99-111.
- [36] Song, Myung-Kwan, Hyuk-Chun Noh, and Chang-Koon Choi. "A new three-dimensional finite element analysis model of high-speed train-bridge interactions." *Engineering Structures* 25.13 (2003): 1611-1626.
- [37] Tanabe, M., Yamada, Y., & Hajime, W. (1987). Modal method for interaction of train and bridge. *Computers & Structures*, 27(1), 119-127.
- [38] Tayabji, Shiraz & Bilow, David. (2001). Concrete Slab Track State of the Practice. *Transportation Research Record*. 1742. 87-96. 10.3141/1742-11.
- [39] Wang, Jinfeng, et al. "Performance of Cement Asphalt Mortar in Ballastless Slab Track over High-Speed Railway under Extreme Climate Conditions." *International Journal of Geomechanics* 19.5 (2019): 04019037.
- [40] Wu, Yean-Seng, and Yeong-Bin Yang. "Steady-state response and riding comfort of trains moving over a series of simply supported bridges." *Engineering Structures* 25.2 (2003): 251-265.
- [41] Xia, He, and Nan Zhang. "Dynamic analysis of railway bridge under high-speed trains." *Computers & Structures* 83.23-24 (2005): 1891-1901.
- [42] Xia, He, Nan Zhang, and Guido De Roeck. "Dynamic analysis of high speed railway bridge under articulated trains." *Computers & Structures* 81.26-27 (2003): 2467-2478.
- [43] Yan, Bin, Gong-Lian Dai, and Nan Hu. "Recent development of design and construction of short span high-speed railway bridges in China." *Engineering Structures* 100 (2015): 707-717.
- [44] Yang, Yeong-Bin, and Bing-Houng Lin. "Vehicle-bridge interaction analysis by dynamic condensation method." *Journal of Structural Engineering* 121.11 (1995): 1636-1643.
- [45] Yang, Yeong-Bin, and Jong-Dar Yau. "Vehicle-bridge interaction element for dynamic analysis." *Journal of Structural Engineering* 123.11 (1997): 1512-1518.

- [46] Yang, Yeong-Bin, and Yean-Seng Wu. "A versatile element for analyzing vehicle–bridge interaction response." *Engineering structures* 23.5 (2001): 452-469.
- [47] Yu, Zhi-wu, et al. "Non-stationary random vibration analysis of a 3D train–bridge system using the probability density evolution method." *Journal of Sound and Vibration* 366 (2016): 173-189.
- [48] Yu, Zhi-wu, and Jian-feng Mao. "Probability analysis of train-track-bridge interactions using a random wheel/rail contact model." *Engineering Structures* 144 (2017): 120-138.
- [49] Yu, Zhi-wu, and Jian-feng Mao. "A stochastic dynamic model of train-track-bridge coupled system based on probability density evolution method." *Applied Mathematical Modelling* 59 (2018): 205-232.
- [50] Zeng, Zhi-Ping, et al. "Random vibration analysis of train–bridge under track irregularities and traveling seismic waves using train–slab track–bridge interaction model." *Journal of Sound and Vibration* 342 (2015): 22-43.
- [51] Zhaohua, Feng, and Robert D. Cook. "Beam Elements on Two-Parameter Elastic Foundations." *Journal of Engineering Mechanics*, vol. 109, no. 6, 1983, pp. 1390-1402.

APPENDIX A: OPENSEES COMMANDS

For the convenience of the reader, this Appendix provides the syntax and input parameter definition (in form of screenshots as obtained from OpenSeesWiki, [32]) for the key OpenSees commands used in creating the HSR bridge model.

model BasicBuilder -ndm \$ndm <-ndf \$ndf>	
\$ndm	spatial dimension of problem (1,2, or 3)
\$ndf	number of degrees of freedom at node (optional) default value depends on value of ndm: ndm=1 -> ndf=1 ndm=2 -> ndf=3 ndm=3 -> ndf=6

Figure A-1. *model* command parameters [32].

node \$nodeTag (ndm \$coords) <-mass (ndf \$massValues)>	
\$nodeTag	integer tag identifying node
\$coords	nodal coordinates (ndm arguments)
\$massValues	nodal mass corresponding to each DOF (ndf arguments) (optional))
The optional -mass string allows analyst the option of associating nodal mass with the node	

Figure A-2. *node* command parameters [32].

fix \$nodeTag (ndf \$constrValues)	
\$nodeTag	integer tag identifying the node to be constrained
\$constrValues	ndf constraint values (0 or 1) corresponding to the ndf degrees-of-freedom. 0 unconstrained (or free) 1 constrained (or fixed)

Figure A-3. *fix* constraint command parameters [32].

equalDOF \$rNodeTag \$cNodeTag \$dof1 \$dof2 ...	
\$rNodeTag	integer tag identifying the retained node (rNode)
\$cNodeTag	integer tag identifying the constrained node (cNode)
\$dof1 \$dof2 ...	nodal degrees-of-freedom that are constrained at the cNode to be the same as those at the rNode Valid range is from 1 through ndf, the number of nodal degrees-of-freedom.

Figure A-4. *equalDOF* constraint command parameters [32].

For a two-dimensional problem:
geomTransf Linear \$transfTag <-jntOffset \$dXi \$dYi \$dXj \$dYj>

For a three-dimensional problem:
geomTransf Linear \$transfTag \$vecxzX \$vecxzY \$vecxzZ <-jntOffset \$dXi \$dYi \$dZi \$dXj \$dYj \$dZj>

\$transfTag	integer tag identifying transformation X, Y, and Z components of <i>vecxz</i> , the vector used to define the local x-z plane of the local-coordinate system. The local y-axis is defined by taking the cross product of the <i>vecxz</i> vector and the x-axis.
\$vecxzX \$vecxzY \$vecxzZ	These components are specified in the global-coordinate system X,Y,Z and define a vector that is in a plane parallel to the x-z plane of the local-coordinate system. These items need to be specified for the three-dimensional problem.
\$dXi \$dYi \$dZi	joint offset values -- offsets specified with respect to the global coordinate system for element-end node i (the number of arguments depends on the dimensions of the current model). The offset vector is oriented from node i to node j as shown in a figure below. (optional)
\$dXj \$dYj \$dZj	joint offset values -- offsets specified with respect to the global coordinate system for element-end node j (the number of arguments depends on the dimensions of the current model). The offset vector is oriented from node i to node j as shown in a figure below. (optional)

Figure A-5. *geomTransfLinear* transformation command parameters [32].

uniaxialMaterial Steel01 \$matTag \$fy \$E0 \$b <\$a1 \$a2 \$a3 \$a4>

\$matTag	integer tag identifying material
\$fy	yield strength
\$E0	initial elastic tangent
\$b	strain-hardening ratio (ratio between post-yield tangent and initial elastic tangent)
\$a1	isotropic hardening parameter, increase of compression yield envelope as proportion of yield strength after a plastic strain of $a_2^2 * (f_y / E_0)$. (optional)
\$a2	isotropic hardening parameter (see explanation under <i>\$a1</i>). (optional).
\$a3	isotropic hardening parameter, increase of tension yield envelope as proportion of yield strength after a plastic strain of $a_4^2 * (f_y / E_0)$. (optional)
\$a4	isotropic hardening parameter (see explanation under <i>\$a3</i>). (optional)

Figure A-6. *Steel01* material command parameters [32].

uniaxialMaterial Steel02 \$matTag \$fy \$E \$b \$R0 \$cR1 \$cR2 <\$a1 \$a2 \$a3 \$a4 \$siglnit>

\$matTag	integer tag identifying material
\$fy	yield strength
\$E0	initial elastic tangent
\$b	strain-hardening ratio (ratio between post-yield tangent and initial elastic tangent)
\$R0 \$cR1 \$cR2	parameters to control the transition from elastic to plastic branches. Recommended values: <i>\$R0</i> =between 10 and 20, <i>\$cR1</i> =0.925, <i>\$cR2</i> =0.15
\$a1	isotropic hardening parameter, increase of compression yield envelope as proportion of yield strength after a plastic strain of $a_2^2 * (f_y / E_0)$. (optional)
\$a2	isotropic hardening parameter (see explanation under <i>\$a1</i>). (optional default = 1.0).
\$a3	isotropic hardening parameter, increase of tension yield envelope as proportion of yield strength after a plastic strain of $a_4^2 * (f_y / E_0)$. (optional default = 0.0)
\$a4	isotropic hardening parameter (see explanation under <i>\$a3</i>). (optional default = 1.0)
\$siglnit	Initial Stress Value (optional, default: 0.0) the strain is calculated from $\epsilon_s = \text{siglnit} / E$ if (siglnit != 0.0) { double epslnit = siglnit/E; eps = trialStrain+epslnit; } else eps = trialStrain;

Figure A-7. *Steel02* material command parameters [32].

uniaxialMaterial Concrete02 \$matTag \$fpc \$epsc0 \$fpcu \$sepsU \$lambda \$ft \$Ets

\$matTag	integer tag identifying material
\$fpc	concrete compressive strength at 28 days (compression is negative)*
\$epsc0	concrete strain at maximum strength*
\$fpcu	concrete crushing strength *
\$sepsU	concrete strain at crushing strength*
\$lambda	ratio between unloading slope at <i>\$sepsU</i> and initial slope
\$ft	tensile strength
\$Ets	tension softening stiffness (absolute value) (slope of the linear tension softening branch)

Figure A-8. *Concrete02* material command parameters [32].

uniaxialMaterial ViscousDamper \$matTag \$K \$Cd \$alpha <\$LGap> <\$NM \$RelTol \$AbsTol \$MaxHalf>	
\$matTag	integer tag identifying material
\$K	Elastic stiffness of linear spring to model the axial flexibility of a viscous damper (e.g. combined stiffness of the supporting brace and internal damper portion)
\$Cd	Damping coefficient
\$alpha	Velocity exponent
\$LGap	Gap length to simulate the gap length due to the pin tolerance
\$NM	Employed adaptive numerical algorithm (default value NM = 1; 1 = Dormand-Prince54, 2=6th order Adams-Bashforth-Moulton, 3=modified Rosenbrock Triple)
\$RelTol	Tolerance for absolute relative error control of the adaptive iterative algorithm (default value 10 ⁻⁶)
\$AbsTol	Tolerance for absolute error control of adaptive iterative algorithm (default value 10 ⁻¹⁰)
\$MaxHalf	Maximum number of sub-step iterations within an integration step (default value 15)

Figure A-9. *ViscousDamper* material command parameters [32].

uniaxialMaterial Elastic \$matTag \$E <\$eta> <\$Eeng>	
\$matTag	integer tag identifying material
\$E	tangent
\$eta	damping tangent (optional, default=0.0)
\$Eeng	tangent in compression (optional, default=E)

Figure A-10. *Elastic* material command parameters [32].

For a three-dimensional problem:

element elasticBeamColumn \$eleTag \$iNode \$jNode \$A \$E \$G \$J \$Iy \$Iz \$transfTag <-mass \$massDens> <-cMass>	
\$eleTag	unique element object tag
\$iNode \$jNode	end nodes
\$A	cross-sectional area of element
\$E	Young's Modulus
\$G	Shear Modulus
\$J	torsional moment of inertia of cross section
\$Iz	second moment of area about the local z-axis
\$Iy	second moment of area about the local y-axis
\$transfTag	identifier for previously-defined coordinate-transformation (CrdTransf) object
\$massDens	element mass per unit length (optional, default = 0.0)
-cMass	to form consistent mass matrix (optional, default = lumped mass matrix)

Figure A-11. *elasticBeamColumn* element command parameters [32].

element dispBeamColumn \$eleTag \$iNode \$jNode \$numIntgrPts \$secTag \$transfTag <-mass \$massDens> <-cMass> <-integration \$intType>	
To change the sections along the element length, the following form of command may be used:	
element dispBeamColumn \$eleTag \$iNode \$jNode \$numIntgrPts -sections \$secTag1 \$secTag2 ... \$transfTag <-mass \$massDens> <-cMass> <-integration \$intType>	
\$eleTag	unique element object tag
\$iNode \$jNode	end nodes
\$numIntgrPts	number of integration points along the element.
\$secTag	identifier for previously-defined section object
\$secTag1 \$secTag2 ...	\$numIntgrPts identifiers of previously-defined section object
\$transfTag	identifier for previously-defined coordinate-transformation (CrdTransf) object
\$massDens	element mass density (per unit length), from which a lumped-mass matrix is formed (optional, default = 0.0)
-cMass	to form consistent mass matrix (optional, default = lumped mass matrix)
\$intType	numerical integration type, options are Lobatto, Legendre, Radau, NewtonCotes, Trapezoidal (optional, default = Legendre)

Figure A-12. *dispBeamColumn* element command parameters [32].

```
element zeroLength SeleTag $iNode $jNode -mat $matTag1 $matTag2 ... -dir $dir1 $dir2 ...<-doRayleigh $rFlag> <-orient $x1 $x2 $x3 $yp1 $yp2 $yp3>
```

SeleTag	unique element object tag
\$iNode \$jNode	end nodes
\$matTag1 \$matTag2 ...	tags associated with previously-defined UniaxialMaterials
\$dir1 \$dir2 ...	material directions: 1,2,3 - translation along local x,y,z axes, respectively; 4,5,6 - rotation about local x,y,z axes, respectively
\$x1 \$x2 \$x3	vector components in global coordinates defining local x-axis (optional)
\$yp1 \$yp2 \$yp3	vector components in global coordinates defining vector yp which lies in the local x-y plane for the element. (optional)
\$rFlag	optional, default = 0 rFlag = 0 NO RAYLEIGH DAMPING (default) rFlag = 1 include rayleigh damping

Figure A-13. *zeroLength* element command parameters [32].

```
element twoNodeLink SeleTag $iNode $jNode -mat $matTags -dir $dirs <-orient <$x1 $x2 $x3> $y1 $y2 $y3> <-pDelta (4 $Mratio)> <-shearDist (2 $sDratios)> <-doRayleigh> <-mass $m>
```

SeleTag	unique element object tag
\$iNode \$jNode	end nodes
\$matTags	tags associated with previously-defined UniaxialMaterial objects
\$dirs	material directions: 2D-case: 1,2 - translations along local x,y axes; 3 - rotation about local z axis 3D-case: 1,2,3 - translations along local x,y,z axes; 4,5,6 - rotations about local x,y,z axes
\$x1 \$x2 \$x3	vector components in global coordinates defining local x-axis (optional)
\$y1 \$y2 \$y3	vector components in global coordinates defining local y-axis (optional)
\$Mratios	P-Delta moment contribution ratios, size of ratio vector is 2 for 2D-case and 4 for 3D-case (entries: [My_iNode, My_jNode, Mz_iNode, Mz_jNode]) My_iNode + My_jNode <= 1.0, Mz_iNode + Mz_jNode <= 1.0. Remaining P-Delta moments are resisted by shear couples. (optional)
\$sDratios	shear distances from iNode as a fraction of the element length, size of ratio vector is 1 for 2D-case and 2 for 3D-case (entries: [dy_iNode, dz_iNode] (optional, default = [0.5 0.5])
-doRayleigh	to include Rayleigh damping from the element (optional, default = no Rayleigh damping contribution)
\$m	element mass (optional, default = 0.0)

Figure A-14. *twoNodeLink* element command parameters [32].

```
section Fiber $secTag <-GJ $GJ> {  
  fiber...  
  patch...  
  layer...  
  ...  
}
```

\$secTag	unique tag among sections
\$GJ	linear-elastic torsional stiffness assigned to the section (optional, default = no torsional stiffness)
fiber...	command to generate a single fiber
patch...	command to generate a number of fibers over a geometric cross-section
layer...	command to generate a row of fibers along a geometric-arc

Figure A-15. *section fiber* command parameters [32].

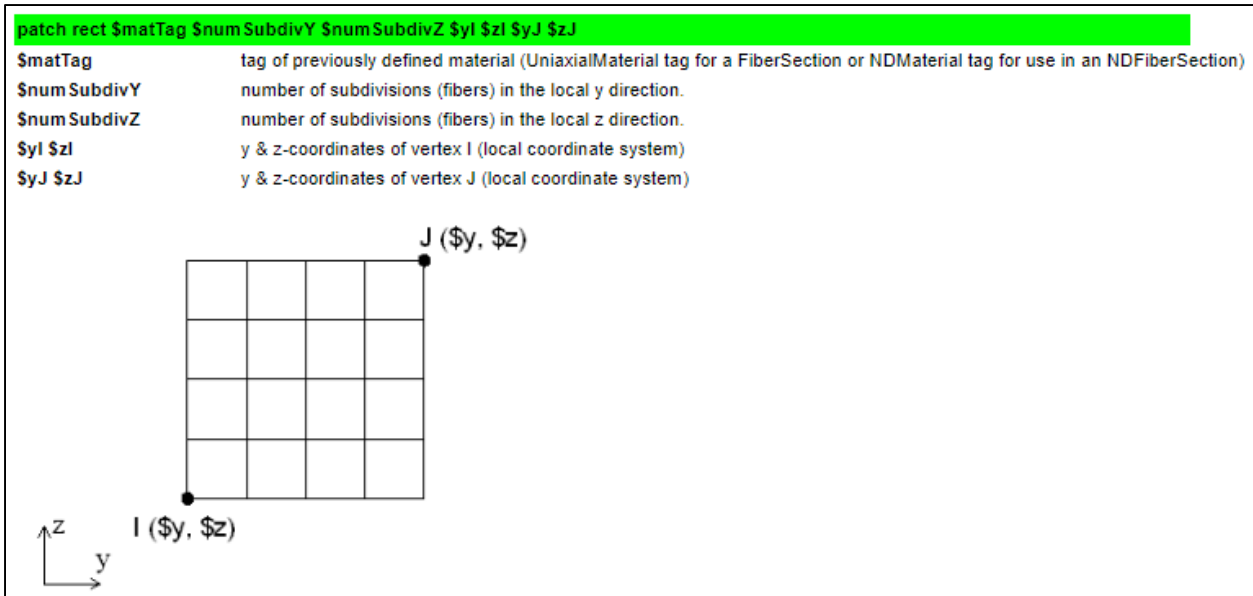


Figure A-16. *patch rect* command parameters [32].

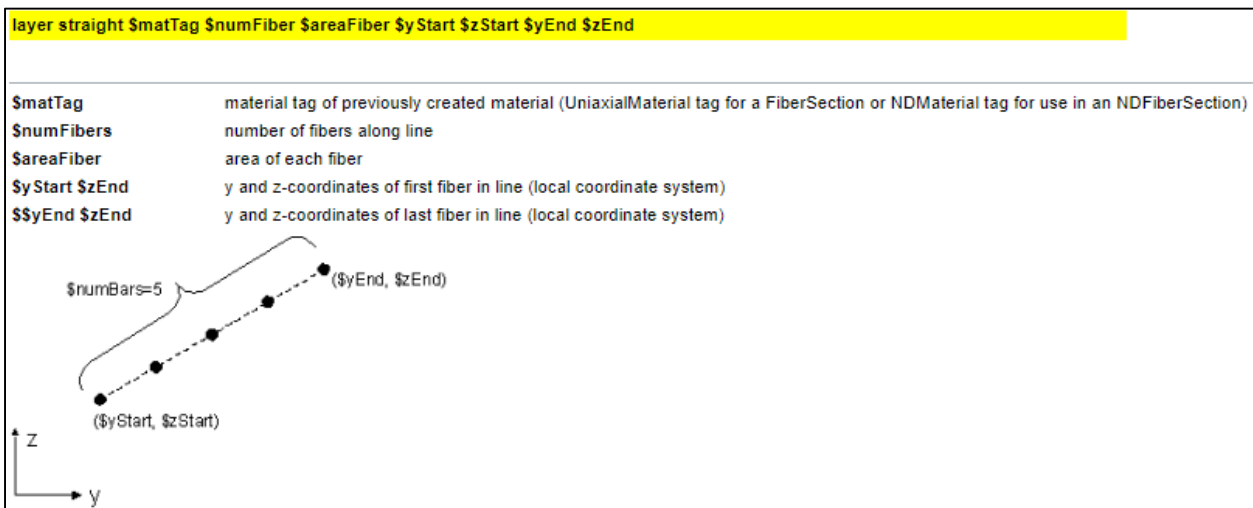


Figure A-17. *layer straight* command parameters [32].

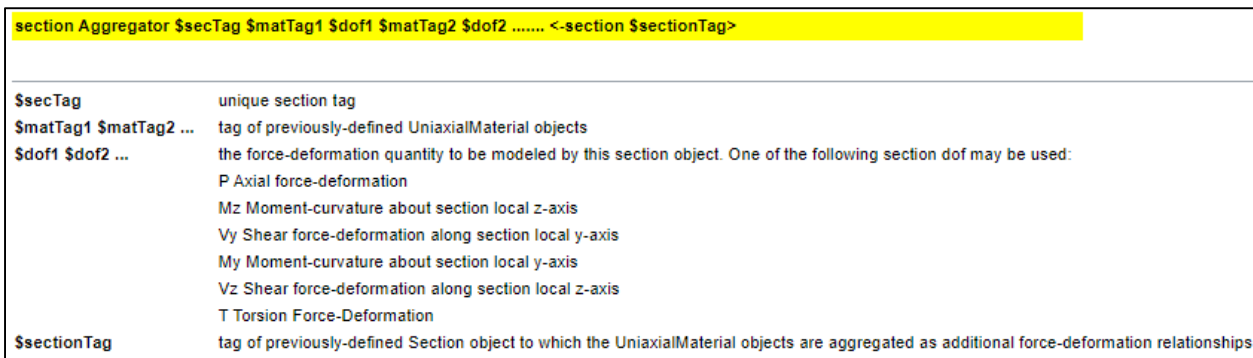


Figure A-18. *section aggregator* command parameters [32].

mass \$nodeTag (ndf \$massValues)	
\$nodeTag	integer tag identifying node whose mass is set
\$massValues	ndf nodal mass values corresponding to each DOF

Figure A-19. *mass* command parameters [32].

eigen <\$solver> \$numEigenvalues	
\$numEigenvalues	number of eigenvalues required
\$solver	optional string detailing type of solver: -genBandArpack, -symmBandLapack, -fullGenLapack (default: -genBandArpack)
RETURNS:	
a tcl string containing eigenvalues.	

Figure A-20. *eigen* analysis command parameters [32].

D = \$alphaM * M + \$betaK * Kcurrent + \$betaKinit * Kinit + \$betaKcomm * KlastCommit	
rayleigh \$alphaM \$betaK \$betaKinit \$betaKcomm	
\$alphaM	factor applied to elements or nodes mass matrix
\$betaK	factor applied to elements current stiffness matrix.
\$betaKinit	factor applied to elements initial stiffness matrix.
\$betaKcomm	factor applied to elements committed stiffness matrix.

Figure A-21. *Rayleigh* damping command parameters [32].

For a load path where the factors are specified in a tcl list with a constant time interval between points:	
timeSeries Path \$tag -dt \$dt -values {list_of_values} <-factor \$cFactor> <-useLast> <-prependZero> <-startTime \$tStart>	
For a load path where the factors are specified in a file for a constant time interval between points:	
timeSeries Path \$tag -dt \$dt -filePath \$filePath <-factor \$cFactor> <-useLast> <-prependZero> <-startTime \$tStart>	
For a load path where the values are specified at non-constant time intervals:	
timeSeries Path \$tag -time {list_of_times} -values {list_of_values} <-factor \$cFactor> <-useLast>	
For a load path where both time and values are specified in a list included in the command	
timeSeries Path \$tag -fileTime \$fileTime -filePath \$filePath <-factor \$cFactor> <-useLast>	
\$tag	unique tag among TimeSeries objects.
\$filePath	file containing the load factors values
\$fileTime	file containing the time values for corresponding load factors
\$dt	time interval between specified points.
{ list_of_times }	time values in a tcl list
{ list_of_values }	load factor values in a tcl list
\$cFactor	optional, a factor to multiply load factors by (default = 1.0)
-useLast	optional, to use last value after the end of the series (default = 0.0)
-prependZero	optional, to prepend a zero value to the series of load factors (default = false). See NOTES.
\$tStart	optional, to provide a start time for provided load factors (default = 0.0)

Figure A-22. *timeSeries* path command parameters [32].

pattern UniformExcitation \$patternTag \$dir -accel \$stsTag <-vel0 \$vel0> <-fact \$cFactor>	
\$patternTag	unique tag among load patterns
\$dir	direction in which ground motion acts 1 - corresponds to translation along the global X axis 2 - corresponds to translation along the global Y axis 3 - corresponds to translation along the global Z axis 4 - corresponds to rotation about the global X axis 5 - corresponds to rotation about the global Y axis 6 - corresponds to rotation about the global Z axis
\$stsTag	tag of the TimeSeries series defining the acceleration history.
\$vel0	the initial velocity (optional, default=0.0)
\$cFactor	constant factor (optional, default=1.0)

Figure A-23. *UniformExcitation* pattern command parameters [32].

APPENDIX B: SELECTED SCRIPTS FROM OPENSEES INPUT FILE

This Appendix provides selected, but detailed, scripts from a sample OpenSees TCL file for modeling and analyzing a full HSR bridge system. The input files for a given bridge configuration and various train positions over the bridge vary from 17,000 to 18,000 lines and could be provided upon request from the author. Nonetheless, the provided scripts herein should be sufficient to reproduce or generate full input files.

```
# Right Track and Left Track Center Line (Looking in the positive x-direction)
set R 3; # Track 1 (Right)
set L -3; # Track 2 (Left)

# Distance between train wheels in the y-direction
set wr 2

# Train Wheel Distance, Wheels are 2 m apart
set R1 [expr $R + $wr/2]; # Rail 1 (Right) in the Track 1
set R2 [expr $R - $wr/2]; # Rail 2 (Left) in the Track 1
set R3 [expr $L + $wr/2]; # Rail 3 (Right) in the Track 2
set R4 [expr $L - $wr/2]; # Rail 4 (Left) in the Track 2

# Rail Height
set hr 16.59; # Column height of 13.5 m + Girder depth of 3.09 m

# Train Vertical Dimensions
set hpm 1.720; # Height of centroid: Power car
set hcm 1.627; # Height of centroid: Passenger car
set hb 0.560; # Height of bogie COM assumption
set hp 0.605; # Vertical distance from top of primary suspension to power car-body COM (Given in reference study)
set hm 0.420; # Vertical distance from top of primary suspension to extreme passenger car-body COM (Given in reference study)
set hc 0.508; # Vertical distance from top of primary suspension to intermediate passenger car-body COM (Given in reference study)

# Train Longitudinal Dimensions
set Lp 14.000; # Length of power car (Given in reference study)
set Lm 18.700; # Length of extreme passenger car (Given in reference study)
set Lc 18.700; # Length of intermediate passenger car (Given in reference study)
set LT 193.150; # Total length of train system

set w 3.000; # Distance between same bogie axle wheels in the x-direction (Given in reference study)
set wp 3.275; # Distance between the power car axle wheel and extreme passenger car axle wheel (Given in reference study)
set x 30.815; # Location of last axle wheel node relative to start of bridge, depends on load case
```

Figure B-1. Predefined geometric locations for train nodes.

# Power Car					
#	NodeTag	(X)	(Y)	(Z)	
node	70011	$\$x$	$\$R1$	$\$hr;$	# Wheel for bogie 1
node	70012	$[\text{expr } \$x + \$w]$	$\$R1$	$\$hr;$	# Wheel for bogie 1
node	80011	$\$x$	$\$R2$	$\$hr;$	# Wheel for bogie 1
node	80012	$[\text{expr } \$x + \$w]$	$\$R2$	$\$hr;$	# Wheel for bogie 1
node	71011	$\$x$	$\$R1$	$[\text{expr } \$hr + \$hb];$	# Bogie 1
node	71012	$[\text{expr } \$x + \$w/2]$	$\$R1$	$[\text{expr } \$hr + \$hb];$	# Bogie 1
node	71013	$[\text{expr } \$x + \$w]$	$\$R1$	$[\text{expr } \$hr + \$hb];$	# Bogie 1
node	610012	$[\text{expr } \$x + \$w/2]$	$\$R$	$[\text{expr } \$hr + \$hb];$	# Bogie 1
node	81011	$\$x$	$\$R2$	$[\text{expr } \$hr + \$hb];$	# Bogie 1
node	81012	$[\text{expr } \$x + \$w/2]$	$\$R2$	$[\text{expr } \$hr + \$hb];$	# Bogie 1
node	81013	$[\text{expr } \$x + \$w]$	$\$R2$	$[\text{expr } \$hr + \$hb];$	# Bogie 1
node	620012	$[\text{expr } \$x + \$w/2]$	$\$R$	$[\text{expr } \$hr + \$hpm - \$hp];$	# Primary Suspension for bogie 1
node	720012	$[\text{expr } \$x + \$w/2]$	$\$R1$	$[\text{expr } \$hr + \$hpm - \$hp];$	# Primary Suspension for bogie 1
node	820012	$[\text{expr } \$x + \$w/2]$	$\$R2$	$[\text{expr } \$hr + \$hpm - \$hp];$	# Primary Suspension for bogie 1
node	70021	$[\text{expr } \$x + \$Lp]$	$\$R1$	$\$hr;$	# Wheel for bogie 2
node	70022	$[\text{expr } \$x + (\$Lp + \$w)]$	$\$R1$	$\$hr;$	# Wheel for bogie 2
node	80021	$[\text{expr } \$x + \$Lp]$	$\$R2$	$\$hr;$	# Wheel for bogie 2
node	80022	$[\text{expr } \$x + (\$Lp + \$w)]$	$\$R2$	$\$hr;$	# Wheel for bogie 2
node	71021	$[\text{expr } \$x + \$Lp]$	$\$R1$	$[\text{expr } \$hr + \$hb];$	# Bogie 2
node	71022	$[\text{expr } \$x + \$Lp + \$w/2]$	$\$R1$	$[\text{expr } \$hr + \$hb];$	# Bogie 2
node	71023	$[\text{expr } \$x + (\$Lp + \$w)]$	$\$R1$	$[\text{expr } \$hr + \$hb];$	# Bogie 2
node	610022	$[\text{expr } \$x + \$Lp + \$w/2]$	$\$R$	$[\text{expr } \$hr + \$hb];$	# Bogie 2
node	81021	$[\text{expr } \$x + \$Lp]$	$\$R2$	$[\text{expr } \$hr + \$hb];$	# Bogie 2
node	81022	$[\text{expr } \$x + \$Lp + \$w/2]$	$\$R2$	$[\text{expr } \$hr + \$hb];$	# Bogie 2
node	81023	$[\text{expr } \$x + (\$Lp + \$w)]$	$\$R2$	$[\text{expr } \$hr + \$hb];$	# Bogie 2
node	620022	$[\text{expr } \$x + \$Lp + \$w/2]$	$\$R$	$[\text{expr } \$hr + \$hpm - \$hp];$	# Primary Suspension for bogie 2
node	720022	$[\text{expr } \$x + \$Lp + \$w/2]$	$\$R1$	$[\text{expr } \$hr + \$hpm - \$hp];$	# Primary Suspension for bogie 2
node	820022	$[\text{expr } \$x + \$Lp + \$w/2]$	$\$R2$	$[\text{expr } \$hr + \$hpm - \$hp];$	# Primary Suspension for bogie 2
node	63001	$[\text{expr } \$x + \$w/2]$	$\$R$	$[\text{expr } \$hr + \$hpm];$	# Car Body 1
node	63002	$[\text{expr } \$x + \$w/2 + \$Lp/2]$	$\$R$	$[\text{expr } \$hr + \$hpm];$	# Car Body 1 (COM)
node	63003	$[\text{expr } \$x + \$Lp + \$w/2]$	$\$R$	$[\text{expr } \$hr + \$hpm];$	# Car Body 1

Figure B-2. Node set up for rear power car.

# Extreme Passenger Car					
#	NodeTag	(X)	(Y)	(Z)	
node	70031	$[\text{expr } \$x + (\$Lp + \$w + \$wp)]$	$\$R1$	$\$hr;$	# Wheel for bogie 3
node	70032	$[\text{expr } \$x + (\$Lp + 2*\$w + \$wp)]$	$\$R1$	$\$hr;$	# Wheel for bogie 3
node	80031	$[\text{expr } \$x + (\$Lp + \$w + \$wp)]$	$\$R2$	$\$hr;$	# Wheel for bogie 3
node	80032	$[\text{expr } \$x + (\$Lp + 2*\$w + \$wp)]$	$\$R2$	$\$hr;$	# Wheel for bogie 3
node	71031	$[\text{expr } \$x + (\$Lp + \$w + \$wp)]$	$\$R1$	$[\text{expr } \$hr + \$hb];$	# Bogie 3
node	71032	$[\text{expr } \$x + (\$Lp + \$w + \$wp) + \$w/2]$	$\$R1$	$[\text{expr } \$hr + \$hb];$	# Bogie 3
node	71033	$[\text{expr } \$x + (\$Lp + 2*\$w + \$wp)]$	$\$R1$	$[\text{expr } \$hr + \$hb];$	# Bogie 3
node	610032	$[\text{expr } \$x + (\$Lp + \$w + \$wp) + \$w/2]$	$\$R$	$[\text{expr } \$hr + \$hb];$	# Bogie 3
node	81031	$[\text{expr } \$x + (\$Lp + \$w + \$wp)]$	$\$R2$	$[\text{expr } \$hr + \$hb];$	# Bogie 3
node	81032	$[\text{expr } \$x + (\$Lp + \$w + \$wp) + \$w/2]$	$\$R2$	$[\text{expr } \$hr + \$hb];$	# Bogie 3
node	81033	$[\text{expr } \$x + (\$Lp + 2*\$w + \$wp)]$	$\$R2$	$[\text{expr } \$hr + \$hb];$	# Bogie 3
node	70041	$[\text{expr } \$x + (\$Lp + \$w + \$wp + \$Lm)]$	$\$R1$	$\$hr;$	# Wheel for bogie 4
node	80041	$[\text{expr } \$x + (\$Lp + \$w + \$wp + \$Lm)]$	$\$R2$	$\$hr;$	# Wheel for bogie 4
node	71041	$[\text{expr } \$x + (\$Lp + \$w + \$wp + \$Lm)]$	$\$R1$	$[\text{expr } \$hr + \$hb];$	# Bogie 4
node	81041	$[\text{expr } \$x + (\$Lp + \$w + \$wp + \$Lm)]$	$\$R2$	$[\text{expr } \$hr + \$hb];$	# Bogie 4
node	620032	$[\text{expr } \$x + (\$Lp + \$w + \$wp) + \$w/2]$	$\$R$	$[\text{expr } \$hr + \$hcm - \$hm];$	# Primary Suspension for bogie 3
node	720032	$[\text{expr } \$x + (\$Lp + \$w + \$wp) + \$w/2]$	$\$R1$	$[\text{expr } \$hr + \$hcm - \$hm];$	# Primary Suspension for bogie 3
node	820032	$[\text{expr } \$x + (\$Lp + \$w + \$wp) + \$w/2]$	$\$R2$	$[\text{expr } \$hr + \$hcm - \$hm];$	# Primary Suspension for bogie 3
node	63004	$[\text{expr } \$x + (\$Lp + \$w + \$wp) + \$w/2]$	$\$R$	$[\text{expr } \$hr + \$hcm];$	# Car Body 2
node	63005	$[\text{expr } \$x + (\$Lp + \$w + \$wp) + \$Lm/2]$	$\$R$	$[\text{expr } \$hr + \$hcm];$	# Car Body 2 (COM)

Figure B-3. Node set up for rear intermediate passenger car.

```

# Intermediate Passenger Cars
set n 1
# NodeTag (X) (Y) (Z)
node 70042 [expr $x + ($lp + $w + $wp + $lm) + ($n)*3 + ($n-1)*($lc - $w)] $R1 $hr; # Wheel for bogie 4
node 70051 [expr $x + ($lp + $w + $wp + $lm) + ($n)*3 + ($n)*($lc - $w)] $R1 $hr; # Wheel for bogie 5
node 80042 [expr $x + ($lp + $w + $wp + $lm) + ($n)*3 + ($n-1)*($lc - $w)] $R2 $hr; # Wheel for bogie 4
node 80051 [expr $x + ($lp + $w + $wp + $lm) + ($n)*3 + ($n)*($lc - $w)] $R2 $hr; # Wheel for bogie 5
node 71042 [expr $x + ($lp + $w + $wp + $lm) + ($n)*3 + ($n-1)*($lc - $w) - $w/2] $R1 [expr $hr + $hb]; # Bogie 4
node 71043 [expr $x + ($lp + $w + $wp + $lm) + ($n)*3 + ($n-1)*($lc - $w)] $R1 [expr $hr + $hb]; # Bogie 4
node 610042 [expr $x + ($lp + $w + $wp + $lm) + ($n)*3 + ($n-1)*($lc - $w) - $w/2] $R [expr $hr + $hb]; # Bogie 4
node 81042 [expr $x + ($lp + $w + $wp + $lm) + ($n)*3 + ($n-1)*($lc - $w) - $w/2] $R2 [expr $hr + $hb]; # Bogie 4
node 81043 [expr $x + ($lp + $w + $wp + $lm) + ($n)*3 + ($n-1)*($lc - $w)] $R2 [expr $hr + $hb]; # Bogie 4
node 71051 [expr $x + ($lp + $w + $wp + $lm) + ($n)*3 + ($n)*($lc - $w)] $R1 [expr $hr + $hb]; # Bogie 5
node 81051 [expr $x + ($lp + $w + $wp + $lm) + ($n)*3 + ($n)*($lc - $w)] $R2 [expr $hr + $hb]; # Bogie 5
node 620042 [expr $x + ($lp + $w + $wp + $lm) + ($n)*3 + ($n-1)*($lc - $w) - $w/2] $R [expr $hr + $hcm - $hc]; # Primary Suspension for bogie 4
node 720042 [expr $x + ($lp + $w + $wp + $lm) + ($n)*3 + ($n-1)*($lc - $w) - $w/2] $R1 [expr $hr + $hcm - $hc]; # Primary Suspension for bogie 4
node 820042 [expr $x + ($lp + $w + $wp + $lm) + ($n)*3 + ($n-1)*($lc - $w) - $w/2] $R2 [expr $hr + $hcm - $hc]; # Primary Suspension for bogie 4
node 63006 [expr $x + ($lp + $w + $wp + $lm) + ($n)*3 + ($n-1)*($lc - $w) - $w/2] $R [expr $hr + $hcm]; # Car Body 2 & 3 (Articulated)
node 63007 [expr $x + ($lp + $w + $wp + $lm) + ($n)*3 + ($n-1)*($lc - $w) - $w/2 + $lc/2] $R [expr $hr + $hcm]; # Car Body 3 (COM)

```

Figure B-4. Node set up for first intermediate passenger car.

```

set Ar 1e3
set Ir 1e5
set Er 1e8
set Gr 1e8
set Jr 1e6

# Bogie arms in the x-direction
#
# element eleTag iNode jNode A E G J Iy Iz transfTag
element elasticBeamColumn 30001 71011 71012 $Ar $Er $Gr $Jr $Ir $Ir $geomTransf
element elasticBeamColumn 30002 71012 71013 $Ar $Er $Gr $Jr $Ir $Ir $geomTransf

```

Figure B-5. Rigid elastic beam-column element for bogie arms in the x-direction.

```

# Bogie arms in the y-direction
#
# element eleTag iNode jNode A E G J Iy Iz transfTag
element elasticBeamColumn 30087 71012 610012 $Ar $Er $Gr $Jr $Ir $Ir $geomTransf
element elasticBeamColumn 30088 610012 81012 $Ar $Er $Gr $Jr $Ir $Ir $geomTransf

```

Figure B-6. Rigid elastic beam-column element for bogie arms in the y-direction.

```

# Primary Suspension arms in the y-direction
#
# element eleTag iNode jNode A E G J Iy Iz transfTag
element elasticBeamColumn 30122 620012 720012 $Ar $Er $Gr $Jr $Ir $Ir $geomTransf
element elasticBeamColumn 30123 620012 820012 $Ar $Er $Gr $Jr $Ir $Ir $geomTransf

```

Figure B-7. Rigid elastic beam-column element for primary suspension arms in the y-direction.

```

# Connection for car-body ends to Primary Suspension system in the z-direction
#
# element eleTag iNode jNode A E G J Iy Iz transfTag
element elasticBeamColumn 30074 620012 63001 $Ar $Er $Gr $Jr $Ir $Ir $geomTransf
element elasticBeamColumn 30075 620022 63003 $Ar $Er $Gr $Jr $Ir $Ir $geomTransf

```

Figure B-8. Rigid elastic beam-column element for primary suspension arms in the z-direction.

```

# Connecting car-bodies in the x-direction
# All car-bodies except the power cars are connected due to the articulated bogie system
#
# element eleTag iNode jNode A E G J Iy Iz transfTag
element elasticBeamColumn 30053 63001 63002 $Ar $Er $Gr $Jr $Ir $Ir $geomTransf
element elasticBeamColumn 30054 63002 63003 $Ar $Er $Gr $Jr $Ir $Ir $geomTransf
element elasticBeamColumn 30055 63004 63005 $Ar $Er $Gr $Jr $Ir $Ir $geomTransf
element elasticBeamColumn 30056 63005 63006 $Ar $Er $Gr $Jr $Ir $Ir $geomTransf
element elasticBeamColumn 30057 63006 63007 $Ar $Er $Gr $Jr $Ir $Ir $geomTransf

```

Figure B-9. Rigid elastic beam-column element for car-bodies.

```

# Power Car
set Kapx 40000
set Kapy 9000
set Kapz 1250

set Capz 10

# Stiffness
uniaxialMaterial Elastic 40 $Kapx; # x-direction
uniaxialMaterial Elastic 41 $Kapy; # y-direction
uniaxialMaterial Elastic 42 $Kapz; # z-direction
# Damping
uniaxialMaterial ViscousDamper 43 0 $Capz 0.01; # z-direction
# Combined
uniaxialMaterial Parallel 44 42 43; # z-direction

#
# eleTag iNode jNode matTag... dir... orient...
element twoNodeLink 301262 71011 70011 -mat 40 41 44 -dir 1 2 3 -orient 1 0 0 0 1 0
element twoNodeLink 301263 71013 70012 -mat 40 41 44 -dir 1 2 3 -orient 1 0 0 0 1 0
element twoNodeLink 301264 71021 70021 -mat 40 41 44 -dir 1 2 3 -orient 1 0 0 0 1 0
element twoNodeLink 301265 71023 70022 -mat 40 41 44 -dir 1 2 3 -orient 1 0 0 0 1 0

element twoNodeLink 301370 81011 80011 -mat 40 41 44 -dir 1 2 3 -orient 1 0 0 0 1 0
element twoNodeLink 301371 81013 80012 -mat 40 41 44 -dir 1 2 3 -orient 1 0 0 0 1 0
element twoNodeLink 301372 81021 80021 -mat 40 41 44 -dir 1 2 3 -orient 1 0 0 0 1 0
element twoNodeLink 301373 81023 80022 -mat 40 41 44 -dir 1 2 3 -orient 1 0 0 0 1 0

element twoNodeLink 301366 71121 70121 -mat 40 41 44 -dir 1 2 3 -orient 1 0 0 0 1 0
element twoNodeLink 301367 71123 70122 -mat 40 41 44 -dir 1 2 3 -orient 1 0 0 0 1 0
element twoNodeLink 301368 71131 70131 -mat 40 41 44 -dir 1 2 3 -orient 1 0 0 0 1 0
element twoNodeLink 301369 71133 70132 -mat 40 41 44 -dir 1 2 3 -orient 1 0 0 0 1 0

element twoNodeLink 301374 81121 80121 -mat 40 41 44 -dir 1 2 3 -orient 1 0 0 0 1 0
element twoNodeLink 301375 81123 80122 -mat 40 41 44 -dir 1 2 3 -orient 1 0 0 0 1 0
element twoNodeLink 301476 81131 80131 -mat 40 41 44 -dir 1 2 3 -orient 1 0 0 0 1 0
element twoNodeLink 301477 81133 80132 -mat 40 41 44 -dir 1 2 3 -orient 1 0 0 0 1 0

```

Figure B-10. Primary suspension system model for the power cars.

```

# Constraining the other DOFs
#
# iNode jNode DOFs...
equalDOF 71011 70011 4 5 6
equalDOF 71013 70012 4 5 6
equalDOF 71021 70021 4 5 6
equalDOF 71023 70022 4 5 6

equalDOF 81011 80011 4 5 6
equalDOF 81013 80012 4 5 6
equalDOF 81021 80021 4 5 6
equalDOF 81023 80022 4 5 6

equalDOF 71121 70121 4 5 6
equalDOF 71123 70122 4 5 6
equalDOF 71131 70131 4 5 6
equalDOF 71133 70132 4 5 6

equalDOF 81121 80121 4 5 6
equalDOF 81123 80122 4 5 6
equalDOF 81131 80131 4 5 6
equalDOF 81133 80132 4 5 6

```

Figure B-11. Power car primary suspension node MP-constraints with *equalDOF*.

```

# Power Car
set Kpx      303
set Kpy      303
set Kpz      1270

set Cpy      100
set Cpz      20
set Cpphi    4230

# Stiffness
uniaxialMaterial Elastic      10  $Kpx;          # x-direction
uniaxialMaterial Elastic      11  $Kpy;          # y-direction
uniaxialMaterial Elastic      12  $Kpz;          # z-direction
uniaxialMaterial Elastic      13  1;            # rz-direction
# Damping
uniaxialMaterial ViscousDamper 14  0  $Cpy  0.01;  # y-direction
uniaxialMaterial ViscousDamper 15  0  $Cpz  0.01;  # z-direction
uniaxialMaterial ViscousDamper 16  0  $Cpphi 0.01;  # rz-direction
# Combined
uniaxialMaterial Parallel      17  11  14;        # y-direction
uniaxialMaterial Parallel      18  12  15;        # z-direction
uniaxialMaterial Parallel      19  13  16;        # rz-direction

#
# eleTag  iNode  jNode  matTag...  dir...  orient...
element twoNodeLink 300002 71012 720012 -mat 10 17 18 -dir 1 2 3 -orient 1 0 0 0 1 0
element twoNodeLink 300001 610012 620012 -mat 19 -dir 6 -orient 1 0 0 0 1 0
element twoNodeLink 300003 81012 820012 -mat 10 17 18 -dir 1 2 3 -orient 1 0 0 0 1 0

element twoNodeLink 300005 71022 720022 -mat 10 17 18 -dir 1 2 3 -orient 1 0 0 0 1 0
element twoNodeLink 300004 610022 620022 -mat 19 -dir 6 -orient 1 0 0 0 1 0
element twoNodeLink 300006 81022 820022 -mat 10 17 18 -dir 1 2 3 -orient 1 0 0 0 1 0

element twoNodeLink 300008 71122 720122 -mat 10 17 18 -dir 1 2 3 -orient 1 0 0 0 1 0
element twoNodeLink 300007 610122 620122 -mat 19 -dir 6 -orient 1 0 0 0 1 0
element twoNodeLink 300009 81122 820122 -mat 10 17 18 -dir 1 2 3 -orient 1 0 0 0 1 0

element twoNodeLink 300011 71132 720132 -mat 10 17 18 -dir 1 2 3 -orient 1 0 0 0 1 0
element twoNodeLink 300010 610132 620132 -mat 19 -dir 6 -orient 1 0 0 0 1 0
element twoNodeLink 300012 81132 820132 -mat 10 17 18 -dir 1 2 3 -orient 1 0 0 0 1 0

```

Figure B-12. Secondary suspension system model for the power cars.

```

# Constraining the other DOFs
#
# iNode  jNode  DOFs...
equalDOF 71012 720012 4 5 6
equalDOF 610012 620012 1 2 3 4 5
equalDOF 81012 820012 4 5 6

equalDOF 71022 720022 4 5 6
equalDOF 610022 620022 1 2 3 4 5
equalDOF 81022 820022 4 5 6

equalDOF 71122 720122 4 5 6
equalDOF 610122 620122 1 2 3 4 5
equalDOF 81122 820122 4 5 6

equalDOF 71132 720132 4 5 6
equalDOF 610132 620132 1 2 3 4 5
equalDOF 81132 820132 4 5 6

```

Figure B-13. Power car secondary suspension node MP-constraints with *equalDOF*.

```

# Car Body

# Power Car
set mass 54.960
set massxx 59.4
set massyy 1132.8
set masszz 1112.9

#      nodeTag  ndf1  ndf2  ndf3  ndf4  ndf5  ndf6
mass  63002  $mass  $mass  $mass  $massxx  $massyy  $masszz
mass  63022  $mass  $mass  $mass  $massxx  $massyy  $masszz

# Extreme Passenger Car
set mass 26.000
set massxx 33.94
set massyy 971.81
set masszz 971.81

#      nodeTag  ndf1  ndf2  ndf3  ndf4  ndf5  ndf6
mass  63005  $mass  $mass  $mass  $massxx  $massyy  $masszz
mass  63019  $mass  $mass  $mass  $massxx  $massyy  $masszz

# Intermediate Passenger Car
#      nodeTag  ndf1  ndf2  ndf3  ndf4  ndf5  ndf6
mass  63007  $mass  $mass  $mass  $massxx  $massyy  $masszz
mass  63009  $mass  $mass  $mass  $massxx  $massyy  $masszz
mass  63011  $mass  $mass  $mass  $massxx  $massyy  $masszz
mass  63013  $mass  $mass  $mass  $massxx  $massyy  $masszz
mass  63015  $mass  $mass  $mass  $massxx  $massyy  $masszz
mass  63017  $mass  $mass  $mass  $massxx  $massyy  $masszz

```

Figure B-14. Mass assignment for train car-bodies.

```

# Bogie

# Power Car
set mass 2.420
set massxx 1.645
set massyy 2.593
set masszz 3.068

#      nodeTag  ndf1  ndf2  ndf3  ndf4  ndf5  ndf6
mass  610012  $mass  $mass  $mass  $massxx  $massyy  $masszz
mass  610022  $mass  $mass  $mass  $massxx  $massyy  $masszz
mass  610122  $mass  $mass  $mass  $massxx  $massyy  $masszz
mass  610132  $mass  $mass  $mass  $massxx  $massyy  $masszz

# Extreme Passenger Car
set mass 2.514
set massxx 2.07
set massyy 3.26
set masszz 3.86

#      nodeTag  ndf1  ndf2  ndf3  ndf4  ndf5  ndf6
mass  610032  $mass  $mass  $mass  $massxx  $massyy  $masszz
mass  610112  $mass  $mass  $mass  $massxx  $massyy  $masszz

# Intermediate Passenger Car
set mass 3.050
set massxx 2.03
set massyy 3.20
set masszz 3.79

#      nodeTag  ndf1  ndf2  ndf3  ndf4  ndf5  ndf6
mass  610042  $mass  $mass  $mass  $massxx  $massyy  $masszz
mass  610052  $mass  $mass  $mass  $massxx  $massyy  $masszz
mass  610062  $mass  $mass  $mass  $massxx  $massyy  $masszz
mass  610072  $mass  $mass  $mass  $massxx  $massyy  $masszz
mass  610082  $mass  $mass  $mass  $massxx  $massyy  $masszz
mass  610092  $mass  $mass  $mass  $massxx  $massyy  $masszz
mass  610102  $mass  $mass  $mass  $massxx  $massyy  $masszz

```

Figure B-15. Mass assignment for train bogies.

```

# Wheel

# Power and Extreme Passenger Car
set mass 1.025
set massxx 1.03
set massyy 0.0008
set masszz 1.03

#      nodeTag  ndf1  ndf2  ndf3  ndf4  ndf5  ndf6
mass  70011  $mass  $mass  $mass  $massxx  $massyy  $masszz
mass  70012  $mass  $mass  $mass  $massxx  $massyy  $masszz
mass  70021  $mass  $mass  $mass  $massxx  $massyy  $masszz
mass  70022  $mass  $mass  $mass  $massxx  $massyy  $masszz
mass  70031  $mass  $mass  $mass  $massxx  $massyy  $masszz
mass  70032  $mass  $mass  $mass  $massxx  $massyy  $masszz
mass  70111  $mass  $mass  $mass  $massxx  $massyy  $masszz
mass  70112  $mass  $mass  $mass  $massxx  $massyy  $masszz
mass  70121  $mass  $mass  $mass  $massxx  $massyy  $masszz
mass  70122  $mass  $mass  $mass  $massxx  $massyy  $masszz
mass  70131  $mass  $mass  $mass  $massxx  $massyy  $masszz
mass  70132  $mass  $mass  $mass  $massxx  $massyy  $masszz

mass  80011  $mass  $mass  $mass  $massxx  $massyy  $masszz
mass  80012  $mass  $mass  $mass  $massxx  $massyy  $masszz
mass  80021  $mass  $mass  $mass  $massxx  $massyy  $masszz
mass  80022  $mass  $mass  $mass  $massxx  $massyy  $masszz
mass  80031  $mass  $mass  $mass  $massxx  $massyy  $masszz
mass  80032  $mass  $mass  $mass  $massxx  $massyy  $masszz
mass  80111  $mass  $mass  $mass  $massxx  $massyy  $masszz
mass  80112  $mass  $mass  $mass  $massxx  $massyy  $masszz
mass  80121  $mass  $mass  $mass  $massxx  $massyy  $masszz
mass  80122  $mass  $mass  $mass  $massxx  $massyy  $masszz
mass  80131  $mass  $mass  $mass  $massxx  $massyy  $masszz
mass  80132  $mass  $mass  $mass  $massxx  $massyy  $masszz

```

Figure B-16. Mass assignment for power and exterior passenger car axle wheels.

```

# Intermediate Passenger Car
set mass 1.000
set massxx 1.03
set massyy 0.0008
set masszz 1.03

#      nodeTag  ndf1  ndf2  ndf3  ndf4  ndf5  ndf6
mass  70041  $mass  $mass  $mass  $massxx  $massyy  $masszz
mass  70042  $mass  $mass  $mass  $massxx  $massyy  $masszz
mass  70051  $mass  $mass  $mass  $massxx  $massyy  $masszz
mass  70052  $mass  $mass  $mass  $massxx  $massyy  $masszz
mass  70061  $mass  $mass  $mass  $massxx  $massyy  $masszz
mass  70062  $mass  $mass  $mass  $massxx  $massyy  $masszz
mass  70071  $mass  $mass  $mass  $massxx  $massyy  $masszz
mass  70072  $mass  $mass  $mass  $massxx  $massyy  $masszz
mass  70081  $mass  $mass  $mass  $massxx  $massyy  $masszz
mass  70082  $mass  $mass  $mass  $massxx  $massyy  $masszz
mass  70091  $mass  $mass  $mass  $massxx  $massyy  $masszz
mass  70092  $mass  $mass  $mass  $massxx  $massyy  $masszz
mass  70101  $mass  $mass  $mass  $massxx  $massyy  $masszz
mass  70102  $mass  $mass  $mass  $massxx  $massyy  $masszz

mass  80041  $mass  $mass  $mass  $massxx  $massyy  $masszz
mass  80042  $mass  $mass  $mass  $massxx  $massyy  $masszz
mass  80051  $mass  $mass  $mass  $massxx  $massyy  $masszz
mass  80052  $mass  $mass  $mass  $massxx  $massyy  $masszz
mass  80061  $mass  $mass  $mass  $massxx  $massyy  $masszz
mass  80062  $mass  $mass  $mass  $massxx  $massyy  $masszz
mass  80071  $mass  $mass  $mass  $massxx  $massyy  $masszz
mass  80072  $mass  $mass  $mass  $massxx  $massyy  $masszz
mass  80081  $mass  $mass  $mass  $massxx  $massyy  $masszz
mass  80082  $mass  $mass  $mass  $massxx  $massyy  $masszz
mass  80091  $mass  $mass  $mass  $massxx  $massyy  $masszz
mass  80092  $mass  $mass  $mass  $massxx  $massyy  $masszz
mass  80101  $mass  $mass  $mass  $massxx  $massyy  $masszz
mass  80102  $mass  $mass  $mass  $massxx  $massyy  $masszz

```

Figure B-17. Mass assignment for intermediate passenger car axle wheels .

```

# Rail 1
#      nodeTag      (x)      (y)      (z)
node   10001      0.000      $R1      $hr
node   10002      3.195      $R1      $hr
node   10003      6.390      $R1      $hr

```

Figure B-18. Node set up for rail 1 of track 1.

```

# Track 1 Base Plate
#      nodeTag      (x)      (y)      (z)
node   51001      0.000      $R      $hr
node   51002      3.195      $R      $hr

```

Figure B-19. Node set up for base plate of track 1.

```

# Track 1 Track Plate
#      nodeTag      (x)      (y)      (z)
node   52001      0.000      $R      $hr
node   52002      3.195      $R      $hr

```

Figure B-20. Node set up for track plate of track 1.

```

set Ar  7.75e-3; # Cross-Sectional Area (m2)
set Iyr 5e-6;   # Moment of Inertia 1 (m4)
set Izr 3.20e-5; # Moment of Inertia 2 (m4)
set Jr  2e-6;   # Torque (kN-m)
set Gr  8.05e6; # Shear Modulus (kN/m2)
set Er  2.06e8; # Modulus of Elasticity (kN/m2)

#
element elasticBeamColumn  9000  31001  31002  $Ar  $Er  $Gr  $Jr  $Iyr  $Izr  $geomTransf
element elasticBeamColumn  9001  31002  31003  $Ar  $Er  $Gr  $Jr  $Iyr  $Izr  $geomTransf

```

Figure B-21. Elastic beam-column element for rail 3 of track 2.

```

set Atp 5.10e-1; # Cross-Sectional Area (m2)
set Iztp 1.70e3; # Moment of Inertia 1 (m4)
set Iytp 2.76e-1; # Moment of Inertia 2 (m4)
set Jtp 6.8e-3; # Torque (kN-m)
set Gtp 1.48e7; # Shear Modulus (kN/m2)
set Etp 3.55e7; # Modulus of Elasticity (kN/m2)

#
element elasticBeamColumn  659  52001  52002  $Atp  $Etp  $Gtp  $Jtp  $Iytp  $Iztp  $geomTransf
element elasticBeamColumn  660  52002  52003  $Atp  $Etp  $Gtp  $Jtp  $Iytp  $Iztp  $geomTransf

```

Figure B-22. Elastic beam-column element for track plates of track 1.

```

set Abp 5.61e-1; # Cross-Sectional Area (m2)
set Izbp 1.69e-3; # Moment of Inertia 1 (m4)
set Iybp 4.06e-1; # Moment of Inertia 2 (m4)
set Jbp 6.74e-3; # Torque (kN-m)
set Gbp 1.25e7; # Shear Modulus (kN/m2)
set Ebp 3.00e7; # Modulus of Elasticity (kN/m2)

#
element elasticBeamColumn  441  51001  51002  $Abp  $Ebp  $Gbp  $Jbp  $Iybp  $Izbp  $geomTransf
element elasticBeamColumn  442  51002  51003  $Abp  $Ebp  $Gbp  $Jbp  $Iybp  $Izbp  $geomTransf

```

Figure B-23. Elastic beam-column element for base plates of track 1.

```

# Fastener
set Fyf 15
set dyf 0.002
set K1f [expr $Fyf/$dyf]

uniaxialMaterial Steel01 600 $Fyf $K1f 0.0

#


|                    | eleTag | iNode | jNode | -mat matTag1... | -dir dir1... |
|--------------------|--------|-------|-------|-----------------|--------------|
| element zeroLength | 1317   | 10001 | 11001 | -mat 600        | -dir 1       |
| element zeroLength | 1318   | 10002 | 11002 | -mat 600        | -dir 1       |


```

Figure B-24. Zero-length element for fastener

```

# Lateral Blocking
set Fyl 453
set dyl 0.002
set K1l [expr $Fyl/$dyl]

uniaxialMaterial Steel01 900 $Fyl $K1l 0.0

#


|                    | eleTag | iNode | jNode | -mat matTag1... | -dir dir1... |
|--------------------|--------|-------|-------|-----------------|--------------|
| element zeroLength | 1757   | 10001 | 11001 | -mat 900        | -dir 2       |
| element zeroLength | 1758   | 10002 | 11002 | -mat 900        | -dir 2       |


```

Figure B-25. Zero-length element for lateral blocking.

```

# CA Mortar Layer
set Fyca 41.5
set dyca 0.0005
set K1ca [expr $Fyca/$dyca]

uniaxialMaterial Steel01 500 $Fyca $K1ca 0.0

#


|                    | eleTag | iNode | jNode | -mat matTag1... | -dir dir1... |
|--------------------|--------|-------|-------|-----------------|--------------|
| element zeroLength | 1097   | 51001 | 52001 | -mat 500        | -dir 1       |
| element zeroLength | 1098   | 51002 | 52002 | -mat 500        | -dir 1       |


```

Figure B-26. Zero-length element for CA layer.

```

# Sliding Layer
set Fys 6
set dys 0.0005
set K1s [expr $Fys/$dys]

uniaxialMaterial Steel01 700 $Fys $K1s 0.0

#


|                    | eleTag | iNode | jNode | -mat matTag1... | -dir dir1... |
|--------------------|--------|-------|-------|-----------------|--------------|
| element zeroLength | 877    | 50001 | 51001 | -mat 700        | -dir 1       |
| element zeroLength | 878    | 50002 | 51002 | -mat 700        | -dir 1       |


```

Figure B-27. Zero-length element for sliding layer.

```

# Shear Reinforcement
set Fysr 22.5
set dysr 0.000075
set Klsr [expr $Fysr/$dysr]

uniaxialMaterial Steel01 800 $Fysr $Klsr 0.0

#
element zeroLength      eleTag  iNode  jNode  -mat matTag1...  -dir dir1...
element zeroLength      2197   50001  51001  -mat 800 800     -dir 1 2
element zeroLength      2198   50011  51011  -mat 800 800     -dir 1 2

```

Figure B-28. Zero-length element for shear reinforcement.

```

equalDOF 51001 52001 2 3 4 5 6
equalDOF 51002 52002 2 3 4 5 6

```

Figure B-29. CA layer node MP-constraints with *equalDOF*.

```

# Rail
set mass 0.1693
set massxx 0.0025
set massyy 0.1459
set masszz 0.1446

#
nodeTag  ndf1  ndf2  ndf3  ndf4  ndf5  ndf6
mass 11001 $mass $mass $mass $massxx $massyy $masszz
mass 11002 $mass $mass $mass $massxx $massyy $masszz

```

Figure B-30. Mass assignment for first two rail 1 nodes.

```

#      nodeTag      (x)      (y)      (z)
node  90001         0         0      $yg; # Span 1
node  90002        3.195         0      $yg
node  90003        6.390         0      $yg
node  90004        9.585         0      $yg
node  90005       12.780         0      $yg
node  90006       15.975         0      $yg
node  90007       19.170         0      $yg
node  90008       22.365         0      $yg
node  90009       25.560         0      $yg
node  90010       28.755         0      $yg
node  90011       31.950         0      $yg
node  90012       32.000         0      $yg; # 0.05 m gap

```

Figure B-31. Node set up for the first bridge girder span.

```

set Ad 9.06; # As given in Li et al.'s study
set Ed 2.45e7; # Decreased from 3.45e7 to be conservative
set Gd 1.44e7; # As given in Li et al.'s study
set Jd 22.6; # As given in Li et al.'s study
set Iyd [expr 0.7*11.0]; # Decreased by 30% to be conservative
set Izd [expr 0.7*94.8]; # Decreased by 30% to be conservative

# 1
element elasticBeamColumn 3311 90001 90002 $Ad $Ed $Gd $Jd $Iyd $Izd $geomTransf
element elasticBeamColumn 3312 90002 90003 $Ad $Ed $Gd $Jd $Iyd $Izd $geomTransf
element elasticBeamColumn 3313 90003 90004 $Ad $Ed $Gd $Jd $Iyd $Izd $geomTransf
element elasticBeamColumn 3314 90004 90005 $Ad $Ed $Gd $Jd $Iyd $Izd $geomTransf
element elasticBeamColumn 3315 90005 90006 $Ad $Ed $Gd $Jd $Iyd $Izd $geomTransf
element elasticBeamColumn 3316 90006 90007 $Ad $Ed $Gd $Jd $Iyd $Izd $geomTransf
element elasticBeamColumn 3317 90007 90008 $Ad $Ed $Gd $Jd $Iyd $Izd $geomTransf
element elasticBeamColumn 3318 90008 90009 $Ad $Ed $Gd $Jd $Iyd $Izd $geomTransf
element elasticBeamColumn 3319 90009 90010 $Ad $Ed $Gd $Jd $Iyd $Izd $geomTransf
element elasticBeamColumn 3320 90010 90011 $Ad $Ed $Gd $Jd $Iyd $Izd $geomTransf

# 2
element elasticBeamColumn 3322 90012 90013 $Ad $Ed $Gd $Jd $Iyd $Izd $geomTransf
element elasticBeamColumn 3323 90013 90014 $Ad $Ed $Gd $Jd $Iyd $Izd $geomTransf
element elasticBeamColumn 3324 90014 90015 $Ad $Ed $Gd $Jd $Iyd $Izd $geomTransf
element elasticBeamColumn 3325 90015 90016 $Ad $Ed $Gd $Jd $Iyd $Izd $geomTransf
element elasticBeamColumn 3326 90016 90017 $Ad $Ed $Gd $Jd $Iyd $Izd $geomTransf
element elasticBeamColumn 3327 90017 90018 $Ad $Ed $Gd $Jd $Iyd $Izd $geomTransf
element elasticBeamColumn 3328 90018 90019 $Ad $Ed $Gd $Jd $Iyd $Izd $geomTransf
element elasticBeamColumn 3329 90019 90020 $Ad $Ed $Gd $Jd $Iyd $Izd $geomTransf
element elasticBeamColumn 3330 90020 90021 $Ad $Ed $Gd $Jd $Iyd $Izd $geomTransf
element elasticBeamColumn 3331 90021 90022 $Ad $Ed $Gd $Jd $Iyd $Izd $geomTransf

```

Figure B-32. Example elastic beam-column elements for bridge girder.

```

# Nodes for Bridge Bearing
set Rb 2; # Right Side
set Lb -2; # Left Side
# Assume bearing distance 3.3m
#
# nodeTag (x) (y) (z)
node 1101 0.000 $Lb 13.500
node 1102 0.000 $Rb 13.500
node 1103 31.950 $Lb 13.500
node 1104 31.950 $Rb 13.500
node 2101 0.000 $Lb 13.500
node 2102 0.000 $Rb 13.500
node 2103 31.950 $Lb 13.500
node 2104 31.950 $Rb 13.500

```

Figure B-33. Node set up for bearings supporting the first span of the bridge.

```

# Fixed Bearing
set Fybear1 5000
set dybear1 0.002
set Klbear1 [expr $Fybear1/$dybear1]
uniaxialMaterial Steel01 300 $Fybear1 $Klbear1 0.0

#
# eleTag iNode jNode -mat matTag1... -dir dir1...
element zeroLength 3475 1101 2101 -mat 300 300 -dir 1 2
element zeroLength 3476 1103 2103 -mat 300 300 -dir 1 2
element zeroLength 3477 1106 2106 -mat 300 300 -dir 1 2
element zeroLength 3478 1108 2108 -mat 300 300 -dir 1 2

```

Figure B-34. Zero-length elements for fixed bearings supporting the first span of the bridge.

```

# Sliding Bearing
set Fybear2 470
set dybear2 0.002
set Klbear2 [expr $Fybear2/$dybear2]
uniaxialMaterial Steel01 400 $Fybear2 $Klbear2 0.0

#
element zeroLength 3495 1102 2102 -mat 400 400 -dir 1 2
element zeroLength 3496 1104 2104 -mat 400 400 -dir 1 2
element zeroLength 3497 1105 2105 -mat 400 400 -dir 1 2
element zeroLength 3498 1107 2107 -mat 400 400 -dir 1 2

```

Figure B-35. Zero-length elements for sliding bearings supporting the first span of the bridge.

```

# Constraining DOF for bearing nodes
equalDOF 1101 2101 3 4 5 6
equalDOF 1102 2102 3 4 5 6
equalDOF 1103 2103 3 4 5 6
equalDOF 1104 2104 3 4 5 6

```

Figure B-36. Bearing node MP-constraints with *equalDOF*.

```

# Nominal concrete compressive strength
set fc 28890; # Concrete compressive strength(KN/m2)
set nu 0.2; # Concrete Poisson's ratio
set Ec [expr 4700*sqrt($fc/1e3)*1e3]; # Concrete elastic modulus (KN/m2)
set Gc [expr $Ec/(2*(1+$nu))]; # Concrete shear modulus (KN/m2)

# Cover concrete (un-confined)
set fc1U $fc; # Unconfined concrete, maximum stress
set eps1U -0.003; # Strain at maximum strength of unconfined concrete
set fc2U [expr 0.2*$fc1U]; # Ultimate stress(KN/m2)
set eps2U -0.01; # Strain at ultimate stress
set lambda 0.1; # Ratio between unloading slope at $eps2 and initial slope $Ec

# Core concrete (confined)
set Kfc 1.3; # Ratio of confined to unconfined concrete strength
set fc1C [expr $Kfc*$fc]; # Confined concrete (Mander model), maximum stress(KN/m2)
set eps1C [expr 2.*$fc1C/$Ec]; # Strain at maximum stress
set fc2C [expr 0.2*$fc1C]; # Ultimate stress(KN/m2)
set eps2C [expr 5*$eps1C]; # Strain at ultimate stress

# Tensile-strength properties
set ftC [expr -0.14*$fc1C]; # Tensile strength + tension confined concrete(KN/m2)
set ftU [expr -0.14*$fc1U]; # Tensile strength + tension unconfined concrete(KN/m2)
set Ets [expr $ftU/0.002]; # Tension softening stiffness (KN/m2)

# Reinforcing steel
set fys 483510; # Reinforcing steel yield strength(KN/m2)
set fsu 725265; # Reinforcing steel ultimate strength(KN/m2)
set Es 200000000; # Reinforcing steel elastic modulus(KN/m2)
set b 0.005; # Strain-hardening ratio
set R0 15; # Parameters to control the transition from elastic to plastic branches
set cR1 0.925; # Parameters to control the transition from elastic to plastic branches
set cR2 0.15; # Parameters to control the transition from elastic to plastic branches

# General Cross-Section matTag E
uniaxialMaterial Elastic 5 1e10

# Cover Concrete matTag fpc epsc fpcu epsU lambda ft Ets
uniaxialMaterial Concrete02 1 $fc1C $eps1C $fc2C $eps2C $lambda $ftC $Ets

# Core Concrete matTag fpc epsc fpcu epsU lambda ft Ets
uniaxialMaterial Concrete02 2 $fc1U $eps1U $fc2U $eps2U $lambda $ftU $Ets

# Reinforcing Steel matTag Fy E b R0 cR1 cR2
uniaxialMaterial Steel02 3 $fys $Es $b $R0 $cR1 $cR2

```

Figure B-37. Material properties for pier columns.

```

# Cross-Section of Column
section Fiber 1 -GJ 0 {
# Cover concrete      tag      divY      divZ      yI      zI      yJ      zJ
patch rect          1      $divy     $divz     [expr -$ycol/2] [expr -$zcol/2] [expr $ycol/2] [expr $zcol/2]

# Core concrete      tag      divY      divZ      yI      zI      yJ      zJ
patch rect          2      [expr (2*$divy)] [expr (2*$divz)] $yy1 $zz1 $yy2 $zz2

# Reinforcing Steel  tag      Nbar      Abar      yStart   zStart   yEnd      zEnd
layer straight     3      $Nbar1    $Abar     $y1      $z1      $y5      $y5
layer straight     3      $Nbar1    $Abar     $y4      $z4      $y8      $y8
layer straight     3      $Nbar2    $Abar     $y2      $z2      $y3      $y3
layer straight     3      $Nbar2    $Abar     $y6      $z6      $y7      $y7
}

#
# secTag      matTag      dof1      sectionTag
section Aggregator 100      5      T      -section 1

```

Figure B-38. Section designer for pier cross-section.

```

set Dtran 12.7e-3; # Transverse reinforcement diameter (m)
set Abar 1006e-3; # Longitudinal reinforcement area (m2)
set Dbar 35.81e-3; # Longitudinal reinforcement diameter (m)
set Nbar1 28; # Number of bars on short end
set Nbar2 60; # Number of bars on long end
set cc 0.04; # Assumption of clear cover (m)
set ycol 5.434; # Y dimension of column (m)
set zcol 2.50; # Z dimension of column (m)
set divy 6; # Number of subdivisions in the local y-direction
set divz 3; # Number of subdivisions in the local z-direction
set s [expr (($ycol - 2*($cc + $Dtran) - $Dbar)/($Nbar2))]; # Spacing of bars in the y-direction (m)

# -----

# Coordinates within the column cross-section to define section
set yy1 [expr -($ycol/2 - ($cc + $Dtran))]
set zz1 [expr -($zcol/2 - ($cc + $Dtran))]
set yy2 [expr ($ycol/2 - ($cc + $Dtran))]
set zz2 [expr ($zcol/2 - ($cc + $Dtran))]

set y1 [expr -($ycol/2 - ($cc + $Dtran + 0.5*$Dbar))]
set z1 [expr -($zcol/2 - ($cc + $Dtran + 0.5*$Dbar))]
set y2 [expr -($ycol/2 - ($cc + $Dtran + 0.5*$Dbar-$s))]
set z2 $z1
set y3 [expr ($ycol/2 - ($cc + $Dtran + 0.5*$Dbar-$s))]
set z3 $z1
set y4 [expr ($ycol/2 - ($cc + $Dtran + 0.5*$Dbar))]
set z4 $z1
set y5 $y1
set z5 [expr ($zcol/2 - ($cc + $Dtran + 0.5*$Dbar))]
set y6 $y2
set z6 $z5
set y7 $y3
set z7 $z5
set y8 $y4
set z8 $z5

```

Figure B-39. Predefined geometric values for pier columns.

```

# Column 1
#      nodeTag      (x)      (y)      (z)
node   111      1.5975      0      0
node   112      1.5975      0      3.375
node   113      1.5975      0      6.75
node   114      1.5975      0      10.125
node   115      1.5975      0      13.5

# Column 2
#      nodeTag      (x)      (y)      (z)
node   211     33.5975      0      0
node   212     33.5975      0      3.375
node   213     33.5975      0      6.75
node   214     33.5975      0      10.125
node   215     33.5975      0      13.5

```

Figure B-40. Node set up for first two columns.

#		eleTag	iNode	jNode	numIntgrPts	secTag	transfTag
element	dispBeamColumn	3420	111	112	\$n	100	\$geomTransf
element	dispBeamColumn	3421	112	113	\$n	100	\$geomTransf
element	dispBeamColumn	3422	113	114	\$n	100	\$geomTransf
element	dispBeamColumn	3423	114	115	\$n	100	\$geomTransf

Figure B-41. Displacement-based fiber-section beam-column elements for first pier column.

```

# Footing Center-of-Mass
#      nodeTag      (x)      (y)      (z)
node   1         -0.025      0      $hf
node   2         31.975      0      $hf
node   3         63.975      0      $hf
node   4         95.975      0      $hf
node   5        127.975      0      $hf
node   6        159.975      0      $hf
node   7        191.975      0      $hf
node   8        223.975      0      $hf
node   9        255.975      0      $hf
node  10        287.975      0      $hf
node  11        319.975      0      $hf

# Ground (Fixed)
#      nodeTag      (x)      (y)      (z)
node  12         -0.025      0      $hf
node  13         31.975      0      $hf
node  14         63.975      0      $hf
node  15         95.975      0      $hf
node  16        127.975      0      $hf
node  17        159.975      0      $hf
node  18        191.975      0      $hf
node  19        223.975      0      $hf
node  20        255.975      0      $hf
node  21        287.975      0      $hf
node  22        319.975      0      $hf

```

Figure B-42. Node set up for column footings and ground.

```

fix 1      0  0  1  1  1  1
fix 2      0  0  1  1  1  1
fix 3      0  0  1  1  1  1
fix 4      0  0  1  1  1  1
fix 5      0  0  1  1  1  1
fix 6      0  0  1  1  1  1
fix 7      0  0  1  1  1  1
fix 8      0  0  1  1  1  1
fix 9      0  0  1  1  1  1
fix 10     0  0  1  1  1  1
fix 11     0  0  1  1  1  1

fix 12     1  1  1  1  1  1
fix 13     1  1  1  1  1  1
fix 14     1  1  1  1  1  1
fix 15     1  1  1  1  1  1
fix 16     1  1  1  1  1  1
fix 17     1  1  1  1  1  1
fix 18     1  1  1  1  1  1
fix 19     1  1  1  1  1  1
fix 20     1  1  1  1  1  1
fix 21     1  1  1  1  1  1
fix 22     1  1  1  1  1  1

```

Figure B-43. Column footings and ground node SP-constraints using *fix*.

```

set KGh 155440.00
uniaxialMaterial Elastic 9 $KGh

set KGr 0.000000
uniaxialMaterial Elastic 8 $KGr

#
element zeroLength 3464 12 1 -mat 9 9 8 8 -dir 1 2
element zeroLength 3465 13 2 -mat 9 9 8 8 -dir 1 2
element zeroLength 3466 14 3 -mat 9 9 8 8 -dir 1 2
element zeroLength 3467 15 4 -mat 9 9 8 8 -dir 1 2
element zeroLength 3468 16 5 -mat 9 9 8 8 -dir 1 2
element zeroLength 3469 17 6 -mat 9 9 8 8 -dir 1 2
element zeroLength 3470 18 7 -mat 9 9 8 8 -dir 1 2
element zeroLength 3471 19 8 -mat 9 9 8 8 -dir 1 2
element zeroLength 3472 20 9 -mat 9 9 8 8 -dir 1 2
element zeroLength 3473 21 10 -mat 9 9 8 8 -dir 1 2
element zeroLength 3474 22 11 -mat 9 9 8 8 -dir 1 2

```

Figure B-44. Zero-length element for bridge-soil interaction.

```

# Footing Elements
#
element elasticBeamColumn 3000 1 111 $Ar $Er $Gr $Jr $Ir $Iz $geomTransf
element elasticBeamColumn 3001 2 211 $Ar $Er $Gr $Jr $Ir $Iz $geomTransf

```

Figure B-45. Rigid elastic beam-column element for footings of columns #1 and #2.

```

# Column-Bearing Connecting Elements
#
element elasticBeamColumn 3011 115 1101 $Ar $Er $Gr $Jr $Ir $Iz $geomTransf
element elasticBeamColumn 3012 1102 115 $Ar $Er $Gr $Jr $Ir $Iz $geomTransf

```

Figure B-46. Rigid elastic beam-column element for column-bearing connections at column #1.

```

# Girder-Bearing Connecting Elements
#
element elasticBeamColumn 3051 90001 2101 $Ar $Er $Gr $Jr $Ir $Iz $geomTransf
element elasticBeamColumn 3052 2102 90001 $Ar $Er $Gr $Jr $Ir $Iz $geomTransf

```

Figure B-47. Rigid elastic beam-column element for girder-bearing connections above column #1.

```

# Girder-Track System Connecting Elements
#
element elasticBeamColumn 3091 90001 50001 $Ar $Er $Gr $Jr $Ir $Iz $geomTransf
element elasticBeamColumn 3092 90002 50002 $Ar $Er $Gr $Jr $Ir $Iz $geomTransf

```

Figure B-48. Rigid elastic beam-column element for first two girder-track system connections.

```

# Girder
set mass 63.7359
set massxx 159.1817
set massyy 61.1692
set masszz 189.1868

#      nodeTag  ndf1  ndf2  ndf3  ndf4  ndf5  ndf6
mass  90001  $mass  $mass  $mass  $massxx  $massyy  $masszz
mass  90002  $mass  $mass  $mass  $massxx  $massyy  $masszz

```

Figure B-49. Mass assignment for first two nodes of bridge girder.

```

# Column
set mass 88.0308
set massxx 300.1776
set massyy 129.4099
set masszz 262.4664

#      nodeTag  ndf1  ndf2  ndf3  ndf4  ndf5  ndf6
mass  111  $mass  $mass  $mass  $massxx  $massyy  $masszz
mass  112  $mass  $mass  $mass  $massxx  $massyy  $masszz

```

Figure B-50. Mass assignment for first two nodes of column #1.

```

# Footing
set mass 629.7408
set massxx 7859.6900
set massyy 7859.6900
set masszz 14122.9870

#      nodeTag  ndf1  ndf2  ndf3  ndf4  ndf5  ndf6
mass  1  $mass  $mass  $mass  $massxx  $massyy  $masszz
mass  2  $mass  $mass  $mass  $massxx  $massyy  $masszz

```

Figure B-51. Mass assignment for footings of column #1 and #2.

# Power Car Body Loads							
#	Node	X	Y	Z	Mx	My	Mz
load	63002	0.000	0.000	-539.158	0.000	0.000	0.000
load	63022	0.000	0.000	-539.158	0.000	0.000	0.000
# Extreme Passenger Car Body Loads							
#	Node	X	Y	Z	Mx	My	Mz
load	63005	0.000	0.000	-255.060	0.000	0.000	0.000
load	63019	0.000	0.000	-255.060	0.000	0.000	0.000
# Intermediate Passenger Car Body Loads							
#	Node	X	Y	Z	Mx	My	Mz
load	63007	0.000	0.000	-255.060	0.000	0.000	0.000
load	63009	0.000	0.000	-255.060	0.000	0.000	0.000
load	63011	0.000	0.000	-255.060	0.000	0.000	0.000
load	63013	0.000	0.000	-255.060	0.000	0.000	0.000
load	63015	0.000	0.000	-255.060	0.000	0.000	0.000
load	63017	0.000	0.000	-255.060	0.000	0.000	0.000
# Power Car Bogie Loads							
#	Node	X	Y	Z	Mx	My	Mz
load	610012	0.000	0.000	-23.740	0.000	0.000	0.000
load	610022	0.000	0.000	-23.740	0.000	0.000	0.000
load	610122	0.000	0.000	-23.740	0.000	0.000	0.000
load	610132	0.000	0.000	-23.740	0.000	0.000	0.000
# Extreme Passenger Car Bogie Loads							
#	Node	X	Y	Z	Mx	My	Mz
load	610032	0.000	0.000	-24.662	0.000	0.000	0.000
load	610112	0.000	0.000	-24.662	0.000	0.000	0.000

Figure B-52. Dead loads for train car-bodies and bogies.

# Intermediate Passenger Car Bogie Loads							
#	Node	X	Y	Z	Mx	My	Mz
load	610042	0.000	0.000	-29.921	0.000	0.000	0.000
load	610052	0.000	0.000	-29.921	0.000	0.000	0.000
load	610062	0.000	0.000	-29.921	0.000	0.000	0.000
load	610072	0.000	0.000	-29.921	0.000	0.000	0.000
load	610082	0.000	0.000	-29.921	0.000	0.000	0.000
load	610092	0.000	0.000	-29.921	0.000	0.000	0.000
load	610102	0.000	0.000	-29.921	0.000	0.000	0.000
# Power and Extreme Passenger Car Wheel Loads							
#	Node	X	Y	Z	Mx	My	Mz
load	70011	0.000	0.000	-10.055	0.000	0.000	0.000
load	70012	0.000	0.000	-10.055	0.000	0.000	0.000
load	70021	0.000	0.000	-10.055	0.000	0.000	0.000
load	70022	0.000	0.000	-10.055	0.000	0.000	0.000
load	70031	0.000	0.000	-10.055	0.000	0.000	0.000
load	70032	0.000	0.000	-10.055	0.000	0.000	0.000
load	80011	0.000	0.000	-10.055	0.000	0.000	0.000
load	80012	0.000	0.000	-10.055	0.000	0.000	0.000
load	80021	0.000	0.000	-10.055	0.000	0.000	0.000
load	80022	0.000	0.000	-10.055	0.000	0.000	0.000
load	80031	0.000	0.000	-10.055	0.000	0.000	0.000
load	80032	0.000	0.000	-10.055	0.000	0.000	0.000
load	70111	0.000	0.000	-10.055	0.000	0.000	0.000
load	70112	0.000	0.000	-10.055	0.000	0.000	0.000
load	70121	0.000	0.000	-10.055	0.000	0.000	0.000
load	70122	0.000	0.000	-10.055	0.000	0.000	0.000
load	70131	0.000	0.000	-10.055	0.000	0.000	0.000
load	70132	0.000	0.000	-10.055	0.000	0.000	0.000
load	80111	0.000	0.000	-10.055	0.000	0.000	0.000
load	80112	0.000	0.000	-10.055	0.000	0.000	0.000
load	80121	0.000	0.000	-10.055	0.000	0.000	0.000
load	80122	0.000	0.000	-10.055	0.000	0.000	0.000
load	80131	0.000	0.000	-10.055	0.000	0.000	0.000
load	80132	0.000	0.000	-10.055	0.000	0.000	0.000

Figure B-53. Dead loads for power and extreme passenger car axle-wheels.

# Intermediate Passenger Car Wheel Loads							
#	Node	X	Y	Z	Mx	My	Mz
load	70041	0.000	0.000	-9.810	0.000	0.000	0.000
load	70042	0.000	0.000	-9.810	0.000	0.000	0.000
load	70051	0.000	0.000	-9.810	0.000	0.000	0.000
load	70052	0.000	0.000	-9.810	0.000	0.000	0.000
load	70061	0.000	0.000	-9.810	0.000	0.000	0.000
load	70062	0.000	0.000	-9.810	0.000	0.000	0.000
load	70071	0.000	0.000	-9.810	0.000	0.000	0.000
load	70072	0.000	0.000	-9.810	0.000	0.000	0.000
load	70081	0.000	0.000	-9.810	0.000	0.000	0.000
load	70082	0.000	0.000	-9.810	0.000	0.000	0.000
load	70091	0.000	0.000	-9.810	0.000	0.000	0.000
load	70092	0.000	0.000	-9.810	0.000	0.000	0.000
load	70101	0.000	0.000	-9.810	0.000	0.000	0.000
load	70102	0.000	0.000	-9.810	0.000	0.000	0.000
load	80041	0.000	0.000	-9.810	0.000	0.000	0.000
load	80042	0.000	0.000	-9.810	0.000	0.000	0.000
load	80051	0.000	0.000	-9.810	0.000	0.000	0.000
load	80052	0.000	0.000	-9.810	0.000	0.000	0.000
load	80061	0.000	0.000	-9.810	0.000	0.000	0.000
load	80062	0.000	0.000	-9.810	0.000	0.000	0.000
load	80071	0.000	0.000	-9.810	0.000	0.000	0.000
load	80072	0.000	0.000	-9.810	0.000	0.000	0.000
load	80081	0.000	0.000	-9.810	0.000	0.000	0.000
load	80082	0.000	0.000	-9.810	0.000	0.000	0.000
load	80091	0.000	0.000	-9.810	0.000	0.000	0.000
load	80092	0.000	0.000	-9.810	0.000	0.000	0.000
load	80101	0.000	0.000	-9.810	0.000	0.000	0.000
load	80102	0.000	0.000	-9.810	0.000	0.000	0.000

Figure B-54. Dead loads for intermediate passenger car axle-wheels.

# Rail Self Weight							
#	Node	X	Y	Z	Mx	My	Mz
load	11001	0.000	0.000	-1.661	0.000	0.000	0.000
load	11002	0.000	0.000	-1.661	0.000	0.000	0.000
load	11003	0.000	0.000	-1.661	0.000	0.000	0.000
load	11004	0.000	0.000	-1.661	0.000	0.000	0.000

Figure B-55. Dead loads for rail 1 (first four nodes).

# Track Plate Self Weight							
#	Node	X	Y	Z	Mx	My	Mz
load	52001	0.000	0.000	-35.196	0.000	0.000	0.000
load	52002	0.000	0.000	-35.196	0.000	0.000	0.000
load	52003	0.000	0.000	-35.196	0.000	0.000	0.000
load	52004	0.000	0.000	-35.196	0.000	0.000	0.000

Figure B-56. Dead loads for track plate for track 1 (first four nodes).

# Base Plate Self Weight							
#	Node	X	Y	Z	Mx	My	Mz
load	51001	0.000	0.000	-38.716	0.000	0.000	0.000
load	51002	0.000	0.000	-38.716	0.000	0.000	0.000
load	51003	0.000	0.000	-38.716	0.000	0.000	0.000
load	51004	0.000	0.000	-38.716	0.000	0.000	0.000

Figure B-57. Dead loads for base plate for track 1 (first four nodes).

# Bridge Girder Self Weight							
#	Node	X	Y	Z	Mx	My	Mz
load	90001	0.000	0.000	-625.249	0.000	0.000	0.000
load	90002	0.000	0.000	-625.249	0.000	0.000	0.000
load	90003	0.000	0.000	-625.249	0.000	0.000	0.000
load	90004	0.000	0.000	-625.249	0.000	0.000	0.000
load	90005	0.000	0.000	-625.249	0.000	0.000	0.000
load	90006	0.000	0.000	-625.249	0.000	0.000	0.000
load	90007	0.000	0.000	-625.249	0.000	0.000	0.000
load	90008	0.000	0.000	-625.249	0.000	0.000	0.000
load	90009	0.000	0.000	-625.249	0.000	0.000	0.000
load	90010	0.000	0.000	-625.249	0.000	0.000	0.000
load	90011	0.000	0.000	-625.249	0.000	0.000	0.000

Figure B-58. Dead loads for first bridge girder span.

# Pier Column Self Weight							
#	Node	X	Y	Z	Mx	My	Mz
load	111	0.000	0.000	-863.582	0.000	0.000	0.000
load	112	0.000	0.000	-863.582	0.000	0.000	0.000
load	113	0.000	0.000	-863.582	0.000	0.000	0.000
load	114	0.000	0.000	-863.582	0.000	0.000	0.000
load	115	0.000	0.000	-863.582	0.000	0.000	0.000

Figure B-59. Dead loads for first pier column.

# Foundation Self Weight							
#	Node	X	Y	Z	Mx	My	Mz
load	1	0.000	0.000	-6177.757	0.000	0.000	0.000
load	2	0.000	0.000	-6177.757	0.000	0.000	0.000
load	3	0.000	0.000	-6177.757	0.000	0.000	0.000
load	4	0.000	0.000	-6177.757	0.000	0.000	0.000
load	5	0.000	0.000	-6177.757	0.000	0.000	0.000
load	6	0.000	0.000	-6177.757	0.000	0.000	0.000
load	7	0.000	0.000	-6177.757	0.000	0.000	0.000
load	8	0.000	0.000	-6177.757	0.000	0.000	0.000
load	9	0.000	0.000	-6177.757	0.000	0.000	0.000
load	10	0.000	0.000	-6177.757	0.000	0.000	0.000
load	11	0.000	0.000	-6177.757	0.000	0.000	0.000

Figure B-60. Dead loads for foundations.

```

# Define Gravity Analysis Parameters

# CONSTRAINTS handler-- Determines how the constraint equations are enforced in the analysis
constraints Penalty !el15 !el16;          # Penalty Method: Uses penalty numbers to enforce constraints

# DOF NUMBERER -- Numbers the degrees of freedom in the domain
numberer RCM;                            # RCM: Renumbers the DOF to minimize the matrix band-width using the Reverse Cuthill-McKee algorithm

# Solution ALGORITHM -- Iterates from the last time step to the current
set algorithmTypeGravity Newton;         # Newton's solution algorithm: Updates tangent stiffness at every iteration
algorithm $algorithmTypeGravity;

# CONVERGENCE test -- Determines if convergence has been achieved at the end of an iteration step
set Tol 1.0e-6;                          # Tolerance
set maxNumIterGravity 100;                # Max number of iterations
set printFlagGravity 1;                  # Flag used to print information on convergence (optional)
set TestTypeGravity NormDispIncr;        # NormDispIncr: Specifies a tolerance on the norm of the displacement increments at the current iteration
test $TestTypeGravity $Tol $maxNumIterGravity $printFlagGravity;

# SYSTEM -- Linear Equation Solvers (how to store and solve the system of equations in the analysis, solves Ku = P)
system UmfPack;                           # UmfPack: Direct UmfPack solver for unsymmetric matrices

# Static INTEGRATOR: -- Determines the next time step for an analysis
set NstepGravity 10;                     # Apply gravity in 10 steps
set DGravity [expr 1.0/$NstepGravity];    # First load increment
integrator LoadControl $DGravity;         # LoadControl: Specifies the incremental load factor to be applied to the loads in the domain

# ANALYSIS -- Defines what type of analysis is to be performed
analysis Static;                         # Static Analysis: Solves the KU = R problem, without the mass or damping matrices

```

Figure B-61. Definition of gravity load analysis parameters.

```

# Perform Gravity Analysis

analyze $NstepGravity;                   # Perform gravity analysis with the amount of steps defined
loadConst -time 0.0;                     # Sets loads constant and resets time to be 0.0

puts "#####"
puts "Gravity Analysis Complete"
puts "#####"

```

Figure B-62. Performance of gravity load analysis.

```

# Perform Modal Analysis

set numModes 10;                         # Number of eigenvalues desired
set lambda [eigen $numModes];            # Eigenvalues

set T {};                                 # Create an empty vector of T (Period)
set pi 3.141593

# Solve for periods using T=2*pi/sqrt(lambda)
foreach lam $lambda {
    lappend T [expr (2*$pi)/sqrt($lam)]
}

# Open output file
set period "DataLC8/Periods.txt"
set Periods [open $period "w"]

# Input data into the T vector
foreach t $T {
    puts $Periods "$t"
}

#Close the file
close $Periods

```

Figure B-63. Set up for modal analysis.

```

# Select two modes for Rayleigh Damping
set wi      [expr sqrt([lindex $ww 0])];      # Natural frequency of mode 1
set wj      [expr sqrt([lindex $ww 6])];      # Natural frequency of mode 6

# Define damping coefficient
set xi      0.02;                             # Damping Coefficient MIGHT CHANGE (2 or 5%)

# Define parameters for damping equation
set alphaM  [expr $xi*(2*$wi*$wj)/($wi+$wj)]; # M-prop. damping; D = alphaM*M
set betaKcurr 0.;                             # K-proportional damping; +betaKcurr*KCurrent
set betaKinit [expr $xi*(2)/($wi+$wj)];       # Initial stiffness proportional damping; +betaKinit*Kini
set betaKcomm 0.;                             # K-prop. damping parameter; +betaKcomm*KlastCommitt

rayleigh $alphaM $betaKcurr $betaKinit $betaKcomm; # Apply Rayleigh Damping

```

Figure B-64. Set up for Rayleigh damping.

```

# Define Dynamic Analysis Parameters
# CONSTRAINTS handler-- Determines how the constraint equations are enforced in the analysis
constraints Transformation;                    # Transformation Method: Performs a condensation of constrained degrees of freedom

# DOF NUMBERER -- Numbers the degrees of freedom in the domain
number RCM;                                  # RCM: Renumbers the DOF to minimize the matrix band-width using the Reverse Cuthill-McKee algorithm

# Solution ALGORITHM: -- Iterates from the last time step to the current
algorithmTypeDynamic Newton;                 # Newton: Uses the tangent at the current iteration to iterate to convergence
algorithm $algorithmTypeDynamic

# CONVERGENCE test -- Determines if convergence has been achieved at the end of an iteration step
set TolDynamic 1.e-9;                        # Tolerance
set maxNumIterDynamic 1000;                  # Maximum number of iterations that will be performed before "failure to converge" is returned
set printFlagDynamic 1;                      # Flag used to print information on convergence (optional)
set testTypeDynamic EnergyIncr;              # EnergyIncr: Specifies a tolerance on the inner product of the unbalanced load and displacement increments at the current iteration
test $testTypeDynamic $TolDynamic $maxNumIterDynamic $printFlagDynamic

# SYSTEM -- Linear Equation Solvers (how to store and solve the system of equations in the analysis, solves Ku = P)
systemTypeDynamic UmfPack;                   # UmfPack: Direct UmfPack solver for unsymmetric matrices
system $systemTypeDynamic

# Dynamic INTEGRATOR: -- Determines the next time step for an analysis
set NewmarkGamma 0.5;                        # Newmark-integrator gamma parameter
set NewmarkBeta 0.25;                        # Newmark-integrator beta parameter
set integratorTypeDynamic Newmark;
integrator $integratorTypeDynamic $NewmarkGamma $NewmarkBeta

# ANALYSIS -- Defines what type of analysis is to be performed
analysis Transient;                          # Transient Analysis: Solves the time-dependent analysis. The time step in this type of analysis is constant.

```

Figure B-65. Definition of seismic load analysis parameters.

```

# Define Ground Motion Parameters

set GMfile "RSN1004_NORTHR_SPV270";          # Ground-motion file from PEER
source ReadSMDFile.tcl;                      # Converts PEER ground-motion to an OpenSees readable format
set inFilename $GMfile.AT2;                  # Original filename and extension (AT2)
set outFilename $GMfile.g3;                  # Set variable holding new filename (PEER files have .at2/dt2 extension)
ReadSMDFile $inFilename $outFilename dt;     # Call procedure to convert the ground-motion file

set DT 0.005;                                # Time-step used in dynamic analysis
set Nstep 9557;                              # Number of steps in dynamic analysis

set GMfact $g;                               # Convert GM acceleration from "g" to m/s2

```

Figure B-66. Definition of ground motion parameters.

```

# Apply Ground Motion to Model

set IDloadTagx 400;                           # For uniformSupport excitation
set GMdirection_x 1;                          # Ground-motion x-direction
set xacc "Series -dt $DT -filePath $outFilename -factor $GMfact"; # Time series information
pattern UniformExcitation $IDloadTagx $GMdirection_x -accel $xacc; # Create uniform excitation

set IDloadTagy 500;                           # For uniformSupport excitation
set GMdirection_y 2;                          # Ground-motion y-direction
set yacc "Series -dt $DT -filePath $outFilename -factor $GMfact"; # Time series information
pattern UniformExcitation $IDloadTagy $GMdirection_y -accel $yacc; # Create uniform excitation

```

Figure B-67. Application of ground motion in both directions.

```

# Perform Dynamic Load Analysis

set ok [analyze $Nstep $DT];          # Perform analysis; returns ok = 0 if analysis was successful

# Create a Loop to Try Other Algorithms and Convergence Test Types if Initial Analysis Fails

set TmaxAnalysis [expr $Nstep*$DT];  # Maximum duration of ground-motion analysis

if {$ok != 0} {
  set ok 0;
  set controlTime [getTime];
  while {$controlTime < $TmaxAnalysis && $ok == 0} {
    set controlTime [getTime]
    set ok [analyze 1 $DT]
    if {$ok != 0} {
      puts "Trying Newton with Initial Tangent .."
      test NormDispIncr $Tol 1000 1
      algorithm Newton -initial
      set ok [analyze 1 $DT]
      test $testTypeDynamic $TolDynamic $maxNumIterDynamic 0
      algorithm $algorithmTypeDynamic
    }
    if {$ok != 0} {
      puts "Trying Broyden .."
      algorithm Broyden 8
      set ok [analyze 1 $DT]
      algorithm $algorithmTypeDynamic
    }
    if {$ok != 0} {
      puts "Trying NewtonWithLineSearch .."
      algorithm NewtonLineSearch .8
      set ok [analyze 1 $DT]
      algorithm $algorithmTypeDynamic
    }
  }; # end while loop
}; # end if ok != 0

puts "#####"
puts "Ground Motion Done. End Time: [getTime]"
puts "#####"

```

Figure B-68. Performance of seismic load analysis.